SPATIAL EVOLUTION OF OPTIMAL DISTURBANCES IN TWO FLUID BOUNDARY LAYERS

Luca Burini

Thermo-Fluids division

Department of Mechanical Engineering

Imperial College London, UK

Submitted in partial fulfilment of the requirements for the degree of Doctor of Philosophy

Department of Mechanical Engineering, Imperial College London

November 2013

Abstract

The transition to turbulence of a laminar boundary layer can be affected by free-stream turbulence (FST). High levels of FST can cause the exponentially growing Tollmien-Schlichting wave to be replaced by algebraically growing streaks. Transient growth theory successfully identified counter-rotating, streamwise-oriented vortices as optimal flow configuration for maximum streaks' amplification.

The introduction of a wall film can significantly alter the amplification and evolution of streaks, influencing the penetration of FST inside the boundary layers, and its effects on modal and non-modal stability are yet to be addressed within the appropriate spatially-developing framework.

In this work, the outcome of the introduction of a wall film on spatial transient amplification is analysed. Under base flow parallelism, optimal disturbances are computed by solving an optimal evolution problem. This study demonstrates that decreasing the viscosity of the film has a direct impact on the efficacy of the vortex tilting mechanism, leading to transient growth reduction.

The different spreading rates of the boundary layer edge and the interface height imply that the effects of stratification vary in the streamwise direction. The assumption of base flow parallelism is therefore relaxed and a framework for the determination of optimal disturbances and spatial transient amplification in two-phase spreading boundary layers is presented, using adjoint optimization techniques. It is shown that spreading effects can alter the prediction of linear stability on streaks amplification.

Beyond the early linear stage, the amplitude of the instability waves and interface deformation become appreciable and nonlinear effects cannot be neglected. As a result, an accurate description of the evolution of disturbances in two-fluid boundary layers must account for nonlinear interactions and mean flow distortion. Direct Numerical Simulation (DNS) with interface tracking is used to study the nonlinear evolution of the optimal disturbances in the two-fluid flow.

Acknowledgements

This research project would not have been possible without the support of many people.
The author wishes to express his gratitude to his supervisor, Dr. T. A. Zaki, who offered invaluable assistance, tireless support and guidance.
Special thanks also to all his group members: Dr. S. Y. Yung, Dr. K. Nolan, Dr. P. Ray and Sandeep, Nick, Laura, Tom, Ed, Philipp, Akshat, Jacob, David for sharing joys and pains of this journey.
The author would also like to acknowledge the Grantham Institute for Climate Change for the financial support.

My deepest love and gratitude go to my family; for your empathetic support and priceless advice. Thank you.

Disclaimer

I, Luca Burini, hereby declare that the work contained within this thesis is original and my own, except from that which is appropriately credited to others. All quotations have been distinguished by quotation marks and all sources of information, text, illustration, tables, images etc. have been specifically acknowledged. The Direct Numerical Simulations reported in this work were carried out by the Author; the code and the simulation setup have been kindly provided by Dr. Zaki and Dr. Jung, to whom the Author is extremely grateful.

Copyright

The copyright of this thesis rests with the author and is made available under a Creative Commons Attribution Non-Commercial No Derivatives licence. Researchers are free to copy, distribute or transmit the thesis on the condition that they attribute it, that they do not use it for commercial purposes and that they do not alter, transform or build upon it. For any reuse or redistribution, researchers must make clear to others the licence terms of this work.

"It is not the critic who counts: not the man who points out how the strong man stumbles or where the doer of deeds could have done better. The credit belongs to the man who is actually in the arena, whose face is marred by dust and sweat and blood, who strives valiantly, who errs and comes up short again and again, because there is no effort without error or shortcoming, but who knows the great enthusiasms, the great devotions, who spends himself for a worthy cause; who, at the best, knows, in the end, the triumph of high achievement, and who, at the worst, if he fails, at least he fails while daring greatly, so that his place shall never be with those cold and timid souls who knew neither victory nor defeat."

- "Citizenship in a Republic",
Speech at the Sorbonne, Paris, April 23, 1910
Theodore Roosevelt

To my family.

Contents

Abstract **3**

Acknowledgements **5**

Disclaimer **7**

Copyright **9**

1 Introduction **25**

1.1 Modal stability 27

1.1.1 Discrete modes 27

1.1.2 Continuous modes and their role in bypass transition 28

1.2 Transient amplification 33

1.2.1 Single-fluid flows 34

1.2.2 Two-fluid flows 36

1.2.3 The spatial approach 37

1.3 The non-linear stage 37

1.4 Problem definition 39

2 Non-modal stability: parallel base flow **43**

2.1 Introduction 43

2.2 Two-fluid boundary layer flow 44

2.3 The parallel base flow 46

2.3.1 Effect of a wall film on the base flow 47

2.4 The linear perturbation equations 49

2.4.1 Governing equations and boundary conditions 49

2.4.2 Polynomial eigenvalue problem 52

2.4.3 Numerical solution . . . 52
2.4.4 The discrete and continuous spectrum . . . 56
2.5 Optimal disturbances . . . 61
2.5.1 The single-fluid boundary layer . . . 66
2.5.2 The two-fluid boundary layer . . . 70
2.5.3 Effect of viscosity stratification . . . 75
2.5.4 Surface tension effects . . . 79
2.6 Conclusions . . . 83

3 Non-modal stability: non-parallel base flow 85
3.1 Introduction . . . 85
3.2 The non-parallel base flow . . . 87
3.3 The linear perturbation equations . . . 89
3.3.1 Governing equations and boundary conditions . . . 91
3.4 Optimal disturbances . . . 95
3.4.1 Numerical Method . . . 99
3.4.2 Non-parallel effects . . . 108
3.4.3 Optimal profiles . . . 111
3.4.4 Evolution . . . 114
3.5 Conclusions . . . 118

4 Non-linear evolution 123
4.1 Introduction . . . 123
4.2 The importance of non-linearity . . . 124
4.3 Direct numerical simulation . . . 125
4.3.1 Governing equations . . . 126
4.3.2 Inflow condition and domain size . . . 127
4.3.3 Treatment of the interface . . . 128
4.3.4 Mean flow distortion . . . 130
4.4 Evolution of optimal disturbances . . . 131
4.4.1 Linear regime . . . 132
4.4.2 Non-linear regime . . . 151
4.5 Conclusions . . . 170

5 Conclusions **173**

5.1 Summary and key results 173

5.1.1 Transient amplification under locally-parallel assumption 173

5.1.2 Transient amplification and nonparallelism 174

5.1.3 Non-linearity 175

5.2 Future work 176

A Two-fluid adjoint perturbation equations **179**

B Validation **189**

C Non-linear mapping of Chebyshev polynomials **195**

D Energy norm and expansion convergence **197**

E Other applications **199**

E.1 Adjoint Navier-Stokes equations 199

Bibliography **218**

List of Figures

1.1 Schematic of modal penetration for low- and high-frequency free-stream vortical perturbations (Saha, 2011) 30
1.2 Variation of penetration depth with viscosity ratio (Saha, 2011) 32
1.3 Schematic of transient growth due to non-orthogonal superposition of two vectors 36

2.1 Two-fluid boundary layer base flow 47
2.2 Effect of viscosity ratio on mean streamwise velocity 48
2.3 Integration contours in the complex k_x-plane (Ashpis & Reshotko, 1990) . 58
2.4 Discrete and continuous eigenfunctions of the Orr-Sommerfeld equation . 59
2.5 Optimal growth in single-fluid boundary layer 66
2.6 Optimal perturbation and response, $\chi_m = 1.5$ 67
2.7 Eigenvalue spectrum in single-fluid boundary layer 68
2.8 Surface and contour plots of maximum amplification for single-fluid boundary layer 69
2.9 Optimal growth in two-fluid boundary layer 71
2.10 Optimal perturbation and response, $\chi_{M_1} = 1.5$ 72
2.11 Downstream-propagating branch of the eigenvalue spectra for a two-fluid boundary layer, $\chi = 1.5$ 73
2.12 Optimal perturbation and response at $\chi_{M_2} = 24$ 73
2.13 Downstream-propagating branch of the eigenvalue spectra for a two-fluid boundary layer, $\chi = 24$ 74
2.14 Energy projection spectra for a two-fluid boundary layer 75
2.15 Amplification factor versus streamwise distance 76
2.16 G_{max} contours for various viscosity ratios 78
2.17 G_{max} surface and contours for $m = 0.55$ and $d = 0.1$ 79

2.18 G_{opt}, ω^o, k_z^o versus viscosity ratio m for $d = 0.05,\ 0.10\ 0.15$ 80
2.19 Reduction of maximum energy amplification versus viscosity ratio m . . . 81
2.20 Optimal reduction and optimal viscosity ratio versus inlet film thickness . 81
2.21 Effect of surface tension on transient growth 82

3.1 Effect of mean flow spreading on streamwise velocity response 86
3.2 Effect of viscosity on boundary layer thickness and interface location . . . 90
3.3 Streamwise evolution of maximum value of $\frac{\partial^2 U}{\partial x^2}$ 91
3.4 Optimal disturbance algorithm flowchart 99
3.5 Sketch of computational grid in physical and mapped space 100
3.6 Spatial evolution of mean streamwise velocity at various locations 109
3.7 Spatial variation of streamwise velocity gradients at the interface 110
3.8 Comparison between two-fluid parallel and spreading optimal growth . . . 111
3.9 Comparison of interface deflection under parallel and non-parallel mean flow 112
3.10 Comparison of optimal initial condition and maximum response in parallel and non-parallel case, $\omega^o = 0.0125$ 113
3.11 Comparison of optimal initial condition and maximum response in parallel and non-parallel case, $\omega^{so} = 0.0010$ 114
3.12 Optimal perturbation and non-parallel response 115
3.13 Contours of streamwise velocity of optimal initial perturbation 116
3.14 Contours of streamwise velocity of optimal initial perturbation 117
3.15 End view on zy-planes of non-parallel and parallel PBl at various streamwise locations, $\omega^o = 0.0125$ 119
3.16 End view on zy-planes of non-parallel and parallel PBl at various streamwise locations, $\omega^{so} = 0.0010$ 120
3.17 Parallel and non-parallel streamwise evolution of u 121

4.1 Mean flow distortion 131
4.2 Full flowfield distortion 131
4.3 Comparison of streamwise evolution of kinetic energy 133
4.4 Comparison of streamwise evolution of interface displacement 134

4.5 End view on zy-plane of PBl and DNS at various streamwise locations, $\epsilon = 0.1\%$, $\omega^o = 0.0125$ 136
4.6 Close view of zy-plane of PBl and DNS at various streamwise locations, $\epsilon = 0.1\%$, $\omega^o = 0.0125$ 137
4.7 Side view of contours of instantaneous fluctuation, $\epsilon = 0.1\%$, $\omega^o = 0.0125$ 138
4.8 Side view of contours of conditional averaged u fluctuation, $\epsilon = 0.1\%$, $\omega^o = 0.0125$ 139
4.9 Side view of contours of conditional averaged v fluctuation, $\epsilon = 0.1\%$, $\omega^o = 0.0125$ 140
4.10 Side view of contours of conditional averaged w fluctuation, $\epsilon = 0.1\%$, $\omega^o = 0.0125$ 140
4.11 Maximum of conditional averaged u fluctuation, $\epsilon = 0.1\%$, $\omega^o = 0.0125$ . . 141
4.12 Maximum of conditional averaged v fluctuation, $\epsilon = 0.1\%$, $\omega^o = 0.0125$ . . 142
4.13 Maximum of conditional averaged w fluctuation, $\epsilon = 0.1\%$, $\omega^o = 0.0125$. 142
4.14 End view on zy-planes of DNS at various streamwise locations, $\epsilon = 0.1\%$, $\omega^{so} = 0.0010$ 144
4.15 Close view of zy-planes of DNS at various streamwise locations, $\epsilon = 0.1\%$, $\omega^{so} = 0.0010$ 145
4.16 Side view of contours of instantaneous fluctuations, $\epsilon = 0.1\%$, $\omega^o = 0.0125$ 146
4.17 Side view of contours of conditional averaged u fluctuation, $\epsilon = \{0.1\%\}$, $\omega^{so} = 0.0010$ 147
4.18 Side view of contours of conditional averaged v fluctuation, $\epsilon = \{0.1\%\}$, $\omega^{so} = 0.0010$ 148
4.19 Side view of contours of conditional averaged w fluctuation, $\epsilon = \{0.1\%\}$, $\omega^{so} = 0.0010$ 148
4.20 Maximum of conditional averaged u fluctuation, $\epsilon = 0.1\%$, $\omega^{so} = 0.0010$. 149
4.21 Maximum of conditional averaged v fluctuation, $\epsilon = 0.1\%$, $\omega^{so} = 0.0010$. 149
4.22 Maximum of conditional averaged w fluctuation, $\epsilon = 0.1\%$, $\omega^{so} = 0.0010$. 150
4.23 Comparison of streamwise evolution of kinetic energy, $\epsilon = \{0.1\%, 0.5\%\}$. 151
4.24 Comparison of streamwise evolution of interface displacement, $\epsilon = \{0.1\%, 0.5\%\}$ 151
4.25 Comparison of streamwise evolution of kinetic energy, $\epsilon = \{0.1\%, 0.5\%\}$. 152
4.26 Comparison of streamwise evolution of interface displacement, $\epsilon = \{0.1\%, 0.5\%\}$ 152

4.27 End view on zy-plane of DNS at various streamwise locations, $\epsilon = \{0.1\%\, 0.5\%\}$, $\omega^o = 0.0125$ 154

4.28 Close view of zy-plane of DNS at various streamwise locations, $\epsilon = \{0.1\%,\ 0.5\%\}$, $\omega^o = 0.0125$ 155

4.29 Side view of contours of instantaneous u fluctuation, $\epsilon = \{0.1\%,\ 0.5\%\}$, $\omega^o = 0.0125$ 156

4.30 Side view of contours of conditional averaged u fluctuation, $\epsilon = \{0.1\%,\ 0.5\%\}$, $\omega^o = 0.0125$ 157

4.31 Side view of contours of conditional averaged v fluctuation, $\epsilon = \{0.1\%,\ 0.5\%\}$, $\omega^o = 0.0125$ 158

4.32 Side view of contours of conditional averaged w fluctuation, $\epsilon = \{0.1\%,\ 0.5\%\}$, $\omega^o = 0.0125$ 158

4.33 Maximum of conditional averaged u fluctuation, $\epsilon = 0.5\%$, $\omega^o = 0.0125$ . . 159

4.34 Maximum of conditional averaged v fluctuation, $\epsilon = 0.5\%$, $\omega^o = 0.0125$ . . 159

4.35 Maximum of conditional averaged w fluctuation, $\epsilon = 0.5\%$, $\omega^o = 0.0125$. 160

4.36 End view on zy-planes of DNS at various streamwise locations, $\epsilon = \{0.1\%,\ 0.5\%\}$, $\omega^{so} = 0.0010$ 162

4.37 Close view of zy-planes of DNS at various streamwise locations, $\epsilon = \{0.1\%,\ 0.5\%\}$, $\omega^{so} = 0.0010$ 163

4.38 Side view of contours of instantaneous u fluctuation, $\epsilon = \{0.1\%,\ 0.5\%\}$, $\omega^{so} = 0.0010$ 164

4.39 Side view of contours of conditional averaged u_{rms} fluctuation, $\epsilon = \{0.1\%,\ 0.5\%\}$, $\omega^{so} = 0.0010$ 165

4.40 Side view of contours of conditional averaged v_{rms} fluctuation, $\epsilon = \{0.1\%,\ 0.5\%\}$, $\omega^{so} = 0.0010$ 166

4.41 Side view of contours of conditional averaged w_{rms} fluctuation, $\epsilon = \{0.1\%,\ 0.5\%\}$, $\omega^{so} = 0.0010$ 166

4.42 Maximum of conditional averaged u fluctuation, $\epsilon = \{0.1\%,\ 0.5\%\}$, $\omega^{so} = 0.0010$ 167

4.43 Maximum of conditional averaged v fluctuation, $\epsilon = \{0.1\%,\ 0.5\%\}$, $\omega^{so} = 0.0010$ 168

4.44 Maximum of conditional averaged w fluctuation, $\epsilon = \{0.1\%, 0.5\%\}$, $\omega^{so} =$ 0.0010 168

B.1 Two-fluid boundary layer eigenvalue spectrum validation 190
B.2 Optimal growth in single fluid Blasius boundary layer validation 191
B.3 Optimal growth in two-fluid boundary layer validation 191
B.4 Streamwise evolution of kinetic energy validation 192
B.5 Two-fluid temporal channel flow eiganvalue validation 193
B.6 Two-fluid temporal channel flow transient growth validation 194

C.1 Chebyshev collocation points 196

D.1 Energy norm convergence 198

Chapter 1

Introduction

Boundary layer flows are observed in many areas of scientific and technical interest ranging from automobile and aircraft aerodynamics to large-scale atmospheric flows. These flows transition from a laminar to a turbulent state due to the presence of disturbances. Transition to turbulence can be considered as a progression of events preceding the onset of turbulence. These involve generation of disturbances from surface roughness or penetration of surrounding disturbances into the boundary layer and their linear and non-linear amplification; this can trigger secondary effects, which might lead to the onset of turbulence. Transitional flows are observed over blades in turbines and can be responsible for loss in efficiency (Hodson & Howell, 2005); this loss can be reduced by controlling the transitional features of the flow (Zhang *et al.*, 2006). A delay in transition is often sought in the aircraft industry as it reduces the drag force leading to better fuel efficiency, longer range and superior speed (Reed *et al.*, 1996; Gad-el Hak, 2000; Kim & Bewley, 2007). Surface roughness, acoustic and vorticity perturbations are some of the sources of disturbances that affect the transition process (Saric *et al.*, 2002). In particular, free-stream disturbances can trigger different transition scenarios, depending on the initial amplitude. Under extremely low levels of free-stream turbulence (FST), boundary layers may be subject to an exponentially-growing instability, the Tollmien-Schlichting (TS) wave (Tollmien, 1929; Schlichting, 1933), which amplifies and undergoes a secondary instability, followed by the breakdown of laminar flow into turbulent spots (Saric *et al.*, 2002). This path to transition has been referred to as the *natural route*. An increased level of FST can, however, force transition of boundary layers from laminar to turbulent regime on a timescale much shorter than those typical for TS waves.

This process is known as *bypass transition*, a term emphasising that the growth of two-dimensional waves and their subsequent secondary instability is bypassed. There is a significant body of literature, in recent years, that explains the origin of bypass transition in boundary layers. Some decisive steps forward were the works by Butler & Farrell (1992) on transient growth and amplification of streaks, by Jacobs & Durbin (1998) on penetration of vortical modes in boundary layers and by Andersson *et al.* (2001) on secondary instability and breakdown of boundary layer streaks.
Hence, the route to turbulence under bypass transition can be summarised into three main steps:

i) receptivity and penetration of free-stream perturbations into the boundary layer;

ii) linear and subsequent nonlinear amplification of perturbation streaks;

iii) secondary instability and breakdown to turbulence.

This sequence of events can be modified or controlled by active or passive control systems. In particular, the presence of wall films can impact the route to transition of boundary layers. For instance, the aerodynamic performance of an aircraft wing diminishes in the presence of de-icing agents during take-off (Yih, 1990; Ozgen *et al.*, 1998, 2002) and the instability of two-fluid flow affects the heat transfer rate in cooling flows. Thin wall-film flows are also relevant to environmental applications. For example, tropospheric winds create wind-driven surface currents that penetrate only a few hundred meters into the water surface (Beres *et al.*, 2002). In this work, the effect of a thin wall-film sheared by an external stream with different viscosity on stage ii) is investigated.

The dynamics of two-fluid boundary layers is governed by the Navier-Stokes (NS) equations. The motivation for this study is to model the early linear amplification mechanism in two-fluid parallel and spatially-evolving boundary layers within the scope of linear stability theory, and to discuss non-linear effects at a later stage. Linear stability analysis concerns the temporal or spatial response of a flow to an infinitesimal perturbation of its basic state, which is a solution of the linearised Navier-Stokes equations. The assumption of infinitesimal perturbations allows for a linearization of the NS equations, leading to an equivalent set of equations that describe the evolution of perturbation's normal velocity and vorticity, named the Orr-Sommerfeld and Squire equations.

The energy growth of infinitesimal disturbances can be exponentially growing or decaying; before reaching its asymptotic state, the perturbation energy can exhibit a transient state. Exponential or transient energy growth are key in the determination of how the base flow reaches the transitional state. In particular, transient amplification can lead to bypass transition scenario. The effects of the introduction of a thin wall-film on transient growth are investigated in this work. The focus is on the characterisation of the spatial amplification mechanism, as it is more suitable for the analysis of spatially-developing flows.

1.1 Modal stability

Two-fluid sheared flows have practical applications in lubrication and coating processes, cooling systems and environmental flow modelling, ranging from low to high Reynolds numbers. The asymptotic stability of such generic configuration has attracted the interest of many researchers, who investigated the eigenvalue spectrum of the Orr-Sommerfeld and Squire equations. In the case of unbounded flows, these exhibit a discrete and a continuous set of modes (Grosch & Salwen, 1978).

1.1.1 Discrete modes

The study of the discrete spectrum in single-fluid boundary layers is historically well-established and concerns the unstable modes in the eigenvalue spectrum of the Orr-Sommerfeld equation. The minimum Reynolds number at which an exponentially unstable mode is found is defined as the critical Reynolds number, beyond which the flow is unstable to infinitesimal perturbations. For example, the natural transition process in a Blasius boundary layer is governed by the growth of the TS wave. The introduction of a wall film alters the stability of the boundary layer by introducing additional unstable modes, due to the presence of an interface.

Two-fluid stability was first addressed by the pioneering work of Miles (1960), Miles (1962*a*,*b*), Yih (1967), Phillips (1957) and Benjamin (1959), who studied the stability of a liquid film sheared by a turbulent boundary layer and pointed out that the introduction of a wall-film of different viscosity can significantly alter the stability of the boundary layer. In fact, theoretical investigations by Hooper & Boyd (1987), Yih (1990), Boomkamp

et al. (1997), Ozgen *et al.* (1998) and Miesen & Boersma (1995) reveal the presence of additional instabilities due to the film and the interface, different from the TS waves.

Yih (1967) investigated the presence of a long-wavelength interfacial instability. The instability, named "soft mode" is generated by viscosity jump across the interface in two-fluid flows. In the long wavelength limit, the author derived an asymptotic solution to the Orr-Sommerfeld equation for two-layer Couette and Poiseuille flows. He also demonstrated that the instability growth rate depends on the viscosity ratio, density ratio and depth ratio of the two layers and that it can exist at any Reynolds number. Renardy (1987) demonstrated that the soft mode is stable when the lower layer is thinner and less viscous than the upper layer.

Hooper & Boyd (1983) investigated short wavelength instability of two-layer flows by considering unbounded Couette flow. They concluded that such flows are always unstable with respect to short wavelength perturbations, although surface tension was found to have a stabilising effect. Hinch (1984) proposed an explanation of the physical mechanism driving the short wavelength instability. This is given by phase differences between vorticity fluctuations in the top and bottom fluid, thereby causing amplification of the disturbance at the interface. Considering realistic values of surface tension, Hinch concluded that the short wavelength instability is unlikely to be observed in experiments.

At high Reynolds numbers, when the kinematic viscosity of the lower bounded fluid is less than that of the upper fluid, another kind of instability arises (Hooper & Boyd, 1987). This instability, named *High Reynolds number instability*, is different from the TS wave and it derives its energy largely from the Reynolds stress in the lower fluid; its wavelength is of the order of the film thickness and it is not affected by surface tension.

1.1.2 Continuous modes and their role in bypass transition

All the exponential instabilities belong to the discrete part of the eigenvalue spectrum. While the effects of discrete instabilities on transition have been clear since the origin of linear stability theory, the role of the continuous part of the spectrum arising from the stability analysis of a parallel boundary layer flow was not fully understood until recent years. Despite being asymptotically stable, continuous modes play a crucial role in the transition process. Since the majority of the literature on continuous modes is for single-fluid boundary layers, this review is centred on the single-fluid problem.

Unlike the eigenfunctions of the discrete modes, the continuous modes are oscillatory in the free stream and decay inside the boundary layer. Salwen & Grosch showed that the discrete and continuous parts of the eigenvalue spectrum of the Orr-Sommerfeld equation form a complete basis (Salwen & Grosch, 1981). Therefore, their superposition can represent any arbitrary disturbance. In particular, due to their oscillatory structure in the free-stream and decaying behaviour inside the boundary layer, continuous modes have been used to model FST and they represent a connection between free stream vortical disturbances and the boundary layer (Zaki & Durbin, 2005, 2006).

The penetration of free-stream disturbances inside the boundary layer is particularly relevant to bypass transition. The ability of free-stream disturbances to penetrate boundary layers is limited by the mean shear. In the inviscid limit, the boundary layer is completely isolated from free-stream disturbances; this phenomenon is known as *shear-sheltering*. At finite Reynolds numbers, the effect of sheltering is weaker, allowing some external disturbances to penetrate the shear. Shear-sheltering of the continuous Orr-Sommerfeld modes for a piecewise linear and infinitely-deep-single fluid boundary layer was studied by Jacobs & Durbin (1998), who showed that penetration is inversely proportional to the Reynolds number, Re, and the disturbance frequency, ω.

Due to the inviscid nature of the shear-sheltering phenomenon, the presence of a thin wall-film of lower viscosity should promote the ability to filter high-frequency vortical perturbations and therefore enhance the boundary layer stability. Penetration in single- and two-fluid boundary layers has been addressed by Zaki & Saha (2009). They carried out an extensive study on penetration of free-stream modes in single- and two-fluid boundary layers using an asymptotic solution of the Orr-Sommerfeld equation. In single-fluid boundary layers, they identified three asymptotic regimes, which are determined by the ratio of the diffusive to the convective terms in the the vorticity equation. In the shear-sheltering regime, the oscillatory free-stream disturbances decay exponentially at the edge of the boundary layer. In the viscous regime, continuous modes penetrate the boundary layer. In the intermediate regime, a composition of the previous two behaviours can be found. Saha (2011) proposed a physical interpretation of modal penetration by considering the relative motion of a free-stream vortical mode and a point P within the shear (figure 1.1). The vortical mode at the edge of the boundary layer convects downstream at speed $c = U_\infty$, and point P has velocity $U(p) = U_\infty + \tau Y$. The influence

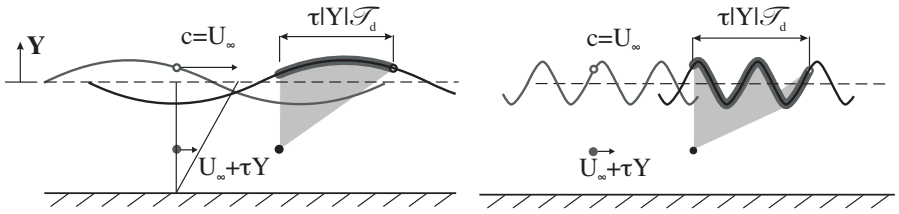


Figure 1.1: Schematic of modal penetration for low- and high-frequency free-stream vortical perturbations (Reproduction of figure 3.10 of Saha (2011)).

of the free-stream disturbance reaches P by wall-normal diffusion *only*. Within the diffusion time-scale, $\mathscr{T}_d \equiv 1/k_y^2\nu$, the free-stream boundary condition which affects P varies due to the relative motion of the wave and the shear flow. As a result, point P is exposed to a number s of wavelengths of the free-stream disturbance, where s is given by,

$$s = \frac{(c - U(p))\,\mathscr{T}_d}{1/k_x} = \frac{k_x \tau |Y|}{k_y^2 \nu}.$$

Note that s is the ratio of relative streamwise convection and wall-normal diffusion time-scales.

For low-k_x, or streamwise elongated waves, $s \to 0$ and the perturbation at the edge of the boundary layer appears seemingly steady relative to point P, over the diffusion time scale $\mathscr{T}_d$. As a result, a free-stream vortical mode diffuses effectively into the boundary layer shear in this limit. On the other hand, for short waves, s tends to ∞ and the edge condition appears to be changing very rapidly with respect to point P. The net effect over the time scale $\mathscr{T}_d$ is a near-zero edge condition relative to point P. As a result, the penetration of high-k_x vortical modes is limited. The filtering effect of high-frequencies is enhanced by the shear, $s \propto k_x \tau Y$, and hence the terminology "shear-sheltering". The precise mechanism is due to the difference in convective speeds between the free-stream perturbation and the flow inside the boundary layer. Therefore, shear-sheltering is cumulative, and s increases with depth. When the convection and diffusion terms are approximately equal, $s \sim O(1)$, and the perturbation is able to partially penetrate the boundary layer, but decays due to the cumulative influence of the shear. Therefore, the vorticity eigenfunctions in this regime are oscillatory near the edge of the boundary layer and exponentially decaying in the near-wall region.

In two-fluid boundary layers, the penetration of vortical modes into the lower fluid

was shown to depend on the viscosity ratio. In particular, Saha (2011) showed that the normal wave number of eigenfunctions in the bottom layer is:

$$\kappa_d = \sqrt{\frac{\nu_T}{\nu_B}(k_x^2 + k_y^2 + k_z^2) - (k_x^2 + k_z^2)}, \tag{1.1}$$

hence the eigensolution in the bottom layer change from oscillatory to exponential behaviout at a critical viscosity ratio $(\nu_B/\nu_T)_c = (k_x^2 + k_y^2 + k_z^2)/(k_x^2 + k_z^2)$. For a viscosity ratio ν_B/ν_T lower than the critical value, an oscillatory solution is obtained; for ν_B/ν_T greater than the critical ratio, the solution is exponential. The change in the wall-normal wavenumber is significant in correctly explaining penetration of vortical disturbances in two-fluid boundary layer. In the single fluid problem, it was shown that modal penetration into the shear is proportional to $k_y^2\nu/k_x\tau\delta$, where k_y^2 is a parameter, and low viscosity implies weak penetration, while higher viscosity enhances penetration. This dependence is not, however, preserved in the two-fluid problem. Instead, the expression for penetration must be updated to account for the modified wave-number, $\kappa_d^2\nu_B/k_x\tau\delta$. A reduction of ν_B, alone, would reduce penetration. However, the associated increase in κ_d causes a net increase in penetration at lower ν_B. Conversely, an increase in ν_B and the associated reduction in κ_d cause an overall reduction in penetration, opposite to the prediction for a single-fluid shear flow. In fact, the decay rate of the continuous modes is imposed by the free-stream viscosity. Due to the different viscosity in the lower fluid, a modified wavenumber in the bottom fluid ensures that the decay rate matches the one imposed by the free-stream. Therefore, lower viscosity films cause the modified wavenumber to increase, leading to deeper penetration, in contrast with the shear sheltering phenomenon in single-fluid boundary layers. Zaki & Saha also showed that penetration does not decrease monotonically as the film viscosity is reduced (figure 1.2). In fact, some ranges of viscosity and film thickness can enhance penetration of vortical modes into the boundary layer, contradicting the idea that a lower viscosity film would promote shear sheltering and hence enhance the stability of boundary layers.

The existence of a receptivity mechanism for free-stream vortical disturbances was suggested by the works of Klebanoff (1971), Westin *et al.* (1994), Matsubara & Alfredsson (2001) and the experiments of Kendall (1991), who showed that an increase in the FST

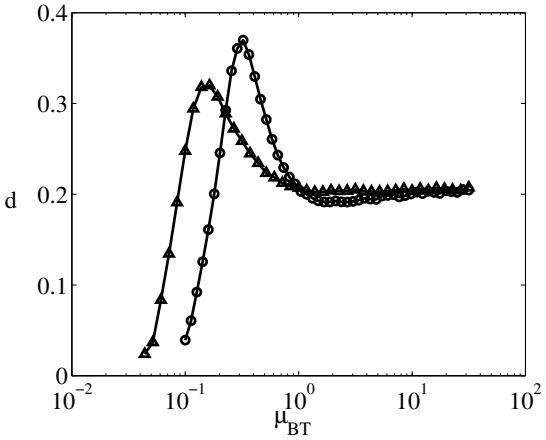


Figure 1.2: Variation of penetration depth d with viscosity ratio where $k_x Re_T = \frac{1}{100}, k_y = \frac{\pi}{4}, k_z = \pi$, $\circ$ $\delta_B = 0.3$, $\triangle$ $\delta_B = 0.2$, (reproduction of figure 3.21 of Saha (2011))

intensity would cause the growth of Klebanoff modes instead of discrete modes. Mechanisms for penetration of disturbances inside single-fluid boundary layers and their subsequent amplification were studied by Jacobs & Durbin, who performed numerical simulation of transition under the influence of free-stream turbulence in single-fluid boundary layers. There are two receptivity mechanism: a linear mechanism, which is more effective for low-frequency disturbances (Brandt *et al.*, 2004), and a non-linear mechanism which is effective in generating streaks for high-frequency perturbations (Berlin & Henningson, 1999). Jacobs & Durbin (2001) simulated the transition process under moderate levels of free-stream turbulence without a leading edge. They considered a turbulent inflow generated by the superposition of continuous Orr-Sommerfeld modes. Zaki & Durbin (2005, 2006) investigated the relation between continuous modes of the Orr-Sommerfeld spectrum and the generation of streaks, showing the existence of a coupling coefficient that measures the tendency of a vortical mode to generate streaks. They considered the interaction of pairs of continuous modes and demonstrated, via Direct Numerical Simulations, that different frequency components of the continuous spectrum play different roles in bypass transition. In particular, low-frequency modes can penetrate the shear and promote the formation of streaks, while the high-frequency modes trigger secondary instability, which may lead to breakdown. At this point, it is important to remark that continuous modes of the Orr-Sommerfeld equation establish a link between free-stream vortical disturbances and inception of perturbations inside the boundary layer; thus,

although decaying, they play an important role in transition.

The studies on continuous mode penetration in single- and two-fluid boundary layers showed that low-frequency disturbances more effectively trigger Klebanoff streaks. However, modal penetration itself does not explain the process of streak generation and subsequent amplification under the effects of FST. The fact that superposition of continuous modes can actually lead to amplification was pointed out by Trefethen *et al.* (1993). They showed that continuous modes of the Orr-Sommerfeld and Squire spectrum, although stable, can lead to significant level of energy amplification. They also suggested that considerable disturbance amplification would lead to a regime where nonlinearity is no longer negligible. To predict such behaviour, a transient (as opposed to asymptotic) stability analysis, referred to as *transient growth*, is essential (Schmid, 2007)

.

1.2 Transient amplification

Disturbances that have penetrated the boundary layer can be subject to amplification and evolve into streaks, which are three-dimensional structures. The origin of streaks at subcritical Reynolds number could not be attributed to the two-dimensional TS waves (Gaster, 1975). In fact, discrete instabilities are eigenmodes of the boundary layer, thefore they represent the asymptotic solution of the stability problem, after any transient has faded out. However, streaks which can be observed at subcritical Reynolds numbers cannot be generated by two-dimensional discrete instabilities. In addition, two-dimentional instabilities have a well defined streamwise extent, which does not relate to the presence of streamwise-independet streaks at subcritical Reynold number. The study of the initial value problem originally addressed the need to model the temporal or spatial evolution of disturbances from an initial condition to address the transient stability problem and fostered the development of transient growth theory over the last three decades. To this extent, the initial investigations intended to prove that amplification of disturbances different from TS waves was possible.

1.2.1 Single-fluid flows

The works of Ellingsen & Palm (1975), Landhal (1980), Gustavsson & Hultgren (1980), Benney & Gustavsson (1981), Gustavsson (1981), Hultgren & Gustavsson (1981) specifically showed that three-dimensional perturbations could amplify linearly with time in various shear flows. Ellingsen & Palm (1975) proved the existence of an inviscid algebraic instability, that could arise even without an inflectional mean velocity profile and was generated by a three-dimensional disturbances. The term "algebraic" was due to the fact that the streamwise velocity amplified linearly in time, unlike instabilities triggered by discrete modes, which developed exponentially. Landhal (1980) examined localized disturbances and concluded that the disturbance kinetic energy could grow indefinitely due to the inviscid lift-up mechanism. However, these studies were limited to inviscid disturbances. Gustavsson & Hultgren (1980) were the first to perform a viscous analysis of nearly streamwise independent disturbances. They showed that the growth of kinetic energy on short time-scale is damped by viscous dissipation, which dominates at long time. In the limit of streamwise independent perturbations, discrete modes are absent from the eigenvalue spectrum of the Orr-Sommerfeld and Squire equations. Thus, perturbations comprising of continuous modes only were proved to cause short time-scale growth, highlighting the importance of modal penetration. The inviscid phenomenon of algebraic instability together with viscous damping constitute what is known as *transient growth*. Due to the action of these two competing mechanisms, amplification curve versus time (or space) are characterised by a single peak, given by the combination of algebraic instability and viscous decay. Benney & Gustavsson (1981), Gustavsson (1981), Hultgren & Gustavsson (1981) investigated the initial value problem in bounded flows and indicated a resonance mechanism as possible explanation for transient growth. In fact, the initial value problem could be viewed as a forced response of normal vorticity to normal velocity component of the perturbation. Therefore resonance between the discrete Orr-Sommerfeld and Squire eigenvalue spectra results in short-time growth; after a certain time, the algebraic instability mechanism is overcome by viscous dissipation and the stability problem is dominated by its leading eigenmode.

The focus of researchers moved to the determination of the initial condition leading to maximum amplification. An innovative framework on optimal initial conditions

maximising the growth of the kinetic energy of the perturbation was provided by Butler & Farrell (1992). They optimised the perturbation energy over all possible initial conditions and computed the maximum possible energy amplification at any instant of time compared to the initial state. Therefore, the computation of optimal disturbances can predict the perturbations that are most likely to occur in flows exposed to random external fluctuations. The same approach was adopted by Henningson & Reddy (1994), who computed the maximum transient amplification of perturbation energy achievable, optimised over all initial conditions. In particular, they expanded the energy norm for a single-fluid system as a convergent series in terms of the eigenfunctions of the Orr-Sommerfeld and Squire equations, providing an efficient method for computation of optimal disturbances.

Transient growth computation have been generally successful in reproducing experiments. In particular, Andersson *et al.* (1999) and Luchini (2000) provided calculations of streamwise velocity components of the downstream response of an optimal disturbance in good agreement with the experimental results by Westin *et al.* (1994). Luchini (2000) also proposed a theoretical analysis that predicts the spanwise lengthscale observed in experiments.

The optimal disturbance in a boundary layer is comprised of counter-rotating streamwise-oriented vortices and causes strong streamwise velocity fluctuations, which are elongated in the streamwise direction. These structures, their spanwise spacing and the downstream development of their maximum streamwise velocity response, predicted by transient growth theory, are in agreement with the experimental observations of Klebanoff (1971), Kendall (1991), Westin *et al.* (1994) and Matsubara & Alfredsson (2001), who observed streamwise extended formations in their works.

From a mathematical point of view, the energy growth is the result of the non-normality of the linearized Navier-Stokes equations (Schmid & Henningson, 2001). In general, the dynamics of a non-normal system is governed by its entire spectrum of eigenmodes, not just by the leading one. Therefore, although individual eigenmodes may decay, their superposition can lead to algebraic growth on short time scales (Schmid, 2007). For instance, consider two vectors ϕ_1 and ϕ_2 at time t_0 and t_1, $t_1 > t_0$ with different decay rates and a measure E at a given time t, $E(\phi_1, \phi_2)(t) = \phi_1(t) + \phi_2(t)$; although ϕ_1 and ϕ_2 are decaying in time, their measure can grow: $E(t_1) > E(t_0)$. A

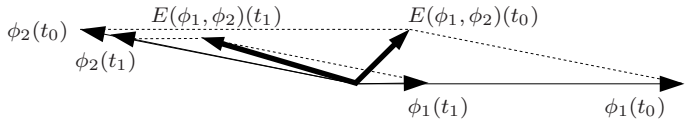


Figure 1.3: Schematic of transient growth due to non-orthogonal superposition of two vectors

sketch of this phenomenon is found in figure 1.3.

The studies on transient growth in single-fluid flows lead to similar investigations in two-fluid flows.

1.2.2 Two-fluid flows

Optimal disturbances in two-fluid shear flows have also been investigated. South & Hooper (1999), Malik & Hooper (2005), Malik & Hooper (2007), Yecko & Zaleski (2005*b*), and Yecko (2008) computed transient growth in Poiseuille and channel flows and two-fluid mixing layers, and reported streamwise oriented vortices in both fluids as initial conditions maximising an energy functional that accounts also for the presence of the interface. For instance, South & Hooper (1999) proposed a norm for two-fluid Poiseuille that includes the variation in viscosity between fluids; Yecko & Zaleski (2005*b*) instead formulated a norm that accounts for surface deflection in two-fluid mixing layers through the introduction of surface tension. The introduction of a term depending on the interface displacement addressed the limitations of the kinetic energy norm, where an unbounded interface displacement is possible. Amplification curves in two-fluid flows are characterised by the presence of multiple energy peaks that cannot be related to the combined action of algebraic instability and viscous dissipation only. An insight into multiple-peaks transient growth envelopes features in two-fluid parallel boundary layer can be found in Saha (2011). He investigated transient growth in two-fluid parallel temporal boundary layers and showed the presence of an additional instability mechanism associated with the interface, which affects the transient amplification curves and leads to multiple peaks. Saha also investigated transient growth reduction upon lowering the viscosity of the bottom fluid. He determined an optimal viscosity ratio and film thickness that result in maximum transient growth reduction.

1.2.3 The spatial approach

The majority of the aforementioned theoretical results were obtained within the framework of temporal theory, both for single- and two-fluid flows, while spatial amplification is observed in experiments. The problems of temporal and spatial maximum amplification are in fact different. The temporal analysis can be regarded as an optimization of initial disturbances at time $t = t_0$ to reach maximum amplification at later time t, whereas an initial value problem for spatial disturbances of prescribed frequency ω can be ill-posed. This is the case of absolutely unstable flows and it represents a main limitation in applying the same optimization procedures used in the temporal case for the spatial equivalent. In single-fluid flows, Schmid *et al.* (1994) carried out the first analysis on spatial transient growth. To overcome the ill-posedness, Luchini (1996, 2000) and Andersson *et al.* (1999) considered spatial non-modal growth in boundary layers within the scope of linearized boundary layer equations. A suitable method for analysis of spatial optimal disturbances in boundary layer flows within the scope of the linearized Navier-Stokes equations has been proposed by Tumin & Reshotko (2001). They showed that the flow-field downstream from a convectively-unstable disturbance source can be represented as an expansion in eigenfunctions of the downstream propagating branches of the continuous and discrete spectrum of the linearized Navier-Stokes equations plus any TS waves (if present). By selecting downstream modes, an optimal growth analysis based on the optimization of an initial value problem can be performed.

At time of writing, the author is not aware of a complete spatial framework for optimal disturbances in two-fluid flows. This will be object of discussion in this work.

1.3 The non-linear stage

Transition is a non-linear problem, but transient growth theory suggests a link between this phenomenon and the non-normality of the evolution operator arising from the linearization of Navier-Stokes equations (Schmid & Henningson, 2001). This is due to the fact that non-normality implies the potential for transient growth, which could trigger non-linearities that would prevent eventual viscous decay. Moreover, the redistribution of streamwise momentum by motion normal to the shear has been related to the three-dimensional character of transition (Henningson & Reddy, 1994). However, these

evidence do not provide a holistic explanation of the transition mechanism. To this end, efforts to identify the missing link between transient growth and transition can be found in literature. For example, Benney & Gustavsson (1981) investigated the class of non-linear interactions that could be triggered by transient growth; in single-phase boundary layers, Andersson *et al.* (2001) investigated the nonlinear evolution of optimal disturbances computed via the linear approach previously described, with the aim of developing a tool for prediction of transition. Schematically, transition and breakdown in boundary layers start with the formation of longitudinal streaks from streamwise vortices through the lift-up mechanism. These streaks grow and undergo secondary instabilities and eventually breakdown in turbulent spots. The importance of non-linearity in spatially developing two-fluid flows has already been pointed out by Cheung & Zaki (2010) in describing the evolution of disturbances beyond the early linear stage. They demonstrated that nonparallelism and nonlinear interactions can alter the prediction of locally-parallel, linear stability analyses and lead to the generation of smaller scale features in the flow.

Some effort has been placed in finding optimal disturbances that incorporate nonlinear dynamics. Zuccher *et al.* (2005) studied three-dimensional algebraic instability in a Blasius boundary layer in the nonlinear regime, showing that inlet streamwise vortices yield to largest transient growth, as in the linear case. However, Pringle & Kerswell (2010) focused on nonlinear disturbances in pipe flow and reached the conclusion that including nonlinearities in the optimal problem substantially changes the prediction from linear stability. Non-linear optimization of disturbances was found to be both computationally expensive and time consuming. Monokrousos (2011) presented some techniques to determine nonlinear optimal disturbances using DNS, via the adjoint looping method.

Referring to the work of Zuccher *et al.* (2005), in the present work linear optimal disturbance are computed and the effects of non-linearity are addressed at a later stage. In particular, linear and non-linear evolution of optimal disturbances are computed via DNS, in order to quantify the impact of nonlinearity on the linear amplification mechanism.

1.4 Problem definition

In the previous four sections, the reader has been provided with a brief overview of the instability mechanisms present in single- and two-fluid boundary layers. The role of continuous modes in the transition process was also discussed and particular importance was given to the fact that their penetration inside the boundary layer can trigger the algebraic instability. The algebraic instability generates Klebanoff modes from streamwise independent perturbations. Finally, the concept of optimal disturbances, their importance in transition and the implications of nonlinearities were introduced.

Boundary layer stability is an elaborate phenomenon, which is complicated further when a film of different viscosity is introduced at the wall. The presence of a wall-film of different viscosity alters the mean-flow profile and the introduction of an interface represents an additional source of disturbances. The objective of this work is to investigate the amplification mechanism within the spatial framework, which is the appropriate approach in the case of spatially developing flows, such as boundary layers. In particular, the effects of viscosity stratification and wall-film thickness on amplification are addressed. Moreover, only a few theoretical results on transient growth considered non-parallel effects of the mean flow (Luchini, 1996; Andersson *et al.*, 1999; Luchini, 2000). In this thesis, non-parallelism is included in the transient growth formulation and its effect on the amplification mechanism within the two-fluid setup is investigated.

Since the mathematical formulation of the optimal problem is based on linear theory, non-linear effects such as mean-flow distortion and modal interactions are not taken into account in the linear model presented. However, to show the non-linear evolution of spreading optimal disturbances in two-fluid boundary layers, direct numerical simulation (DNS) is used to correctly represent the linear and nonlinear growth of streaks.

The results presented in this work were computed at the subcritical Reynolds number $Re = 800$; this choice allowed the Author to relate the current investigation to the previous temporal work by Saha (2011) and to show streaks formation in DNS on a reasonable computation domain.

This thesis is organised into five chapters. In this chapter, the study of linear stability theory was motivated. Subsequently, the relevant literature on modal and non-modal stability in single- and two-fluid flows was reviewed. Chapter 2 deals with the spatial

transient growth of disturbances in two-fluid *parallel* boundary layers. At first, the equations governing the base flow and the effects of viscosity stratification on mean quantities are examined. Thereafter linear perturbation equations leading to the Orr-Sommerfeld and Squire spatial eigenvalue problem for two-fluid boundary layers are formulated. The eigenvalue spectrum and the complexity of the spatial initial value problem are explained. The optimization problem leading to the determination of optimal disturbances is formulated; details of the numerical solution are given and effects of viscosity stratification and film thickness are quantified. An optimal choice of parameters leading to the greatest reduction of transient growth is found.

In Chapter 3, the assumption of mean-flow parallelism is relaxed and a complete framework for the determination of *spatially developing* optimal disturbances is given. At first, the base flow dynamics are analysed; then linear perturbation equations under the boundary layer approximation are derived. The optimal growth problem in the case of spatially-dependent mean flow is formulated. The formulation makes use of the two-fluid adjoint perturbation equations, which are derived in Appendix A. Details of the numerical methods used are given. After the mathematical formulation is set, the effects of mean-flow spreading on the optimal set of parameters arising from the earlier parallel analyses are quantified. A new, spreading, optimal disturbance is computed and used as inlet perturbation for the non-linear calculations, described in Chapter 4. Non-linear evolution of the spatial optimal disturbance is analysed in Chapter 4.

The last chapter summarises the work presented and highlights the key results. Implications of current findings are made and a line of future work is drawn.

Appendices are very important to this work. In particular, Appendix A contains the complete and detailed derivation of the two-fluid adjoint perturbation equations for spreading disturbances. This formulation is core to the mathematical foundation of this thesis. It would deserve an entire chapter for its importance; there is not any work in literature, at time of writing, on adjoint equations for two-fluid flows.

Additional information and discussion on the validation of the results presented are in Appendix B. Appendix C is dedicated to spectral method used for the discretization of the governing equations. In particular, details of the non-linear mapping of Chebyshev polynomials are given. At last, a brief discussion on the energy norm adopted in the present work and its convergence is reported in Appendix D. Appendix E contains

additional derivation that might be useful to future students but are not core to this work.

Chapter 2

Non-modal stability: parallel base flow

2.1 Introduction

Free-stream perturbations can force transition of boundary layers on timescales much shorter than those typical for Tollmien-Schlichting (TS) waves, which lead to natural transition in Blasius boundary layers (Schubauer & Skramstad, 1941). When the growth of two-dimensional waves and their subsequent instability are bypassed, the transition process is named *bypass* transition. The penetration of normal velocity perturbations into the boundary layer can generate normal vorticity perturbations by a vortex-tilting mechanism (Trefethen *et al.*, 1993; Zaki & Durbin, 2005, 2006), which tilts vortex lines to generate vorticity (Panton, 1996). This results in the growth of streamwise velocity perturbations similar to the streaks observed in boundary layer transition (Zaki & Durbin, 2005).

Although the problem of transient evolution of linear perturbation in boundary layers suggests a spatial investigation (Andersson *et al.*, 1999; Zaki & Durbin, 2005; Brandt & Henningson, 2002), many researchers (Ellingsen & Palm, 1975; Landhal, 1980; Hultgren & Gustavsson, 1981; Salwen & Grosch, 1981; Butler & Farrell, 1992; S. C. Reddy & Henningson, 1993; Trefethen *et al.*, 1993; Schmid & Henningson, 2001; Schmid, 2007) have focused on its temporal formulation, due to its reduced complexity and computational cost. The work of Lasseigne *et al.* (1999) clearly established a connection between temporal and spatial evolution in the transient period. They investigated the temporal and spatial evolution of disturbances within a boundary layer by examining a series of initial value problems. A strong correlation between temporal and spatial results was found, suggesting that temporal and spatial analyses are, in some sense, equivalent. However,

they did not provide any theoretical explanation supporting this correlation; Tumin & Reshotko (2001) showed differences between temporal and spatial analyses. Therefore, the present work focuses on the spatial formulation for transient amplification in two-fluid shear flows, which requires the solution of a fourth-order non-linear eigenvalue problem and an initial boundary value problem.

The aim of this chapter is to:

(a) formulate the spatial stability problem in two-fluid boundary layers, under the assumption of parallel base flow;

(b) compute the spatial transient amplification;

(c) and to study the effect of a wall-film on transient evolution.

This chapter is arranged into 6 sections. The following section discusses the geometry and the two-fluid setup; §2.3 addresses the mean flow equations and the effect of viscosity stratification on the mean velocity profile. Section §2.4 gives the details of the governing equations and boundary conditions under the assumption of parallel base flow, along with the numerical procedure for the determination of the discrete and continuous spectrum. After a brief discussion of the challenges of a correct formulation of the initial value problem for spatial disturbances, the optimal disturbance problem is introduced and discussed in §2.5. Results of single- and two-fluid boundary layers are presented and an optimal choice of film-thickness and viscosity ratio providing maximum transient growth reduction are found. Conclusions and a summary of the key results of the chapter are in §2.6.

2.2 Two-fluid boundary layer flow

Consider the semi-infinite domain $\bar{\Omega} = \Omega \times [t_0,\, t_f]$; the space Ω is divided into two subspaces Ω_T and Ω_B separated by an interface Γ, such that $\Omega_T \cup \Omega_B = \Omega$ and $\Omega_T \cap \Omega_B = \Gamma$. The space Ω is a three-dimensional space $\Omega = \Omega_x \times \Omega_y \times \Omega_z = [x_0,\, x_f] \times \Omega_y \times (-\infty,\, +\infty)$. Consider an unsteady, incompressible two-fluid flow in $\bar{\Omega}$; the direction of the flow is denoted by $x \in \Omega_x$, $y \in \Omega_y$ is the normal direction, and $z \in \Omega_z$ denotes the spanwise direction. The flow comprises two fluids which belong to the subspaces Ω_T and Ω_B and uniquely identified by their physical properties density ρ_j and viscosity μ_j, where the subscript $j = \{T, B\}$ denotes the two subspaces. Note the two fluids are separated by the

interface Γ, which might in fact not have an explicit representation in the coordinates (x, y, z). However, in the case that Γ does not undergo topology changes and in the applications considered in this work, the interface set can be written as a function in $\bar{\Omega}$. Therefore, consider the normal direction Ω_y as $\Omega_y = \{[0, \mathcal{F}] \cup [\mathcal{F}, +\infty)\}$, where $\mathcal{F} = \mathcal{F}(x, z, t)$, $t \in [t_0,\, t_f]$. For each $t \in [t_0,\, t_f]$, the representation of the interface Γ is $d = d(x, z)$, such that $y > d$ identifies the top fluid and $y < d$ the bottom fluid. Top and bottom space are thus $\Omega_T = [x_0,\, x_f] \times [d, +\infty) \times (-\infty,\, +\infty)$ and $\Omega_B = [x_0,\, x_f] \times [0, d] \times (-\infty,\, +\infty)$, respectively.

The evolution in time and space of the velocity vector field $\mathcal{U}$ of the unsteady, incompressible two-fluid flow in $\bar{\Omega}$ is governed by the Navier-Stokes (NS) equations along with the continuity condition:

$$\partial_t \mathcal{U}_j + (\mathcal{U}_j \cdot \nabla)\mathcal{U}_j = -\frac{\nabla \mathcal{P}_j}{\rho_j} + \nu_j \Delta \mathcal{U}_j \tag{2.1}$$

$$\nabla \cdot \mathcal{U}_j = 0 \tag{2.2}$$

where $\mathcal{P}$ is the pressure field. The two fluids are separated by the interface, $\mathcal{F}$, so that $\forall y \geq \mathcal{F} :\ j = T$ and $\forall y \leq \mathcal{F} :\ j = B$.
Incompressibility condition imposes interfacial conditions on the velocity vector, $\mathcal{U}$, and the stress tensor, τ to be satisfied on $\mathcal{F}$:

$$[\![\mathcal{U} \cdot \hat{\mathbf{n}}]\!] = 0; \qquad [\![\mathcal{U} \cdot \hat{\mathbf{t}}]\!] = 0; \qquad [\![\tau \cdot \hat{\mathbf{n}}]\!] = [\![\mathcal{P}]\!]\hat{\mathbf{n}} - \sigma\kappa\hat{\mathbf{n}}; \qquad [\![\tau \cdot \hat{\mathbf{t}}]\!] = 0. \tag{2.3}$$

where $\hat{\mathbf{n}}$ and $\hat{\mathbf{t}}$ denote the unit normal and tangent vector to the interface, $\mathcal{F}$, the curvature of which is denoted by κ; the surface tension is σ.
The objective of stability theory is to determine the evolution of an infinitesimal disturbance $\mathbf{u}$ to the underlying mean flow $\mathbf{U}$, which is a solution of (2.1)-(2.2). The disturbance equations are derived considering the decomposition

$$\mathcal{U}_j = \mathbf{U}_j + \epsilon\hat{\mathbf{u}}_j \tag{2.4}$$

$$\mathcal{P}_j = P_j + \epsilon\hat{p}_j \tag{2.5}$$

of equations (2.1)-(2.2). The mean pressure, P, is perturbed by the pressure disturbance

$\hat{p}$.

When no topological changes take place, the interface displacement, $\mathcal{F} = \mathcal{F}(x, z, t) = f + \hat{f}$, follows the kinematic condition:

$$\left[\left(\frac{\partial}{\partial t} + \mathcal{U}_j \cdot \nabla\right)\mathcal{F}\right] \cdot \hat{\mathbf{n}} = \mathcal{U}_j \cdot \hat{\mathbf{n}}. \tag{2.6}$$

2.3 The parallel base flow

Far from the leading edge, the boundary layer flow can be considered parallel. Hence, consider a parallel two-fluid boundary layer flow of the form $\mathbf{U} = [U_j(y),\ 0,\ 0]$ in a semi-infinite domain Ω.

A representation of the base flow is shown in figure 2.1. We define r and m to be the ratios of densities and viscosities, respectively, i.e. $r = \frac{\rho_j}{\rho_T}$ and $m = \frac{\mu_j}{\mu_T}$ for $j = \mathsf{T}, \mathrm{B}$; the kinematic viscosities $\nu_j = \frac{\mu_j}{\rho_j}$ and their ratio is $n = \frac{m}{r}$; the free stream velocity is U^∞. The mean velocity profile is obtained by solving the two-fluid boundary layer equations presented in Nelson *et al.* (1995) with a parallel approximation according to the approach described in Schlichting (1987, pp. 187-191).
Introducing the boundary-layer variable $\mathtt{y} = y\sqrt{\frac{U^\infty}{2\nu_T x}}$, as $x \to +\infty$, the mean flow satisfies:

$$FF'' + \nu_j F''' = 0 \tag{2.7}$$

where $F = \frac{\Psi}{2\nu_T U^\infty x}$ with Ψ as the streamfunction, $F' = \frac{\partial F}{\partial \mathtt{y}}$, $U = U^\infty \frac{\partial F}{\partial \mathtt{y}}$. The interface height is denoted by $\mathtt{d} = d\sqrt{\frac{U^\infty}{2\nu_T x}}$. At $\mathtt{y} = \mathtt{d}$, continuity of velocities and stresses is enforced:

$$[\![F]\!] = 0\ ; \qquad \left[\!\!\left[\frac{\partial F}{\partial \mathtt{y}}\right]\!\!\right] = 0\ ; \qquad \left[\!\!\left[\frac{\partial^2 F}{\partial \mathtt{y}^2}\right]\!\!\right]_m = 0\ ; \tag{2.8}$$

where the operator $[\![\cdot]\!]$ denotes the change across the interface, $(\cdot)_T - (\cdot)_B$ and $[\![\cdot]\!]_m = (\cdot)_T - m(\cdot)_B$.
In addition, the free-stream and wall boundary conditions are:

$$F(0) = 0; \qquad \left.\frac{\partial F(\mathtt{y})}{\partial \mathtt{y}}\right|_{\mathtt{y}=0} = 0; \qquad \lim_{\mathtt{y}\to+\infty} \frac{\partial F(\mathtt{y})}{\partial \mathtt{y}} = 1. \tag{2.9}$$

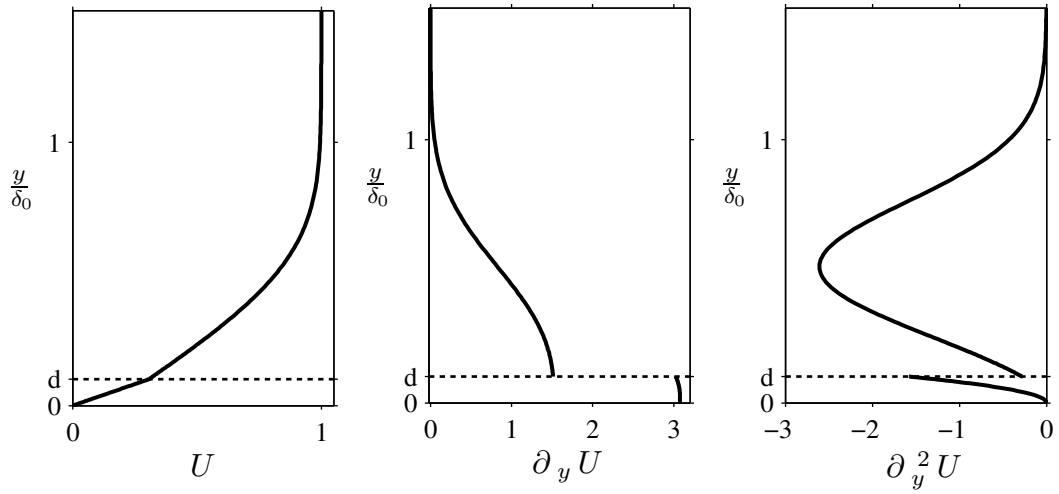


Figure 2.1: Two-fluid boundary layer base flow for viscosity ratio $m = 0.5$ and bottom fluid thickness $d = 0.1$

2.3.1 Effect of a wall film on the base flow

Stratification has a significant impact on the base flow. As the viscosity ratio m decreases, the boundary layer thickness, δ, shortens (figure 2.2b), making it an unsuitable lengthscale for stability calculations, due to the lack of correspondence between the results for different values of m. Hence, the single fluid Blasius boundary layer thickness $\delta_0 \equiv 4.9\sqrt{\frac{\nu_T x_0}{U^\infty}}$ is chosen as the reference lengthscale even for the two-fluid computations. Physical quantities are made dimensionless according to a length scale L and velocity scale U^*, set by the base flow. In particular, $U^* = U^\infty$, $\rho^* = \rho_T$, $\mu^* = \mu_T$. This yields the non-dimensional parameters, the Reynolds number, $Re = \frac{\rho^* U^* L}{\mu^*} = \frac{\rho_T U^\infty \delta_0}{\mu_T}$ and the Weber number, $We = \frac{\rho^* U^{*2} L}{\sigma} = \frac{\rho_T U^{\infty 2} \delta_0}{\sigma}$ where $L = \delta_0$ and σ is the surface tension. The Weber number We represents the ratio of inertial to capillary forces.

The mean shear distribution $\tau_{xy} = n\frac{\partial}{\partial y}U$, which plays a primary role in the transient amplification of disturbances, is also affected by viscous stratification. Figures 2.2c and 2.2d represent the quantities $d_y U$ and τ_{xy} respectively for values of the viscosity ratio $m = \{0.2,\ 0.5,\ 1,\ 2\}$. Reduction of the viscosity ratio m causes τ_{xy} to weaken in the top fluid and strengthen in the wall film, due to shear-stress continuity imposed by equation 2.8 at the mean interface location d, resulting in the thinning of the boundary layer thickness δ.

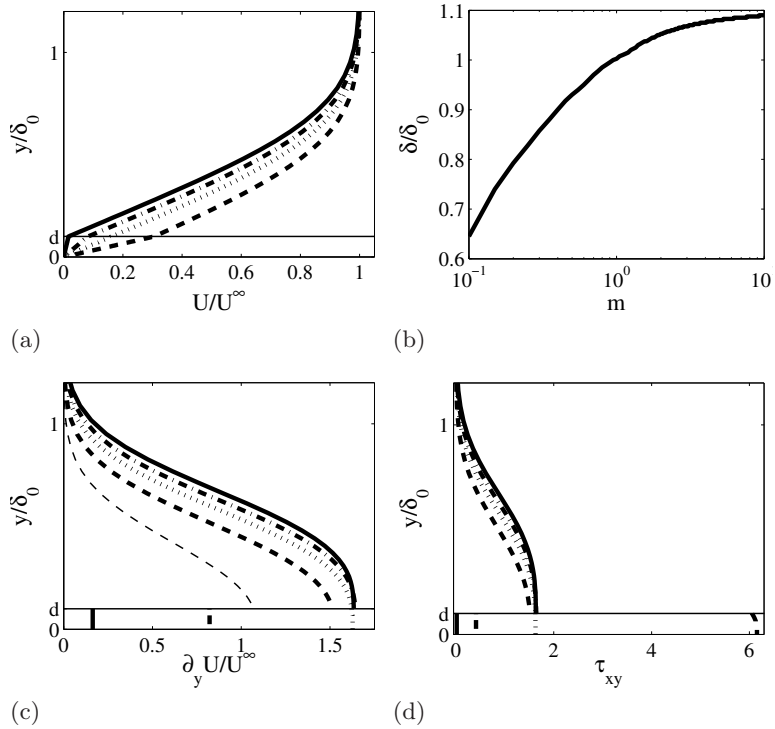


Figure 2.2: (2.2a) Effect of viscosity ratio on mean streamwise velocity U at inlet, $d_0 = 0.10$; (2.2b) Dependence of δ on viscosity ratio m; (2.2c) Effect of viscosity on mean $d_y U$ at inlet, $d_0 = 0.10$; (2.2d) Effect of viscosity on mean shear τ_{xy} at inlet, $d_0 = 0.10$. —— $m = 1$, -·- $m = 0.8$, · · · · $m = 0.6$,- - - $m = 0.4$, – – – $m = 0.2$

2.4 The linear perturbation equations

Linear perturbation equations for parallel, two-fluid flow are given in this section.
Let Ω be the semi-infinite domain with smooth boundary $\partial\Omega$ and let t be a given time, $t \in [t_0, t_f]$. Under the assumption that $\epsilon \ll 1$ and discarding terms of order $\mathcal{O}(\epsilon^2)$, for a vector function $\hat{\mathbf{u}} = (\hat{u}, \hat{v}, \hat{w})$ and a scalar function $\hat{p}$, the Linearized Navier-Stokes (LNS) equations describe the evolution of the disturbance field $(\hat{\mathbf{u}}, \hat{p})$ to the underlying mean flow $\mathbf{U}$ and mean pressure P in $\Omega \times [t_0, t_f]$:

$$\partial_t \hat{\mathbf{u}}_j + (\mathbf{U}_j \cdot \nabla)\, \hat{\mathbf{u}}_j + (\hat{\mathbf{u}}_j \cdot \nabla)\, \mathbf{U}_j = -\frac{\nabla \hat{p}_j}{\rho_j} + \nu_j \Delta \mathcal{U}_j \tag{2.10}$$

$$\nabla \cdot \hat{\mathbf{u}}_j = 0 \tag{2.11}$$

The additional boundary and initial conditions

$$\hat{\mathbf{u}}_j|_{\partial(\Omega_y \times \Omega_z)} = 0 \tag{2.12}$$

$$\hat{\mathbf{u}}_j|_{t=t_0} = \hat{\mathbf{u}}_{0_j} \tag{2.13}$$

make (2.10)-(2.13) a well-defined initial-boundary value problem for the disturbance field $(\hat{\mathbf{u}}, \hat{p})$.

2.4.1 Governing equations and boundary conditions

Homogeneity of streamwise and spanwise directions and time-periodicity allows the disturbance $\hat{\mathbf{u}}$ to be written in the form:

$$\hat{\mathbf{u}}_j(x, y, z, t) = \mathbf{u}_j(y) e^{ik_x x + ik_z z} e^{-i\omega t} \tag{2.14}$$

where k_x and k_z denote the streamwise and spanwise wavenumber and ω the temporal frequency. Under the assumption of parallel flow, i.e. $\mathbf{U} = [U(y), 0, 0]$, LNS equations can be written in terms of normal velocity $\hat{v}_j$ and normal vorticity $\hat{\eta}_j = ik_z \hat{u}_j - ik_x \hat{w}_j$,

leading to the well-known Orr-Sommerfeld (2.15) and Squire (2.16) equations:

$$\Big[(-i\omega + ik_x U_j) \left(\frac{\partial^2}{\partial y^2} - k_x^2 - k_z^2 \right) - ik_x \frac{\partial^2 U_j}{\partial y^2} - \frac{m}{r\,Re} \left(\frac{\partial^2}{\partial y^2} - k_x^2 - k_z^2 \right)^2 \Big] v_j = 0 \quad (2.15)$$

$$\Big[-i\omega + ik_x U_j - \frac{m}{r\,Re} \left(\frac{\partial^2}{\partial y^2} - k_x^2 - k_z^2 \right) \Big] \eta_j = -ik_z \frac{\partial U_j}{\partial y} v_j \quad (2.16)$$

satisfying the conditions $\hat{v}_j|_{\partial\Omega} \to 0$, $\hat{\eta}_j|_{\partial\Omega} \to 0$, that is:

$$v_j(y=0) = 0; \qquad \left. \frac{\partial v_j(y)}{\partial y} \right|_{y=0} = 0; \qquad \eta_j(y=0) = 0; \quad (2.17)$$

$$v_j(y) \to 0; \qquad \frac{\partial v_j(y)}{\partial y} \to 0; \qquad \eta_j(y) \to 0, \quad \text{for } y \to +\infty. \quad (2.18)$$

The Orr-Sommerfeld and Squire problems along with the homogeneous boundary conditions represent an eigenvalue problem that can be used to investigate either the spatial or temporal stability of a parallel base flow. The latter concerns the solution of a linear eigenvalue problem providing the time-response of the system to a disturbance characterised by fixed streamwise and spanwise wavelengths. In the spatial case, the base state is perturbed by a disturbance with fixed temporal frequency (Ashpis & Reshotko, 1990; Tumin & Reshotko, 2001) and its (downstream) evolution is studied. The spatial problem is a non-linear eigenvalue problem (Haj-Hariri, 1988; Danabasoglu & Biringen, 1990; Schmid & Henningson, 2001) and it is investigated in this chapter. In the two-fluid problem, velocity and pressure disturbances perturb the interface, of which displacement must be accounted for.

Equation 2.6 can be linearized around the mean interface location $y = f = d$, leading to the kinematic condition for displacement of the interface due to the perturbation only, $\hat{f}$:

$$\left(\frac{\partial}{\partial t} + U_j \frac{\partial}{\partial x} \right) \hat{f} \delta_\Gamma (y - d) = \hat{v}_j \delta_\Gamma (y - d) \quad (2.19)$$

where $\delta_\Gamma(y - d)$ denotes a Dirac distribution, centered at the mean interface location d. The linearised interfacial conditions for the perturbation field $(\mathbf{u}, p)$ are derived from

equations 2.3 and written in terms of normal velocity and vorticity only:

$$[\![\hat{v}]\!] = 0 \tag{2.20}$$

$$\left[\!\!\left[\frac{\partial \hat{v}}{\partial y}\right]\!\!\right] - \left[\!\!\left[\frac{\partial U}{\partial y}\right]\!\!\right] \frac{\partial \hat{f}}{\partial x} = 0 \tag{2.21}$$

$$[\![\hat{\eta}]\!] + \left[\!\!\left[\frac{\partial U}{\partial y}\right]\!\!\right] \frac{\partial \hat{f}}{\partial z} = 0 \tag{2.22}$$

$$\left[\!\!\left[\frac{\partial \hat{\eta}}{\partial y}\right]\!\!\right]_m + \left[\!\!\left[\frac{\partial^2 U}{\partial y^2}\right]\!\!\right]_m \frac{\partial \hat{f}}{\partial z} = 0 \tag{2.23}$$

$$\left(\frac{\partial^2}{\partial y^2} + \frac{\partial^2}{\partial z^2}\right) [\![\hat{v}]\!]_m - \frac{\partial^2}{\partial x^2} [\![\hat{v}]\!]_m - \left[\!\!\left[\frac{\partial^2 U}{\partial y^2}\right]\!\!\right]_m \frac{\partial}{\partial x} \hat{f} = 0 \tag{2.24}$$

$$\begin{aligned} &\frac{\partial}{\partial t} \left[\!\!\left[\frac{\partial \hat{v}}{\partial y}\right]\!\!\right]_r - \frac{m}{r\,Re} \left[\!\!\left[\frac{\partial^3 \hat{v}}{\partial y^3} + 3\frac{\partial^2}{\partial z^2}\frac{\partial \hat{v}}{\partial y}\right]\!\!\right]_m - \frac{1}{We}\frac{\partial^4 \hat{f}}{\partial z^4} \\ &\quad + U_\Gamma \frac{\partial}{\partial x}\Big(\left[\!\!\left[\frac{\partial \hat{v}}{\partial y}\right]\!\!\right]_r - \left[\!\!\left[\frac{\partial U}{\partial y}\hat{v}\right]\!\!\right]_r \Big) - \frac{\partial}{\partial x^2}\Big(\frac{3m}{r\,Re} \left[\!\!\left[\frac{\partial \hat{v}}{\partial y}\right]\!\!\right]_m + \frac{2}{We}\frac{\partial^2 \hat{f}}{\partial z^2} \Big) - \frac{1}{We}\frac{\partial^4 \hat{f}}{\partial x^4} = 0 \end{aligned} \tag{2.25}$$

Under the assumptions of streamwise and spanwise homogeneity and time-periodicity, equation 2.19 can be written in the form:

$$(-i\omega + ik_x U_j)\, f \delta_\Gamma (y-d) = v_j \delta_\Gamma (y-d) \tag{2.26}$$

and the following matching conditions for velocities and stresses continuity in wavenumber and frequency space are applied at location $y = d$:

$$[\![v]\!] = 0 \tag{2.27}$$

$$\left[\!\!\left[\frac{\partial v}{\partial y}\right]\!\!\right] - ik_x \left[\!\!\left[\frac{\partial U}{\partial y}\right]\!\!\right] f = 0 \tag{2.28}$$

$$[\![\eta]\!] + ik_z \left[\!\!\left[\frac{\partial U}{\partial y}\right]\!\!\right] f = 0 \tag{2.29}$$

$$\left[\!\!\left[\frac{\partial \eta}{\partial y}\right]\!\!\right]_m + ik_z \left[\!\!\left[\frac{\partial^2 U}{\partial y^2}\right]\!\!\right]_m f = 0 \tag{2.30}$$

$$\left(\frac{\partial^2}{\partial y^2} + k_z^2\right) [\![v]\!]_m + k_x^2 [\![v]\!]_m - ik_x \left[\!\!\left[\frac{\partial^2 U}{\partial y^2}\right]\!\!\right]_m f = 0 \tag{2.31}$$

$$\begin{aligned} &-i\omega \left[\!\!\left[\frac{\partial v}{\partial y}\right]\!\!\right]_r - \tfrac{m}{r\,Re} \left[\!\!\left[\frac{\partial^3 v}{\partial y^3} - 3k_z^2 \frac{\partial v}{\partial y}\right]\!\!\right]_m - \tfrac{k_x^4}{We} f \\ &\quad + ik_x U_\Gamma \Big(\left[\!\!\left[\frac{\partial v}{\partial y}\right]\!\!\right]_r - \left[\!\!\left[\frac{\partial U}{\partial y} v\right]\!\!\right]_r \Big) + k_x^2 \Big(\tfrac{3m}{r\,Re} \left[\!\!\left[\frac{\partial v}{\partial y}\right]\!\!\right]_m - \tfrac{2k_z^2}{We} f \Big) - \tfrac{k_x^4}{We} f = 0 \end{aligned} \tag{2.32}$$

2.4.2 Polynomial eigenvalue problem

The Orr-Sommerfeld, Squire and interface equations, along with the stated interface and boundary conditions, constitute a polynomial eigenvalue problem ($\mathcal{P}_\Lambda$) for the streamwise wavenumber k_x:

$$\begin{aligned}
&\left[\mathbf{A_4}^j k_x^4 + \mathbf{A_3}^j k_x^3 + \mathbf{A_2}^j k_x^2 + \mathbf{A_1}^j k_x + \mathbf{A_0}^j\right] v_j = 0 \\
&\left[\mathbf{B_2}^j k_x^2 + \mathbf{B_1}^j k_x + \mathbf{B_0}^j\right] \eta_j = \mathbf{B_3}^j v_j \\
&\left[\mathbf{C_1}^j k_x + \mathbf{C_0}^j\right] f\delta_\Gamma\left(y-d\right) = v_j \delta_\Gamma\left(y-d\right)
\end{aligned} \tag{2.33}$$

in which the polynomial coefficients are:

$$\begin{aligned}
\mathbf{A_0}^j &= i\omega\frac{r\,Re}{m}\left(\frac{\partial^2}{\partial y^2} - k_z^2\right) - 2k_z^2\frac{\partial^2}{\partial y^2} + k_z^4 + \frac{\partial^4}{\partial y^4} & \mathbf{B_0}^j &= k_z^2 - \frac{\partial^2}{\partial y^2} - i\omega Re \\
\mathbf{A_1}^j &= -i\frac{r\,Re}{m}U_j\left(\frac{\partial^2}{\partial y^2} - k_z^2\right) + i\frac{r\,Re}{m}\frac{\partial^2 U_j}{\partial y^2} & \mathbf{B_1}^j &= i\frac{r\,Re}{m}U_j \\
\mathbf{A_2}^j &= -2\left(\frac{\partial^2}{\partial y^2} - k_z^2\right) - i\omega\frac{r\,Re}{m} & \mathbf{B_2}^j &= 1 \\
\mathbf{A_3}^j &= i\frac{r\,Re}{m}U_j & \mathbf{B_3}^j &= -ik_z\frac{\partial U_j}{\partial y} \\
\mathbf{A_4}^j &= 1 & \mathbf{C_1}^j &= iU_j \\
\mathbf{C_2}^j &= -i\omega.
\end{aligned} \tag{2.34}$$

Boundary and interfacial conditions already stated in equation (2.17), (2.18), (2.26), (2.27)- (2.32) apply.

2.4.3 Numerical solution

The polynomial eigenvalue problem $\mathcal{P}_\Lambda$ can be split into two separate eigenvalue problems, $\mathcal{P}_{\mathrm{OS}}$ and $\mathcal{P}_{\mathrm{SQ}}$, since there is an unidirectional coupling between the Orr-Sommerfeld, interface displacement and Squire equations. Vorticity, in fact, can only be created by the normal velocity or the displacement of the interface. Therefore, the eigenvalues of $\mathcal{P}_{\mathrm{OS}}$ and $\mathcal{P}_{\mathrm{SQ}}$ can be found independently. Each Orr-Sommerfeld mode ${k_x}^{\mathrm{OS}} \in \Lambda(\mathcal{P}_{\mathrm{OS}})$ corresponds to a vector eigenfunction $\mathbf{q}_{\mathrm{OS}}$ constituted by a normal velocity component, the corresponding interfacial displacement and a particular normal vorticity solution, i.e.

$\mathbf{q}_{\mathrm{OS}} = [v_j \ {\eta_j}^p \ f]^T$. Squire modes ${k_x}^{\mathrm{SQ}} \in \Lambda(\mathcal{P}_{\mathrm{SQ}})$ are associated only with a normal vorticity eigenfunction ${\eta_j}^h$, $\mathbf{q}_{\mathrm{SQ}} = [0 \ {\eta_j}^h \ 0]^T$, which solves the Squire homogeneous problem (Schmid & Henningson, 2001). Therefore, the following non-linear eigenvalue problems result:

$$\mathcal{P}_{\mathrm{OS}}: \quad \begin{bmatrix} \mathcal{L}_{\mathrm{OS}j} & 0 \\ 0 & \mathcal{L}_{\mathrm{int}} \end{bmatrix} \begin{bmatrix} v_j \\ f \end{bmatrix} = \begin{bmatrix} 0 \\ v_j \end{bmatrix} \text{ , interfacial conditions (2.27), (2.28), (2.31), (2.32)}$$

$$\mathcal{P}_{\mathrm{SQ}}: \qquad \mathcal{L}_{\mathrm{SQ}_j} {\eta_j}^h = 0 \ , \quad \text{interfacial conditions } [\![{\eta_j}^h]\!] = 0 \ , \ [\![\partial_y {\eta_j}^h]\!]_m = 0.$$

where

$$\mathcal{L}_{\mathrm{OS}j} = \mathbf{A_4}^j k_x^4 + \mathbf{A_3}^j k_x^3 + \mathbf{A_2}^j k_x^2 + \mathbf{A_1}^j k_x + \mathbf{A_0}^j \ ; \tag{2.35}$$

$$\mathcal{L}_{\mathrm{int}j} = \mathbf{C_1}^j k_x + \mathbf{C_0}^j \ ; \tag{2.36}$$

$$\mathcal{L}_{\mathrm{SQ}j} = \mathbf{B_2}^j k_x^2 + \mathbf{B_1}^j k_x + \mathbf{B_0}^j \ . \tag{2.37}$$

The free-stream and wall boundary conditions presented in (2.17), (2.18) hold.

The discretization of equation (2.33) uses the spectral method described in Orszag (1971). The details of the numerical implementation for single fluid Couette and Poiseuille flow are in Schmid & Henningson (2001). The method was extended to single- and two-fluid boundary layer flows. The numerical approach is to expand normal velocity and vorticity in terms of complete orthogonal polynomials and find the unique set of weights that satisfies the discrete version of (2.33). Chebyshev polynomials have historically been the preferred choice for the eigenfunction expansion, due to the progressively increasing resolution towards the boundary of the Gauss-Lobatto interval, on which the Chebyshev polynomials are computed.

Mapping In order to ensure accurate resolution in the wall-normal direction near the wall and the interface and to accurately represent the discontinuities of mean and perturbation variables at the interface, the top (Ω_y^T) and bottom (Ω_y^B) domains are discretised with different grids, on which separate mapped Chebyshev expansions provide a complete representation of the disturbance in Ω_y^T, Ω_y^B (van Noorden *et al.*, 1998).
Let $\tilde{T}_n(\zeta)$, $n = 1, \ldots, N$ be N Chebyshev polynomials in their natural domain $I = [-1, 1]$

and $y = \vartheta(\zeta)$ a mapping function between I and $\Omega_y^\ell = \{[0, d] \cup [d, \ell]\}$, $\zeta \in I$, $y \in \Omega_y$, with ℓ a large but finite location in the y direction. The value of ℓ is chosen such that results are independent upon its further increase.

We define $T_n(y) := \tilde{T}_n\left(\vartheta^{-1}(y)\right)$ as the mapped Chebyshev polynomial onto the domain Ω. Two sets of Chebyshev polynomials have been used to independently represent the bottom and top fluids. In particular, $T_n^T = \tilde{T}_n\left(\vartheta^{-1}(y)\right)$, $y \geq d$ and $T_n^B = \tilde{T}_n\left(\vartheta^{-1}(y)\right)$, $y \leq d$, where ϑ is the mapping function between the Chebyshev interval I and the finite physical space Ω_y^ℓ. Details on the mapping function and on the mapped Chebyshev polynomials can be found in Appendix C.

The grid ζ_j is generated in the Chebyshev interval I using the N_j Gauss-Lobatto points $\zeta_{j,k} = \cos\left(\frac{\pi k}{N_j - 1}\right)$ and mapped to computational space, such that $\{y\} = \{y_T\} \cup \{y_B\} \in \Omega_y^\ell$. The number of Chebyshev polynomials used in the top domain Ω_y^T is of order $150 - 200$ and the bottom fluid counterpart is chosen according to the relation $\frac{\ell}{N_T} \approx \frac{d_0}{\frac{N_B}{10}} \approx 0.1$.

Linear and non-linear mapping functions ϑ were considered. Non-linear mapping increases the grid resolution near the interface and this has been found to be beneficial when computing discrete modes. The drawback of non-linear mapping is that it affects the grid resolution in the free stream, which is particularly important when computing continuous modes. Therefore, linear mapping was found to be a good compromise between free stream resolution and accuracy of discrete (if any) and interfacial modes.

Discretization Eigenfunctions of (2.33) are expanded in series of mapped Chebyshev polynomials (Mason & Phillis, 2005):

$$v_T(y) = \sum_{n=0}^{N_T} c_{v,n}^T T_n^T(y) \qquad \eta_T(y) = \sum_{n=0}^{N_T} c_{\eta,n}^T T_n^T(y) \tag{2.38}$$

$$v_B(y) = \sum_{n=0}^{N_B} c_{v,n}^B T_n^B(y) \qquad \eta_B(y) = \sum_{n=0}^{N_B} c_{\eta,n}^B T_n^B(y) \tag{2.39}$$

where $c_{v,n}^j$ and $c_{\eta,n}^j$ represent respectively the coefficients of the n^{th} Chebyshev polynomial T_n^j for normal velocity and vorticity eigenfunctions.

The expansions (2.38), (2.39) are substituted into the non-linear eigenvalue problem in (2.33), providing a set of algebraic equations at the mapped Gauss-Lobatto points, which constitute a non-linear discretized eigenvalue problem $\mathcal{P}^*$, that is split into $\mathcal{P}_{\text{OS}}^*$

and $\mathcal{P}^*_{\mathrm{SQ}}$.

Methods to find the eigenvalues of $\mathcal{P}^*_{\mathrm{OS}}$ and $\mathcal{P}^*_{\mathrm{SQ}}$ are described by Ruhe (1973), Guillame (1999), Tisseur & Meerbegen (2001); the latter was considered in this work.

Define $\mathbf{c}_{\mathrm{OS}} = [\mathbf{c}_{\mathbf{v}j} \;\; f]^{\mathsf{T}}$, where $\mathbf{c}_{\mathbf{v}j}$ is the weight vector of the Chebyshev differentiation matrices for the normal velocity component in the top and bottom fluids and the new vector $\mathbf{c}^*_{\mathrm{OS}} = [\mathbf{c}_{\mathrm{OS}} \;\; k_x\mathbf{c}_{\mathrm{OS}} \;\; k_x^2\mathbf{c}_{\mathrm{OS}} \;\; k_x^3\mathbf{c}_{\mathrm{OS}}]^{\mathsf{T}}$. Since $\mathcal{P}^*_{\mathrm{OS}}$ is in fact a polynomial eigenvalue problem of the 4^{th} order, it can be converted into an ordinary linear generalised eigenproblem $\mathbf{M^*}_{\mathrm{OS}}\mathbf{c}^*_{\mathrm{OS}} = \lambda_v\mathbf{N^*}_{\mathrm{OS}}\mathbf{c}^*_{\mathrm{OS}}$ of four times the size $\mathcal{P}^*_{\mathrm{OS}}$ with $\mathbf{M^*}_{\mathrm{OS}}$ and $\mathbf{N^*}_{\mathrm{OS}}$ as follows:

$$\mathbf{M^*}_{\mathrm{OS}} = \begin{bmatrix} -\mathcal{A}_3\mathbf{D_3} & -\mathcal{A}_2\mathbf{D_2} & -\mathcal{A}_1\mathbf{D_1} & -\mathcal{A}_0\mathbf{D_0} \\ 0 & \mathbf{D_0} & 0 & 0 \\ 0 & 0 & \mathbf{D_0} & 0 \\ 0 & 0 & 0 & \mathbf{D_0} \end{bmatrix} \quad \mathbf{N^*}_{\mathrm{OS}} = \begin{bmatrix} \mathcal{A}_4\mathbf{D_4} & 0 & 0 & 0 \\ \mathbf{D_0} & 0 & 0 & 0 \\ 0 & \mathbf{D_0} & 0 & 0 \\ 0 & 0 & \mathbf{D_0} & 0 \end{bmatrix} \tag{2.40}$$

where $\mathbf{D_0}$, $\mathbf{D_1}$, $\mathbf{D_2}$, $\mathbf{D_3}$, $\mathbf{D_4}$ are the Chebyshev differentiation matrices for the top and bottom fluids:

$$\mathbf{D_n} = \begin{bmatrix} \mathcal{D}_n^T & 0 & 0 \\ 0 & \mathcal{D}_n^B & 0 \\ 0 & 0 & 1 \end{bmatrix} \tag{2.41}$$

in which $\mathcal{D}_n$ is the n^{th} differentiation matrix as described in Schmid & Henningson (2001). Note that the n^{th} column of the matrix $\mathcal{D}_n^j$ is the n^{th} Chebyshev polynomial T_n^j in the expansion (2.38), (2.39). The matrices $\mathcal{A}_0$, $\mathcal{A}_1$, $\mathcal{A}_2$, $\mathcal{A}_3$, $\mathcal{A}_4$ are given by:

$$\mathcal{A}_0 = \begin{bmatrix} \mathbf{A_0}^T & 0 & 0 \\ 0 & \mathbf{A_0}^B & 0 \\ 0 & 0 & \mathbf{C_0}^T \end{bmatrix} \quad \mathcal{A}_1 = \begin{bmatrix} \mathbf{A_1}^T & 0 & 0 \\ 0 & \mathbf{A_1}^B & 0 \\ 0 & 0 & \mathbf{C_1}^T \end{bmatrix} \quad \mathcal{A}_2 = \begin{bmatrix} \mathbf{A_2}^T & 0 & 0 \\ 0 & \mathbf{A_2}^B & 0 \\ 0 & 0 & 0 \end{bmatrix} \tag{2.42}$$

$$\mathcal{A}_3 = \begin{bmatrix} \mathbf{A_3}^T & 0 & 0 \\ 0 & \mathbf{A_3}^B & 0 \\ 0 & 0 & 0 \end{bmatrix} \quad \mathcal{A}_4 = \begin{bmatrix} \mathbf{A_4}^T & 0 & 0 \\ 0 & \mathbf{A_4}^B & 0 \\ 0 & 0 & 0 \end{bmatrix} \tag{2.43}$$

The same process applies to the discretised Squire problem $\mathcal{P}^*_{\mathrm{SQ}}$. Let us define $\mathbf{c}_{\mathrm{SQ}} = [\mathbf{c}_{\eta_j}]$, where $\mathbf{c}_{\eta_j}$ is the weight vector of the Chebyshev differentiation matrices for the normal vorticity component in the top and bottom fluids and the new vector $\mathbf{c}^*_{\mathrm{SQ}} = [\mathbf{c}_{\mathrm{SQ}} \;\; k_x\mathbf{c}_{\mathrm{SQ}}]^{\mathsf{T}}$. $\mathcal{P}^*_{\mathrm{SQ}}$ is a quadratic polynomial eigenvalue problem and it can be converted into an ordinary linear generalised eigenproblem $\mathbf{M}^*{}_{\mathrm{SQ}}\mathbf{c}^*_{\mathrm{SQ}} = \lambda_\eta \mathbf{N}^*{}_{\mathrm{SQ}}\mathbf{c}^*_{\mathrm{SQ}}$ twice the size of $\mathcal{P}^*_{\mathrm{SQ}}$ with $\mathbf{M}^*{}_{\mathrm{SQ}}$ and $\mathbf{N}^*{}_{\mathrm{SQ}}$ as the following:

$$\mathbf{M}^*{}_{\mathrm{SQ}} = \begin{bmatrix} -\mathcal{B}_\mathbf{1}\mathbf{D_1} & -\mathcal{B}_\mathbf{0}\mathbf{D_0} \\ 0 & \mathbf{D_0} \end{bmatrix} \quad \mathbf{N}^*{}_{\mathrm{SQ}} = \begin{bmatrix} \mathcal{B}_\mathbf{2}\mathbf{D_2} & 0 \\ \mathbf{D_0} & 0 \end{bmatrix} \tag{2.44}$$

where $\mathbf{D_0}$, $\mathbf{D_1}$, $\mathbf{D_2}$ are the Chebyshev differentiation matrices for top and bottom fluids:

$$\mathbf{D_n} = \begin{bmatrix} \mathcal{D}_n^T & 0 \\ 0 & \mathcal{D}_n^B \end{bmatrix} \tag{2.45}$$

and $\mathcal{B}_\mathbf{0}$, $\mathcal{B}_\mathbf{1}$, $\mathcal{B}_\mathbf{2}$ are given by

$$\mathcal{B}_\mathbf{0} = \begin{bmatrix} \mathbf{B_0}^T & 0 \\ 0 & \mathbf{B_0}^B \end{bmatrix} \; \mathcal{B}_\mathbf{1} = \begin{bmatrix} \mathbf{B_1}^T & 0 \\ 0 & \mathbf{B_1}^B \end{bmatrix} \; \mathcal{B}_\mathbf{2} = \begin{bmatrix} \mathbf{B_2}^T & 0 \\ 0 & \mathbf{B_2}^B \end{bmatrix}. \tag{2.46}$$

The eigenvalues of the linearized discrete systems $\mathcal{P}^*{}_{\mathrm{OS}}$, $\mathcal{P}^*{}_{\mathrm{SQ}}$ were obtained using the standard mathematical libraries in MATLAB (Higham *et al.*, 2007). The eigenvalues obtained from the spectral code were validated against results reported by Schmid & Henningson (2001), Butler & Farrell (1992), Malik & Hooper (2005), Yecko (2003),Yecko & Zaleski (2005*b*), Yecko (2008), Ozgen *et al.* (1998), Tumin & Reshotko (2001). Additional details on the validation of the parallel and spreading framework can be found in the Appendix B.

2.4.4 The discrete and continuous spectrum

A method for computing the eigenvalues of (2.33) was given in the previous section; in this section, the eigenvalue spectra of single- and two- fluid boundary layers is briefly discussed. This is a necessary step towards the understanding of the challenges of formulating a suitable method for optimal disturbances in the spatial framework; it also provide numerical evidence of the discussion on discrete and continuous modes already

presented in section §1.1.1 and §1.1.2.

The modes of the spectrum of the Blasius boundary layer can be divided into two classes: discrete and continuous. The former have phase speed $c_r = \Re(\omega/k_x) < U^\infty$, growth rate $c_i = \Im(\omega/k_x)$, peak inside the boundary layer and decay exponentially in the free stream. The latter propagate at the free-stream velocity, U^∞, have an oscillatory behaviour in the free stream and decay inside the boundary layer. Zhigulev *et al.* (1980) and Salwen & Grosch (1981) characterised the features of the spatial continuous spectrum by considering the asymptotic behaviour of the linearized Navier-Stokes equations in the free stream. As $y \to +\infty$, $U \to U^\infty = 1$, $\frac{\partial U}{\partial y}\Big|_{y\to+\infty} \to 0$, the solution of linear NS is a linear combination of fundamental exponential functions $e^{\lambda y}$, where λ satisfy the characteristic equation

$$\left(k_x^2 - \lambda^2\right)\left[\lambda^2 - k_x^2 - iRe\left(k_x - \omega\right)\right] = 0\,, \tag{2.47}$$

that is

$$\lambda_{1,2} = \mp k_x\,; \qquad \lambda_{3,4} = \pm\sqrt{k_x^2 + iRe\left(k_x - \omega\right)}\,. \tag{2.48}$$

If $\Re\left(\lambda_n\right) \neq 0$, two decaying fundamental solutions are admissible, related to the discrete spectrum of k_x. The continuous spectrum arises when either $\Re\left(\lambda_{1,2} = 0\right)$ or $\Re\left(\lambda_{3,4} = 0\right)$. In the case $\lambda_{1,2} = \pm ik$ in (2.47) $\forall\, k > 0 \in \mathbb{R}$, $k_{x1,2} = \pm i\sqrt{k_y^2 + k_z^2}$; these solutions correspond to pressure waves. When $\lambda_{3,4} = -k_y^2$, (2.47) reduces to the dispersion relation

$$k_x^2 + k_y^2 + k_z^2 + iRe\left(k_x - \omega\right) = 0\,, \tag{2.49}$$

that admits branches

$$k_{x3,4} = -\frac{iRe}{2}\left[1 \mp \sqrt{1 + \frac{4\left(k_y^2 + k_z^2 - i\omega Re\right)}{Re^2}}\right]\,, \tag{2.50}$$

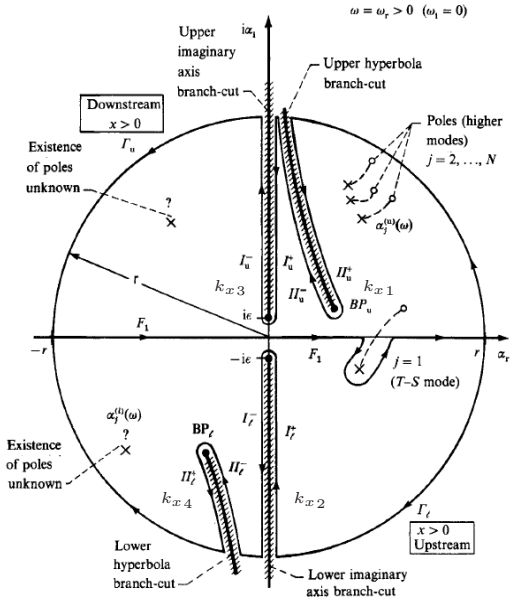


Figure 2.3: Integration contours in the complex k_x-plane (Ashpis & Reshotko, 1990)

which can be written as $k_x = k_{x_\Re} + ik_{x_\Im}$ (Jacobs & Durbin, 1998):

$$
\begin{aligned}
k_x{}^{\Re} &= \frac{Re}{2}\sqrt{\sqrt{\beta^2 + \frac{4\omega^2}{Re^2}} - \beta}\ , \\
k_x{}^{\Im} &= \frac{Re}{2}\left(\frac{\omega}{k_x{}^{\Re}} - 1\right)\ , \\
\beta &= \frac{1 + \left(\frac{2}{Re}k_y\right)^2}{2}\ .
\end{aligned}
\tag{2.51}
$$

These spatial continuous eigenvalues are related to vortical continuous eigensolutions, of interest in the study of bypass transition due to free stream turbulence.

The four branches are shown in figure 2.3 (reproduction of figure 4 by Ashpis & Reshotko (1990)). Ashpis & Reshotko (1990) showed that the branches $k_{x2}(k)$ and $k_{x4}(k)$ can admit arbitrary large negative values of $\Im(k_x)$, thus allowing arbitrary large growth rate and making an initial value problem ill-posed in such particular case. In fact, through the argument of the signaling problem, Ashpis & Reshotko (1990) reached the conclusion that the branches k_{x1} and k_{x3} of the continuous spectrum in figure 2.3 describe the flow response downstream of the source, while the branches k_{x2} and k_{x4} apply to the upstream field.

Figure 2.3 also depicts the contours of integration in the inverse Fourier transform in the

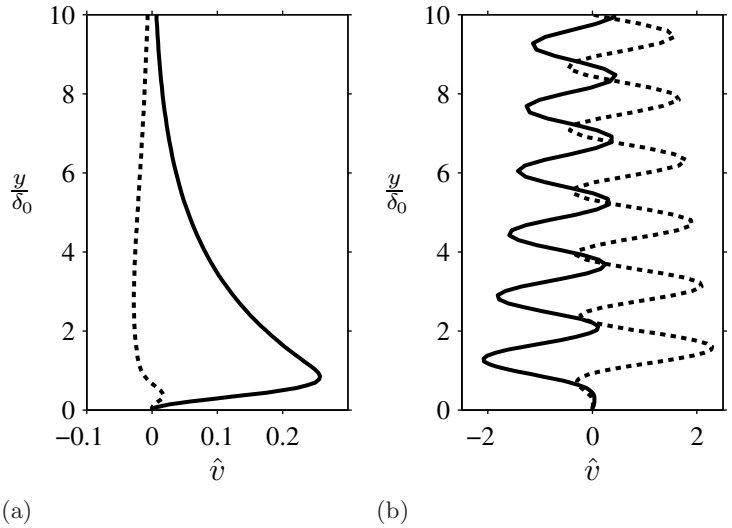


Figure 2.4: (2.4a) Eigenfunction of the discrete mode $k_x = 0.36456 + 0.077089i$. (2.4b) Eigenfunction of a continuous Orr-Sommerfeld mode $\omega = 0.125$, $k_x = 0.12531 + 0.019719i$, $k_z = 0$, $Re = 800$. —— , real component; - - - imaginary component.

complex k_x plane, showing that discrete modes growing in the downstream direction are taken into account in the downstream response of the flow. Whenever it is possible to indefify a suitable contour for integration in Fourier space, the initial value problem is well posed. Therefore, the downstream propagating disturbances may be represented as an expansion of eigenfunctions belonging to the branches k_{x1} and k_{x3} plus any growing discrete mode. The restriction to downstream propagating modes removes the ill-posedness of the spatial initial-value problem. The formulation of a consistent initial-value problem for the spatial problem makes the determination of optimal disturbances similar to the temporal counterpart, from which the well-established tools used are borrowed.

Stratification Given the background on discrete and continuous modes in single fluid boundary layer, the attention is focused on how stratification changes the discrete and continuous spectra, as this affects the amplification mechanism.

Discrete modes The presence of a wall-film changes the stability characteristics of the boundary layer flow and can trigger three discrete instability mechanisms (short wavelength instability, long wavelength instability, High Reynolds number instability) in addition to the well-known TS wave mechanism (Saha, 2011; Yih, 1967; Hooper & Boyd, 1983, 1987). Saha (2011) analysed the four types of instability in the temporal problem

through the energy transfer mechanisms for values of Re above and below the critical Reynolds number Re_{crit} and for viscosity ratios m lower and greater than 1. He showed that:

i) the short wavelength instability exists in all regimes discussed, although it is easily suppressed by the presence of surface tension;

ii) the boundary layer is stable at subcritical Reynolds numbers (based on single fluid boundary layer thickness) if $m < 1$;

iii) as $|1 - m|$ increases, the viscosity stratification has a stabilising effect on all of the unstable modes in a two-fluid boundary layer.

Since the two-fluid boundary layer is asymptotically stable to long wavelength perturbations when the lower fluid is less viscous, the algebraic instability is likely to dominate under such circumstances. For this reason, focus is on the stable branch of the downstream propagating spectrum, comprising of continuous modes, which are relevant to the growth of the algebraic instability.

Continuous modes Zaki & Saha (2009) investigated the structure of the continuous modes in single- and two-fluid boundary layers and their penetration inside the boundary layer. They identified three regimes, determined by the ratio of the diffusive to the convective terms in the disturbance equation:

i) a shear-sheltering regime, in which free stream disturbances are convected by the mean flow and decay at the edge of the boundary layer;

ii) a viscous regime, in which free-stream disturbances penetrate the boundary layer to the wall;

iii) an intermediate regime, in which wall-normal diffusion and shear sheltering coexist.

They also showed that penetration of continuous modes into the wall-film depends on the viscosity ratio m, which forces a modified wall-normal wavenumber in the bottom fluid in

order to match the decay rate set by the free stream. Therefore, a lower viscosity ratio can enhance penetration, due to the modified wavenumber across the interface. As pointed out in section 1.1.2, this contradicts what usually happens in single-fluid boundary layers, where lower viscosities increase the shear sheltering effect, reducing penetration of continuous modes. Zaki & Saha revealed that long wavelength perturbations penetrate the most inside the boundary layer and couple most effectively to the mean shear. However, penetration depth of vortical disturbances does not fully determine and explain the linear amplification of disturbances. Transient growth of disturbances also depends on how normal vorticity perturbations are generated by normal velocity. Furthermore, the presence of an interface can play a leading role in generating transient amplification.
In this and previous sections the reader was provided with a quantitative method to compute the discrete and continuous spectra in two-fluid boundary layers, which completes the theoretical discussion on modal stability in sections §1.1.1-1.1.2. Neither discrete instabilities nor penetration of continuous modes inside the boundary layer can systematically explain transient amplification. Hence, the aim of the next section is to explore the transient growth mechanism.

2.5 Optimal disturbances

Following the discussion on the signaling problem, the well-posedness of an initial-value problem for spatial disturbances is ensured by considering the downstream perturbation flowfield as an expansion of eigenfunctions from the branches k_{x2}, k_{x4}. The set of eigenfunctions that solves the eigenvalue problem $\mathcal{P}_\Lambda$ is non-orthogonal, so transient energy growth is expected. In fact, even though the imaginary part of the eigenvalues of $\mathcal{P}_\Lambda$ is strictly positive for a particular choice of Re and m corresponding to linear, asymptotic, exponentially decaying stability of the laminar state, transient growth of energy is also possible. This transient behaviour has been suggested as a possible trigger for non-linear effects sustaining turbulence (Henningson & Reddy, 1994).
The work of Ellingsen & Palm (1975) and Landhal (1980) demonstrated the need to consider the evolution of linear perturbations from initial conditions. Although the possibility of formulating an initial-value problem for spatial disturbances has been stated, the analyses of the Orr-Sommerfeld (2.15) and Squire (2.16) equations reveal only the asymptotic stability of the system. A method to investigate spatial optimal evolution of

perturbations is therefore necessary to characterise the transient behaviour and is presented in this section.

Consider a two-phase disturbance constituted of a velocity vector $\hat{\mathbf{u}}_j = (\hat{u}_j, \hat{v}_j, \hat{w}_j)$ and a pressure field $\hat{p}_j$ satisfying the linearized Navier-Stokes equations (2.10)-(2.11) for each of the top $j = T$ and bottom $j = B$ fluids around a parallel base flow $\mathbf{U} = (U(y), 0, 0)$; the perturbation is homogeneous in the spanwise direction and has a frequency ω. The interface displacement $\hat{f} = \tilde{f}(x)e^{ik_z z - i\omega t}$ is governed by the kinematic condition $U\frac{\partial}{\partial x}\hat{f} = i\omega\hat{f} + \hat{v}\,\delta_\Gamma(y-d)$.

Schmid & Henningson (2001) showed that it is possible to arrange the LNS equations as a spatial evolution equation in terms of the normal velocity $\hat{v}_j(x,y,z,t) = \tilde{v}_j(x,y)e^{ik_z z - i\omega t}$ and normal vorticity $\hat{\eta}_j = \partial_z\hat{u}_j - \partial_x\hat{w}_j = \tilde{\eta}_j(x,y)e^{ik_z z - i\omega t}$:

$$\frac{\partial\tilde{\mathbf{q}}}{\partial x} = \tilde{\mathcal{L}}\tilde{\mathbf{q}} \tag{2.52}$$

with $\tilde{\mathbf{q}} = [\tilde{v}_j(x,y),\ \tilde{\eta}_j(x,y)\ \tilde{f}(x),]^T$. The explicit form of $\tilde{\mathcal{L}}$ is not relevant at this point and it will be given in Chapter 3. It is sufficient to notice that $\tilde{\mathcal{L}}$ has the same eigenvalue spectra as $\mathcal{P}_\Lambda$. The eigenfunctions of $\mathcal{P}_\Lambda$ represent a complete set (Salwen & Grosch, 1981), so any perturbation $\tilde{\mathbf{q}}$ can be written as a linear combination of the eigenfunctions $\mathbf{q}_n$ of $\mathcal{P}_\Lambda$, that is:

$$\tilde{\mathbf{q}}(x,y) = \sum_{n=0}^{\infty} \varkappa_n(x)\mathbf{q}_n(y) \tag{2.53}$$

Therefore, (2.52) is equivalent to the trivial system of ODEs:

$$\frac{\partial\varkappa}{\partial x} = \mathbf{\Lambda}_{\mathcal{P}_\Lambda}\varkappa \tag{2.54}$$

where $\mathbf{\Lambda}_{\mathcal{P}_\Lambda}$ is a diagonal matrix containing the discretized eigenvalue spectra of $\mathcal{P}_\Lambda$. For the solution to be well-posed, $\mathbf{\Lambda}_{\mathcal{P}_\Lambda}$ is restricted to be $\mathbf{\Lambda}^r_{\mathcal{P}_\Lambda} = \{k_{x2},\ k_{x4}\}$, in which only N least-stable downstream propagating modes are included. This reduction of basis determines, in fact, a parabolization of the system (2.52).

Consider the Hilbert space generated by the N least-stable downstream-propagating eigenvectors, that is $\mathcal{H}_N = span\{\mathbf{q}_1,\ \mathbf{q}_2, \cdots, \mathbf{q}_N\}|_{\Lambda^r_{\mathcal{P}_\Lambda}}$; for any initial condition $\mathbf{q}(x_0) \in$

$\mathcal{H}_N$, the initial value problem governed by the dynamical system (2.52) is well-posed and can exhibit transient amplification before reaching its asymptotic state. The disturbance $\mathbf{q_0}(x)$ is defined as *optimal* if it maximises a chosen functional norm at a certain location $x > x_0$. To proceed further, the concept of the norm must be discussed.

Denote with $\mathcal{H}(\Omega_y^\ell)$ the Hilbert space on which any vectors $\mathbf{a}$ and $\mathbf{b}$ of the form $\mathbf{a} = [v_j,\ \eta_j,\ f]^\mathsf{T}$ are defined. The following inner product naturally holds:

$$\langle \mathbf{a}, \mathbf{b} \rangle = \sum_{j=T,B} \int_{\Omega_y^j} \mathbf{a}^\mathsf{H} \mathbf{b}\ dy \quad , \qquad \forall \mathbf{a}, \mathbf{b} \in \mathcal{H}(\Omega_y^\ell) \tag{2.55}$$

where $\cdot^\mathsf{H}$ denotes the Hermitian operator. Note that $\|\mathbf{a}\|^2 = \langle \mathbf{a}, \mathbf{a} \rangle$.
Following Yecko & Zaleski's approach, the *norm* of a perturbation $\mathbf{q}$ is defined to be its mechanical energy, which consists of the kinetic energy of velocity perturbation and the potential contribution due to the interface deflection (Yecko & Zaleski, 2005*b*):

$$\|\mathbf{q}\|_\varepsilon^2 = \frac{1}{2} \int_\Omega r|\mathbf{u}|^2\, d\Omega + \frac{|f|^2}{We}\,. \tag{2.56}$$

Note that equation 2.56 is equivalent to the condition:

$$\|\mathbf{q}\|_\varepsilon^2 = \langle \mathbf{q}, \mathbf{E}\mathbf{q} \rangle = \langle \mathbf{C}\mathbf{q}, \mathbf{C}\mathbf{q} \rangle \quad , \qquad \forall\, \mathbf{q} \in \mathcal{H}(\Omega), \tag{2.57}$$

where $\mathbf{E} = \mathbf{C}^H \mathbf{C}$ accounts for the mechanical energy and $\mathbf{C}$ given by:

$$\mathbf{C} = \begin{bmatrix} \mathbf{K} & 0 & 0 \\ 0 & r\mathbf{K} & 0 \\ 0 & 0 & I \end{bmatrix}, \quad \text{with} \qquad \mathbf{K} = \frac{1}{\sqrt{2}} \begin{bmatrix} \frac{k_x}{k^2}\frac{\partial}{\partial y} & -\frac{k_z}{k^2} \\ 1 & 0 \\ \frac{k_z}{k^2}\frac{\partial}{\partial y} & \frac{k_x}{k^2} \end{bmatrix} \tag{2.58}$$

where $I = \frac{k^2}{\sqrt{We}}$, $k^2 = \left(k_x^2 + k_z^2\right)$.

Any downstream propagating disturbance can be approximated as an expansion in terms of N least stable modes of $\mathbf{\Lambda}_\mathcal{P}^r$

$$\tilde{\mathbf{q}}(x, y) = \sum_{n=1}^{N} \varkappa_n(x) \mathbf{q}_n(y) = \mathcal{Q}\kappa(x) \tag{2.59}$$

where the N columns of the matrix $\mathcal{Q}$ are the reduced basis vectors $\mathbf{q}_n(y)$, $n = 1, \cdots, N$. Note that $\mathcal{Q}$ is non-singular, therefore the coefficient $\kappa(x)$ are the solution of a linear system.

At this point, the aim is to find the initial condition $\mathbf{q_0}(x_0)$ that maximises the functional

$$\mathbf{J}(\mathbf{q}; \mathbf{q_0}; x) = \frac{\|\mathbf{q}(x)\|_\epsilon^2}{\|\mathbf{q_0}(x_0)\|_\epsilon^2} \tag{2.60}$$

at any location $x \in \Omega_x$.

Let the growth factor $G(x)$ be the maximum value of the functional $\mathbf{J}(\mathbf{q}; \mathbf{q_0}; x)$ at location x for *any* possible, non-trivial initial condition $\mathbf{q_0}(x_0) \in \mathcal{H}_N$ satisfying the reduced initial-value problem governed by (2.52). The optimization problem that determines $G(x)$ is defined as the following:

$$\begin{aligned} G(x) &= \max_{\|\mathbf{q_0}(x_0)\|_\epsilon \neq 0} \mathbf{J}(\mathbf{q}; \mathbf{q_0}, x) \\ &\text{s.t.} \\ &\begin{cases} \frac{\partial \mathbf{q}}{\partial x} = \mathcal{L}\mathbf{q} \\ \mathbf{q}(x_0) = \mathbf{q_0} \in \mathcal{H}_N \end{cases} \\ &\text{and} \quad \mathcal{L} \ : \Lambda(\mathcal{L}) \subseteq \Lambda_{\mathcal{P}}^r \end{aligned} \tag{2.61}$$

Under (2.59), (2.61) reduces to:

$$\begin{aligned} G(x) &= \max_{\|\mathbf{q_0}(x_0)\|_\epsilon \neq 0} \frac{\|\mathbf{q}(x)\|_\epsilon^2}{\|\mathbf{q}(x_0)\|_\epsilon^2} = \max_{\|\mathbf{q_0}(x_0)\|_\epsilon \neq 0} \frac{\langle \mathbf{q}(x), \mathbf{E}\mathbf{q}(x) \rangle}{\langle \mathbf{q}(x_0), \mathbf{E}\mathbf{q}(x_0) \rangle} \\ &= \max_{|\kappa(x_0)| \neq 0} \frac{\langle \mathcal{Q}\kappa(x), \mathbf{E}\mathcal{Q}\kappa(x) \rangle}{\langle \mathcal{Q}\kappa(x_0), \mathbf{E}\mathcal{Q}\kappa(x_0) \rangle} = \max_{|\kappa(x_0)| \neq 0} \frac{\langle \mathbf{C}\mathcal{Q}\kappa(x), \mathbf{C}\mathcal{Q}\kappa(x) \rangle}{\langle \mathbf{C}\mathcal{Q}\kappa(x_0), \mathbf{C}\mathcal{Q}\kappa(x_0) \rangle} \\ &= \max_{|\kappa(x_0)| \neq 0} \frac{\|\mathbf{F}\kappa(x)\|^2}{\|\mathbf{F}\kappa(x_0)\|^2} = \max_{|\kappa(x_0)| \neq 0} \frac{\left\|\mathbf{F}e^{i\Lambda_{\mathcal{P}}^r x}\kappa(x_0)\right\|^2}{\|\mathbf{F}\kappa(x_0)\|^2} = \left\|\mathbf{F}e^{i\Lambda_{\mathcal{P}}^r x}\mathbf{F}^{-1}\right\|^2 \end{aligned} \tag{2.62}$$

where the matrix $\mathbf{F} := \mathbf{C}\mathcal{Q}$ is the Cholesky factorization of the Gramiam matrix $\mathcal{M} = \mathbf{F}^{\mathsf{H}}\mathbf{F}$, defined as

$$\mathcal{M}_{ij} = \langle \mathbf{q}_i, \mathbf{E}\mathbf{q}_j \rangle \tag{2.63}$$

$\mathbf{q}_n$ being the component of the eigenfunction basis in (2.59). Note that $\mathcal{M}$ is Hermitian and positive definite by definition.

The computation of $G(x)$ reduces to determine the 2−norm of the operator $\mathcal{L}_{\mathbf{F}} = \mathbf{F}e^{i\Lambda_{\mathcal{P}}^{r}x}\mathbf{F}^{-1}$, which is, by definition, the square of the its largest eigenvalue. This quantity is also denoted as largest singular value θ_1 (Henningson & Reddy, 1994). It is possible to decompose $\mathcal{L}_{\mathbf{F}}$ in terms of its singular values. This decomposition is called *Singular Value Decomposition* (SVD) and follows the relation:

$$\mathcal{L}_{\mathbf{F}} = \Phi\Theta\Psi^{\mathsf{H}} \ , \tag{2.64}$$

where Θ is the diagonal matrix of singular values and its term $\Theta_{1,1} = \theta_1$ is the largest singular value. The matrices Φ and Ψ contain the so-called left and right principal vectors, respectively. The first column of Ψ is the principal right singular vector, which is the initial condition $\mathbf{q_0}_x$ that will be amplified by a factor of θ_1 at location x and transformed into the principal left singular vector, that is the first row of Θ.

Alternative methods for optimal disturbances exist: Butler & Farrell (1992) computed optimal disturbances using a variational approach; Andersson *et al.* (1997), Luchini (2000), Corbett & Bottaro (2000) used repeated integrations of regular and adjoint equations in a power iteration procedure. This method will be used in the next chapter to characterise optimal disturbances on spreading boundary layers, where a complete basis of eigenfunctions is not available.

Choice of norm The results of the optimization that are presented in the next section depend on the objective functional **J** and on the choice of the energy norm. The former represents the gain of the response, under a measure, to the initial condition; the latter is the measure under which the perturbations are quantified. Although the majority of literature on optimal disturbances assumes the gain functional as objective function, less agreement is found on the selection of a measure. If the kinetic energy of a disturbance is widely accepted as suitable measure in single-fluid flows, the choice of the norm is a relevant problem in two-phase flows. In fact, Renardy (1987) and South & Hooper (1999) have noted that an interface displacement must appear in the energy norm for the transient growth calculations to converge, even in the absence of an interfacial energy (i.e. $\sigma = 0,\ We \to \infty$); the optimization problem would be otherwise ill-posed, due to possible unbounded growth of the interfacial disturbance. South & Hooper (1999), Yecko (2003), Malik & Hooper (2005) have provided different norms

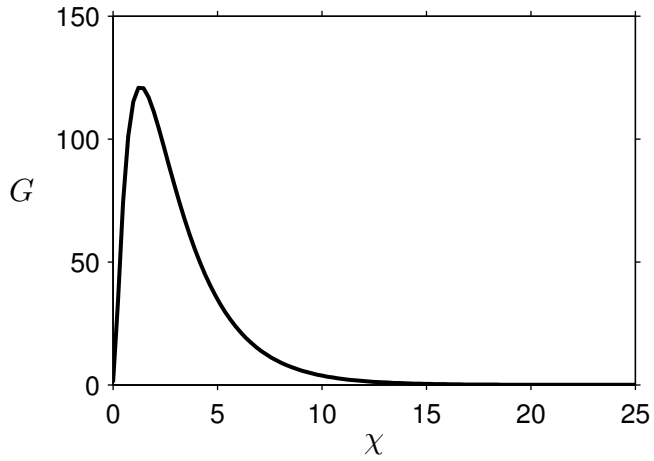


Figure 2.5: Optimal growth in single-fluid boundary layer, $\omega = 0.001$, $k_z = 2.205$, $Re = 800$.

that take into account the interface deflection. Their work is related to the temporal problem and Schmid & Henningson have pointed out that these norms might not be relevant in the spatial counterpart. However, in this work, non-linear interactions or energy transfer mechanisms are not considered, therefore the energy measure reported by Yecko & Zaleski (2005*b*) is adopted; note that the potential energy of the interface displacement in presence of surface tension is considered. Convergence studies of the chosen norm are available in the Appendix D.

At this point, the reader has been provided with a method for computing the maximum possible amplification of a disturbance by solving (2.62). Hence, the next subsections present G for single- and two-fluid boundary layers.

2.5.1 The single-fluid boundary layer

The single fluid case is presented to highlight the main features of the transient growth mechanism and as a reference benchmark for the computation of G in two-fluid flows. The maximum amplification curve G as a function of the normalised streamwise location $\chi = \frac{x-x_0}{x_0}$ in a single fluid boundary layer is represented in figure 2.5. The energy amplifies over a lengthscale of $O(1)$, due to the vorticity tilting mechanism. After the first peak, the viscous decay becomes dominant, in agreement with the asymptotic stability of the system. The envelope of all possible evolutions of any initial condition is denoted with $G(x)$; note that every point on the curve was originated by a different initial condition. The

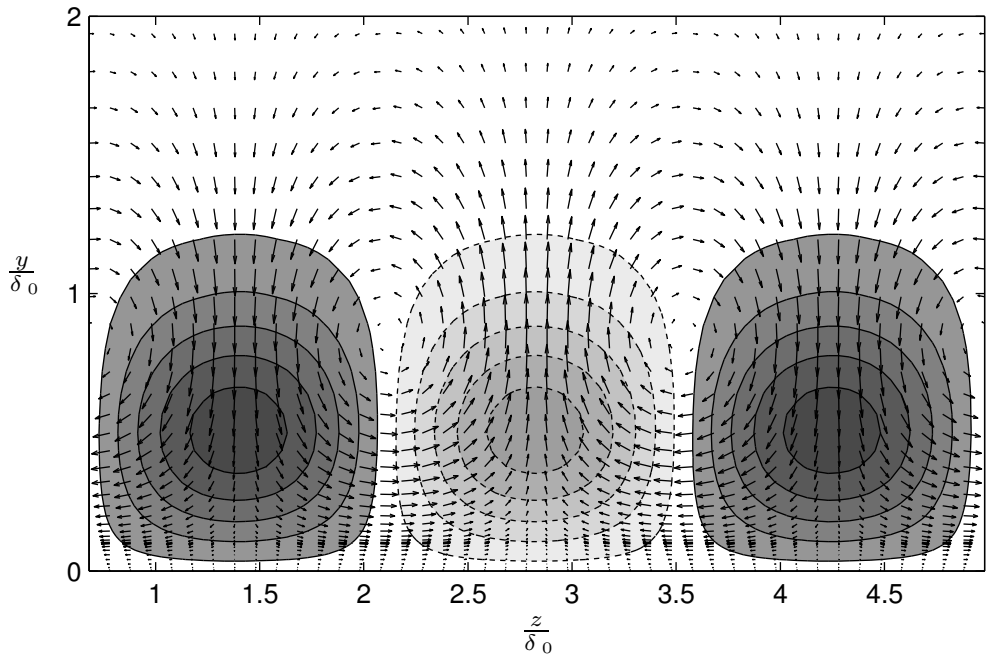


Figure 2.6: Optimal perturbation and response, $\omega = 0.001$, $k_z = 2.205$, $Re = 800$. The vector plot shows the initial optimal disturbace field $(\zeta, v, w), \zeta \ll 1$. The contour plot shows the contours of streamwise velocity u at location of maximum amplification $\chi_m = 1.5$; solid and dashed lines denote positive and negative velocity fluctuations respectively. Contour levels range from -4 to 4 with spacing of 0.25

maximum possible amplification achievable in Ω_x is $G_{max} = \max_x G(x),\ G_{max} = G(x_m)$; the associated initial condition is the *optimal disturbance*.

The initial condition corresponding to G_{max} (vector plot in figure 2.6) is a streamwise oriented vortex inside the boundary layer and evolves into a streamwise oriented structure, of which contours of the streamwise velocity perturbation at location x_{max} are presented (contour plot in figure 2.6). The spanwise location where the streamwise response is maximum occurs at the location where the initial normal velocity perturbation is maximum.

The eigenvalue spectrum, which comprises only the continuous spectrum, is shown in figure 2.7. The corresponding projection spectrum at location χ_m shows the weights $\kappa(\chi_m)$ as a function of the decay rate $\Im(k_{xi})$; the quantity $|\kappa_n(\chi_m)|$ represents the energy density of the eigenfunction $\mathbf{q}_n$ for the corresponding k_{xn} mode. The most energetic eigenfunctions have a decay rate of $O(10^{-2})$, therefore, from the dispersion relation, their length-scale $1/k_y$ is $O(\delta)$. Note that the mean shear d_yU, which plays an important role

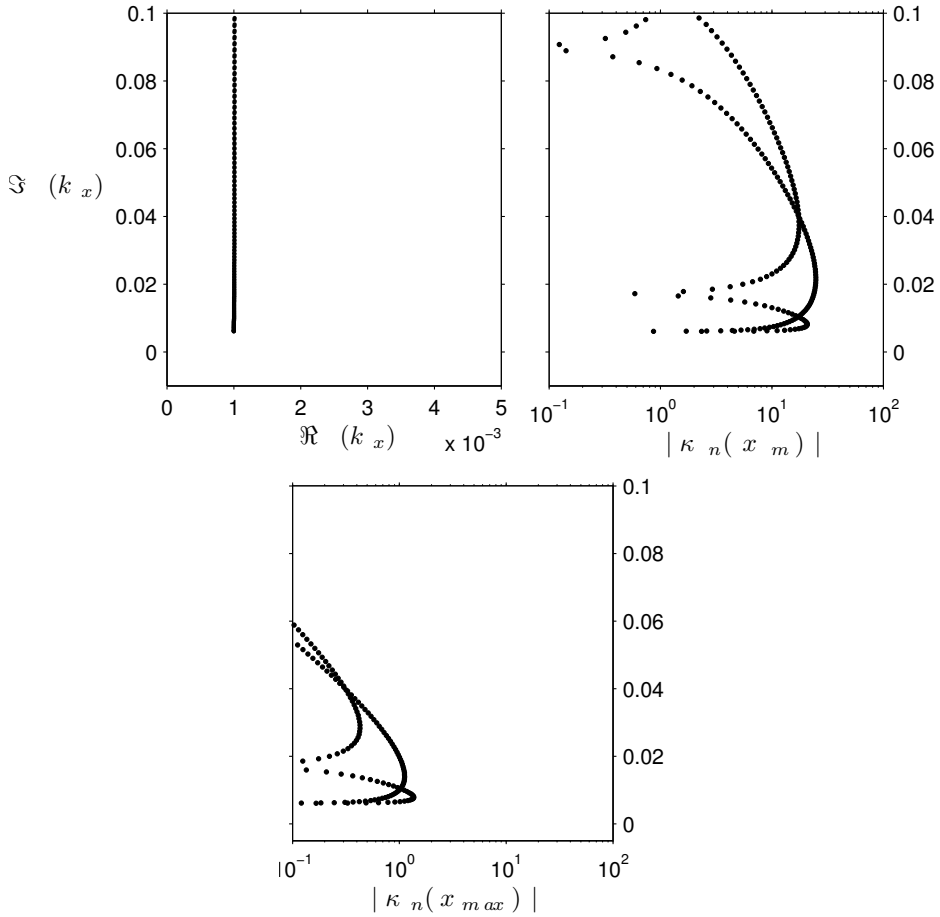


Figure 2.7: Eigenvalue spectrum in single-fluid boundary layer, $\omega = 0.001$, $k_z = 2.205$, $Re = 800$ and energy projection spectrum at initial and maximum location.

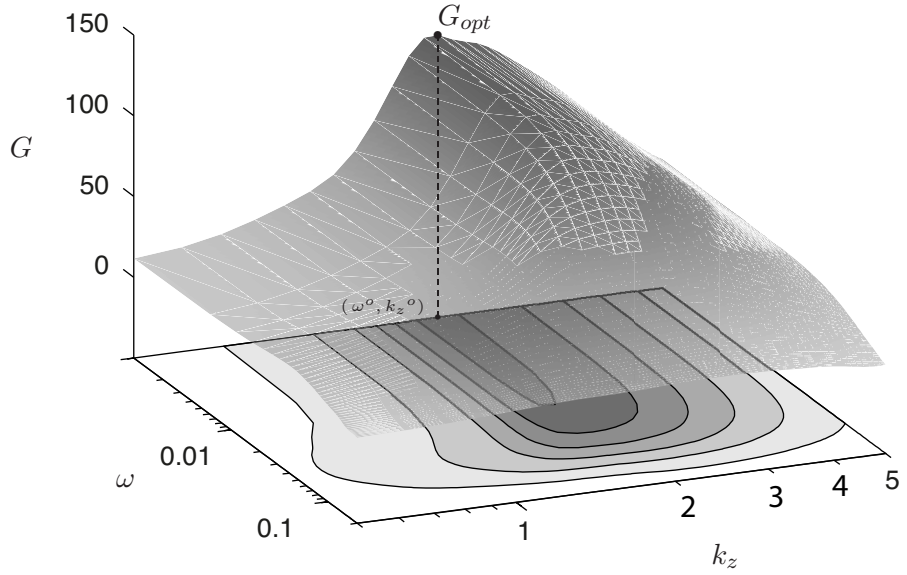


Figure 2.8: Surface plot and contours of G_{max} for single fluid Blasius boundary layer.

in the vorticity tilting mechanism (equation 2.30), varies on the same $O(\delta)$ lengthscale.

Contours of G_{max} are depicted in figure 2.8 for a single fluid boundary layer. Quasi-steady perturbations are associated with strong transient amplification. This is similar to what is generally observed in the temporal problem, where disturbances with large streamwise lengthscale are amplified the most. An optimal spanwise wavenumber $O(\delta)$ is observed, leading to maximum energy growth. The maximum possible amplification optimised over any spanwise wavenumber k_z and frequency ω is defined G_{opt}, that is:

$$G_{opt} = \max_{\omega,\ k_z} G_{max} = G_{max}\left(\omega^o, {k_z}^o\right) \tag{2.65}$$

where $(\omega^o, {k_z}^o)$ are optimal frequency and spanwise wavenumber at which G_{opt} occurs. Explanation of the transient growth mechanism comes from the investigations on the temporal initial value problem from Hultgren & Gustavsson (1981), Benney & Gustavsson (1981) and Gustavsson (1981) who indicated that short-time amplification could be attributed to a resonance mechanism between Orr-Sommerfeld and Squire eigenfunctions. These authors argued that the initial value problem is equivalent to a forced response problem where the normal vorticity is driven by the normal velocity component of the perturbation. Zaki & Durbin (2005) studied the forced temporal evolution of

normal vorticity by a continuous Orr-Sommerfeld mode and explicitly demonstrated that the extent of the amplification of the resonant Squire is determined by the forcing term, $k_z \partial_y U$. This quantity represent the coupling between normal velocity perturbation and mean shear and hence representative of the vorticity tilting mechanism. The coupling term is determined by the penetration depth of the continuous Orr-Sommerfeld modes and the mean shear distribution. Both penetration of continuous modes and mean shear distribution are affected by introduction of a wall-film layer. In the case of lower viscosity films ($m < 1$), the mean shear of the top fluid is absorbed by the film due to the tangential stress continuity at the interface. As a result, the shear is weaker in the top fluid and stronger inside the film. The coupling between mean shear and normal velocity fluctuations therefore depends on the viscosity ratio. Hence, the viscosity ratio of the system would affect the efficacy of the vorticity tilting mechanism in causing spatial amplification of linear perturbations.

The main findings on transient amplification on single fluid boundary layers were presented in this section; in the next sections, the focus is on optimal disturbances in two-fluid boundary layers and on the effect of stratification and surface tension on the energy amplification mechanism. When no Weber number is specified in simulations, assume $We = \infty$, which is equivalent to disregarding the surface tension.

2.5.2 The two-fluid boundary layer

The previous subsection described the optimal initial condition that leads to maximum amplification in a single-fluid boundary layer. In this section, the initial optimal condition and its maximum energy response in a two-fluid boundary layer are considered.

At first, a chosen set of spanwise wavenumber, temporal frequency, film thickness and viscosity is investigated to highlight how the introduction of a wall film generally affects the transient growth mechanism in two-fluid boundary layers; then a global optimization procedure is performed to establish the optimal set of parameters yielding to optimal transient growth reduction.

The energy amplification envelope as a function of the normalised streamwise location χ is shown in figure 2.9. It is clear that another competing mechanism other than vorticity tilting is affecting the energy growth. Two peaks of $G(x)$ can be observed on distinct length-scales: the first one occurs at a streamwise distance of $\chi = 1.5$, the second one

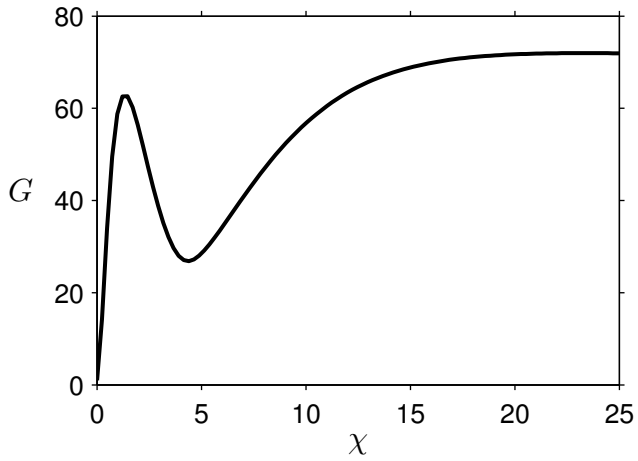


Figure 2.9: Optimal growth in two-fluid boundary layer, $\omega = 0.001$, $k_z = 2.205$, $Re = 800$, $m = 0.45$.

becomes dominant on a much larger lengthscale $\chi \approx 20$. The former is related to the vorticity tilting mechanism and it is characterized by the same streamwise peak location than the single fluid Saha (2011). Inside the boundary layer, the normal velocity tilts the mean vorticity that, in turn, generates perturbation vorticity. Therefore the normal vorticity grows and then decays due to viscous dissipation. The latter does not depend on mean shear, but it is related to the deformation of the interface (Saha, 2011). Saha has investigated the temporal equivalent and related the energy growth to the vorticity generation by the displacement of the interface.

After the first viscous peak, as the magnitude of normal velocity perturbation decreases, the normal vorticity equations is purely driven by the interfacial matching conditions and interfacial displacement, which is able to generate normal vorticity by means of the jump in mean vorticity across the interface. Recalling (2.29), the jump in vorticity, $[\![\eta]\!]$, is proportional to $(1-m)\left.\frac{\partial U}{\partial y}\right|_{y=d} f$. As $(1-m)$ increases, the jump of mean vorticity strengthens, forcing a larger normal vorticity perturbation in response to the interface deformation. The generation of normal vorticity by the interfacial displacement is referred to as the *interface deformation mechanism*. The energy amplification due to the interface deformation mechanism exceeds that caused by the vorticity tilting mechanism at this viscosity ratio, $m = 0.45$.

The optimal amplification curve in figure 2.9 has two distinct peaks at locations $\chi_{M_1} = 1.5$ and $\chi_{M_2} = 24$, at which eigenvalue and projection spectra are given in figures 2.11,

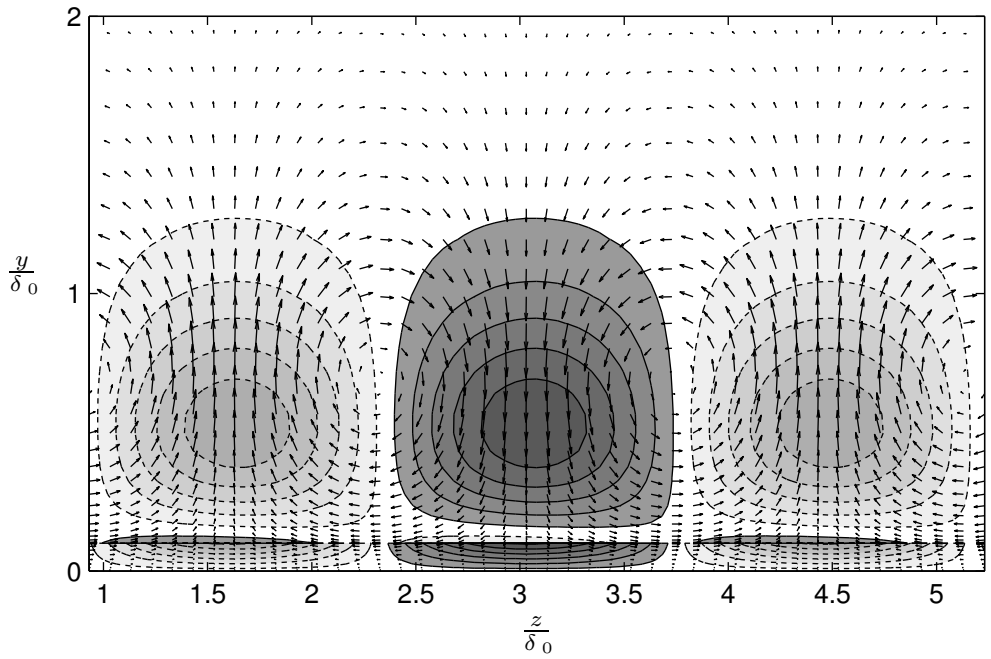


Figure 2.10: Optimal perturbation and response at $\chi_{M_1} = 1.5$, $\omega = 0.001$, $k_z = 2.205$, $Re = 800$. The vector plot shows the initial optimal disturbace field $(\zeta, v, w), \zeta \ll 1$. The contour plot shows the contours of streamwise velocity u at location of maximum amplification $\chi_{M_1} = 1.5$; solid and dashed lines denote positive and negative velocity fluctuations respectively. Contour levels range from -4 to 4 with spacing of 0.25

2.13, and the initial and optimal disturbances are given in figures 2.10 and 2.12 respectively.

The vector plot in figure 2.10 represents the initial disturbance velocity field that leads to the energy amplification at peak $\chi_{M_1} = 1.5$. It is a streamwise oriented vortex inside the boundary layer and evolves into a streamwise oriented structure, of which contours of the streamwise velocity perturbation at location χ_{M_1} are presented (contour plot in figure 2.6). The spanwise location where the streamwise response is maximum occurs at the location where the initial normal velocity perturbation is maximum.

The corresponding eigenvalue spectrum is presented in figure 2.11, along with the projection spectrum of the initial disturbance. The introduction of the wall-film layer and its interface does not affect the energy scale of the continuous spectrum; the energy-containing modes of the two-fluid boundary layer are of the same lengthscales of those ones of the single-fluid boundary layer. The relative energy density of the interface mode is $\epsilon_{int} = |\kappa_{int}| / \sum_n |\kappa_n| = 0.0086$, which is ~ 1.6 times larger than the most energetic

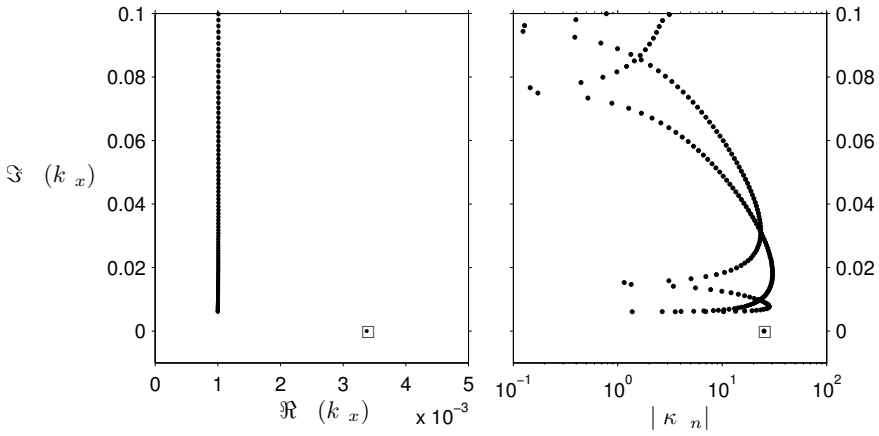


Figure 2.11: Downstream-propagating branch of the eigenvalue spectra for a two-fluid boundary layer, $\omega = 0.001$, $k_z = 2.205$, and initial energy projection spectrum to yield maximum energy response at $\chi = 1.5$. The interface mode is marked by $\square$.

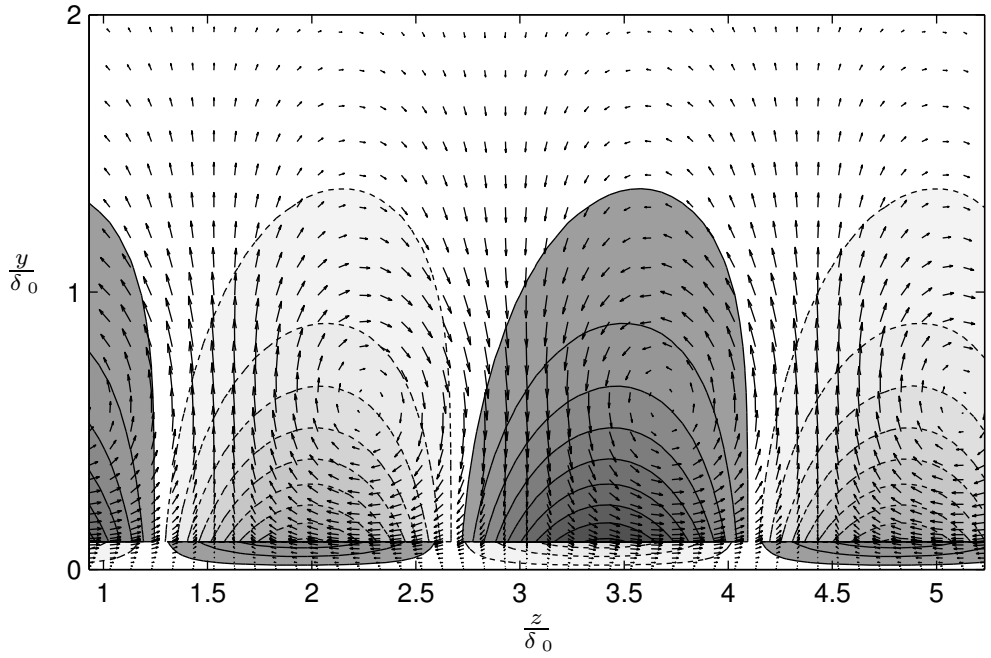


Figure 2.12: Optimal perturbation and response at $\chi_{M_2} = 24$, $\omega = 0.001$, $k_z = 2.205$, $Re = 800$. The vector plot shows the initial optimal disturbace field $(\zeta, v, w)\,, \zeta \ll 1$. The contour plot shows the contours of streamwise velocity u at location of maximum amplification $\chi_{M_2} = 24$; solid and dashed lines denote positive and negative velocity fluctuations respectively. Contour levels range from -4 to 4 with spacing of 0.25

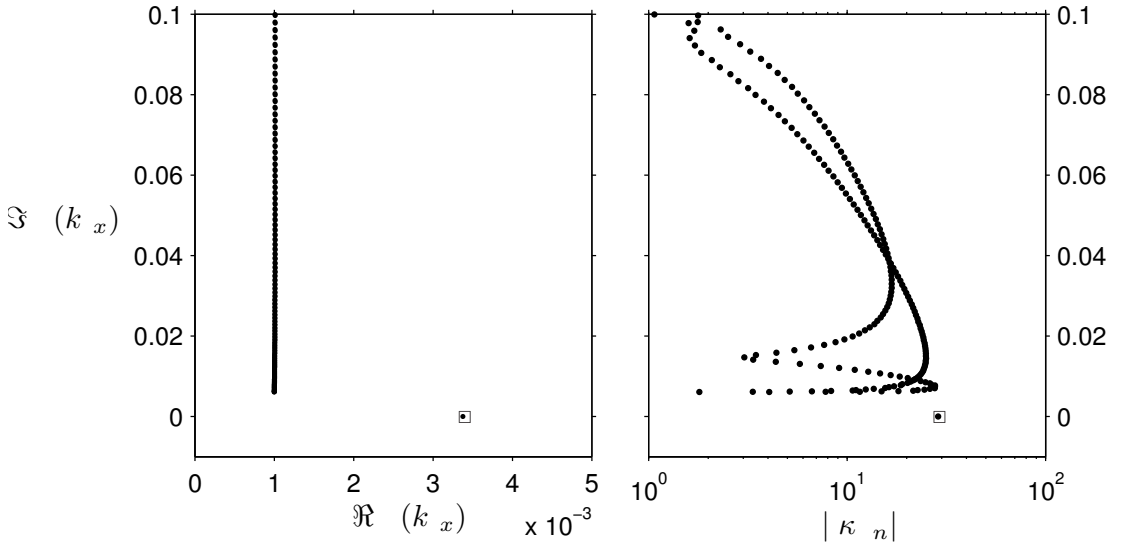


Figure 2.13: Downstream-propagating branch of the eigenvalue spectra for a two-fluid boundary layer, $\omega = 0.001$, $k_z = 2.205$, and initial energy projection spectrum to yield maximum energy response at $\chi = 24$. The interface mode is marked by $\boxdot$.

continuous mode, whose relative energy is $\epsilon_{max} = \kappa_{max}/\sum_n |\kappa_n| = 0.0052$. Contours of streamwise velocity perturbation are also shown. The optimal disturbance is concentrated in a lengthscale of $O(\delta)$ and it is a streamwise oriented vortex located inside the boundary layer. The spanwise location of maximum u is determined by the lift-up effect.

The projection spectrum of the initial disturbance that leads to maximum amplification at location peak χ_{M_2} (figure 2.13) is similar to the one at location χ_{M_1}: energetic modes have a lengthscale of $O(\delta)$ and the neutrally stable interface mode has energy density comparable to the continuous spectrum. Its relative energy density is $\epsilon_{int} = 0.0102$, which ~ 1.6 times larger than $\epsilon_{max} = 0.0061$. The vector plot of figure 2.12 shows that the optimal disturbance is also a streamwise oriented vortex inside the boundary layer. However, a stronger w component is present in the bottom fluid. The streamwise velocity component at location χ_{M_2} is qualitatively different from what observed in figure 2.10. In fact, the location of maximum u is not at the region of upwelling and downwelling, meaning that the vorticity tilting mechanism is not responsible for the energy amplification. The perturbation velocity u is instead related to the interface deformation, from which it is generated (equation 2.29). The phase shift between the top and the bottom perturbations is due to the jump in mean velocity gradient: higher shear in the bottom fluid requires the less viscous lower fluid to slow down (and the top one to accelerate) in

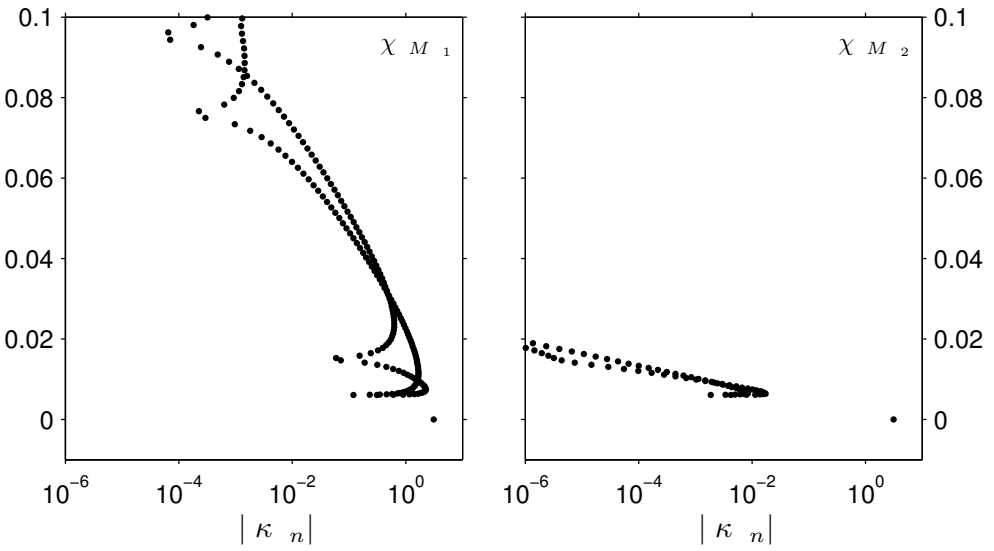


Figure 2.14: Energy projection spectra for a two-fluid boundary layer at locations χ_{M_1} and χ_{M_2}

the case of an upward displacement of the interface (equations 2.29, 2.30).

The difference in the response at peaks χ_{M_1} and χ_{M_2} is further highlighted by the comparison of the projection spectra in figure 2.14. At location χ_{M_1}, the interface mode has a considerable amount of energy, although comparable with the relative energy of the continuous modes. The energy of the optimal response at location χ_{M_2} is instead entirely determined by the interface mode, which accounts for the majority of the relative energy $\epsilon_{int} = 0.9148$, ~ 4 times larger than the most energetic continuous mode at that location.

2.5.3 Effect of viscosity stratification

The interface mode plays an important role in determining the linear amplification of disturbances and is directly related to the film thickness and viscosity ratio. In fact, particular combinations of film thickness and viscosity ratio can make the interfacial mode unstable, leading to unbounded energy growth.

The amplification curves just presented depend on spanwise wavenumber, temporal frequency, film thickness and viscosity ratio; hence, it is important to identify an optimal film thickness d^o and an optimal viscosity ratio m^o for which the maximum transient growth reduction is achieved, for any wavenumber, k_z, and frequency, ω; assume $r = 1$. From definition (2.65), note that G_{opt}, which is the maximum amplification achievable

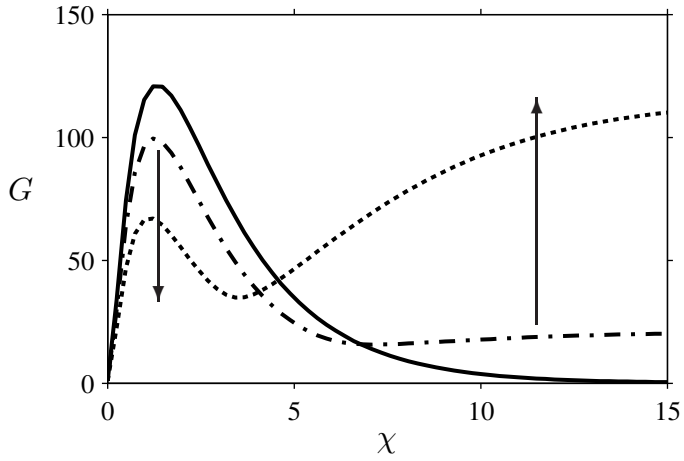


Figure 2.15: Amplification factor versus streamwise distance. —— $m = 1$, - · - $m = 0.7$, - - - $m = 0.4$, $d = 0.1$, $\omega = 0.001$, $k_z = 2.205$, $Re = 800$.

for any wavenumber k_z and frequency ω, depends on film thickness d and viscosity ratio m, that is

$$G_{opt} = G_{opt}\,(d\,, m)\,. \tag{2.66}$$

Let G_0 be the optimal amplification in the single fluid case. The optimal transient growth gain R_{opt} is defined as

$$R = R\,(d\,; m) = \frac{G_{opt}}{G_0} - 1 \tag{2.67}$$

$$R_{opt} = R_{opt}\,(d) = \min_{m} R. \tag{2.68}$$

Therefore, R_{opt} is the minimum gain achievable for any viscosity ratio m, at a given film thickness d. The purpose of this section is to determine m^o and d^o for which maximum amplification reduction is achieved. As a first approach, the film thickness is chosen to be $d = 10\%\delta_0$ and the viscosity stratification effect is investigated.

The effect of viscosity stratification on the amplification factor for various viscosity ratios is shown in figure 2.15. As discussed previously, the lift-up mechanism, which is responsible for the first peak in energy, is weakened by a reduction in the viscosity ratio m, whilst the interface deformation mechanism, responsible for the second peak, is strengthened. The two mechanisms are dominant at different viscosity ratios suggesting

the presence of a critical viscosity ratio where the leading linear mechanism for amplification changes from vorticity tilting to the interface deformation mechanism.
To identify the optimal viscosity ratio m^o, which determines the lowest amplification for $d = 0.1$, consider $G_{opt}\,(\,m\,, d = 0.1)$, that is the maximum amplification for any value of ω and k_z. Figure 2.16 shows contours of G_{max} for viscosity ratios $m = \{1.00\,,\, 0.80\,,\, 0.50\,,\, 0.40\,\}$. It is important to note that the optimal ω^o and ${k_z}^o$ at which G_{opt} occurs varies with m. In particular, as viscosity is lowered, the peak location $p_m = (\omega^o, k_z^o)$ moves away from the single-fluid optimal $p_{1.00} = (\,0\,,\, 2.205)$ to $p_{0.55} = (\,0.0125\,,\, 1.5)$, where the lowest G_{opt} is reached. As the viscosity ratio is further lowered, the peak location moves towards the low-ω, low-k_z region. G_{max} surface for the set of parameters leading to G_{opt} is shown in figure 2.17.

The maximum amplification factor G_{max} is computed over a range of spanwise wavenumbers and frequencies at various viscosity ratios. The global optimization procedure evaluates the optimal amplification factor G_{opt} and quantifies the maximum transient growth gain in the worst case scenario of the most amplifying wave number ${k_z}^o$ and frequency ω^o as a function of viscosity ratio m. Figures 2.18a-2.18c present respectively G_{opt},${k_z}^o$ and ω^o versus various viscosity ratios m for values of film thickness $d_0 = 0.05, 0.1, 0.15$.

The gain coefficient, R, is computed and its variation is shown in figure 2.19. As the viscosity ratio is reduced from the single-fluid limit, R gradually increases for viscosity ratios in the range $m \in [0.55, 1]$, at the limit of which the R_{max} can be found. For $m \in [0.4, 0.55]$, the gain coefficient decreases from the its maximum value R_{max} at $m = 0.55$ to the single-fluid value; for $m < 0.4$ positive gain is registered, meaning that the two-fluid system performs worse than the single-fluid one. In the range $m \in [0.4, 1]$, the reduction is due to the weakening of the lift-up effect, while for $m \in [0.01, 0.4]$ there is a substantial production of energy due to growth of the interface disturbance.

The gain coefficient R was optimised over all possible film thickness, $d \in [0.01, 1]\delta_0$ and the optimal gain at any film thickness, R_{opt}, was determined. A plot of R_{opt} versus film thickness is shown in figure 2.20a and corresponding optimal viscosity ratio per film thickness is reported in figure 2.20b. The optimal viscosity ratio m^o is correlated to the film thickness. This relation can be explained recalling the fact that the mean shear, which is responsible for the vorticity tilting mechanism, is absorbed by the low-viscous film, proportionally to the film thickness and to the quantity $(1 - m)$. Assume fixed

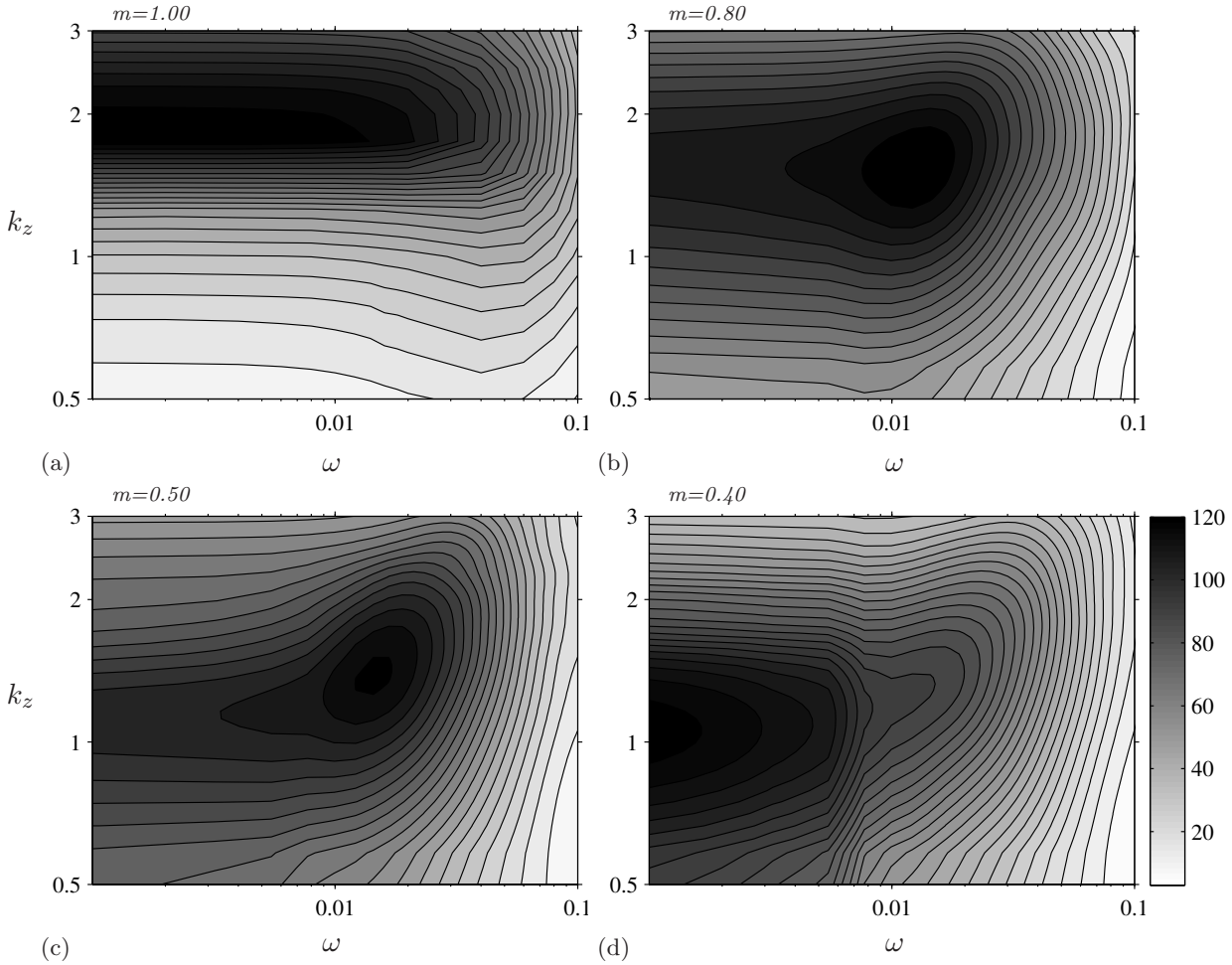


Figure 2.16: G_{max} contours for viscosity ratios of $m = 0.4$ (figure 2.16d), $m = 0.5$ (figure 2.16c), $m = 0.8$ (figure 2.16b) and $m = 1.0$ (figure 2.16a) and $d = 0.1$.

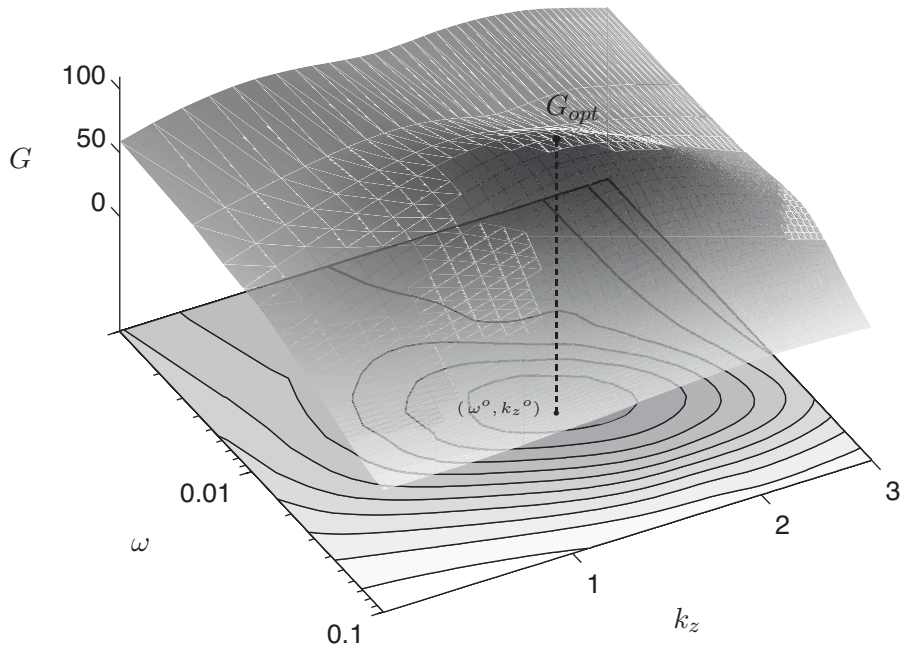


Figure 2.17: G_{max} surface and contours for $m = 0.55$ and $d = 0.1$.

reduction; therefore, when d is small, a higher absorption of mean shear is achieved by maximising $(1 - m)$, that is for low values of m; on the contrary, when d is as large as the boundary layer, the mean shear is totally absorbed by the film, thus little additional contribution from the viscosity mismatch is needed to achieve the same reduction. However, the process is in fact more complex, as higher film thickness have a destabilising effect on the interface mode, which becomes unstable. As shown in figure 2.20a, 2.20b, for $d > 0.3\delta_0$, there is at least a wavenumber couple $(\omega^o, k_z{}^o)$ for which the flow is unstable or the gain coefficient $R > 1$, meaning that the two fluid configuration performs worse than the single fluid benchmark. Therefore, $m^o = 1$ and $R_{opt} = 1$ when $d > 0.3$. The optimal film thickness d^o is found to be $10\%\delta_0$, for which the maximum reduction of $-R_{opt} = 28\%$ is achieved (figure 2.20a).

2.5.4 Surface tension effects

As discussed in section §2.4.4, surface tension can have a stabilising effect on discrete instabilities (Hooper & Boyd, 1983; Saha, 2011). In two-fluid boundary layers, at the

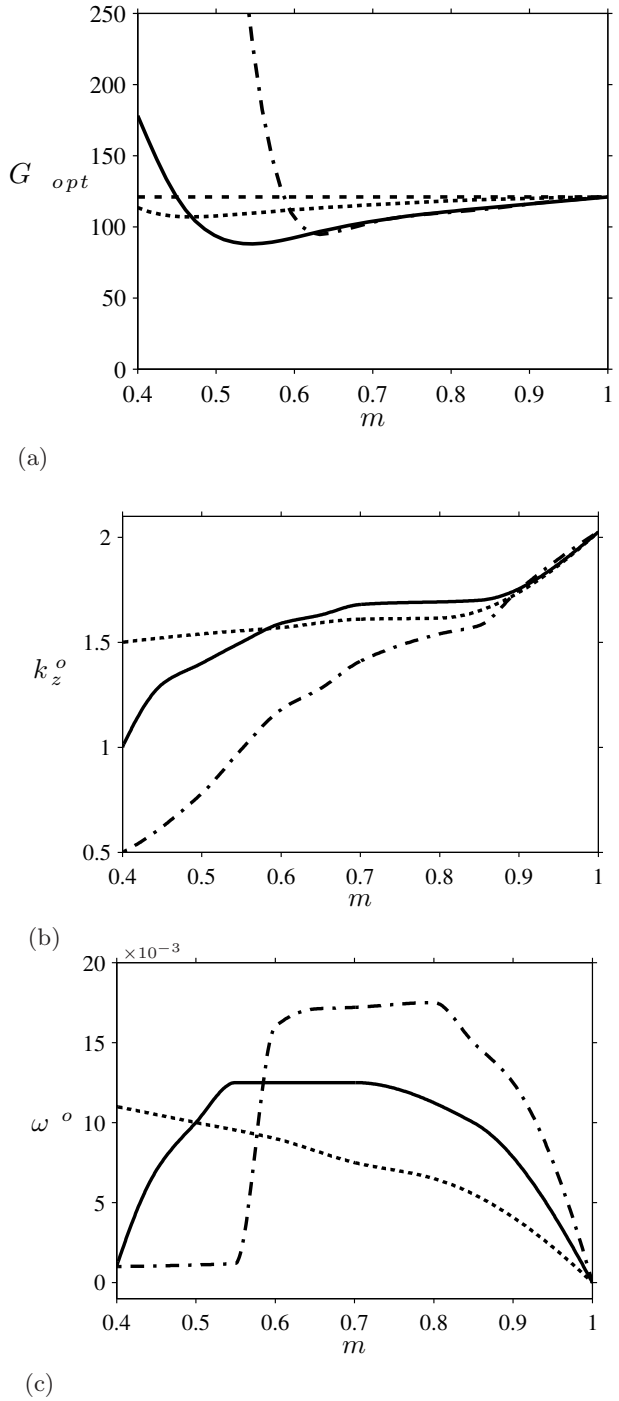


Figure 2.18: a) Maximum amplification factor G_{opt} versus viscosity ratio m; b) optimal temporal frequency ω^o versus viscosity ratio m; c) optimal spanwise wavenumber ${k_z}^o$ versus viscosity ratio m. - - - $d_0 = 0.05$, —— $d_0 = 0.10$, - · - $d_0 = 0.15$

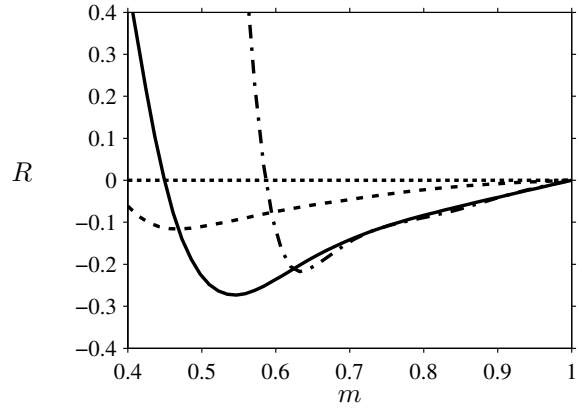
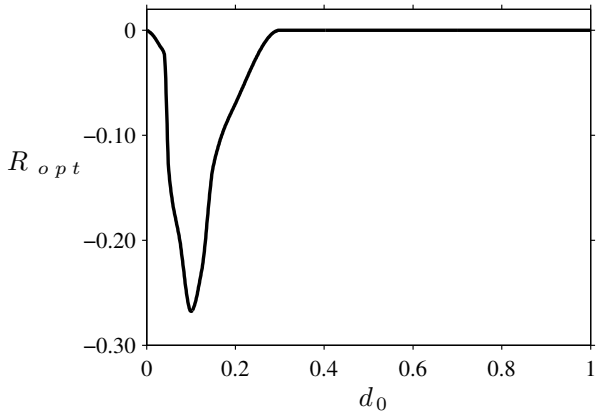
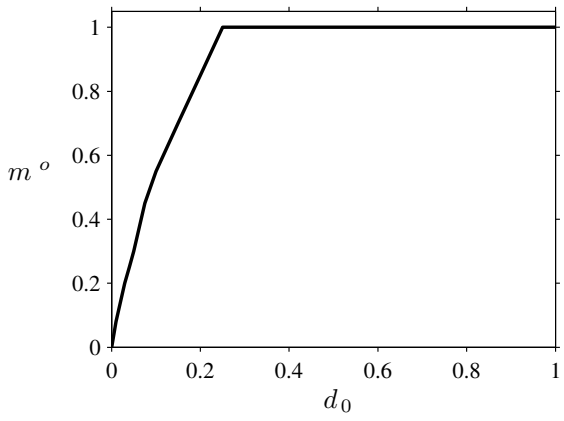


Figure 2.19: Reduction of maximum energy amplification versus viscosity ratio m, - - - $d_0 = 0.05$, —— $d_0 = 0.10$, - · - $d_0 = 0.15$



(a)



(b)

Figure 2.20: (2.20a) Optimal reduction and (2.20b) optimal viscosity ratio versus inlet film thickness d_0

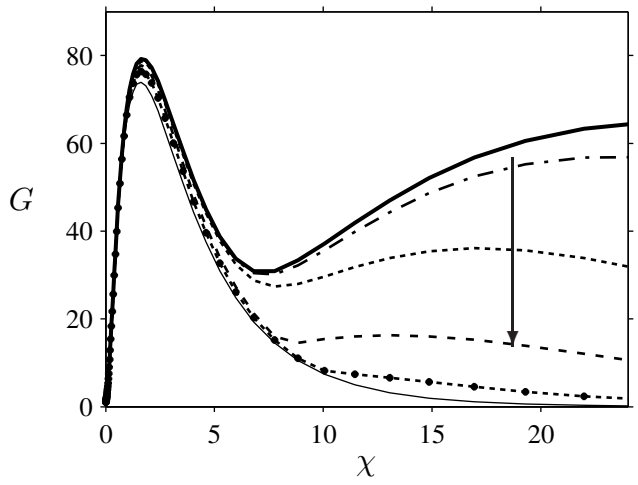


Figure 2.21: Effect of surface tension on transient growth for $m = 0.55$, $k_z = 1.5$, $\omega = 0.001$. ——— $We = +\infty$, – ·– $We = 50\times10^3$, ····· $We = 10\times10^3$, – – – $We = 4\times10^3$, – ·– $We = 2\times10^3$, —— $We = 1\times10^3$

Reynolds number and viscosity ratio presented in this work, it affects the amplification mechanism by stabilising the interfacial mode and reducing the ability of the interfacial energy generation mechanism to produce disturbances. Figure 2.21 shows the effect of surface tension on energy amplification for $m = 0.55$, $k_z = 1.5$, $\omega = 0.001$, $Re = 800$ and $We = \{1,\ 2,\ 4,\ 10,\ 50,\ +\infty\} \times 10^3$. These values of We are common in physical and industrial application mentioned in Chapter 1; wind shearing the ocean surface has a Weber number 7000.

Larger values of We correspond to lower surface tension. Surface tension has little influence on the wavenumber or magnitude of peak transient growth, but it acts directly on the interface mode, weakening its effect on transient growth, as We decreases. The quantity We^{-1} can be considered as a lagrangian multiplier for f. Consider equations 2.32 for normal stress continuity; when $We^{-1} = 0$, τ_{yy} is independent of f, therefore any large interface deflection is in fact compatible with the interfacial conditions. As We^{-1} increases, the product $We^{-1}f$ is now part of the relation for τ_{yy} and forces smaller values for f. For low values of We (i.e. high surface tension), the interface mode disappears and is replaced by capillary modes (Yecko & Zaleski, 2005a). At the viscosity ratio presented, the capillary modes have a stabilising effect on transient growth; at larger viscosity and density ratios ($m = 0.018$, $m = 0.0012$), Yecko & Zaleski (2005a) showed instead that transient growth in temporal mixing layers increases as We increases.

2.6 Conclusions

In this chapter, the characteristics of transient growth with parallel-flow assumption were explored. Evolution equations for infinitesimal disturbances in parallel two-fluid boundary layers were derived and presented. Due to the parallel-flow assumption, the solution of the governing equations is represented by a 4^{th}-order polynomial eigenvalue problem, which is solved using mapped Chebyshev polynomials and a standard eigenvalue solver. Details of the discrete and continuous eigenvalue spectra were briefly discussed, in order to explain the challenges related to the formulation of the spatial initial-boundary-value problem.

The optimization problem for the determination of optimal disturbances was formulated. The mechanism of transient growth was investigated for single and two-fluid boundary layers, highlighting the presence of a mechanism of energy production due to the presence of an interface mode, similar to the one investigated by Saha (2011). This mechanism was found to be efficient at low ω and damped by increasing surface tension

Furthermore, the effect of viscosity stratification on amplification was investigated. The addition of a lower viscosity wall-film introduces a competition between the lift-up mechanism (weakened by decreasing viscosity ratio) and the interfacial mechanism (strengthened by the increasing jump in viscosity). This competition leads to a critical viscosity ratio and film-thickness that maximise the beneficial effects of the film on amplification. A parametric optimization was thus performed to establish an optimal set of parameters for reduction of reduction of transient growth.

The theoretical and numerical results presented in this chapter are valid under a locally-parallel base-flow assumption, which might be particularly restrictive in the case of two-fluid boundary layers, due the different spreading rates of the mean flow and the film. These issues are investigated in the next chapter, in which the parallelism assumption is relaxed, a spreading framework for optimal disturbances is derived and comparisons with parallel-flow stability results are made.

Chapter 3

Non-modal stability: non-parallel base flow

3.1 Introduction

Streamwise variation of the boundary layer affects the accuracy of growth rates predicted by locally-parallel methods, for both discrete and algebraic instabilities. Nonparallel effects are small and of order $\mathcal{O}(Re^{-1})$, but still important (Herbert, 1997). The weak streamwise dependence of boundary layers has historically been disregarded in order to satisfy the stability theory built on the Orr-Sommerfeld and Squire theory. This has resulted in some deficiencies of the parallel analysis, namely:

a) the mean flow nonparallelism is neglected;

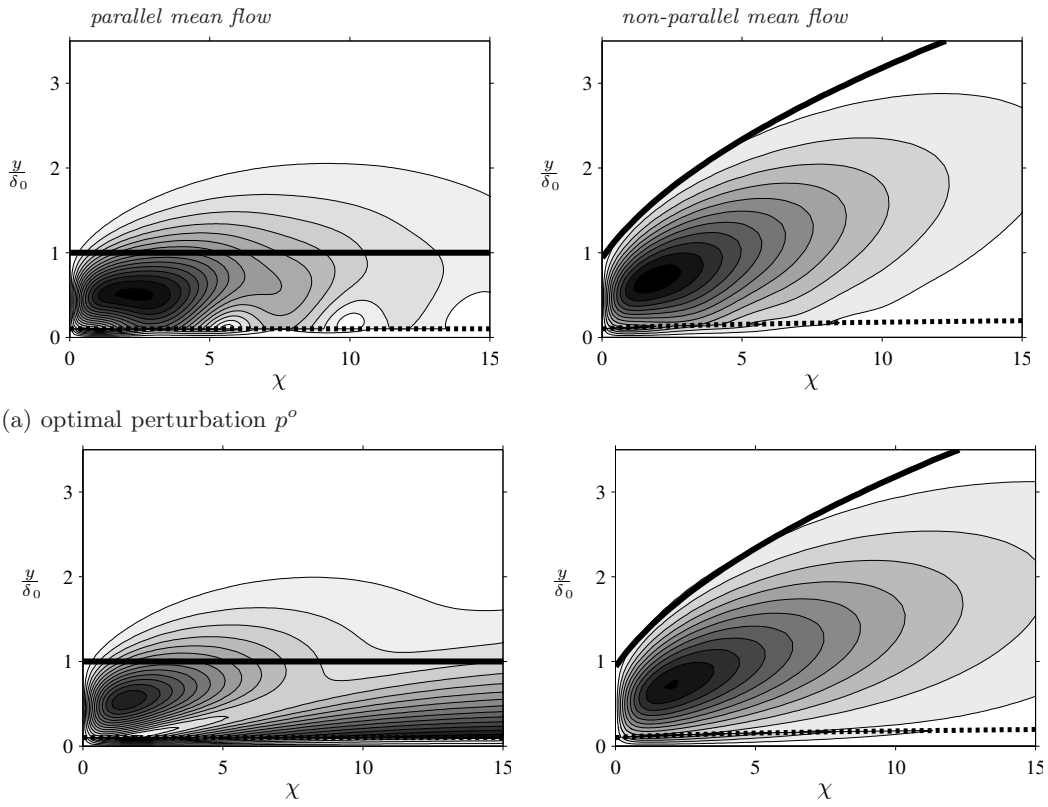
b) the upstream history of convected disturbances, both in temporal and spatial analyses, is not considered;

c) scale conversion and energy transfer between modes are not considered.

To address the above limitations, stability theory of boundary layers has expanded to methods based on parabolic partial differential equations, that would account for nonparallelism, non-linearity and propagation history. This parabolic framework was successfully modified and merged into the so-called Parabolized Stability Equations (PSE), which describe the evolution of linear and non-linear disturbances in weakly streamwise dependent flows (Herbert, 1997). In this chapter, the effects of nonparallelism on optimal disturbances are addressed following a parabolic framework, whilst nonlinear effects are temporarily disregarded and are analysed by Direct Numerical Simulation (DNS) in the

next chapter.

A motivation for the need to incorporate mean flow Non-parallel effects lies in the fact



(a) optimal perturbation p^o

(b) sub-optimal perturbation p^{so}

Figure 3.1: Effect of mean flow spreading on streamwise velocity response, u_{rms}. $d_0^o = 0.10$; $k_z^o = 1.5$; $m^o = 0.55$; (3.1b) $\omega^{so} = 0.0010$, (3.1a) $\omega^o = 0.0125$. —— boundary layer's edge; - - - mean interface location.

that the evolution of a disturbance under parallel mean flow assumption can be radically different from its spreading counterpart. In particular, in two-fluid boundary layers, the interface location spreads at a different rate than the boundary layer thickness (Nelson *et al.*, 1995), causing the effect of a wall film on the upper fluid to vary in the streamwise direction. In particular, consider the optimal disturbance determined in the previous chapter for the parameter set $p^o : \{\omega^o = 0.0125,\ k_z^o = 1.5,\ m^o = 0.55,\ d^o = 0.10\}$ and the sub-optimal disturbance for the parameter set $p^{so} : \{\omega = 0.0010,\ k_z^o = 1.5,\ m^o = 0.55,\ d^o = 0.10\}$; figure 3.1 reports contours in χy-plane of streamwise response of $|u|$ to the inlet optimal and sub-optimal disturbances under parallel and non-parallel mean flow assumptions. In the case of the suboptimal set p^{so} (figure 3.1b), the velocity response at large streamwise distance radically different. In particular, the interfacial deformation

mechanism does not appear to play an important role when the boundary layer spreads (figure 3.1b). Note that the u-response close to the interface is generally weaker also in the optimal set p^o (figure 3.1a). Therefore, it is legitimate to question how the findings under the parallel linear stability framework might evolve when some of the constitutive assumptions are discarded. In particular, in this chapter the assumption on base flow parallelism is dropped and spatial evolution effects are incorporated into a (new) linear stability framework for optimal disturbances.

A method for the determination of optimal disturbance in two-fluid non-parallel boundary layers is developed, exploiting the fact that the mean flow is governed by the boundary-layer approximation and, moreover, that the second derivatives of the disturbance velocity profile with respect to the streamwise direction are sufficiently small and can therefore be neglected without loss of accuracy.

This chapter is organised into 5 sections. The next section describes the mean flow equations along with boundary conditions. Effects of stratification on mean quantities are shown. In §3.3, details of the disturbance equations and boundary conditions are given. The optimal problem for determination of the most amplifying disturbances in two-fluid non-parallel boundary layers is formulated in §3.4. Details of the numerical method, which includes non-linear domain transformation and Chebyshev polynomial expansion, are given. Non-parallel effects are quantified and optimal streamwise amplification and optimal disturbances are compared with previous parallel results. A summary of the key results of the chapter can be found in §3.5.

3.2 The non-parallel base flow

The spatial evolution of an infinitesimal disturbance in a laminar, incompressible, two-fluid non-parallel boundary layer with surface tension is considered. Details of the base flow, governing equations, optimal disturbance formulation and details of the numerical solution are given in this section.

The general consideration on mean governing equations and domain topology given in §2.2 hold.

Consider a domain $\Omega = \Omega_x \times \{\Omega_y^B \cup \Omega_y^T\} \times \Omega_z = [x_0, x_f] \times \{[0, d] \cup [d, +\infty)\} \times (-\infty, +\infty)$ with smooth boundaries. The base flow consists of a two-fluid non-parallel boundary layer flow in direction $x \in \Omega_x$ of the form $\mathbf{U} = [U_j(x, y),\ V_j(x, y),\ 0]$ with physical

properties density ρ_j and viscosity μ_j, where the subscript $j = \{T, B\}$ denotes the top ($y \geq d$) and bottom ($y \leq d$) fluids respectively and $y \in \Omega_y$ is the wall-normal direction. We define r and m to be the ratios of densities and viscosities, respectively, i.e. $r = \rho_j/\rho_T$ and $m = \mu_j/\mu_T$. Note that $d = d(x, z)$ and $d_0 = d(x_0, z)$. The mean velocity profile is obtained by solving the two-fluid boundary-layer equations presented in Nelson *et al.* (1995) according to the approach described in (Schlichting, 1987, pp. 187-191). In boundary layer coordinates, the mean flow satisfies:

$$FF'' + \nu_j F''' - \mathtt{x}\left(F'\frac{\partial F'}{\partial \mathtt{x}} - F''\frac{\partial F}{\partial \mathtt{x}}\right) = 0 \tag{3.1}$$

where $F = \frac{\Psi}{2\nu_T U_\infty x}$ with Ψ as the streamfunction and $F' = \frac{\partial F}{\partial \mathtt{y}}$, $F'' = \frac{\partial^2 F}{\partial \mathtt{y}^2}$, $F''' = \frac{\partial^3 F}{\partial \mathtt{y}^3}$, $\mathtt{x} = \sqrt{\frac{U_\infty x}{2\nu_T}}$, $\mathtt{y} = y\sqrt{\frac{U^\infty}{2\nu_T x}}$, $U = U^\infty \frac{\partial F}{\partial \mathtt{y}}$, $V = U^\infty \mathtt{y}\frac{\partial F}{\partial \mathtt{y}} - F - \mathtt{x}\frac{\partial F}{\partial \mathtt{x}}$. The free-stream velocity is denoted by U^∞, the kinematic viscosity by ν and x is the downstream location relative to the leading edge. The interface height $\mathtt{d} = d\sqrt{\frac{U^\infty}{2\nu_T x}}$ is governed by the kinematic condition:

$$\frac{\partial \mathtt{d}}{\partial \mathtt{x}} = \frac{1}{\mathtt{x}}\left(\frac{V\delta_\Gamma(\mathtt{y}-\mathtt{d})}{U\delta_\Gamma(\mathtt{y}-\mathtt{d})} - \mathtt{d}\right) \tag{3.2}$$

where $U\delta_\Gamma(\mathtt{y}-\mathtt{d})$, $V\delta_\Gamma(\mathtt{y}-\mathtt{d})$ are the mean streamwise and wall-normal velocities at the interface. At $\mathtt{y} = \mathtt{d}$, continuity of velocities and stresses is applied:

$$[\![F]\!] = 0\ ; \qquad \left[\!\!\left[\frac{\partial F}{\partial \mathtt{y}}\right]\!\!\right] = 0\ ; \qquad \left[\!\!\left[\frac{\partial^2 F}{\partial \mathtt{y}^2}\right]\!\!\right]_m = 0\ ; \tag{3.3}$$

where the operator $[\![\cdot]\!]$ denotes the change across the interface, $(\cdot)_T - (\cdot)_B$ and $[\![\cdot]\!]_m = (\cdot)_T - m(\cdot)_B$.

In addition, the wall and free-stream boundary conditions are:

$$F(\mathtt{x}, 0) = 0; \qquad \left.\frac{\partial F(\mathtt{x},\mathtt{y})}{\partial \mathtt{y}}\right|_{\mathtt{y}=0} = 0; \qquad \lim_{\mathtt{y}\to\infty}\frac{\partial F(\mathtt{x},\mathtt{y})}{\partial \mathtt{y}} = 1. \tag{3.4}$$

Physical quantities are made dimensionless according to a length scale L and velocity scale U^*, set by the base flow. In particular, $U^* = U^\infty$, $\rho^* = \rho_T$, $\mu^* = \mu_T$. This yields

the non-dimensional parameters Reynolds and Weber numbers respectively:

$$Re = \frac{\rho^* U^* L^*}{\mu^*} = \frac{\rho_T U^\infty \delta_0}{\mu_T} \; ; \qquad We = \frac{\rho^* U^{\infty 2} L^*}{\sigma} = \frac{\rho_T U^{\infty 2} \delta_0}{\sigma} \tag{3.5}$$

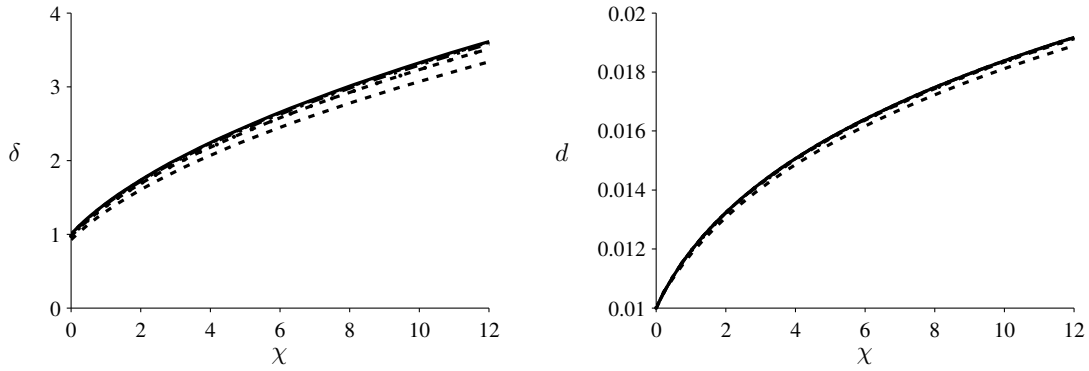
where $L = \delta_0 = 4.9\sqrt{\frac{\nu_T x_0}{U^\infty}}$ and σ is the surface tension.

As already discussed in the previous chapter, δ depends on the viscosity ratio m; the reference scale for two-fluid computations is therefore normalised to the single fluid Blasius boundary layer thickness δ_0 at the inlet of the domain.

Figure 3.2 show the dipendency of the boundary layer thickness δ and mean interface location d on the viscosity ratio m, for different values of the film thickness $d_0 = \{0.01, 0.10, 0.25\}$. In particular, a very thin film ($d_0 = 0.01$, figures 3.2a-3.2b), regardless its viscosity, has a limited effect on the spreading of the mean flow; as the thickness of the film is increased ($d_0 = 0.10$, figures 3.2c-3.2d), the viscosity ratio m can affect the spreading of the meanflow and of the interface. If the thickness of the wall layer is further increased ($d_0 = 0.25$, figures 3.2e-3.2f), lowering the viscosity ratio m can significantly affect the evolution of the mean interface location and the thickness of the boundary layer.

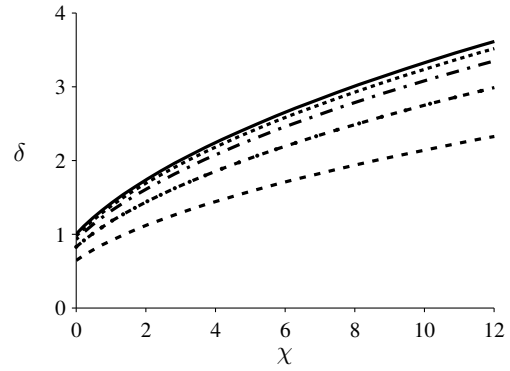
3.3 The linear perturbation equations

In general, the thickness of the boundary layer varies in the streamwise direction. Consider a location x_0 far downstream from the leading edge: the purpose of this section is to find a set of linear governing equations which describes the spatial evolution of disturbances and which is parabolic in nature. Such a system can be efficiently solved by streamwise marching techniques (Herbert, 1997). This approach is similar to Andersson *et al.* (1999), although unsteadiness is also accounted for, which is important in the case of two-fluid flows. As seen in the previous chapter, relevant amplification, due to the interface, can be found at frequencies $\omega \neq 0$; a steady-state assumption would thus neglect the interfacial dynamics. These considerations motivate the use of the *boundary layer approximation* (BL) of the incompressible Navier-Stokes equations. Figure 3.3 shows the maximum value of $\frac{\partial^2 U}{\partial x^2}$ versus the streamwise distance χ; note that $\frac{\partial^2 U}{\partial x^2} \ll 1$.

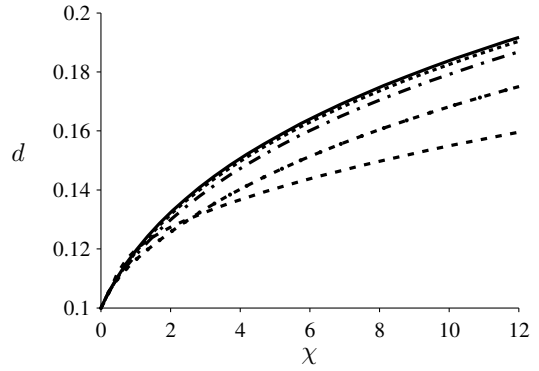


(a) $\delta(\chi)$, $d_0 = 0.01$

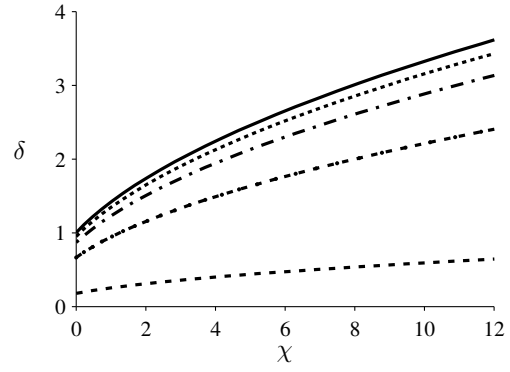
(b) $d(\chi)$, $d_0 = 0.01$



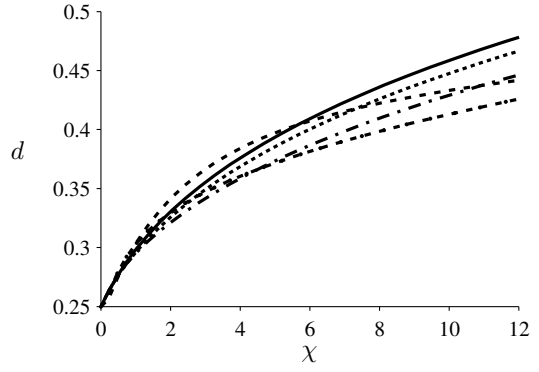
(c) $\delta(\chi)$, $d_0 = 0.10$



(d) $d(\chi)$, $d_0 = 0.10$



(e) $\delta(\chi)$, $d_0 = 0.25$



(f) $d(\chi)$, $d_0 = 0.25$

Figure 3.2: Effect of viscosity on boundary layer thickness $\delta(\chi)$, (3.2a) $d_0 = 0.010$, (3.2c) $d_0 = 0.10$, (3.2e) $d_0 = 0.25$; Effect of viscosity on mean interface location d, (3.2b) $d_0 = 0.010$, (3.2d) $d_0 = 0.10$, (3.2f) $d_0 = 0.25$. —— $m = 1 -$ Blasius, $\cdots\cdots$ $m = 0.75$, – · – $m = 0.5$, – – – $m = 0.25$, – – – $m = 0.1$

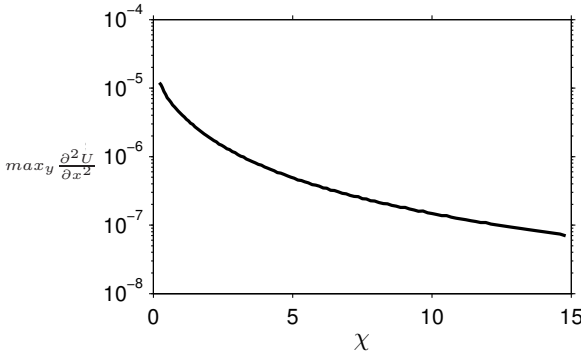


Figure 3.3: Streamwise evolution of maximum value of $\frac{\partial^2 U}{\partial x^2}$

3.3.1 Governing equations and boundary conditions

Consider the semi-infinite Hilbert space $\mathcal{H}(\Omega)$ in which the incompressible Navier-Stokes equations (NS), stated in equations 2.1, 2.2, along with the interfacial condition 2.3, are satisfied by a vector field $\mathcal{U}$ and scalar field $\mathcal{P}$. Under BL, these equations are as follows:

$$\partial_t \mathcal{U}_j + (\mathcal{U}_j \cdot \nabla)\,\mathcal{U}_j = -\frac{\nabla \mathcal{P}_j}{\rho_j} + \nu_j \Delta^* \mathcal{U}_j \tag{3.6}$$

$$\nabla \cdot \mathcal{U}_j = 0 \tag{3.7}$$

where $\Delta^* = \left(\frac{\partial^2}{\partial y^2} + \frac{\partial^2}{\partial z^2}\right)$. The decomposition stated in equation 2.5 is applied and the base state $\mathbf{U}$ is perturbed by an infinitesimal disturbance field $\hat{\mathbf{q}}_j = (\hat{\mathbf{u}}, \hat{p})_j = (\hat{u}, \hat{v}, \hat{w}, \hat{p})_j \in \mathcal{H}(\Omega)$ which satisfies the BL. These equations are linearized to model the spatial linear evolution of three-dimensional disturbances around the base flow $\mathbf{U}$, resulting in the following governing equations:

$$\partial_t \hat{\mathbf{u}}_j + (\mathbf{U}_j \cdot \nabla)\,\hat{\mathbf{u}}_j + (\hat{\mathbf{u}}_j \cdot \nabla)\,\mathbf{U}_j = -\frac{\nabla \hat{p}_j}{\rho_j} + \nu_j \Delta^* \mathcal{U}_j \tag{3.8}$$

$$\nabla \cdot \hat{\mathbf{u}}_j = 0 \tag{3.9}$$

The additional boundary and initial conditions

$$\hat{\mathbf{u}}_j|_{\partial(\Omega_y \times \Omega_z)} = 0 \tag{3.10}$$

$$\hat{\mathbf{u}}_j|_{t=0} = \hat{\mathbf{u}}_{0_j} \tag{3.11}$$

Equations 3.6-3.11 can be written as:

$$\hat{\mathcal{L}}_j \hat{\mathbf{q}}_j = \frac{\partial}{\partial x}\left(\hat{\mathbf{A}}_j \hat{\mathbf{q}}_j\right) - \left(\hat{\mathbf{B_0}}_j + \hat{\mathbf{B_1}}_j \frac{\partial}{\partial y} + \hat{\mathbf{B_2}}_j \frac{\partial^2}{\partial y^2}\right)\hat{\mathbf{q}}_j = 0 \tag{3.12}$$

where

$$\hat{\mathbf{A}}_j = \begin{bmatrix} 1 & 0 & 0 & 0 \\ U_j & 0 & 0 & 1 \\ V_j & U_j & 0 & 0 \\ 0 & 0 & U_j & 0 \end{bmatrix}$$

$$\hat{\mathbf{B_0}}_j = \begin{bmatrix} 0 & 0 & -\frac{\partial}{\partial z} & 0 \\ \frac{\partial}{\partial t} - \frac{m}{r}\frac{1}{Re}\frac{\partial^2}{\partial z^2} & -\frac{\partial U_j}{\partial y} & 0 & 0 \\ 0 & \frac{\partial}{\partial t} - \frac{m}{r}\frac{1}{Re}\frac{\partial^2}{\partial z^2} - 2\frac{\partial V_j}{\partial y} & -V_j\frac{\partial}{\partial z} & 0 \\ 0 & 0 & \frac{\partial}{\partial t} - \frac{m}{r}\frac{1}{Re}\frac{\partial^2}{\partial z^2} - \frac{\partial V_j}{\partial y} & -\frac{\partial}{\partial z} \end{bmatrix}$$

$$\hat{\mathbf{B_1}}_j = \begin{bmatrix} 0 & -1 & 0 & 0 \\ -V_j & 0 & 0 & 0 \\ 0 & -2V_j & 0 & -\frac{1}{r} \\ 0 & 0 & -V_j & 0 \end{bmatrix} \quad \hat{\mathbf{B_2}}_j = \begin{bmatrix} 0 & 0 & 0 & 0 \\ -\frac{m}{r}\frac{1}{Re} & 0 & 0 & 0 \\ 0 & -\frac{m}{r}\frac{1}{Re} & 0 & 0 \\ 0 & 0 & -\frac{m}{r}\frac{1}{Re} & 0 \end{bmatrix}. \tag{3.13}$$

The dynamics of the interface follows the relation stated in equation 2.6. The mean interface location d is perturbed by an infinitesimal displacement $\hat{f}$; the interface displacement follows the kinematic condition:

$$\left(\hat{\mathcal{I}}_j \hat{f} + \hat{\mathcal{C}}\hat{\mathbf{q}}_j\right)\delta_\Gamma(y-d) = 0 \tag{3.14}$$

where

$$\hat{\mathcal{I}}_j \hat{f} = \frac{\partial}{\partial x}\left(U_j \hat{f}\right) - \left(\frac{\partial}{\partial t} - \frac{\partial V_j}{\partial y}\right)\hat{f}; \qquad \hat{\mathcal{C}}_j \hat{\mathbf{q}} = -\hat{v}_j. \tag{3.15}$$

At the interface, continuity of velocities and stresses apply:

$$[\![\hat{u}]\!] + \left[\!\!\left[\frac{\partial U}{\partial y}\right]\!\!\right] \hat{f} = 0 \tag{3.16}$$

$$[\![\hat{v}]\!] + \left[\!\!\left[\frac{\partial V}{\partial y}\right]\!\!\right] \hat{f} = 0 \tag{3.17}$$

$$[\![\hat{w}]\!] = 0 \tag{3.18}$$

$$\left[\!\!\left[\frac{\partial \hat{u}}{\partial y} + \frac{\partial \hat{v}}{\partial x}\right]\!\!\right]_m + \left[\!\!\left[\frac{\partial^2 U}{\partial y^2}\right]\!\!\right]_m \hat{f} = 0 \tag{3.19}$$

$$\left[\!\!\left[\frac{\partial \hat{w}}{\partial y} + \frac{\partial \hat{v}}{\partial z}\right]\!\!\right]_m + \left[\!\!\left[\frac{\partial V}{\partial y}\right]\!\!\right]_m \frac{\partial \hat{f}}{\partial z} = 0 \tag{3.20}$$

$$[\![-\hat{p}]\!]_{\frac{1}{r}} + \frac{2}{Re}\left[\!\!\left[\frac{\partial \hat{v}}{\partial y}\right]\!\!\right]_m + 2\left[\!\!\left[\frac{\partial^2 V}{\partial y^2}\right]\!\!\right]_m \hat{f} = \frac{1}{We}\frac{\partial^2 \hat{f}}{\partial z^2}. \tag{3.21}$$

Under the assumptions of homogeneity of span-wise directions and time-harmonic behaviour, the perturbation field $\hat{\mathbf{q}}_j$ can be written as $\hat{\mathbf{q}}_j = \mathbf{q}_j(x,y)e^{-i\omega t + ik_z z}$. Its spatial evolution satisfies the following relation:

$$\mathcal{L}_j \mathbf{q}_j = \frac{\partial}{\partial x}\left(\mathbf{A}_j \mathbf{q}_j\right) - \left(\mathbf{B_0}_j + \mathbf{B_1}_j \frac{\partial}{\partial y} + \mathbf{B_2}_j \frac{\partial^2}{\partial y^2}\right)\mathbf{q}_j = 0 \tag{3.22}$$

where

$$\mathbf{A}_j = \begin{bmatrix} 1 & 0 & 0 & 0 \\ U_j & 0 & 0 & c \\ V_j & U_j & 0 & 0 \\ 0 & 0 & U_j & 0 \end{bmatrix}$$

$$\mathbf{B_0}_j = \begin{bmatrix} 0 & 0 & -i\beta & 0 \\ i\omega - \frac{m}{r}\frac{\beta^2}{Re} & -\frac{\partial U_j}{\partial y} & 0 & 0 \\ 0 & i\omega - \frac{m}{r}\frac{\beta^2}{Re} - 2\frac{\partial V_j}{\partial y} & -i\beta V_j & 0 \\ 0 & 0 & i\omega - \frac{m}{r}\frac{\beta^2}{Re} - \frac{\partial V_j}{\partial y} & -i\beta \end{bmatrix}$$

$$\mathbf{B_1}_j = \begin{bmatrix} 0 & -1 & 0 & 0 \\ -V_j & 0 & 0 & 0 \\ 0 & -2V_j & 0 & -\frac{1}{r} \\ 0 & 0 & -V_j & 0 \end{bmatrix} \quad \mathbf{B_2}_j = \begin{bmatrix} 0 & 0 & 0 & 0 \\ -\frac{m}{r}\frac{1}{Re} & 0 & 0 & 0 \\ 0 & -\frac{m}{r}\frac{1}{Re} & 0 & 0 \\ 0 & 0 & -\frac{m}{r}\frac{1}{Re} & 0 \end{bmatrix}. \tag{3.23}$$

The contribution of the streamwise gradient of pressure is represented by c. To avoid ill-posedness, $c = 0$ (Ashpis & Reshotko, 1990).

The infinitesimal interface displacement $\hat{f}$ can be written as $\hat{f} = f(x)\delta_\Gamma(y-d)e^{-i\omega t+ik_z z}$, thus following the kinematic condition:

$$\left(\mathcal{I}_j f + \mathcal{C}\mathbf{q}_j\right)\delta_\Gamma(y-d) = 0 \tag{3.24}$$

where

$$\mathcal{I}_j f = \frac{\partial}{\partial x}\left(U_j f\right) - \left(i\omega - \frac{\partial V_j}{\partial y}\right) f; \qquad \mathcal{C}_j\mathbf{q} = -v_j. \tag{3.25}$$

Let $\phi = [\mathbf{q}_j, f]^\mathsf{T}$. The spatial evolution of an infinitesimal disturbance ϕ_0 in a non-parallel two-fluid boundary layer system is the solution of:

$$\mathcal{S}\phi = \begin{bmatrix} \mathcal{L}_j & 0 \\ \mathcal{C} & \mathcal{I} \end{bmatrix}\begin{bmatrix} \mathbf{q}_j \\ f \end{bmatrix} = 0\ , \qquad \forall\phi \in \mathcal{H}(\Omega) \tag{3.26}$$

with boundary conditions:

$$\begin{aligned} &u_B = v_B = w_B = 0\ , \qquad y = 0 \\ &u_T,\ w_T,\ p_T \to +\infty\ , \qquad y \to +\infty \end{aligned} \tag{3.27}$$

and matching conditions at $y = d$, $\forall x \in \Omega_x$:

$$[\![u]\!] + \left[\!\!\left[\frac{\partial U}{\partial y}\right]\!\!\right] f = 0 \tag{3.28}$$

$$[\![v]\!] + \left[\!\!\left[\frac{\partial V}{\partial y}\right]\!\!\right] f = 0 \tag{3.29}$$

$$[\![w]\!] = 0 \tag{3.30}$$

$$\left[\!\!\left[\frac{\partial u}{\partial y} + \frac{\partial v}{\partial x}\right]\!\!\right]_m + \left[\!\!\left[\frac{\partial^2 U}{\partial y^2}\right]\!\!\right]_m f = 0 \tag{3.31}$$

$$\left[\!\!\left[\frac{\partial w}{\partial y} + i\beta v\right]\!\!\right]_m + i\beta\left[\!\!\left[\frac{\partial V}{\partial y}\right]\!\!\right]_m f = 0 \tag{3.32}$$

$$[\![-p]\!]_{\frac{1}{r}} + \frac{2}{Re}\left[\!\!\left[\frac{\partial v}{\partial y}\right]\!\!\right]_m + 2\left[\!\!\left[\frac{\partial^2 V}{\partial y^2}\right]\!\!\right]_m f = \frac{\beta^2}{We} f \tag{3.33}$$

and initial condition

$$\phi(x_0, y) = \phi_0 \ \in \mathcal{H}(\Omega_y). \tag{3.34}$$

The interface curvature κ has been approximated to $\kappa \approx \Delta^* f \approx \beta^2 f$, in agreement with the boundary layer approximation already made.

Equations (3.26)-(3.34) constitute the initial boundary value problem for a downstream-propagating disturbance, ϕ_0.

3.4 Optimal disturbances

Modal stability analysis has focused on the unstable asymptotic behaviour of the disturbance ϕ_0 and linked its exponential growth to turbulence. On the contrary, the asymptotic stability of ϕ_0 does not imply that the underlying flow is stable. In fact, as stated earlier, transient growth of fluctuation energy could trigger non-linear effects sustaining turbulence and represent a mechanism for bypass transition (Andersson *et al.*, 1999).
In analogy to what has been done in §2.5, the perturbation ϕ_0 is defined as *optimal* if it maximises a chosen functional norm.
The main purpose of this section is to introduce a *measure* for a general disturbance and to give details of the optimal amplification problem.

Consider the Hilbert space $\mathcal{H}(\Omega)$, any $\mathbf{a}, \mathbf{b} \in \mathcal{H}(\Omega)$ of the form $\mathbf{a} = [\mathbf{q}_j, f]^\mathsf{T} = [\mathbf{u}_j, p_j, f]^\mathsf{T}$ and the following internal products and norm:

$$(\mathbf{a}, \mathbf{b}) = \sum_{j=T,B} \int_{\Omega_y^j} \mathbf{a}^H \mathbf{b} \, dy \quad , \qquad \forall \mathbf{a}, \mathbf{b} \in \mathcal{H}(\Omega) \tag{3.35}$$

$$\langle \mathbf{a}, \mathbf{b} \rangle = \int_{\Omega_x} \sum_{j=T,B} \int_{\Omega_y^j} \mathbf{a}^H \mathbf{Q} \ \mathbf{b} \, dy \, dx = \int_{\Omega_x} (\mathbf{a}, \mathbf{Q}\mathbf{b}) \, dx \quad , \qquad \forall \mathbf{a}, \mathbf{b} \in \mathcal{H}(\Omega) \tag{3.36}$$

$$\|\mathbf{a}\|_\varepsilon^2 = (\mathbf{a}, \mathbf{E}\mathbf{a}) \tag{3.37}$$

where the superscript $\cdot^H$ denotes the standard Hermitian operator, $\mathbf{E}$ being the mechanical energy matrix in the primitive variable formulation and $\mathbf{Q}$ the internal product

matrix defined as the following:

$$\mathbf{E} = \begin{bmatrix} \mathbf{K}_j & 0 \\ 0 & \frac{1}{We} \end{bmatrix}, \qquad \mathbf{K}_j = \begin{bmatrix} r\mathbf{I}^{3x3} & 0 \\ 0 & 0 \end{bmatrix}, \tag{3.38}$$

$$\mathbf{Q} = \begin{bmatrix} \mathbf{K}_j^p & 0 \\ 0 & 0 \end{bmatrix}, \qquad \mathbf{K}_j^p = \begin{bmatrix} \mathbf{I}^{3x3} & 0 \\ 0 & 1 \end{bmatrix}. \tag{3.39}$$

The aim is to find the initial condition $\phi_0 \in \Omega$ that maximises the functional

$$\mathbf{J}(\phi; \phi_0; x) = \frac{\|\phi_x\|_\varepsilon^2}{\|\phi_0\|_\varepsilon^2} \tag{3.40}$$

at a given location $x \in \Omega_x$. This is equivalent to finding the initial condition that will amplify the most at location x.

The growth factor $G(x)$ is defined as the maximum value of the functional $\mathbf{J}(\phi; \phi_0; x)$ at location x for any possible non-trivial initial condition, ϕ_0, satisfying the Cauchy problem in (3.26)-(3.34).

The initial-boundary-value problem defined by equations (3.26)-(3.34) is linear, therefore $\exists \mathcal{A}\ linear:\ \phi_x = \mathcal{A}_x \phi_0$. The amplification factor, $G(x)$, has the following expression:

$$\begin{aligned} G(x) &= \max_{\phi_0 \neq 0} \mathbf{J}(\phi; \phi_0; x) \qquad (3.41) \\ &= \max_{\phi_0 \neq 0} \frac{\|\phi(x)\|_\varepsilon^2}{\|\phi(x_0)\|_\varepsilon^2} = \max_{\phi_0 \neq 0} \frac{\|\mathcal{A}_x \phi_0\|_\varepsilon^2}{\|\phi_0\|_\varepsilon^2} = \max_{\phi_0 \neq 0} \frac{(\mathcal{A}_x \phi_0, \mathbf{E}\mathcal{A}_x \phi_0)}{(\phi_0, \mathbf{E}\phi_0)} \\ &= \max_{\phi_0 \neq 0} \frac{\left(\mathcal{A}^\dagger{}_x \mathbf{E}\mathcal{A}_x \phi_0, \phi_0\right)}{(\mathbf{E}\phi_0, \phi_0)} = \max_{\phi_0 \neq 0} \frac{\left(\mathcal{A}^\dagger{}_x \mathbf{E}\mathcal{A}_x \mathbf{F}^{-1}\mathbf{F}\phi_0, \mathbf{F}^{-1}\mathbf{F}\phi_0\right)}{(\mathbf{E}\mathbf{F}^{-1}\mathbf{F}\phi_0, \mathbf{F}^{-1}\mathbf{F}\phi_0)} \\ &= \max_{\phi_0 \neq 0} \frac{\left(\mathbf{F}^{-\mathsf{H}}\mathcal{A}^\dagger{}_x \mathbf{E}\mathcal{A}_x \mathbf{F}^{-1}\mathbf{F}\phi_0, \mathbf{F}\phi_0\right)}{(\mathbf{F}^{-\mathsf{H}}\mathbf{E}\mathbf{F}^{-1}\mathbf{F}\phi_0, \mathbf{F}\phi_0)} = \max_j \{\Lambda_j \left(\mathbf{F}^{-\mathsf{H}}\mathcal{A}^\dagger{}_x \mathbf{E}\mathcal{A}_x \mathbf{F}^{-1}\right)\}\ . \end{aligned}$$

where $\mathbf{E} = \mathbf{F}^{\mathsf{H}}\mathbf{F}$ and $\mathcal{A}^\dagger$ is the adjoint operator of $\mathcal{A}$, satisfying the internal product

$$\left\langle \mathbf{a}, \mathcal{A}\mathbf{b} \right\rangle = \left\langle \mathcal{A}^\dagger \mathbf{a}, \mathbf{b} \right\rangle, \quad \forall \mathbf{a}, \mathbf{b} \in \mathcal{H}(\Omega). \tag{3.42}$$

The derivation of the adjoint operator $\mathcal{A}^\dagger$ and adjoint boundary conditions are given in Appendix A. Note that, although bounded to the appendix, the derivation of the two-fluid spatial adjoint equations is a fundamental achievement of this work. It represents a

new and powerful tool for optimization and control in two-fluid non-parallel flows. The original derivation is based on very general assumptions, so that it can be adapted to various framework; the boundary layer approximation on the adjoint equations is presented as a particular case.

Amplification as largest singular value

According to (3.41), $G(x) = \max_j\{\Lambda_j\left(\mathbf{F}^{-\mathsf{H}}{\mathcal{A}^\dagger}_x\mathbf{E}\mathcal{A}_x\mathbf{F}^{-1}\right)\}$, i.e. the maximum amplification at location x is given by the leading (maximum) eigenvalue of the system $\mathcal{L}_\mathbf{F} = \mathbf{F}^{-\mathsf{H}}{\mathcal{A}^\dagger}_x\mathbf{E}\mathcal{A}_x\mathbf{F}^{-1}$. Recall that, given an operator $\mathbf{A}$ satisfying equation 3.42, than the following relations hold:

$$\text{if } \mathcal{A}\mathbf{a} = \lambda\mathbf{a}, \text{ then } \mathcal{A}^\dagger\mathbf{a} = \lambda^\mathsf{H}\mathbf{a}\ , \text{therefore } \mathcal{A}^\dagger\mathcal{A}\mathbf{a} = \lambda^\mathsf{H}\lambda\mathbf{a}\ \ \forall\mathbf{a}. \tag{3.43}$$

Therefore $\left\|\mathcal{A}^\dagger\mathcal{A}\right\| = \theta_1$, that is the largest singular value, as defined in the previous chapter, §2.5. Thus the computation of the norm is reduced to the determination of the leading eigenvalue of the operator $\mathcal{L}_\mathbf{F}$. Explicitly constructing the operators $\mathcal{A}$ and $\mathcal{A}^\dagger$ is usually expensive and not possible in this case, due to the missing streamwise pressure gradient term. Therefore we do not attempt to compute the entire spectrum of the system $\mathbf{F}^{-\mathsf{H}}{\mathcal{A}^\dagger}_x\mathbf{E}\mathcal{A}_x\mathbf{F}^{-1}$. Note that the matrices $\mathbf{F}$ and $\mathbf{F^{-1}}$ only provide a link between the energy norm and the 2−norm of the linear operator $\mathcal{A}_x$, without modifying its eigenvalues. As discussed in the previous chapter, the norm of the operator $\mathcal{L}_\mathbf{F}$ is represented by its principal singular value, that is:

$$|\mathcal{L}_\mathbf{F}| = \max_J \Lambda_j \tag{3.44}$$

where Λ_j is an element of Λ, which satisfies $\Lambda\mathbf{a} = \mathcal{L}_\mathbf{F}\mathbf{a}\ , \quad \forall\mathbf{a} \in \mathcal{H}(\Omega)$.
The leading eigenvalue providing maximum amplification at location x and the relative initial condition ϕ_0 are directly computed via the Von Misen (power iteration) method:

$$\lambda_x\phi_0^{n+1}(x) = \frac{\mathcal{L}_\mathbf{F}\phi_0^n(x)}{\|\mathcal{L}_\mathbf{F}\phi_0^n(x)\|}\ , \tag{3.45}$$

that is:

$$\lambda_x \phi_0^{n+1}(x) = \frac{\mathbf{F}^{-\mathsf{H}} \mathcal{A}^{\dagger}{}_x \mathbf{E} \mathcal{A}_x \mathbf{F}^{-1} \phi_0^n(x)}{\| \mathbf{F}^{-\mathsf{H}} \mathcal{A}^{\dagger}{}_x \mathbf{E} \mathcal{A}_x \mathbf{F}^{-1} \phi_0^n(x) \|} \ . \tag{3.46}$$

At every iteration n the vector $\phi_0^n(x)$ is multiplied by the matrix $\mathbf{F}^{-\mathsf{H}} \mathcal{A}^{\dagger}{}_x \mathbf{E} \mathcal{A}_x \mathbf{F}^{-1}$ and normalised. Assuming that:

i) $\mathcal{L}_{\mathbf{F}}$ has an eigenvalue λ_x^{max} that is stricly greater then the other eigenvalues in magnitude;

ii) the initial vector $\phi_0^0(x)$ has non-zero projection in the direction of the eigenvector associated with λ_x^{max} leading eigenvalue, that is: $\phi_0^0(x) \cdot \mathbf{a}_x{}^{max} \neq 0$, where $\lambda_x^{max} \mathbf{a}_x^{max} = \mathcal{L}_{\mathbf{F}} \mathbf{a}_x^{max}$, $\forall \mathbf{a}_x^{max} \in \mathcal{H}(\Omega)$;

iii) it exists a subsequence of vectors $(\phi_0^n(x))$ convergent to the leading eigenvector, that is $\exists\, \epsilon \in \mathbb{R}^+$ such that $\left\| \phi_0^{n+1}(x) - \phi_0^n(x) \right\| < \epsilon$;

then $\phi_0^{n+1}(x)$ converges to the leading eigenvector $\mathbf{a}_x^{max}$ and λ_x converges to the leading eigenvalue λ_x^{max} of Λ:

$$|\lambda_x - \lambda_x^{max}| < \epsilon \ . \tag{3.47}$$

Under the assumption in (3.47), $G(x)$ at location x is constructed by solving (3.26)-(3.34) with a feasible initial condition $\hat{\phi}_0$ and (A.39)-(A.54) with final condition $\phi_x^{\dagger} = \mathcal{F}^{-1} \phi_x$ until the convergence condition $\left\| \phi_0^{n+1} - \phi_0^n \right\| < \epsilon$ is met at the $(n+1)^{th}-$iteration. The operator $\mathcal{F}$ and its inverse follow from the rescaling conditions (A.37)-(A.38) and is given by:

$$\mathcal{F} = \begin{bmatrix} \mathbf{A}_j & 0 \\ 0 & 1 \end{bmatrix} \qquad \mathcal{F}^{-1} = \begin{bmatrix} \mathbf{A}_j^{\dagger} & 0 \\ 0 & 1 \end{bmatrix} . \tag{3.48}$$

A sketch of the algorithm is given in figure 3.4. Additional details on the optimization procedure are given later on in this chapter, where the numerical implementation is discussed.

In order to start the adjoint looping procedure, a feasible initial guess $\hat{\phi}_0$ satisfying

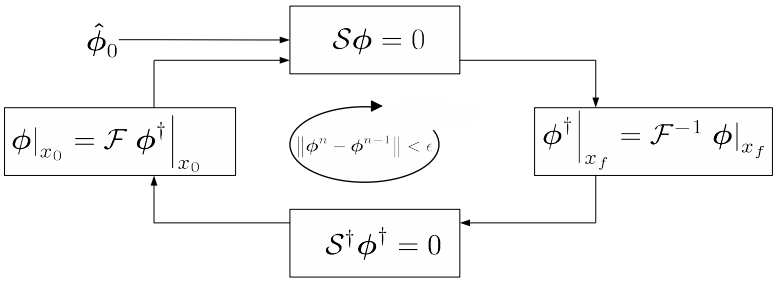


Figure 3.4: Optimal disturbance algorithm flowchart

(3.26)-(3.34) is required. At x_0, a locally-parallel assumption is taken, such that the problem $\mathcal{S}(x_0, y)\phi = 0$ can be converted in into the eigenvalue problem:

$$i\alpha_{x_0}\tilde{\mathcal{S}}(y)\tilde{\phi} = 0 \tag{3.49}$$

Let $\tilde{\phi}_n$, $n = 1, 2, \cdots, K$, be the K least-stable eigenfunctions of (3.49). The initial condition needed to initialise the power iteration in (3.46) can be created as the following:

$$\hat{\phi}_0 = \sum_{j=1}^{K} w_j \tilde{\phi}_j \tag{3.50}$$

with

$$w_j = \mathcal{U}(0,1)\ , \qquad \mathcal{U}(0,1) \text{ uniform random variable in } [0,1].$$

Thus $\hat{\phi}_0$ is given by a random superposition of eigenfunctions of (3.49). Note that, by construction, $\hat{\phi}_0$ satisfies the Cauchy problem defined by (3.26)-(3.34) and has non-zero scalar product with the leading eigenvector $\mathbf{a}_x^{max}$.
The next sections deal with technical challenges of solving equations $\mathcal{S}\phi = 0$ and $\mathcal{S}^\dagger\phi^\dagger = 0$ on a two-fluid non-parallel base flow, such as spreading mean interface location and resolution at the interface.

3.4.1 Numerical Method

When dealing with non-parallel flow, one of the main considerations is to keep constant wall-normal grid resolution inside the boundary layer. In the case of a two-fluid spreading boundary layer, as the boundary layer grows, the mean location of the interface moves. For a well-resolved simulation, a high resolution is needed at the interface. However, this poses the problem of refining the mesh at every x location or having a constant refined

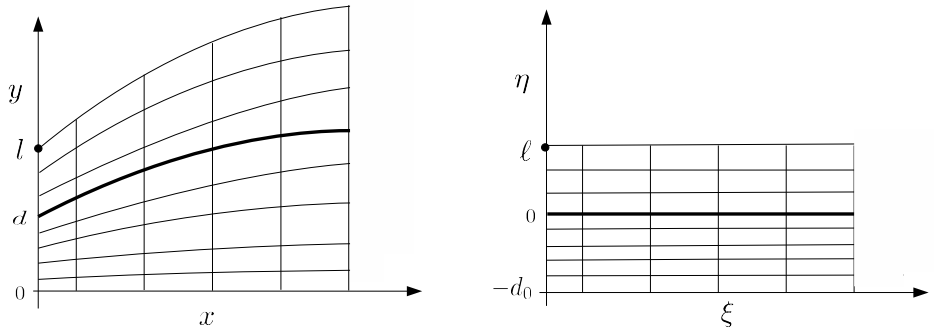


Figure 3.5: Sketch of computational grid in physical (figure 3.5a) and mapped (figure 3.5b) space.

mesh that covers the mean interface location displacement. Moreover, interfacial matching conditions are valid and must be imposed at the spreading interface location, which makes it impossible to build an evolution operator in physical coordinates. To overcome these limitations and to avoid computational expense, a mapping function that depends on the mean interface location is applied, such that the spreading mean interface location in physical space is mapped to a flat mean interface location in computational space. The mapping process allows for high resolution at the interface location throughout the x domain, without suffering of lack of resolution due to the spreading of the base flow. The mapping also provides a fixed grid point in the normal direction where the interfacial boundary conditions are imposed.
The next paragraph gives detailed information on the discretization approach and numerical solution.

Coordinates transformation

The semi-infinite physical domain Ω_y is approximated with $\Omega_y^l = \{[0, d] \cup [d, l)\}$, l being a large number and $l > 25\delta_0$. This assures that the top wall does not affect the correct representation of the physical process near the boundary layer. Let $\mathcal{T}(x, y) \in \mathcal{C}^2(\mathbb{R}^2)$ be a mapping function such that $(x, y) \in \mathbb{R}^2 \rightarrow (\xi, \eta) \in \mathbb{R}^2$:

$$\mathcal{T} : \begin{cases} \xi = x \\ \eta = d_0 \frac{y-d}{d} \end{cases} \tag{3.51}$$

The computational domain in (ξ,η) coordinates is $\Omega_{\mathcal{T}} = \Omega_{\mathcal{T}}^{\xi} \times \Omega_{\mathcal{T}}^{\eta} = [\xi_0, \xi_f] \times \{[-d_0, 0] \cup [0, \ell]\}$. The top wall location is denoted by $\ell = \min_x \eta = d_0 \left(\frac{l}{d_f} - 1\right)$, where $d_0 = d(x_0)$, $d_f = d(x_f)$; the mean interface location in mapped coordinates satisfies the equation $\eta \equiv 0 \; \forall \, \xi \in \Omega_{\mathcal{T}}^{\xi}$. The bottom wall $y = 0$ is an invariant for the transformation $\mathcal{T}$.

Metrics

A sketch of the effect of the non-linear mapping $\mathcal{T}$ on the computational grid in physical space is depicted in figure 3.5, where $\eta = 0$ represents the spreading interface in (ξ,η) coordinates. The Jacobian of the transformation is

$$\mathbf{J}_{\mathcal{T}} = \begin{bmatrix} \frac{\partial \xi}{\partial x} & \frac{\partial \xi}{\partial y} \\ \frac{\partial \eta}{\partial x} & \frac{\partial \eta}{\partial y} \end{bmatrix} = \begin{bmatrix} 1 & 0 \\ -\frac{d_0 y d'}{d^2} & \frac{d_0}{d} \end{bmatrix} = \begin{bmatrix} 1 & 0 \\ g_x & g_y \end{bmatrix},$$
$$\det \mathbf{J}_{\mathcal{T}} \neq 0 \; \forall x, y \in \Omega \tag{3.52}$$

Differential operators in (ξ,η) coordinates have the following expression:

$$\frac{\partial}{\partial x} = \left(\frac{\partial}{\partial \xi}\right)\left(\frac{\partial \xi}{\partial x}\right) + \left(\frac{\partial}{\partial \eta}\right)\left(\frac{\partial \eta}{\partial x}\right) = \frac{\partial}{\partial \xi} + g_x \frac{\partial}{\partial \eta} \tag{3.53}$$

$$\frac{\partial}{\partial y} = \left(\frac{\partial}{\partial \xi}\right)\left(\frac{\partial \xi}{\partial y}\right) + \left(\frac{\partial}{\partial \eta}\right)\left(\frac{\partial \eta}{\partial y}\right) = g_y \frac{\partial}{\partial \eta} \tag{3.54}$$

$$\frac{\partial^2}{\partial y^2} = \left(\frac{\partial}{\partial \xi}\right)\left(\frac{\partial^2 \xi}{\partial y^2}\right) + \left(\frac{\partial}{\partial \eta}\right)\left(\frac{\partial^2 \eta}{\partial y^2}\right) + \left(\frac{\partial^2}{\partial \xi^2}\right)\left(\frac{\partial \xi}{\partial y}\right)^2 + \frac{\partial^2}{\partial \eta^2}\left(\frac{\partial \eta}{\partial y}\right)^2 + \frac{\partial^2}{\partial \eta}\xi \left(\frac{\partial \eta}{\partial y}\right)\left(\frac{\partial \xi}{\partial y}\right) = g_y^2 \frac{\partial^2}{\partial \eta^2} \tag{3.55}$$

and are used to transform forward and adjoint equations from physical to computation space.

Forward evolution equations

The operators governing the forward evolution in the new coordinate system are:

$$\tilde{\mathcal{S}}\phi = \begin{bmatrix} \tilde{\mathcal{L}}_j & 0 \\ \tilde{\mathcal{C}} & \tilde{\mathcal{I}} \end{bmatrix} \begin{bmatrix} \mathbf{q}_j \\ f \end{bmatrix} \quad \forall\, \mathbf{q}_j, f \in \mathcal{H}(\Omega_{\mathcal{T}}) \tag{3.56}$$

with (3.57)

$$\tilde{\mathcal{L}}_j \mathbf{q}_j = \frac{\partial}{\partial \xi}\left(\tilde{\mathbf{A}}_j \mathbf{q}_j\right) - \tilde{\mathbf{B_0}}_j \mathbf{q}_j - \tilde{\mathbf{B_1}}_j \frac{\partial}{\partial \eta}\mathbf{q}_j - \tilde{\mathbf{B_2}}_j \frac{\partial^2}{\partial \eta^2}\mathbf{q}_j$$

$$\tilde{\mathbf{A}}_j = \mathbf{A}_j$$

$$\tilde{\mathbf{B_0}}_j = \mathbf{B_0} - g_x \frac{\partial}{\partial \eta}\mathbf{A}_j$$

$$\tilde{\mathbf{B_1}}_j = g_y \mathbf{B_1} - g_x \mathbf{A}_j$$

$$\tilde{\mathbf{B_2}}_j = g_y^2 \mathbf{B_2}_j$$

$$\tilde{\mathcal{C}} = \mathcal{C}$$

$$\tilde{\mathcal{I}} f = \frac{\partial}{\partial \xi}(Uf) - \left(i\omega - g_x \frac{\partial U}{\partial \eta} - g_y \frac{\partial V}{\partial \eta}\right) f \tag{3.58}$$

and boundary conditions

$$u_B(-d_0) = 0 \tag{3.59}$$

$$v_B(-d_0) = 0 \tag{3.60}$$

$$w_B(-d_0) = 0 \tag{3.61}$$

$$u_T(\ell) = 0 \tag{3.62}$$

$$w_T(\ell) = 0 \tag{3.63}$$

$$p_T(\ell) = 0 \tag{3.64}$$

$$[\![u]\!] + \left[\!\!\left[g_y \frac{\partial U}{\partial \eta} \right]\!\!\right] f = 0 \tag{3.65}$$

$$[\![v]\!] + \left[\!\!\left[g_y \frac{\partial V}{\partial \eta} \right]\!\!\right] f = 0 \tag{3.66}$$

$$[\![w]\!] = 0 \tag{3.67}$$

$$\left[\!\left[\frac{\partial v}{\partial \xi}\right]\!\right]_m + \left[\!\left[g_y\frac{\partial u}{\partial \eta} + g_x\frac{\partial v}{\partial \eta}\right]\!\right]_m + \left[\!\left[g_y^2\frac{\partial^2 U}{\partial \eta^2}\right]\!\right]_m f = 0 \tag{3.68}$$

$$\left[\!\left[g_y\frac{\partial w}{\partial \eta} + i\beta v\right]\!\right]_m + i\beta\left[\!\left[g_y\frac{\partial V}{\partial \eta}\right]\!\right]_m f = 0 \tag{3.69}$$

$$[\![-p]\!]_{\frac{1}{r}} + \frac{2}{Re}\left[\!\left[g_y\frac{\partial v}{\partial \eta}\right]\!\right]_m + 2\left[\!\left[g_y^2\frac{\partial^2 V}{\partial \eta^2}\right]\!\right]_m f = \frac{\beta^2}{We} f\,. \tag{3.70}$$

Adjoint evolution equations

The operators governing the adjoint evolution in the new coordinate system are:

$$\tilde{\mathcal{S}}^\dagger \phi_j^\dagger = \begin{bmatrix} \tilde{\mathcal{L}}^\dagger & 0 \\ \tilde{\mathcal{C}}^\dagger & \tilde{\mathcal{I}}^\dagger \end{bmatrix} \begin{bmatrix} \mathbf{q}^\dagger \\ f^\dagger \end{bmatrix} = 0 \tag{3.71}$$

with

$$\tilde{\mathcal{L}}^\dagger \mathbf{q}^\dagger = \left[-\tilde{\mathbf{A}}_j^H \frac{\partial}{\partial \xi} - \tilde{\mathbf{B}_0}_j^H + \tilde{\mathbf{B}_1}_j^H \frac{\partial}{\partial \eta} - \tilde{\mathbf{B}_2}_j \frac{\partial^2}{\partial \eta^2}\right] \mathbf{q}^\dagger \tag{3.72}$$

$$\begin{aligned} \tilde{\mathbf{A}}_j &= \mathbf{A}_j \\ \tilde{\mathbf{B}_0}_j &= \mathbf{B_0}_j - g_y \frac{\partial \mathbf{B_1}_j}{\partial \eta} \\ \tilde{\mathbf{B}_1}_j &= g_x \mathbf{A}_j - g_y \mathbf{B_1}_j \\ \tilde{\mathbf{B}_2}_j &= g_y^2 \mathbf{B_2}_j \end{aligned} \tag{3.73}$$

$$\begin{aligned} \tilde{\mathcal{C}}^\dagger \mathbf{q}^\dagger = &-\tfrac{1}{Re}\left[\!\left[g_y^2\frac{\partial^2 U}{\partial \eta^2}\right]\!\right]_m u^\dagger + \tfrac{m}{Re}\left[\!\left[g_y\frac{\partial^2 U}{\partial \eta}\right]\!\right] g_y \frac{\partial^2 u_B^\dagger}{\partial \eta} - \left(\tfrac{2}{Re}\left[\!\left[g_y^2\frac{\partial^2 V}{\partial \eta^2}\right]\!\right]_m - \tfrac{\beta^2}{We}\right) v^\dagger + \\ &\tfrac{m}{Re}\left[\!\left[g_y\frac{\partial U}{\partial \eta}\right]\!\right] g_x \frac{\partial v_B^\dagger}{\partial \eta} + \tfrac{2m}{Re}\left[\!\left[g_y\frac{\partial V}{\partial \eta}\right]\!\right] g_y \frac{\partial v_B^\dagger}{\partial \eta} + \\ &\tfrac{1}{Re}\left[\!\left[g_y\frac{\partial U}{\partial \eta}\right]\!\right] \frac{\partial v_B^\dagger}{\partial \xi} - \tfrac{i\beta}{Re}\left[\!\left[g_y\frac{\partial V}{\partial \eta}\right]\!\right]_m w^\dagger + r\left[\!\left[g_y\frac{\partial V}{\partial \eta}\right]\!\right] p_B^\dagger \end{aligned} \tag{3.74}$$

$$\tilde{\mathcal{I}}^\dagger f^\dagger = \left(i\omega + U\frac{\partial}{\partial \xi}\right) f^\dagger \tag{3.75}$$

and boundary conditions:

$$u_B^\dagger(-d_0) = 0 \tag{3.76}$$

$$v_B^\dagger(-d_0) = 0 \tag{3.77}$$

$$w_B^\dagger(-d_0) = 0 \tag{3.78}$$

$$p_T^\dagger(\ell) + 2V v_T^\dagger(\ell) + \tfrac{1}{Re} g_y \frac{\partial v^\dagger}{\partial \eta}(\ell) = 0 \tag{3.79}$$

$$u_T^\dagger(\ell) = 0 \tag{3.80}$$

$$w_T^\dagger(\ell) = 0 \tag{3.81}$$

$$[\![u^\dagger]\!] = 0 \tag{3.82}$$

$$[\![v^\dagger]\!] = 0 \tag{3.83}$$

$$[\![w^\dagger]\!] = 0 \tag{3.84}$$

$$\left[\!\!\left[\frac{\partial v^\dagger}{\partial \xi}\right]\!\!\right]_m + \left[\!\!\left[g_y \frac{\partial u^\dagger}{\partial \eta} + g_x \frac{\partial v^\dagger}{\partial \eta}\right]\!\!\right]_m = 0 \tag{3.85}$$

$$\left[\!\!\left[g_y \frac{\partial w^\dagger}{\partial \eta} + i\beta v^\dagger\right]\!\!\right]_m = 0 \tag{3.86}$$

$$\left[\!\left[p^\dagger\right]\!\right]_r + \tfrac{2}{Re}\left[\!\!\left[g_y \frac{\partial v^\dagger}{\partial \eta}\right]\!\!\right]_m = f^\dagger \tag{3.87}$$

Discretization

As in the case of parallel flow, the discretization of the evolution equations and boundary conditions uses Chebyshev spectral method. A sufficient resolution near the wall and an accurate representation of the discontinuities of mean and perturbation variables at the interface are ensured by discretising top and bottom domains with different grids, on which separate mapped Chebyshev expansions provide a complete representation of the disturbance in $\Omega_{\mathcal{T}}^\eta = \Omega_{\mathcal{T}}^{\eta\,B} \cup \Omega_{\mathcal{T}}^{\eta\,T} = [-d_0, 0] \cup [0, \ell]$. The domain $\Omega_{\mathcal{T}}^\eta$ is discretised according to the Gauss-Lobatto quadrature, on which two sets of mapped Chebyshev polynomials $\tilde{T}(\eta)^j$, $j = T, B$, are considered.

For sake of clarity, details of the spectral discretization used are reported again. Let $\tilde{T}_n(\zeta)$, $n = 1, \ldots, N$ be N Chebyshev polynomials in the interval $I = [-1, 1]$ and $\eta = \vartheta(\zeta)$ a mapping function between I and $\Omega_{\mathcal{T}}^\eta$, $\zeta \in I$, $\eta \in \Omega_{\mathcal{T}}^\eta$. Define $T_i(\eta) := \tilde{T}_i\left(\vartheta^{-1}(\eta)\right)$ as the mapped Chebyshev polynomial onto the domain $\Omega_{\mathcal{T}}^\eta$. Two sets of Chebyshev polynomial have been used to represent independently bottom and top fluid. In particular, $T_i^T =$

$\tilde{T}_i\left(\vartheta^{-1}(\eta)\right),\ \eta \in {\Omega_{\mathcal{T}}^{\eta}}^T$ and $T_i^B = \tilde{T}_i\left(\phi^{-1}(\eta)\right),\ \eta \in {\Omega_{\mathcal{T}}^{\eta}}^B$; as in the case of locally-parallel analysis, details of the mappinging function ϑ are given in Appendix C. The grid $\zeta_{j,k}$ is generated in the Chebyshev interval I using the N_j Gauss-Lobatto points $\zeta_{j,k} = \cos\left(\frac{\pi k}{N_j - 1}\right)$ and mapped to physical space, such that $\{\eta\} = \{\eta_T\} \cup \{\eta_B\} \in \Omega_{\mathcal{T}}^{\eta}$. The number of Chebyshev polynomials used in the top domain ${\Omega_{\mathcal{T}}^{\eta}}^T$ is of order $150 - 200$ and the bottom fluid counterpart ${\Omega_{\mathcal{T}}^{\eta}}^B$ is chosen according to the relation $\frac{\ell}{N_T} \approx \frac{10 d_0}{N_B} \approx 0.1$. In analogy with the parallel case, highly-stretched grids near the interface were found to introduce inaccurate representation of the oscillatory behaviour of the continuous modes in the free stream. Grids with clustering factors comparable to linear mapping are able to provide good resolution near the interface and in the free stream. In fact, free-stream resolution is key to a correct representation of the continuous spectrum, which is responsible for the amplification of energy.

Disturbance functions are then expanded in series of mapped Chebyshev polynomials:

$$\mathbf{q}_j(\xi, \eta) = \sum_{n=0}^{N_j} c_{q_j}^n(\xi) T_n^j(\eta) = \mathbf{T_0}_j \mathbf{c}_j(\xi) \tag{3.88}$$

where the weights $\mathbf{c}_j(\xi)$ fully characterise the streamwise evolution of the initial condition $\phi_0 = \mathbf{T_0 c}(0)$.

Resolution

To solve the iterative method presented in equation (3.46), forward and adjoint equations must be intergrated in the Ω_x domain.

In computational space, the domain $\Omega_{\mathcal{T}}^{\xi}$ is discretised with a set of points $\{\xi_0,\ \xi_1,\ \cdots, \xi_{n_x-1}, \xi_{n_x}\}$ such that $\Omega_{\mathcal{T}}^{\xi} = \sum_{i=0}^{n_x-1} \Delta\xi_i$, where $\Delta\xi_i = \xi_{i+1} - \xi_i$. The forward equation (3.56) along with interfacial boundary conditions (3.65)-(3.70) are approximated in the streamwise direction with a fully implicit Euler scheme, extending the single-fluid approach of Andersson *et al.* (1999). Equation (3.56) can be written as:

$$\frac{\partial}{\partial \xi}(\mathbf{M}\phi) = \mathbf{L}\phi \tag{3.89}$$

where

$$\mathbf{M} = \begin{bmatrix} \tilde{\mathbf{A}}_j & 0 \\ 0 & g_x U \end{bmatrix}, \qquad \mathbf{L} = \begin{bmatrix} \tilde{\mathbf{B_0}}_j + \tilde{\mathbf{B_1}}_j \frac{\partial}{\partial \eta} + \tilde{\mathbf{B_2}}_j \frac{\partial^2}{\partial \eta^2} & 0 \\ 0 & i\omega - g_y \frac{\partial V}{\partial \eta} \end{bmatrix}.$$

The schemes used for the calculations are:

$$1^{st} \text{ order:} \quad (\mathbf{M}\phi)^{i+1} - (\mathbf{M}\phi)^{i} = \Delta\xi_i \, (\mathbf{L}\phi)^{i+1} \tag{3.90}$$

$$2^{nd} \text{ order:} \quad \tfrac{3}{2} (\mathbf{M}\phi)^{i+1} - 2 (\mathbf{M}\phi)^{i} + \tfrac{1}{2} (\mathbf{M}\phi)^{i-1} = \Delta\xi_i \, (\mathbf{L}\phi)^{i+1} \tag{3.91}$$

$$3^{rd} \text{ order:} \quad \tfrac{11}{6} (\mathbf{M}\phi)^{i+1} - 3 (\mathbf{M}\phi)^{i} + \tfrac{3}{2} (\mathbf{M}\phi)^{i-1} - \tfrac{1}{3} (\mathbf{M}\phi)^{i-2} = \Delta\xi_i \, (\mathbf{L}\phi)^{i+1}. \tag{3.92}$$

It was found that the order of integration does not sensibly affect the computation of G, as the lack of streamwise ellipticity in (3.89) allows for arbitrary small $\Delta\xi_i$.
At each streamwise position ξ_i, a one-dimensional boundary-value problem in the wall-normal direction is solved with the aid of mapped Chebyshev polynomials $\tilde{T}_i$. The chosen streamwise discretization scheme is imposed at the Chebyshev mapped collocation points η along with interfacial and wall boundary conditions, leading to the determination of the Chebyshev spectral coefficients in (3.88) by Gauss elimination of the resulting dense linear system of dimensions $4\,(N_T + N_B) + 1$. The adjoint problem stated in (3.71) may be written as an evolution problem:

$$-\mathbf{M}^{\dagger} \frac{\partial \phi^{\dagger}}{\partial \xi} = \mathbf{L}^{\dagger} \phi^{\dagger} \tag{3.93}$$

where

$$\mathbf{M}^{\dagger} = \begin{bmatrix} \tilde{\mathbf{A}}_j^{H} & 0 \\ 0 & U \end{bmatrix}, \qquad \mathbf{L}^{\dagger} = \begin{bmatrix} \tilde{\mathbf{B_0}}_j - \tilde{\mathbf{B_1}}_j^{H} \frac{\partial}{\partial \eta} + \tilde{\mathbf{B_2}}_j^{H} \frac{\partial^2}{\partial \eta^2} & 0 \\ \tilde{\mathcal{C}}^{\dagger} & i\omega \end{bmatrix}.$$

and discretized as the forward equations. This leads to the determination of the *discretized adjoint*. A different approach to the discretization of problem (3.41) is to discretise the base equation (3.89) and to introduce a discretised measure equivalent to (3.37). From the choice of discretization of the forward problem and the definition of the discrete disturbance measure, the *discrete adjoint* problem is well defined, without the need to introduce any independent discretization of the adjoint equations (Andersson

et al., 1999). It is well known that this last approach is the most consistent when solving problem (3.41), where computing adjoint equations becomes a matter of transposing the matrices associated with the discretization (Berggren, 1995; Berggren *et al.*, 1996). However, care has to be taken, as this may lead to inconsistency between the transposed stencil of a differential operator and the stencil of its adjoint operator; also, the discretization of the adjoint derived by transposition of the forward problem would not contemplate the presence of additional source terms. When spectral methods are used, the derivation of the discrete adjoint is less natural and less straightforward. Consistency of the discretized adjoint formulation with the discretization of the forward problem was checked under parallel-base-flow assumption computing the eigenvalue sets of (3.89) and (3.93), which resulted to be one complex-conjugate of the other within 10^{-12} accuracy. Additional details on the validation procedures and results are contained in Appendix B.

It is fundamental to remark that the optimization problem (3.41) is particularly well-conditioned and very few iterations of the algorithm described in (3.46) are needed for convergence. Thus the approximation introduced by the discretization is unlikely to be of any importance. The robustness of problem (3.41) is due to the fact that the largest eigenvalue of the operator $\mathcal{L}_{\mathbf{F}}$ is well separated from the rest of the spectrum (Andersson *et al.*, 1999; S. C. Reddy & Henningson, 1993; Schmid, 2007; Trefethen *et al.*, 1993).

The optimization algorithm

This section describes the steps involved in the power iteration, introduced in (3.46), to compute the largest eigenvalue of $\mathcal{L}_{\mathbf{F}}$.

At every target location $\xi \in \Omega_{\xi}^{\mathcal{T}}$, iterate steps 1-4

1. Solve forward initial-boundary value problem in (3.89), using the wall and interfacial boundary conditions stated in (3.59)-(3.70). At the first iteration, the initial condition ϕ_0 is chosen using (3.50); at later iterations, it is obtained from step 4.

2. Project forward-solution ϕ at location ξ onto adjoint space and determine initial adjoint condition $\phi_0^{\dagger} = \mathcal{F}^{-1}\phi(\xi)$ solving (3.48).

3. Solve backward final-boundary value problem in (3.93), using the wall and interfacial boundary conditions stated in (3.76)-(3.87).

4. Project adjoint solution $\phi^\dagger$ at location ξ_0 onto forward space and determine new initial condition $\phi_0 = \mathcal{F}\phi^\dagger(\xi_0)$ solving (3.48). Scale if needed.

until $\left\|\phi_0^{n+1} - \phi_0^n\right\| < \epsilon$ at the $(n+1)^{th}-$iteration. The optimal initial condition that maximises (3.40) is ϕ_0.

The number of iterations needed for convergence to be reached varies with location and Reynolds number, but it is usually of order $5 - 15$. Similar convergence rates were found by Andersson *et al.* (1999) and Luchini (2000).

So far, a robust formulation to study the effects of stratification on spatially developing disturbances in non-parallel flows was built. A very important step was the introduction of the domain transformation discussed in (3.51), which leads to a computational domain with constant resolution at the interface and that allows for an easy implementation of interfacial boundary conditions on spreading flows.
The next sections are dedicated to the analysis of the effects of the spreading of the base flow on stratification and to the characterisation of the evolution of optimal disturbances over a non-parallel base flow.

3.4.2 Non-parallel effects

The non-parallel evolution of the mean flow has a substantial impact on the transient growth mechanism, lowering the effect of the lift-up mechanism and diminishing the coupling with the interfacial mode (equation 3.28 and figure 3.7). In this section, a mean flow with optimal viscosity ratio $m^o = 0.55$ is analysed within the framework of linearized boundary layer equations, with no assumptions on mean flow parallelism. As the mean flow spreads, the mean interface location grows accordingly. However, the mean flow spreading rate ($\delta \approx x^{\frac{1}{2}}$) is faster than the interface spreading rate ($d \approx x^{\frac{1}{4}}$), resulting in a reduction of the film thickness with respect to local δ-coordinates. In fact, in the limit of $x \to +\infty$, $d/\delta \to 0$, recovering the single-fluid limit behaviour.

Figure 3.6a shows the streamwise evolution of U. As the flow spreads, more shear is absorbed by the lower-viscous film (figure 3.6b). The mean interface location d spreads at

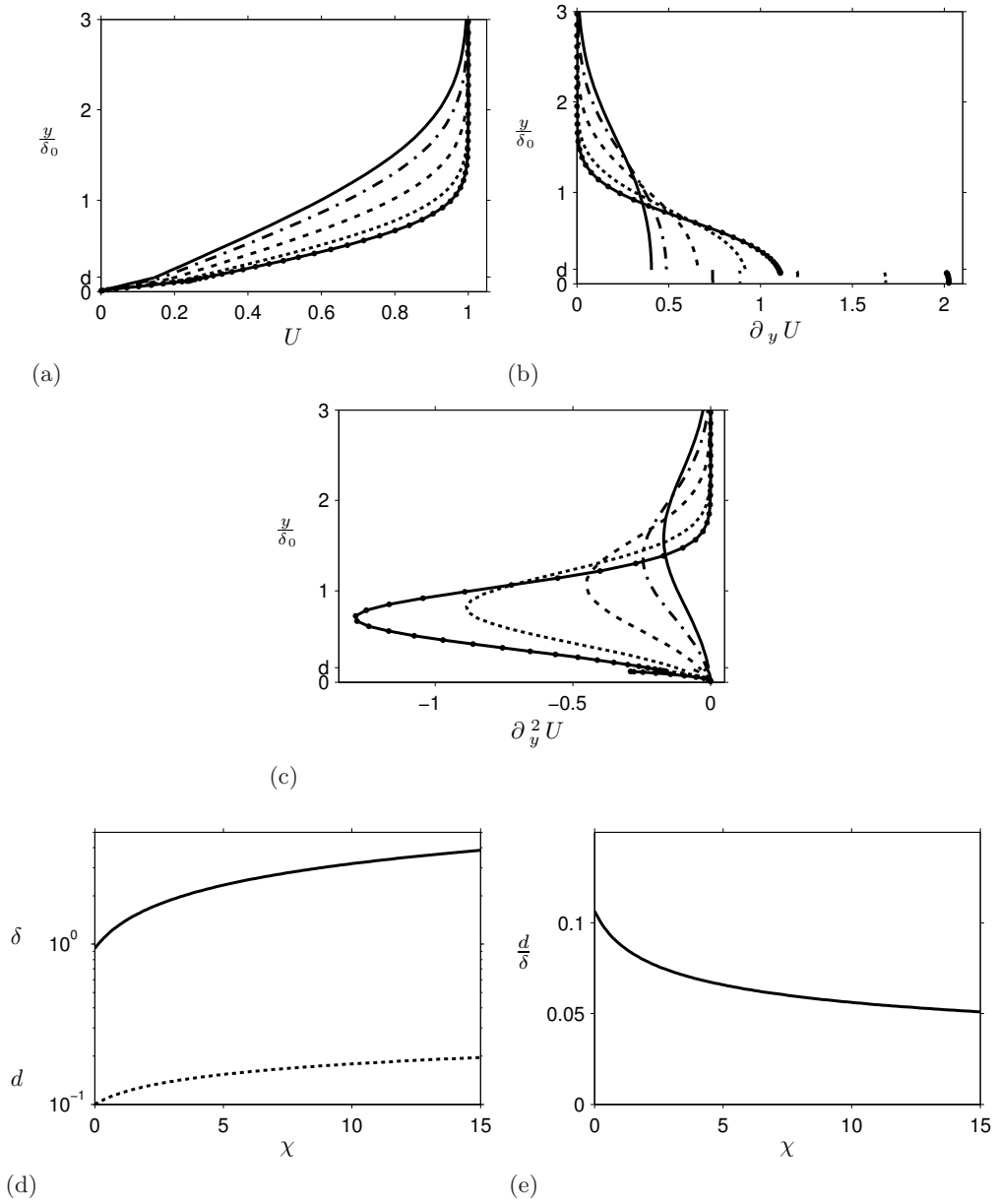


Figure 3.6: Spatial evolution of mean streamwise velocity U, (3.6a), $\partial_y U$, (3.6b), $\partial_y^2 U$, (3.6c), respectively at locations: -•-$\chi = 1$, $\cdots\chi = 2$, - - -$\chi = 5$, - ·-$\chi = 10$, ——$\chi = 15$, $d_0 = 0.10$, $m = 0.55$. (3.6d): Boundary layer thickness δ and mean interface location d versus streamwise location χ. (3.6e): ratio $\frac{d}{\delta}$ versus streamwise location χ.

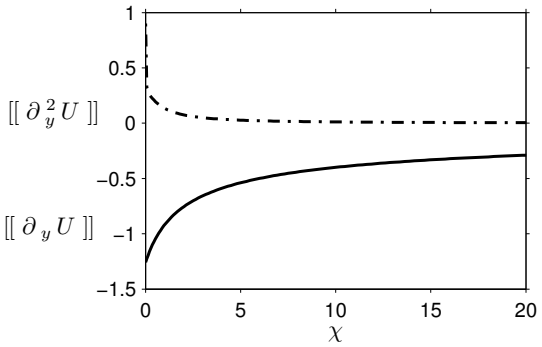


Figure 3.7: $[\![\partial_y U]\!]$, $[\![\partial_y^2 U]\!]$ at the interface versus streamwise location χ; $d_0 = 0.1$, $m = 0.55$

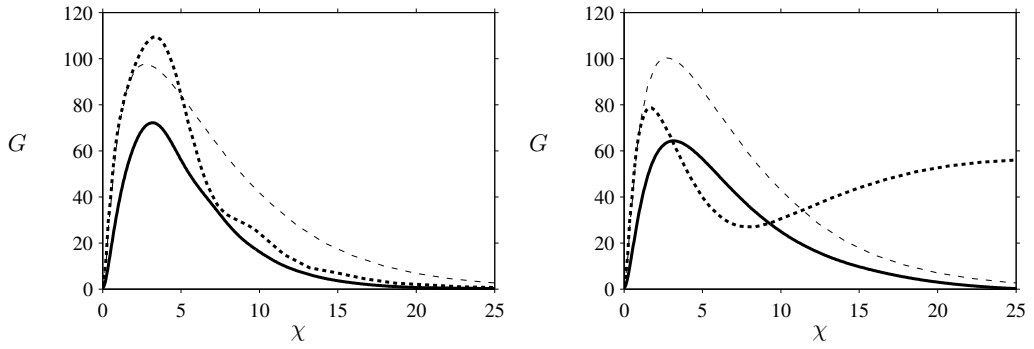
a lower rate then δ, as shown in figure 3.6d, thus the influence of the lower viscosity film on the mean flow profile decreases with streamwise distance. As the flow develops downstream, the two-fluid boundary layer converges to a single-fluid boundary layer and the mechanism of energy production through interfacial deformation becomes unimportant. Moreover, the jump at the interface of mean shear, $\partial_y U$, which fosters the production of energy through interface corrugation, weakens very quickly. The streamwise evolution of $\left[\!\left[\frac{\partial U}{\partial y}\right]\!\right]$, $\left[\!\left[\frac{\partial^2 U}{\partial y^2}\right]\!\right]$ is given in figure 3.7. For $m = 0.55$, $\left[\!\left[\frac{\partial U}{\partial y}\right]\!\right]$ becomes half of its parallel-limit value at about $\chi \approx 2$ and a third at $\chi \approx 10$.

The parallel-flow assumption has shown the presence of a new mechanism of energy production that is predominant for low viscosity ratio m and effective on long distances ($\chi > 10$). Here figures 3.6, 3.7 suggest that, when the mean flow spreads:

i) the production of energy through interface deformation might not be relevant and/or present at all;

ii) the benefit of a lower-viscosity film near the wall might not persit over a meaningful streamwise distance due to the different spreading rate of mean interface location d and the boundary layer thickness δ.

Under parallel flow assumptions, the above considerations are trivial, as the mean flow is constantly identical in the streamwise direction. Relaxing the assumption of parallelism introduces instead additional degrees of complexity, which are going to be addressed in this and the following chapter.



(a) optimal set p^o (b) sub-optimal set p^{so}

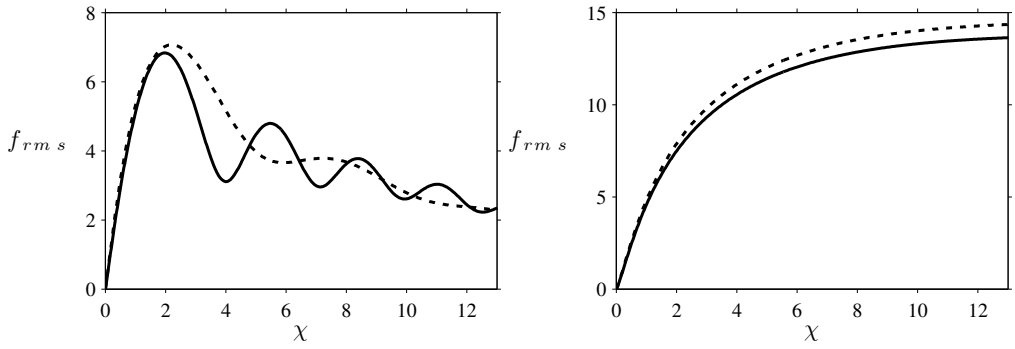
Figure 3.8: Comparison between two-fluid parallel and spreading optimal growth, $k_z = 1.5$, $d_0 = 0.1$, $m = 0.55$, (3.8b) $\omega^{so} = 0.0010$, (3.8a) $\omega^o = 0.0125$. $k_z = 1.5$, $m = 0.55$, $d_0 = 0.1$, $Re = 800$. —— non-parallel, - - - parallel mean flow , $\cdots$ $m = 1$, non-parallel mean flow.

3.4.3 Optimal profiles

In the previous chapter, under the parallel flow assumption, a global parametric optimization on film thickness, viscosity ratio, spanwise wavenumber and temporal frequency was performed, leading to the determination of the optimal set of parameters $p^o : \{m^o = 0.55, d_0^o = 0.1, \omega^o = 0.0125, {k_z}^o = 1.5\}$ resulting in optimal amplification reduction. Importance was given also to the suboptimal set $p^{so} : \{m^o = 0.55, d_0^o = 0.1, \omega^{so} = 0.001, {k_z}^o = 1.5\}$, that highlights the interfacial energy mechanism. In this chapter, optimal growth results under spreading base flow for the parameter sets p^o and p^{so} are computed and presented.

Optimal growth curves for parallel and non-parallel case are compared in figure 3.8 for the parameter sets p^o (figure 3.8a) and p^{so} (figure 3.8b). The spreading of the mean flow weakens the mean shear and its variation through the interface; as a result, the viscous peak is reduced and the effect of the interface distortion is very limited. Consider the parameter set p^{so}; in the parallel case, for $\chi > 6$, an interface disturbance starts to grow (figure 3.8b) and a very strong and energetic perturbation develops and remains throughout the domain, due to the neutrally-stable interfacial mode. In the spreading case, as the mean velocity gradients at the interface quickly decrease (figure 3.7), the coupling with the interface sharply decays, resulting in a much weaker interfacial perturbation. Thus the spreading of the mean flow dampens the neutral interface mode.

In the non-parallel case, only the lift-up mechanism can convert normal velocity



(a) optimal set p^o (b) sub-optimal set p^{so}

Figure 3.9: Comparison of interface perturbation under parallel (– – –) and non-parallel (——) mean flow (a): $\omega^o = 0.0125$, (b) $\omega^{so} = 0.0010$.

disturbances into streamwise velocity perturbations and the multiple peaks due to the interface corrugation effect are not visible. In the parallel case, the energy growth of the neutral interface mode over long distances ($\chi > 10$) is a major limitation to transient growth reduction; in the non-parallel case, the mean flow spreading acts in competition to the interfacial mechanism, reducing its effect on energy growth.

The relaxation of mean flow parallelism has an effect on the dynamics of the interface. Figure 3.9 depicts the effect of the spreading of the mean flow on the interfacial perturbation f. Consider the interfacial dynamics for parallel flow (eq. 2.19); its streamwise solution is coupled to the normal velocity v and modulated by $e^{\frac{-i\omega}{U}(x-x_0)}$. The interfacial dynamics in non-parallel flows (eq. 3.24) is instead modulated (first-order approximation) by $e^{\left.\frac{-i\omega+\frac{\partial V(x)}{\partial y}}{U(x)}\right|_{x_0}^{x}(x-x_0)+o(|x-x_o|^2)}$; therefore, the streamwise frequency of f shifts from $\sim \frac{-i\omega}{U}$ to $\sim \left.\frac{-i\omega+\frac{\partial V(x)}{\partial y}}{U(x)}\right|_{x_o}^{x}$, which explains the streamwise wavelength change in figure 3.9a. For lower values of omega (figure 3.9b), this effect is marginal and would disappear in the case of steady disturbances.

Profiles of the optimal disturbances for the non-parallel and parallel cases are given in figures 3.10 and 3.11 for p^o, p^{so} parameter sets.

At the optimal disturbance frequency $\omega^o = 0.0125$, $|v|$ and $|w|$ have comparable magnitude (figure 3.10a) both in parallel and non-parallel case; the response $|u|$ (figure 3.10b) highlights that the jump of mean quantities forces a much stronger response in the parallel case rather than in the spreading flow.

The optimal inlet profiles of $|v|$ and $|w|$ (figure 3.11a) and their maximum streamwise

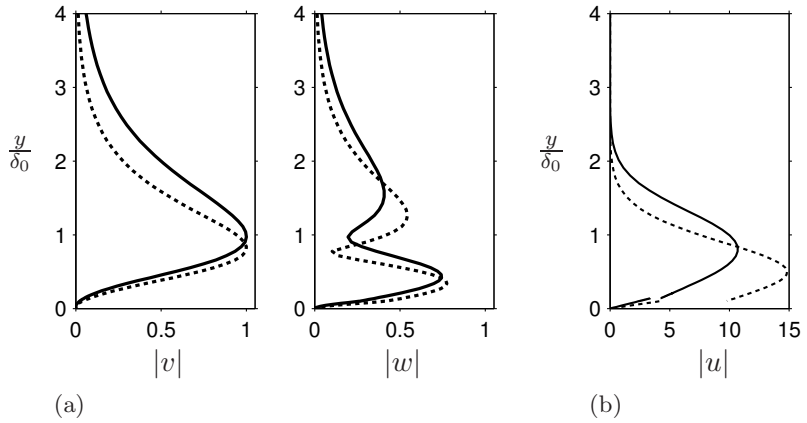


Figure 3.10: (3.10a) Optimal initial condition and (3.10b) maximum response, $\omega^o = 0.0125$, $k_z = 1.5$, $m = 0.55$, $d_0 = 0.1$, $Re = 800$. —— non-parallel, - - - parallel mean flow.

response $|u|$ (figure 3.11b) show the difference between non-parallel and parallel optimal disturbances in the case of $\omega^{so} = 0.0010$. Although the optimal inlet condition is a counter-rotating vortex in both cases, the optimal condition arising from non-parallel optimization sits higher in the boundary layer and exhibits a weaker w component; these differences are due to the introduction of the normal component of the base flow V, which modifies the coupling term and the continuity relation. The response is weaker in the spreading case due to the reduction in mean shear.

As figure 3.7 shows, the streamwise velocity response in the non-parallel case is not forced to compensate for the large jump in gradients at the interface characteristic of the parallel flow assumption; therefore, a weaker response is registered along with a weaker interfacial jump in $|u|$.

A vector plot of suboptimal and optimal inlet disturbance are reported in figures 3.12a and 3.12b along with contour levels of the respective streamwise response u, at the maximum amplification location. The edge of the boundary layer is marked. The lift-up mechanism still plays a fundamental role in the generation of streamwise velocity perturbations, since the spanwise location of maximum u response is aligned with the maximum downward v component.

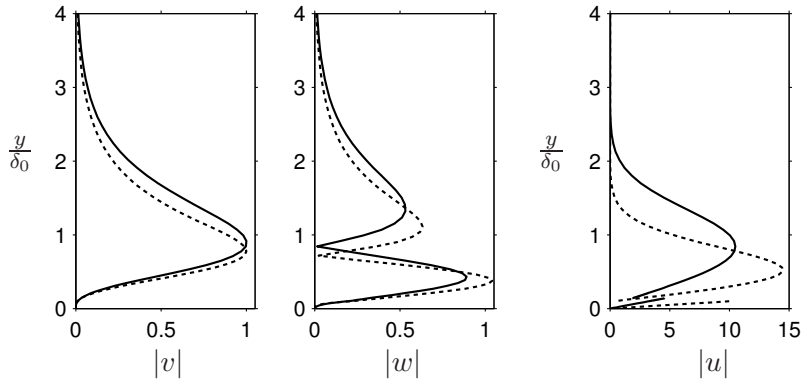


Figure 3.11: (3.11a) Optimal initial condition and (3.11b) maximum response, $\omega^{so} = 0.0010$, $k_z = 1.5$, $m = 0.55$, $d_0 = 0.1$, $Re = 800$. —— non-parallel, - - - parallel mean flow.

3.4.4 Evolution

The linear evolution of optimal disturbances under non-parallel and parallel mean flow is presented in figures 3.13, 3.14 for p^o and p^{so} parameter sets, respectively.

Streamwise contours of $|u|$ response are depicted in figures 3.13a-3.13c (p^o) and 3.14a-3.14c (p^{so}) for non-parallel and parallel setup; contours of interface perturbation are shown in figures 3.13b-3.13d (p^o) and 3.14b-3.14d (p^{so}) for non-parallel and parallel setup.

In the case quasi-steady disturbances ($\omega < 0.001$), in the parallel setup, a strong interface displacement develops and persists throughout the domain (figure 3.14d), forcing a strong u perturbation (figure 3.14c); in the non-parallel setup, although the interface displacement is virtually unaffected by the spreading of the mean flow (figure 3.14b), its coupling with the streamwise velocity perturbation is systematically reduced by the weakening of the jump of mean gradients with streamwise distance(figure 3.14a). For $\chi > 9$, the effect of the interface displacement weakens significantly, preventing any substantial energy growth via the interface coupling mechanism.

When the frequency increases ($\omega^o = 0.0125$), the interface disturbance exhibits a peak at location comparable to the viscous peak (figure 3.9a), suggesting that a positive feedback mechanism could be present and responsible for an enhanced transient growth. Although the streamwise frequency of the interface disturbance changes from parallel (figure 3.13d) to non-parallel (figure 3.13b) setup, parallel (figure 3.13c) and non-parallel (figure 3.13a)

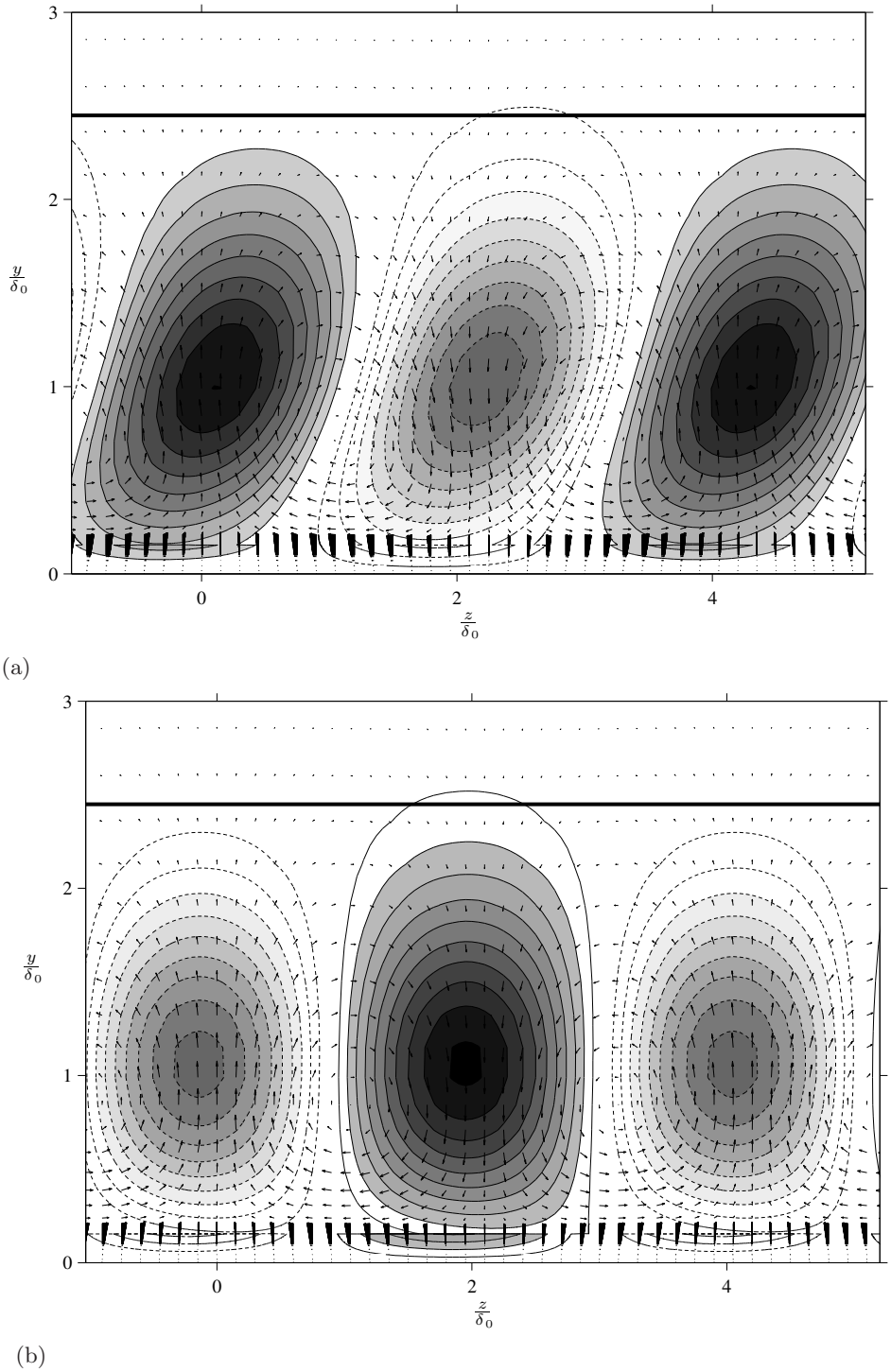


Figure 3.12: Optimal perturbation and response, (a): $\omega = 0.001$, (b) $\omega = 0.0125$. The vector plot shows the initial optimal disturbace field $(0, v, w)$. The contour plot shows the contours of streamwise velocity u at location of maximum amplification; the edge of the boundary layer is marked by a thick solid line; solid and dashed lines denote positive and negative velocity fluctuations respectively. Contour levels range from -10 to 10 with spacing of 1

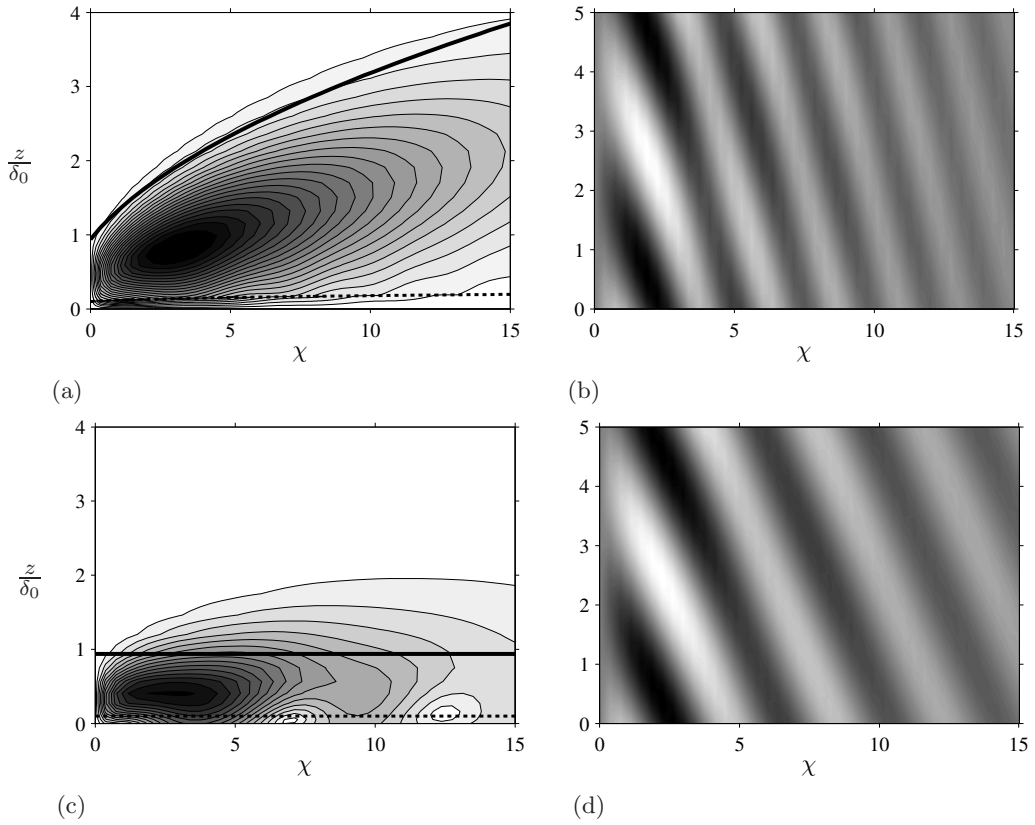


Figure 3.13: Contours of $|u|$ showing the streamwise evolution of the optimal initial perturbation depicted in figure (3.10a) for p^o configuration for non-parallel (3.13a) and parallel (3.13c) flow. Contours range from 0 to 10 with 0.5 step. —— marks the location of δ, - - - the mean interface location. $Re = 800$, $m = 0.55$, $d_0 = 0.1$. (3.13b), (3.13d) Contours of interfacial perturbation for non-parallel and parallel flow.

evolution of u velocity are governed by a similar mechanism.

Transient growth in parallel and non-parallel cases is mainly driven by the lift-up mechanism. Figures 3.15 and 3.16 show the comparison between parallel and non-parallel evolution for p^o and p^{so} parameter sets on the zy-plane at streamwise locations $\chi = \{1.5, 2.7, 5.0\}$. The vector plot represent the (v, w) perturbation field and contours depict u response. As the flow evolves downstream, the streamwise counter-rotating features of the optimal inlet disturbance induce a u streak, drawing faster fluid from the bulk of the flow and lifting slower fluid for the near-wall region.

Figure 3.17 presents a comparison between parallel and non-parallel streamwise evolution of u perturbation velocity and perturbed interface location, for optimal and sub-optimal parameter sets.

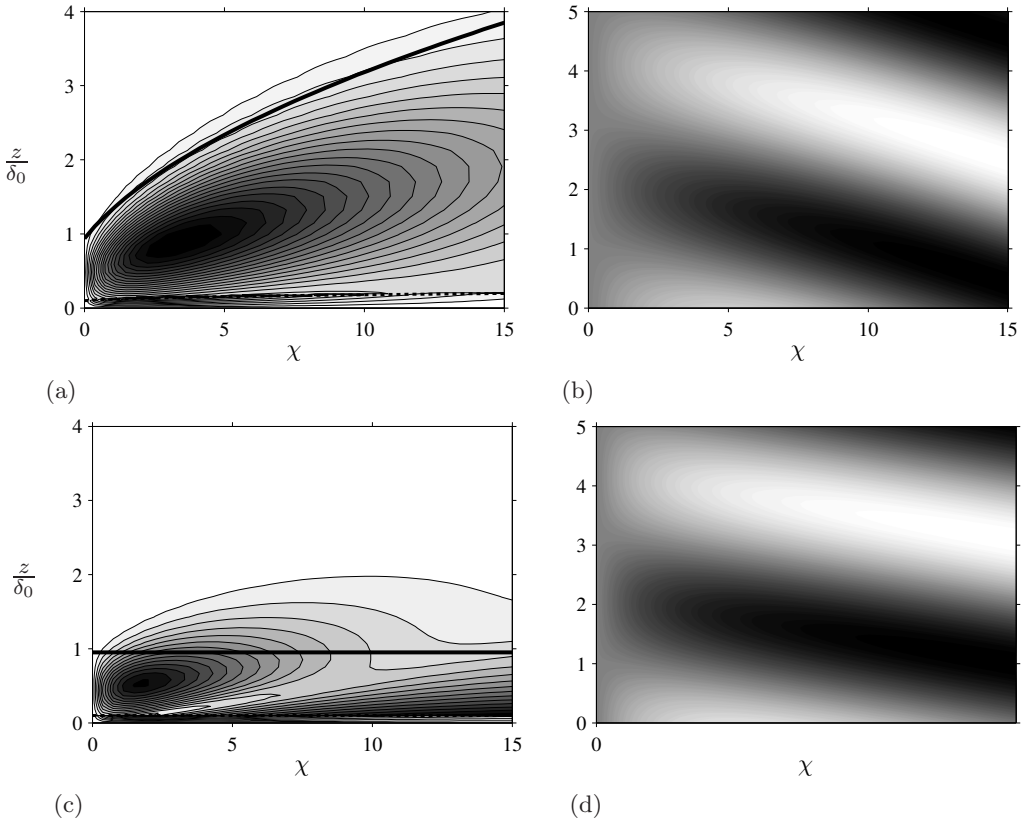


Figure 3.14: Contours of $|u|$ showing the streamwise evolution of the optimal initial perturbation depicted in figure (3.10a) for p^o configuration for non-parallel (3.14a) and parallel (3.14c) flow. Contours range from 0 to 10 with 0.5 step. —— marks the location of δ, - - - the mean interface location. $Re = 800$, $m = 0.55$, $d_0 = 0.1$. (3.14b), (3.14d) Contours of interfacial perturbation for non-parallel and parallel flow.

It is important to notice that, although the spreading of the mean flow does not change the structure of the optimal disturbance and response, the maximum energy amplification is overall weakened by the reduction of the quantity $[\![\frac{\partial U}{\partial y}]\!]$ in the streamwise direction. In fact, the response in the spreading case is only partially affected by the presence of an interface. The interfacial deformation mechanism, which creates substantial perturbation energy production under a parallel mean flow, loses its strength as the jump in mean streamwise velocity gradient $[\![\frac{\partial U}{\partial y}]\!]$ weakens in the streamwise direction (figure 3.7).

3.5 Conclusions

In this chapter, a new framework for the study of optimal disturbances and transient energy amplification in non-parallel two-fluid boundary layers was presented. The mean flow formulation for two-fluid boundary layers from Nelson *et al.* (1995) was summarised and the impact of stratification on mean variables quantified. Linear perturbation equations for the spatial evolution of an infinitesimal perturbation to the base flow were derived under the boundary layer approximation.

The optimization problem leading to the determination of optimal energy amplification and optimal perturbation was formulated and details of the numerical solution were presented. In particular, the maximum energy response at a given streamwise location was determined via the use of the adjoint system to the linear perturbation equations and computed via power iterations.

The details of the theoretical formulation of the adjoint derivation are reported in Appendix A; it is important to stress that it is a core concept to this thesis.

In order to adapt the spectral discretization based on Chebyshev polynomials to the two-fluid non-parallel problem, the physical coordinates were mapped to a computational space, where the interface is flat. This simplified the implementation of the interfacial boundary conditions and made the grid resolution near the interface independent of streamwise location, minimising the computational cost.

The optimal and sub-optimal parameter set p^o and p^{so}, found in the previous chapter to respectively yield to maximum energy amplification reduction and interfacial production of energy, were adopted to analyse optimal disturbances over a spreading base flow. This

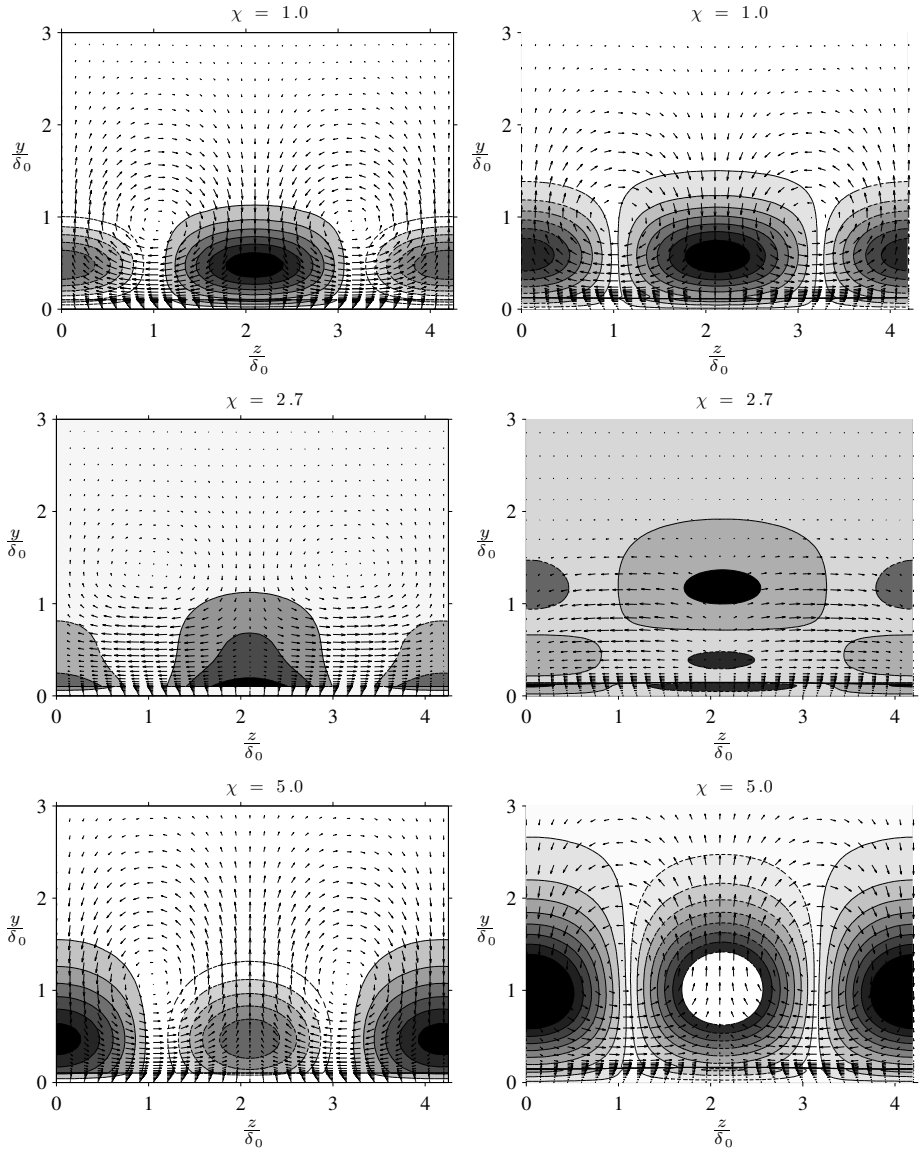


Figure 3.15: End view on zy-plane at location $\chi = \{1.5, 2.7, 5.0\}$, for $\omega^o = 0.0125$; arrows show the vector field (v, w). Contours of streamwise velocity u are also represented. PBl with parallel mean flow assumption on the left, spreading mean flow on the right.

showed that results from parallel analyses are partial and inaccurate, mainly when predicting the effect of the interfacial energy generation mechanism. In fact, the different spreading rates between mean flow and thin film lead to a reduced effect of the wall layer on the bulk of the fluid; the thin film is therefore able to absorb less mean shear as the base flow spreads. Moreover, jumps of mean quantities rapidly diminish as the flow develops downstream, reducing the effectiveness of the interfacial energy generation.

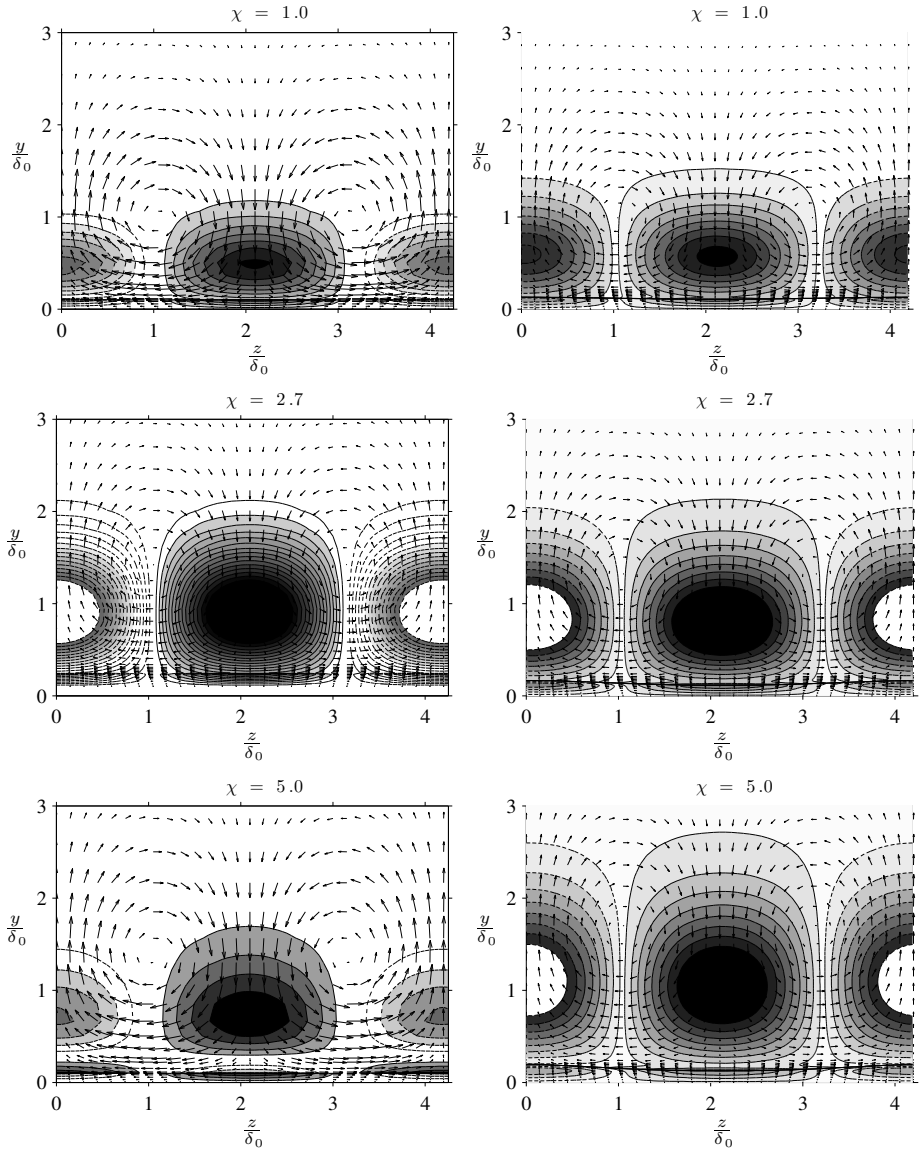


Figure 3.16: End view on zy-plane at location $\chi = \{1.5, 2.7, 5.0\}$, for $\omega^{so} = 0.0010$; arrows show the vector field (v, w). Contours of streamwise velocity u are also represented. PBl with parallel mean flow assumption on the left, spreading mean flow on the right.

The results presented indicate that an accurate description of the transient growth mechanism in two-fluid boundary layers requires the spreading of the mean flow to be taken into account.

So far, the linear evolution of non-parallel optimal disturbances was characterised and their relation to the parallel counterpart was presented. In the following chapter, the intent is to relax the assumption of linearity and focus on the non-linear evolution of spatially developing optimal disturbances. Thus, the next chapter deals with non-linear

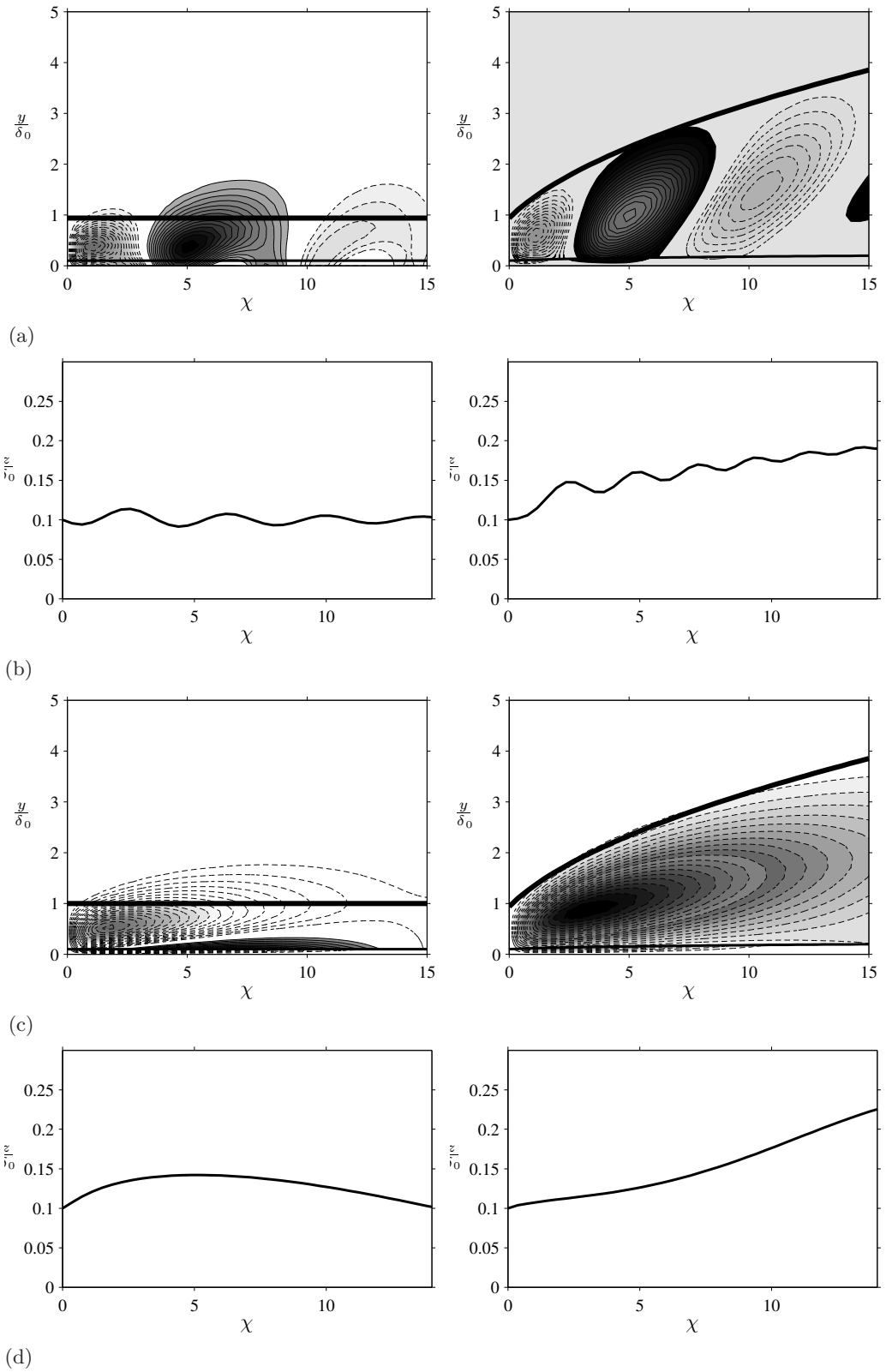


Figure 3.17: Parallel and non-parallel streamwise evolution of u and perturbed interface location.

effects on energy amplification.

Chapter 4

Non-linear evolution

4.1 Introduction

Disturbances that have penetrated the boundary layer can be subject to amplification. The early linear stages of the amplification mechanism were investigated in the previous chapters, under the assumption of infinitesimal disturbances. The linear approach followed so far relies on the underlying assumptions that even consistent energy amplification of disturbances would not trigger non-linear effects or cause interactions with the base flow. In this framework, energy amplification is independent from the initial disturbance's amplitude, allowing for potentially unbounded transient growth. In fact, Andersson *et al.* (2001) investigated the nonlinear evolution of optimal disturbances in single-fluid boundary layers and showed that the streamwise evolution of the perturbation's energy strongly depends on its initial level.

If the assumptions taken in the previous chapters on infinitesimal disturbances and interfacial deformation are discarded, the evolution of disturbances in two-fluid boundary layers is governed by NS equations, which can be solved via Direct Numerical Simulation (DNS).

The linear stability framework developed in the previous chapters represents the semi-analytical limit of DNS of disturbances with very low initial amplitude; as the perturbation's initial amplitude is increased, nonlinear terms are no longer neglegible and can play a fundamental role in the evolution process. Moreover, the interfacial deformation can reach finite amplitude and, eventually, force the interface to break. In particular, DNS can account for nonlinear evolution of a disturbance and its interaction with the mean flow, finite interface distortion and topology change.

Thus, this chapter reports on DNS of spatially-evolving optimal disturbance in two-fluid boundary layer.

The optimal perturbation corresponding to the parameter set $p^o : \{\omega^o = 0.0125;\ k_z^o = 1.5;\ m^o = 0.55;\ d^o = 0.1\}$ is prescribed as inlet condition for DNS; its evolution for different values of its initial amplitude is computed to investigate potential energy saturation due to nonlinearity. Similar approach is conducted on the suboptimal perturbation given by the set $p^{so} : \{\omega^{so} = 0.0010;\ k_z^o = 1.5;\ m^o = 0.55;\ d^o = 0.1\}$.

The aim of this chapter is:

i) to compare DNS and semianalytical results within the linear regime, in order to cross-validate both DNS and adjoint-looping optimization;

ii) to qualitatively show the impact of nonlinearity on the evolution of optimal disturbances.

This chapter is organised in 5 sections. The next section describes the importance of non-linearity in the amplification of disturbances and transition to turbulence process. In §4.3, the governing equations of DNS and the details of numerical method used to compute the non-linear evolution of spatially-evolving optimal initial condition are given. Importance is also given to the treatment of the interface. The main results on linear and non-linear evolution are presented and discussed in §4.4. The last section is a summary of the key results of this chapter.

Note that the DNS code for the simulations presented in this chapter was provided by Dr. T. A. Zaki and Dr. S. J. Yung, who were responsible for the code setup. The Author performed the simulations, validated and analysed the results, which add completeness to this work. The gratitude of the Author towards Dr. T. A. Zaki and Dr. S. J. Jung for their efforts could not be greater.

4.2 The importance of non-linearity

The idea that nonlinearity could play an important role in transition to turbulence can be traced back to the early work of Reynolds (1883), Bohr (1909), who focused their attention on the observation of fluid motion, and to that of Noether (1921) and Heisenberg (1951), who proposed analytical investigations on simple models. A consistent and rigorous nonlinear stability theory was laid later on by Landau (Landau, 1944; Landau

& Lifshitz, 1959), who linked the development of linear instability to the onset of turbulence.

As explained previously, the linear stability theory is concerned with the determination of the growth rates of the modal spectrum of the base flow. Below the critical Reynolds number, these modes are stable and might exhibit algebraic growth, though no energy transfer between modes takes place. It is now recognised that non-linear self-interaction of the dominant mode generates harmonics and distorts the mean flow, thus moderating the dominant mode's growth rate (Drazin & Rein, 1981). Linear theory does not take into account mean flow distortion and modal interaction, limiting the validity of the results presented so far to the early stage of the evolution of a disturbance only. Although the inclusion of mean flow spreading in the linear formulation represents a step forward in capturing the correct process of amplification, the influence of the perturbation on the mean flow is not included. However, after an early linear stage, perturbations can no longer be considered infinitesimal and their effects on the underlying base flow must be accounted for (Cheung & Zaki, 2010).

A successful approach that overcomes the limitation of linear theory without the computational complexity of direct solution of the Navier-Stokes equation is to solve the Nonlinear Parabolized stability Equations (NPSE), which can capture some of the nonlinear features arising after the linear stage (Herbert, 1997; Cheung, 2007). The PSE formulation assumes a modal decomposition, which makes this method unsuitable for tracking the evolution of optimal disturbances without decomposing them into eigenmodes. Tempelmann *et al.* (2010) proposed a modified linear PSE method for analysing non-modal growth in three-dimensional single-fluid boundary layers. At time of writing, the author is unaware of any two-phase NPSE method able to accurately model the streamwise evolution of optimal disturbances in two-phase boundary layers. Moreover, DNS can be used to investigate the full bypass process, which is far beyond PSE capabilities. Therefore, the choice of DNS as the main tool to address the effects of nonlinearity is evident.

4.3 Direct numerical simulation

Direct numerical simulations (DNS) account for non-linearity in two-fluid boundary layers, which was not captured in the previous linear analyses. Direct numerical simulations

of two-fluid boundary layers with small-amplitude inflow perturbations are carried out to complement and extend the results of linear theory.
The optimal disturbance from the spreading optimization for the parameter sets:

- optimal $p^o : \{\omega^o = 0.0125;\ k_z^o = 1.5;\ m^o = 0.55;\ d^o = 0.1\}$;

- suboptimal $p^{so} : \{\omega^{so} = 0.0010;\ k_z^o = 1.5;\ m^o = 0.55;\ d^o = 0.1\}$

are prescribed at the inflow of the computational domain and their spatial evolution is computed for different level of initial amplitude. Varying the level of initial amplitude of the inlet disturbance is equivalent to varying the weight of the nonlinear terms in the NS solution; the evolution of disturbances is therefore affected by their initial amplitude and the relative energy amplification can be dependent on nonlinearity.
This and the next section have the dual purpose of:

i) proving that, for low amplitude of the initial disturbance, when the nonlinear terms in NS equation can be neglected, the DNS evolution recovers the analytical behaviour predicted by linear stability;

ii) investigating potential amplification saturation due to nonliner effects.

A brief summary of governing equations and numerical methods used in the current DNS are given in this section, followed by the details on the DNS setup, interface treatment and an overview of the potential mean flow distortion due to nonlinearity.

4.3.1 Governing equations

The Navier-Stokes (NS) equations along with the continuity condition govern the evolution in time and space of an unsteady, incompressible two-fluid flow, $\mathcal{U}$, in the semi-infinite domain Ω. Although already presented in equations (2.2), (2.3), the NS equation are reported here for sake of completeness and emphasis is given to their full nonlinear numerical solution:

$$\partial_t \mathcal{U}_j + (\mathcal{U}_j \cdot \nabla)\,\mathcal{U}_j = -\frac{\nabla \mathcal{P}_j}{\rho_j} + \nu_j \Delta \mathcal{U}_j \tag{4.1}$$

$$\nabla \cdot \mathcal{U}_j = 0 \tag{4.2}$$

The pressure field is denoted by $\mathcal{P}$. The two fluid are separated by an interface, $\Gamma, \Gamma \in \partial\Omega$. Incompressibility condition imposes interfacial conditions on the velocity vector, $\mathcal{U}$, and the stress tensor, τ, to be satisfied on Γ:

$$[\![\mathcal{U} \cdot \hat{\mathbf{n}}]\!] = 0; \qquad [\![\mathcal{U} \cdot \hat{\mathbf{t}}]\!] = 0; \qquad [\![\tau \cdot \hat{\mathbf{n}}]\!] = [\![\mathcal{P}]\!]\hat{\mathbf{n}} - \sigma\kappa\hat{\mathbf{n}}; \qquad [\![\tau \cdot \hat{\mathbf{t}}]\!] = 0. \tag{4.3}$$

where $\hat{\mathbf{n}}$ and $\hat{\mathbf{t}}$ denote the unit normal and tangent vector to the interface, Γ, the curvature of which is denoted by κ.

A fractional step method is used to solve the time-dependent, incompressible Navier-Stokes equations. The computational algorithm is based on a staggered grid with a local volume flux formulation in curvilinear coordinates (Rosenfeld *et al.*, 1991). The 2^{nd}-order Adams-Bashforth scheme is implemented for the explicit time advancement of convective terms. A fully implicit Euler scheme is used for the treatment of the pressure terms; the Crank-Nicolson method is applied to the diffusion term. The combination of the schemes Adam-Bashforth and Crank-Nicolson for the discretization of the nonlinear convection/diffusion terms was successfully used by Kim & Moin (1991). The code is parallelised using Message Passing Interface (MPI).

4.3.2 Inflow condition and domain size

The inflow is composed of a two-fluid boundary layer profile and the optimal perturbation at the inlet Reynolds number, $Re = 800$, based on the inlet single-fluid boundary-layer thickness and free-stream velocity. According to the linear decomposition presented in equations (2.5), the velocity vector field $\mathcal{U}$ is composed by adding the optimal disturbance $\mathbf{u}$ to the mean flow, $\mathbf{U}$, so that $\mathcal{U} = \mathbf{U} + \epsilon\mathbf{u}$. The parameter ϵ is used to rescale the perturbation with respect to the mean flow, that is $\epsilon = \frac{|v|}{U^\infty}$; v is normalised so that $max_y v = 1$.

The computational domain is $(L_x/\delta_0,\, L_y/\delta_0,\, L_z/\delta_0)$=$(450, 20, \frac{2\pi}{k_z})$. The number of grid points used is $(N_x,\, N_y,\, N_z)$=$(1025, 193, 65)$. The grid is uniformly spaced in the streamwise x and spanwise z directions, and is clustered near the interface in the wall-normal y direction.

The height of the computational domain is selected to be sufficiently large in order to ensure that the boundary layer is unaffected by the far-field boundary conditions. The convective outflow condition is applied at the exit plane. A no-slip boundary condition

is imposed at the solid wall. At the free stream boundary, $u = U_\infty$ and $v = V_\infty$. Periodic boundary conditions are employed in the spanwise direction.
Different initial amplitudes of the inlet perturbation are explored: $\epsilon = 0.01\%,\ 0.1\%,\ 0.5\%$.

4.3.3 Treatment of the interface

In the present DNS, a level-set method is employed for capturing the interface between the two fluids. In the level-set approach, the interface is represented implicitly by an iso-surface of a smooth function, $g = g(\mathbf{x}, t)$, with $\mathbf{x} \in \Omega\,,\ t \in [t_0, t_f]$. This can be chosen to be the signed distance from the interface, i.e.,

$$|g(\mathbf{x}, t)| = |\mathbf{x} - \mathbf{x}_\Gamma|\,, \tag{4.4}$$

where $\mathbf{x}_\Gamma$ corresponds to the closest point on the interface from $\mathbf{x}$, and $g(\mathbf{x}, t) > 0$ on one side of the interface, and $g(\mathbf{x}, t) < 0$ on the other side. Therefore, the interface is the iso-surface given by $g(\mathbf{x}, t) = 0$, which can be transported according to:

$$\frac{\partial g}{\partial t} + \mathcal{U}_j \cdot \nabla g = 0\,, \tag{4.5}$$

and differentiated to compute the normal vector $\hat{\mathbf{n}}$ and the curvature κ of the interface, defined as:

$$\hat{\mathbf{n}} = \frac{\nabla g}{|\nabla g|}\,, \tag{4.6}$$

and

$$\kappa = -\nabla \cdot \hat{\mathbf{n}}\,. \tag{4.7}$$

Advantages of the level-set method include automatic handling of topological changes, efficient parallelisation as well as easy representation of the interface curvature. The conventional level-set technique relies on representing the interface as the zero level set of a signed distance function. However, one of the main limitations of this method is poor mass conservation. The present study exploits the conservative level-set method in conjunction with a ghost fluid approach (Desjardins *et al.*, 2008). The conservative level set method was originally proposed by Olsson & Kreiss (2005) and Olsson & Kreiss (2007), who employed a hyperbolic tangent function, $h = h(\mathbf{x}, t)$, instead of the signed

distance function in equation (4.4). The scalar field h is defined as:

$$h(\mathbf{x},t) = \frac{1}{2}\left(\tanh\left(\frac{g(\mathbf{x},t)}{2e}\right)+1\right), \tag{4.8}$$

where e is a parameter that sets the thickness of the profile. The location of interface is defined as the $h = 0.5$ iso-surface. The transport of the interface can still be performed by solving the same equation as (4.5) for h. However, provided that relation (4.2) holds, the interface transport equation can be re-written in conservative form, that is:

$$\frac{\partial h}{\partial t} + \nabla\cdot(\mathcal{U}_j h) = 0\,. \tag{4.9}$$

Therefore, the scalar field h is a conserved quantity. However, in order to preserve the shape of the hyperbolic tangent profile, a re-initialization equation is needed to ensure an accurate and conservative transport of the interfacial profile. This equation is as the following:

$$\frac{\partial h}{\partial t} + \nabla\cdot(h(1-h)\hat{\mathbf{n}}) = \nabla\cdot(e(\nabla h\cdot\hat{\mathbf{n}})\hat{\mathbf{n}})\,. \tag{4.10}$$

Equation (4.10) consists of a balance between the sharpening effect of the left-hand side and the diffusion term on the right-hand side, which ensures that the profile remains of characteristic thickness e. Since equation (4.10) is also written in conservative form, the successive solution of equations (4.9) and (4.10) accomplishes the transport of the $h = 0.5$ iso-surface, preserving the shape of the hyperbolic tangent profile and imposing the conservation of h.

In order to handle large density variations across the interface, the ghost fluid method (Fedkiw *et al.*, 1999) is used to account for the density jump and surface tension through the pressure term; the jump in the viscous stresses are modelled using the continuum surface force approach (Brackbill *et al.*, 1992).

The treatment of the interface as described ensures that the discontinuity features can be captured by the DNS. However, it must be pointed out that, due to computational cost and numerical issues, sharp variations of physical quantities are modelled using smooth approximation of Heaviside function, i.e.:

$$H(|\mathbf{x}-\mathbf{x}_\Gamma|) \approx \frac{1}{1+e^{-2k|\mathbf{x}-\mathbf{x}_\Gamma|}} \tag{4.11}$$

where k is a parameter controlling the sharpness of the transition. The DNS therefore accounts for sharply-varying physical quantities rather than discontinuous ones as in the two-phase spatially-evolving perturbation equation presented in the previous chapters. This difference of formulation of interfacial conditions and representation has to be considered when comparing results from DNS and linear stability close to the interface.

Instantaneous and time-averaged flowfield

In the case of two-fluid flows, it is necessary to clarify the concept of mean quantities within the DNS framework. Whilst the PBl has a native discontinuous representation of the velocity and pressure fields, and therefore there is no confusion on the meaning of averaging, the DNS models the two-fluid flow as continuous flow field with sharply-varying physical properties. Hence, the standard averaging methodology would not be entirely appropriate. It is possible to consider averaged quantities conditional to which portion of the flow they belong to; these averages are called conditional averages. The inlet disturbance has an oscillation period $T = \frac{1}{\omega}$, which is used to correctly sample and average instantaneous quantities over time:

$$\bar{\mathbf{u}} = \frac{1}{\epsilon}\frac{1}{T}\int_T \mathbf{u}\, dt \quad , \text{ time average ;} \tag{4.12}$$

$$\bar{\mathbf{u}}_j = \frac{1}{\epsilon}\frac{1}{T}\int_T \mathbf{u}_j\, dt \quad , \text{ conditional time average, } j = \mathsf{T}, \mathrm{B}; \tag{4.13}$$

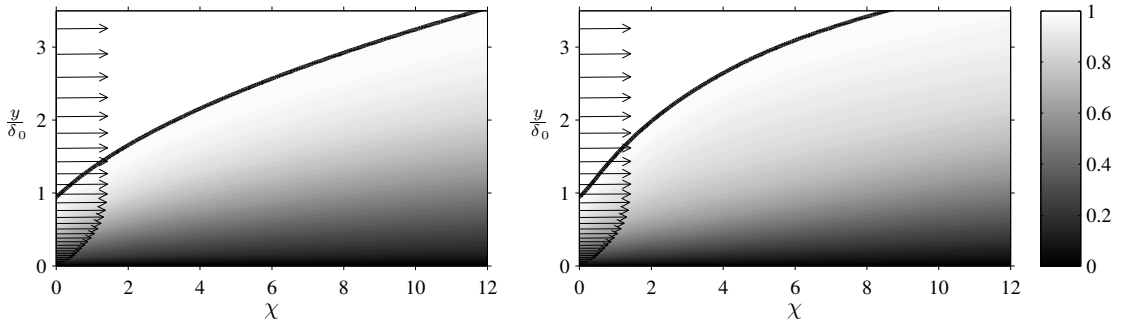
$$\mathbf{u}_{rms}{}^j = \frac{1}{\epsilon}\left|\frac{1}{L_z}\int_{\Omega_z} \bar{\mathbf{u}}_j\, dz\right| \quad , \text{ root mean square, } j = \mathsf{T}, \mathrm{B}. \tag{4.14}$$

Averaging over the oscillation period ensures that both principal and harmonic frequencies of the inlet disturbance are correctly sampled.

4.3.4 Mean flow distortion

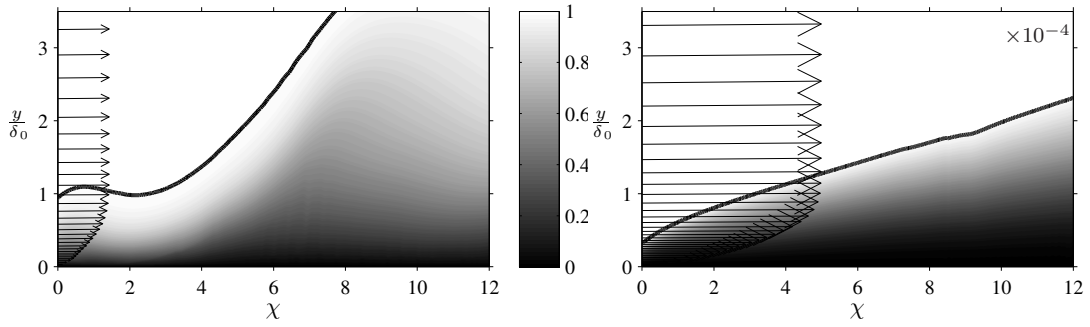
When the assumption on infinitesimality of disturbances is discarded, nonlinear interactions between the base flow and the perturbation are allowed. Therefore, the base flow is subject to modification in relation to ϵ. As ϵ increases, nonlinear effects of the perturbation on the base flow become appreciable (figure 4.1). In the nonlinear case, the inlet disturbace has an increasing weight in determining the solution of the base flow; as a result, as ϵ increases, the boundary layer thickens. Figure 4.2 shows the full flowfield $\mathcal{U} = \mathbf{U} + \mathbf{u}$ for $\epsilon = 1\%$ and inlet optimal perturbation determined by the parameter set

p^o. The presence of a non-infinitesimal perturbation introduces distortion in the flow field, which might eventually create inflection points and trigger other instabilities.



(a) linear (b) nonlinear

Figure 4.1: Mean flow distortion due to nonlinearity. Thick solid line marks the edge of the boundary layer.



(a) $U + \epsilon u$ (b) $V + \epsilon v$

Figure 4.2: Instantaneous full flowfield $\mathcal{U}$ nonlinear distortion. Thick solid line marks the edge of the boundary layer.

4.4 Evolution of optimal disturbances

In this section, the evolution of optimal disturbances computed in Chapter 3 is discussed. In particular, the spatial initial value problem imposed by the optimal disturbances is solved using the parabolic boundary layer approximation (PBl) (equations 3.26-3.34) and compared to full nonlinear DNS solution.

The perturbation streamwise kinetic energy $E = E(x)$, defined as:

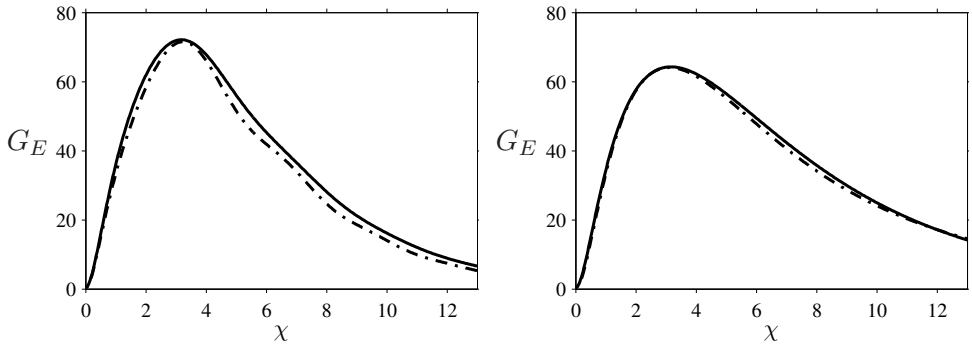
$$E = \int_{\Omega_z} \int_{\Omega_y} |\hat{u}|^2 + |\hat{v}|^2 + |\hat{w}|^2 \, d\Omega_y \, d\Omega_z \ , \tag{4.15}$$

is used to quantify the differences in the streamwise evolution of disturbances between PBl and DNS. As DNS accounts for nonlinearity and finite interface deformation, the initial amplitude of the inlet disturbance determines in fact the streamwise evolution of the disturbance itself. The parameter ϵ can be considered as a controller of the nonlinear behaviour of the evolution. In particular, consider different values of the controller ϵ_i and the corresponding energy evolution $E_i(\chi)$; if the relation $E_j(\chi) = \epsilon_j E_i(\chi)/\epsilon_i$ holds, ϵ_i, ϵ_j are in the range addressed in this work as "Linear Regime"; when the opposite is true, ϵ_j belongs to the parameter space that in this work is referred to as the "Nonlinear Regime". According to this rule, low values of ϵ ($\epsilon \approx 0.01\% - 0.1\%$) are not able to trigger nonlinear effects, which become instead evident as ϵ is increased to 0.5%.
In the next subsection, the evolution of optimal and suboptimal disturbances in Linear and Nonlinear regimes are presented. Note that only results for one value of ϵ in the Linear Regime ($\epsilon = 0.1\%$) and Nonlinear Regime ($\epsilon = 0.5\%$) are presented in this chapter.
The analyses are presented in a systematic manner: firstly, an overview of the perturbation streamwise kinetic energy and interface displacement are given, then a side-by-side comparison between PBl and DNS (for the Linear Regime) and linear DNS and nonlinear DNS (for the Nonlinear Regime) follows. In particular, instantaneous and conditional averaged flow fields and interface displacement are compared.

4.4.1 Linear regime

In the linear regime, the initial amplitude of the inlet disturbances is set to be $0.01 - -0.1\%$ of the free-stream velocity; this choice ensures that the nonlinear terms in the NS equations have negligible effect.
Define the amplification of kinetic energy as $G_E(x) = \frac{E(x)}{\epsilon E(x_0)}$. The streamwise evolution of perturbation's amplification kinetic energy G_E for the optimal (p^o) and suboptimal (p^{so}) disturbances are shown in figure 4.3, for a value of $\epsilon = 0.1\%$ in the linear regime.
In the linear regime, very good agreement between PBl and DNS is found, as both methods provide the same prediction on maximum energy amplification and peak location.

The streamwise evolution of the interface displacement perturbation f for boundary layer equations and signed distance function for DNS is presented in figure 4.4. Note



(a) p^o (b) p^{so}

Figure 4.3: Comparison of streamwise evolution of amplification of kinetic energy G_E for (4.3a) $\omega^o = 0.0125$, (4.3b) $\omega^{so} = 0.0010$, ${k_z}^o$, m^o, d^o, $Re = 800$, $\epsilon = 0.1\%$. —— PBl, – · – DNS.

that the interfacial displacement in DNS is reconstructed solving equation 4.8 for the isosurface of level 0.5.

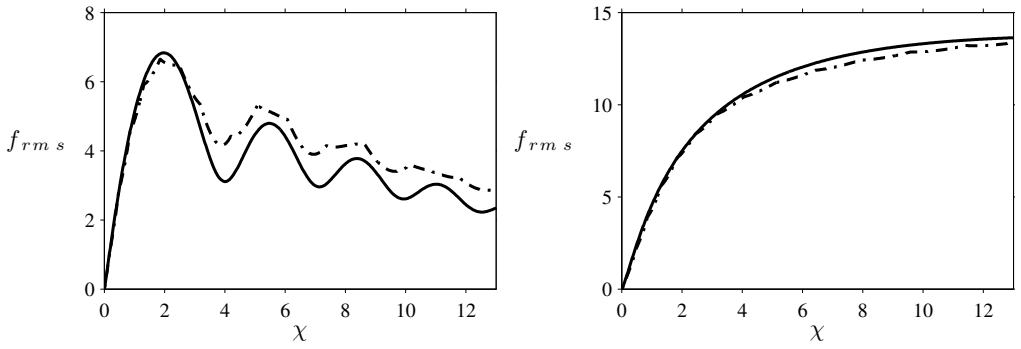
Figure 4.4b highlights the interfacial behaviour at low ω: the interface displacement saturates as χ increases, forcing a jump in the streamwise velocity profile; as discussed in the previous chapter, the spreading of the mean shear reduces the ability of the interface displacement to generate u perturbations.

Both linear theory and linear DNS show agreement of the computation of the interface perturbation.

At the optimal frequency, $\omega^o = 0.0125$, f exhibits multiple peaks (4.4a) modulated by $\sim e^{\left.\frac{-i\omega+\frac{\partial V(x)}{\partial y}}{U(x)}\right|_{x_o}^{x}}$.

The appreciable difference of the interface displacement perturbation between PBl and DNS is due to the different instric representation of the interface in these two methods. In particular, the assumption of linearity allows for direct tracking of the interface displacement in the PBl, as it was shown in the previous chapter (eq. 3.24). This is not possible in the DNS, which can account also for changes of topology. The interface displacement is therefore retrieved through isosurfaces of h (eq. 4.8).

An accurate energy growth prediction relies on the correct rappresentation of the interface displacement and interfacial boundary conditions. Both the approaches followed with the two-fluid parabolized boundary layer equations and with the DNS ensure this.



(a) p^o (b) p^{so}

Figure 4.4: Comparison of streamwise evolution of interface displacement for (4.4a) $\omega^o = 0.0125$, (4.4b) $\omega^{so} = 0.0010$, $k_z = 1.5$, $m = 0.55$, $Re = 800$, $\epsilon = 0.1\%$. —— PBl, - · - DNS.

Linear evolution of optimal disturbance p^o

Consider the linear ($\epsilon = 0.1\%$) evolution of the optimal disturbance for the parameter set p^o. A comparison between PBl (on the left hand side) and DNS (on the right hand side) evolution is presented through spanwise and streamwise section views of the perturbation flowfield, for instantaneaous and conditional averaged data in figures 4.5-4.13. The aim of this section is to compare PBl and linear DNS in order to cross-validate the two formulations.

Instantaneous fields Sections of yz-plane at streamwise locations $\chi = \{1.0, 2.7, 5\}$ are depicted in figure 4.5. The vector plots show the normal and spanwise velocity fluctuations (v, w); the streamwise velocity fluctuation, u, is represented by contour lines. Solid and dashed lines mark positive and negative values. The interface location is also shown. Both PBl and DNS describe the same counterrotating vortices evolving downstream. The spanwise wavenumber and location inside the boundary layer of u-velocity and (v, w) velocity field of the perturbation are in strong agreement. In particular, as the inlet perturbation evolves (figure 4.5a- 4.5b), fast fluid is pushed towards the interface, forcing the growth of a streak in the streamwise direction. Due to the unsteadiness of the inlet disturbance, the streamwise extent of the streaks is proportional to $2\pi/\omega^o$: along the streamwise direction, positive streaks move higher in the boundary layer (figure 4.5c-4.5d) and are replaced by negative streaks further downstream (figure 4.5e-4.5f). A

closer view of the interface location is given in figure 4.6. In figures 4.6a-4.6b and 4.6e-4.6f it is appreciable how the streamwise evolution of the counterrotating vortices forces downward and upward motion of the interface. Although countour plots of (v, w) velocity fields are plotted on different grids, both PBl and DNS present the same dynamics of the interface and flowfield.

Figure 4.7 presents a side view comparison of the linear streamwise velocity field components and perturbed interface location.

The inlet perturbation (4.7b-4.7c) forces the growth of the streamwise streak (4.7a) and deforms the interface (4.7d). The unsteadiness of the inlet perturbation is further remarked in figure 4.7, which highlights the spatial frequency in the streamwise direction. As inlet vortex decays, u and f grow, sustaining also a perturbation in the spanwise direction.

Note that PBl and linear DNS yield to the same description of the velocity field and interface displacement. In particular, both the lift-up mechanism and the growth of streaks are well represented in both cases; the non discontinuous formulation of the velocity field in the DNS does not appear to be a limiting factor. These comparison show that, for instantaneous data, the linear DNS retrieve the semi-analytical solution of PBl.

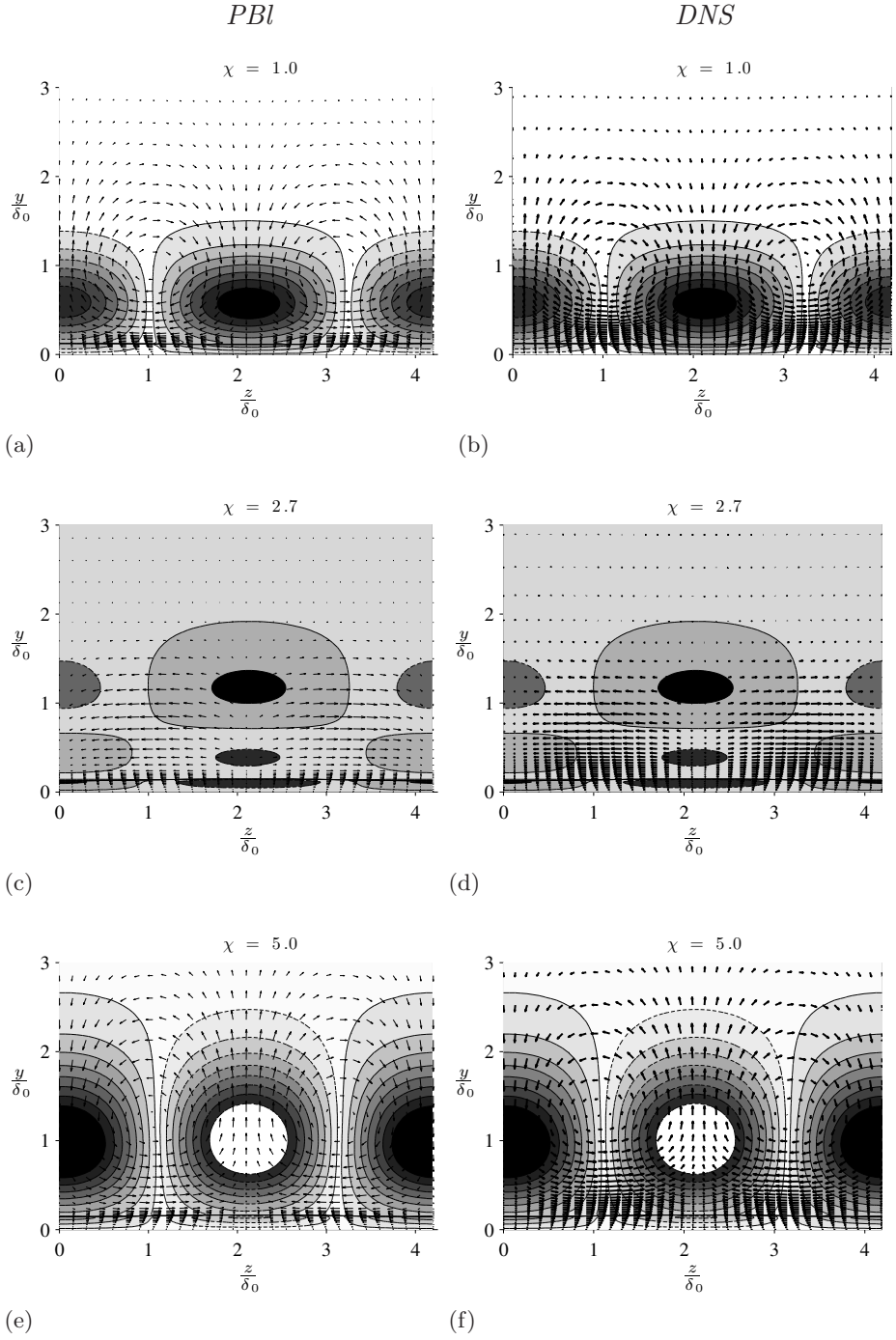


Figure 4.5: End view on zy-plane at location $\chi = \{1.0, 2.7, 5\}$, for $\omega^o = 0.0125$ and $\epsilon = 0.1\%$ (linear). Solid line delimits the interface; arrows show the vector field (v, w). Contours of streamwise velocity u are also represented.

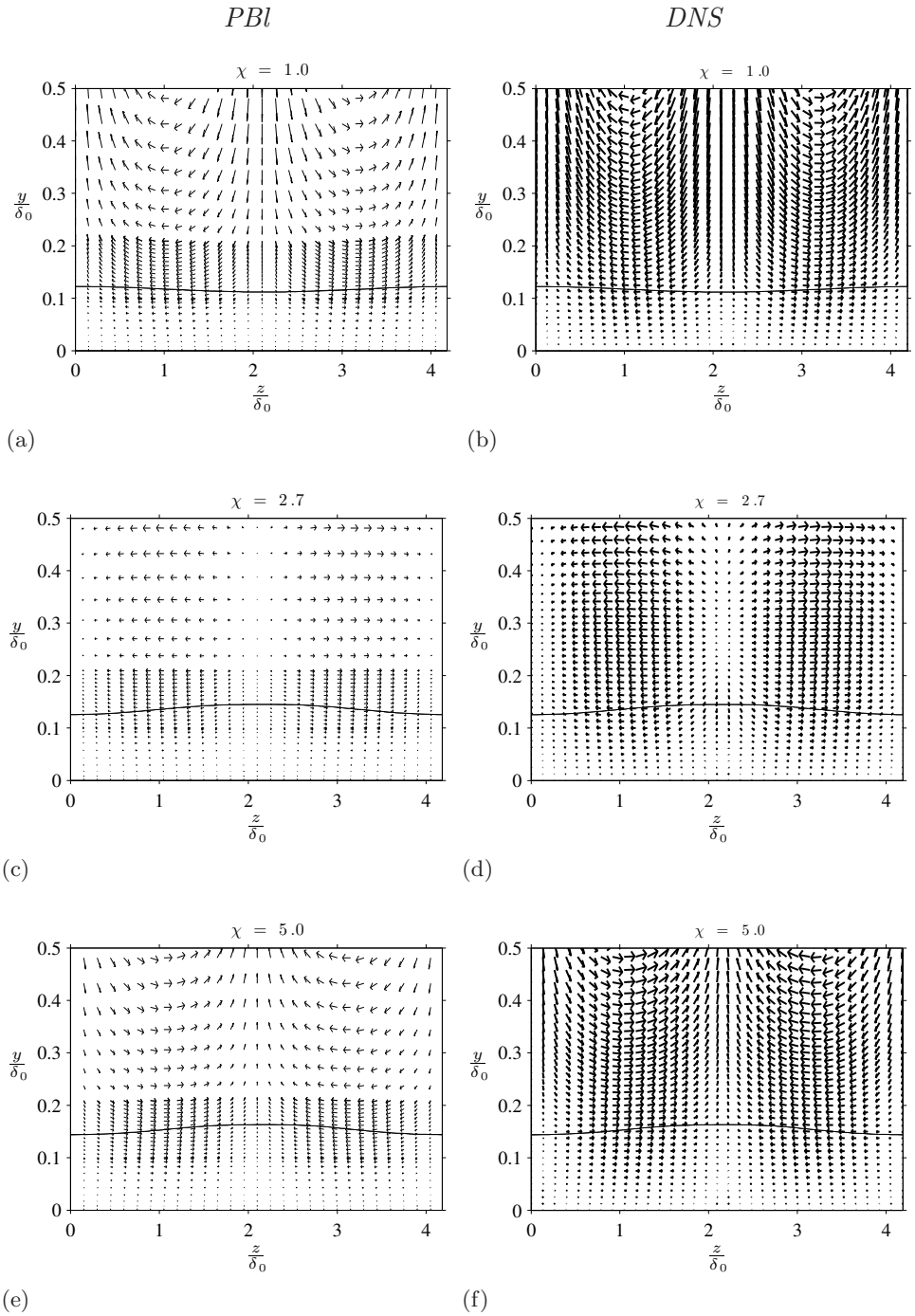


Figure 4.6: End view on zy-plane at location $\chi = \{1.5, 2.7, 5.0\}$, for $\omega^o = 0.0125$ and $\epsilon = 0.1\%$ (linear). Solid line delimits the interface.

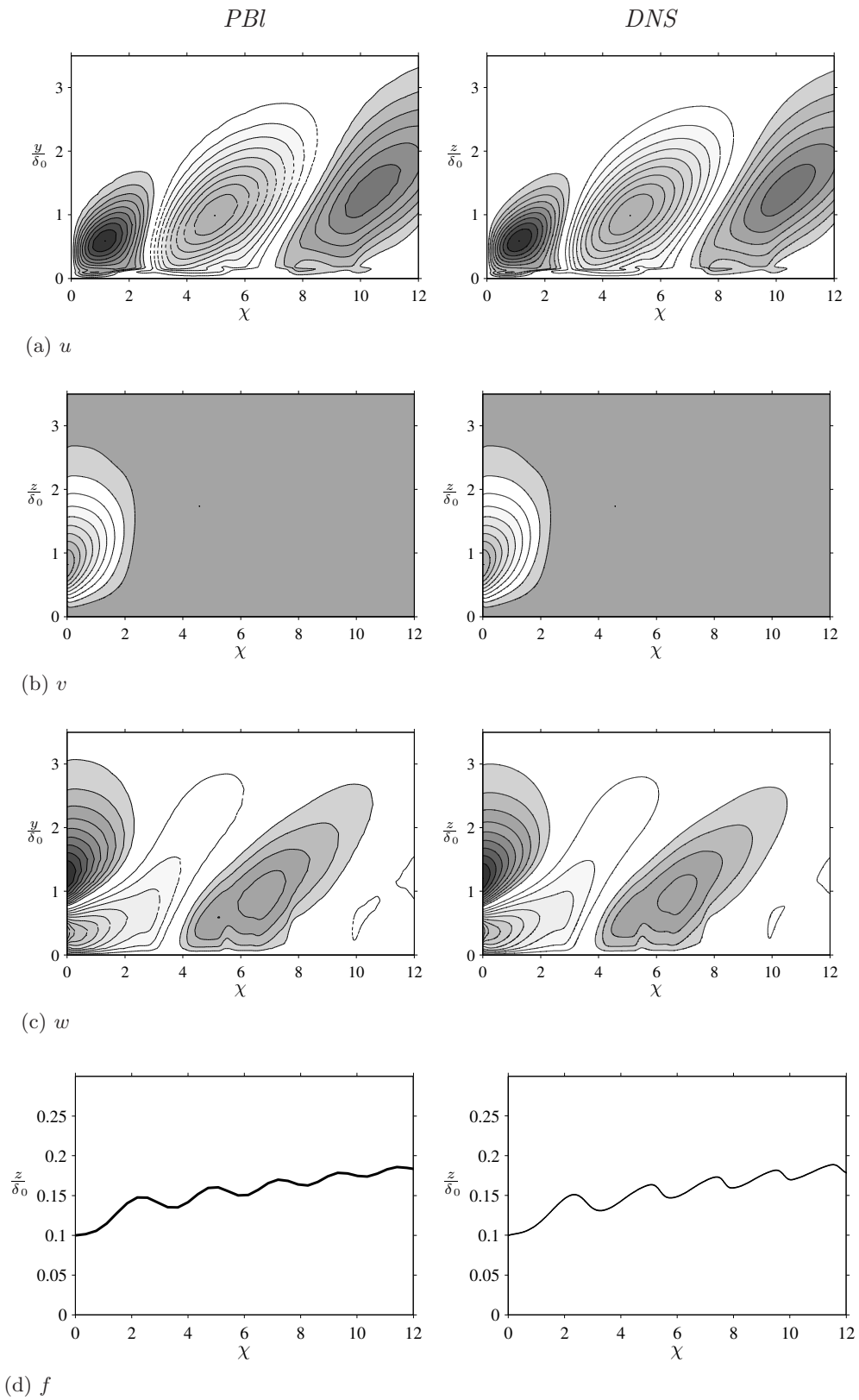
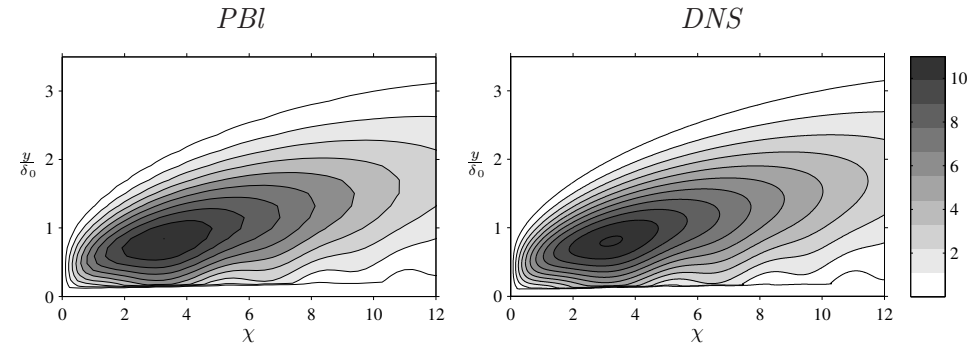
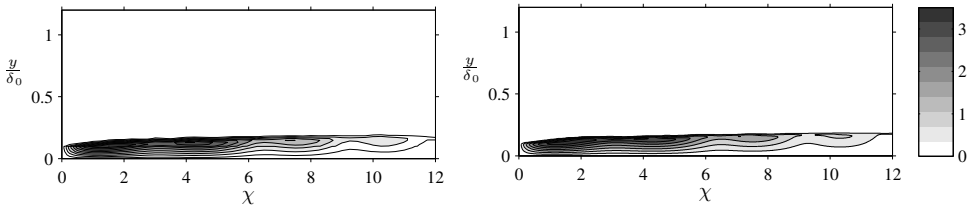


Figure 4.7: (4.7a)-(4.7c) Side view of contours of instantaneous u, v, w fluctuation in PBl (left) and linear DNS (right). (4.7d) Interface location in PBl and linear DNS, $\omega^o = 0.0125$, $\epsilon = 0.1\%$.



(a) top fluid



(b) bottom fluid

Figure 4.8: Side view of contours of conditional averaged u fluctuation in the top and bottom fluids, $\epsilon = 0.1\%$, $\omega^o = 0.0125$

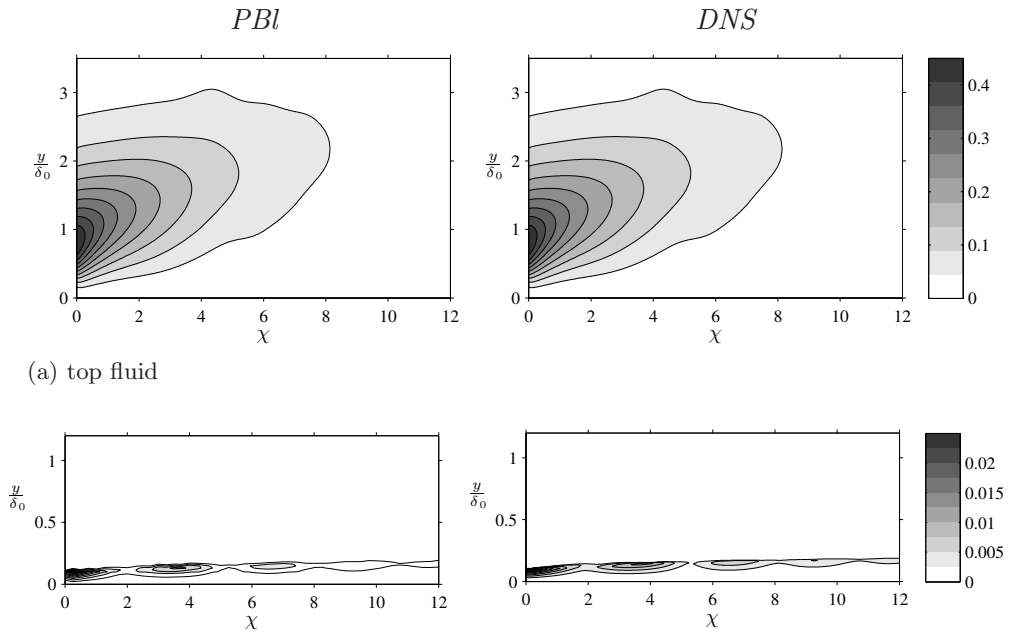
Averaged data Contours of conditional averages of u, v, w velocity components are depicted in figures 4.8-4.10. In particular, figures 4.8a- 4.8b present a comparison of streamwise evolution of u_{rms} between PBl and DNS; figures 4.9a-4.9b and 4.10a-4.10b show that the streamwise decay of the inlet disturbance v_{rms} and w_{rms} is consistent between PBl and DNS in the top and bottom fluid. Very good agreement between PBl and linear DNS is found. The data presented were sampled over 10 oscillation periods; overall, figures 4.8-4.10 highlights that DNS averages converged to the linear solution. In the linear limit, provided that the sampling time is larger than the native perturbation period, DNS can retrieve the semi-analytical description of averaged velocities.

Denote with u_M^j the maximum value of u_{rms} at any location χ in top and bottom fluid ($j = T, B$), normalised by its maximum value, and with y_M^j the $y-$ location at which u_M^j occurs, normalised by δ (by $\delta/(d_0/\delta_0)$, if $j = \mathrm{B}$), that is:

$$u_M^j = \frac{\max_y u_{rms}^j}{\max_\chi \max_y u_{rms}^{\mathsf{T}}}\,, \quad j = \mathsf{T}, \mathrm{B} \tag{4.16}$$

$$y_{M_u}^{\mathsf{T}} = (y \,:\, u_M^{\mathsf{T}} = \max_y u_{rms}^{\mathsf{T}})/\delta\,, \tag{4.17}$$

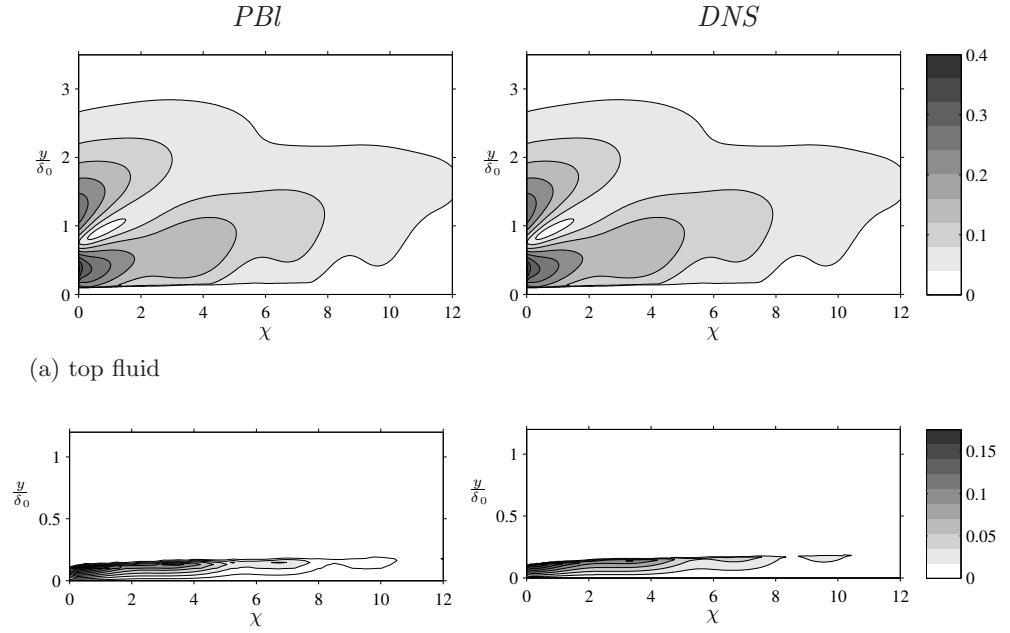
$$y_{M_u}^{\mathrm{B}} = (y \,:\, u_M^{\mathrm{B}} = \max_y u_{rms}^{\mathrm{B}})/\delta/(d_0/\delta_0)\,; \tag{4.18}$$



(a) top fluid

(b) bottom fluid

Figure 4.9: Side view of contours of conditional averaged v fluctuation in the top and bottom fluids, $\epsilon = 0.1\%$, $\omega^o = 0.0125$



(a) top fluid

(b) bottom fluid

Figure 4.10: Side view of contours of conditional averaged w fluctuation in the top and bottom fluids, $\epsilon = 0.1\%$, $\omega^o = 0.0125$

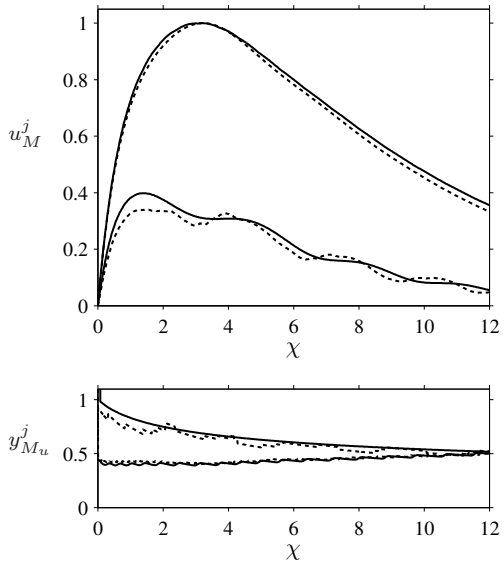


Figure 4.11: Comparison of maximum of conditional averaged u fluctuation, $\epsilon = 0.1\%$, $\omega^o = 0.0125$ between PBl and DNS. ——: PBl, - - -: DNS

and define $v_M^j, y_{M_v}^j$ and $w_M^j, y_{M_w}^j$ accordingly.

Figures 4.11-4.13 report the comparison between PBl and linear DNS of the quantities $u_M^j, y_{M_u}^j$, $v_M^j, y_{M_v}^j$ and $w_M^j, y_{M_w}^j$.

Very good agreement is found on the prediction of the maximum value of averaged velocities and its relative location in the top fluid; in the bottom fluid, due to the mean velocity distribution in the normal direction and the no-slip boundary condition at the bottom wall, the maximum fluctuation velocity occurs near the interface. Figures 4.11-4.13 highlight that the growth of u fluctuation velocity in the streamwise direction is triggered and sustained by the decay of $v-$ and $w-$components. The normal location of the maximum streamwise velocity in the top fluid evolves downstream at the spreading rate of the boundary layer; hence, $y_{M_u}^T$ is approximately located at half of the boundary layer extent, throughout the $x-$domain. In the bottom fluid, the location $y_{M_u}^B$ follows the spreading of the interface. Due to the different spreading rates between δ and d, the location $y_{M_u}^B$ is seen to move towards the wall during the evolution. Similar consideration apply to $y_{M_v}^B$, $y_{M_w}^B$.

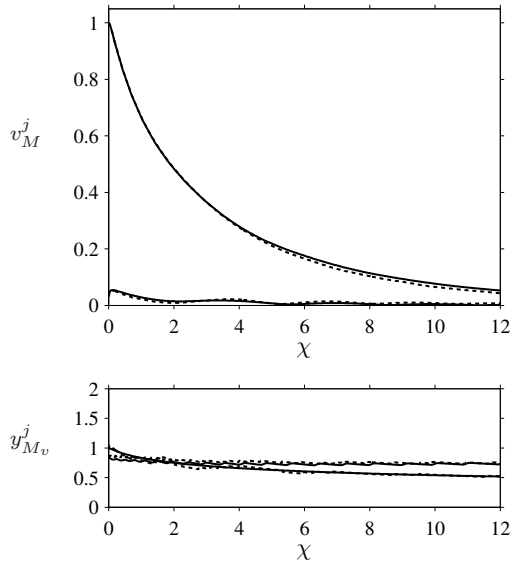


Figure 4.12: Comparison of maximum of conditional averaged v fluctuation, $\epsilon = 0.1\%$, $\omega^o = 0.0125$ between PBl and DNS. ——: PBl, - - -: DNS

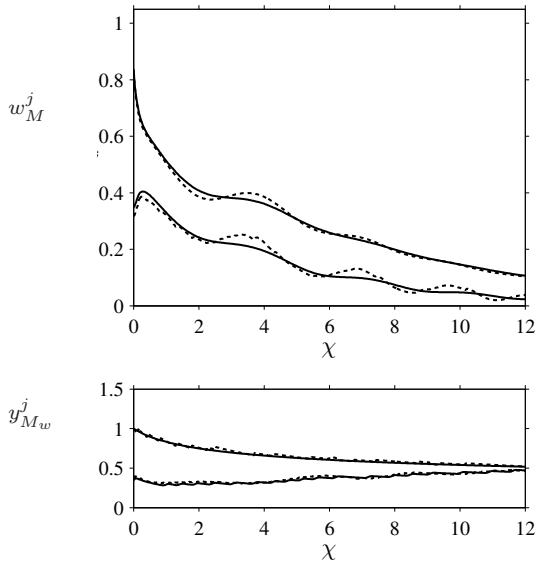


Figure 4.13: Comparison of maximum of conditional averaged w fluctuation, $\epsilon = 0.1\%$, $\omega^o = 0.0125$ between PBl and DNS. ——: PBl, - - -: DNS

Linear evolution of suboptimal disturbance p^{so}

In this subsection, the streamwise evolution of sub-optimal disturbance for the parameter set p^{so} between PBl and DNS in linear regime ($\epsilon = 0.1\%$) is compared.

Instantaneous fields Sections of yz-plane at streamwise locations $\chi = \{1.0, 2.7, 5.0\}$ are depicted in figure 4.14, where a comparison between PBl and DNS is presented, velocity data are instantaneous unless otherwise specified. The vector plots show the normal and spanwise velocity fluctuations (v, w); the streamwise velocity fluctuation, u, is represented by contour lines. Solid and dashed lines mark positive and negative values. The interface location is also shown. PBl and DNS show agreement in the description of the counterrotating (v, w) field and u response. As the two-fluid boundary layer spreads, the optimal disturbance evolves into a streak due to the lift up mechanism (figures 4.14a-4.14b). Due to the quasi-steadiness of the inlet disturbance, the streamwise extent of the streaks is larger than the computational domain, which does not capture the spatial variation of u-fluctuations. A close view of the interface deformation is given in figure 4.15, where the downward flow deflects the interface. PBl and DNS grids are different, however the main structures of (v, w) flowfield are coherently represented. Note that the counterrotating vortices deflect and stretch the interface.

Figure 4.16 depicts a conparison of streamwise velocity and interface deflection in the $\chi y-$plane. Figures 4.16b-4.16c highlight that the decay of the v and w components fosters the growth of u fluctuation in the streamwise direction. Due to the low temporal frequency of p^{so}, figure 4.16 show only a positive streak and negative interface deflection throughtout the χ domain.

The comparison on instantaneous data presented in figures 4.14-4.16 show that the linear PBl code can correctly capture the spreading of the interface and the main flow structures and, in particular, the spreading rate of the streaks and the interface disturbance in the linear DNS converge to the semi-analytical solution of PBl.

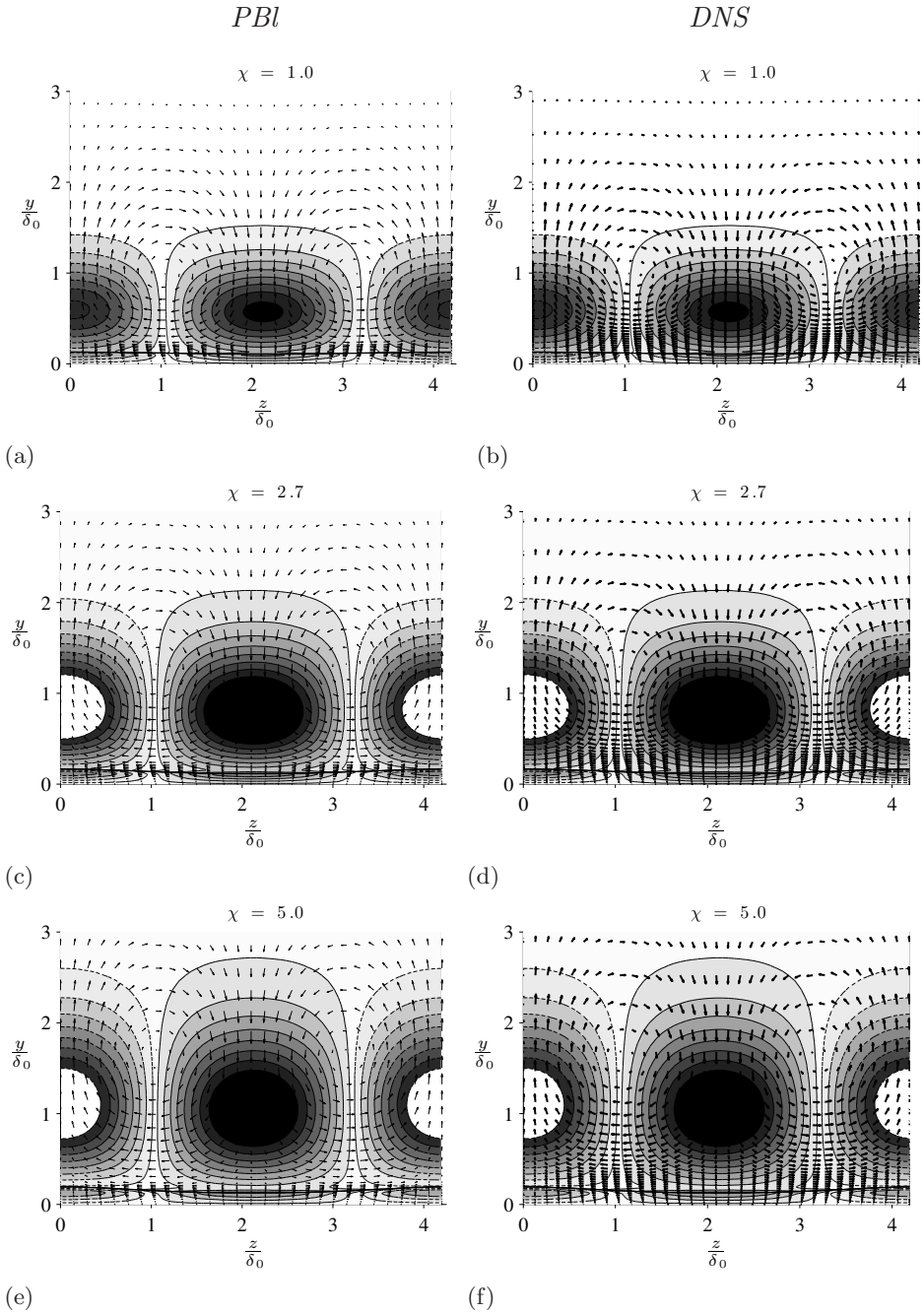


Figure 4.14: End view on zy-plane at location $\chi = \{1.0, 2.7, 5.0\}$, for $\omega^{so} = 0.0010$ and $\epsilon = 0.1\%$ (linear). Solid line delimits the interface; arrows show the vector field (v, w). Contours of streamwise velocity u are also represented. PBl on the left, DNS on the right.

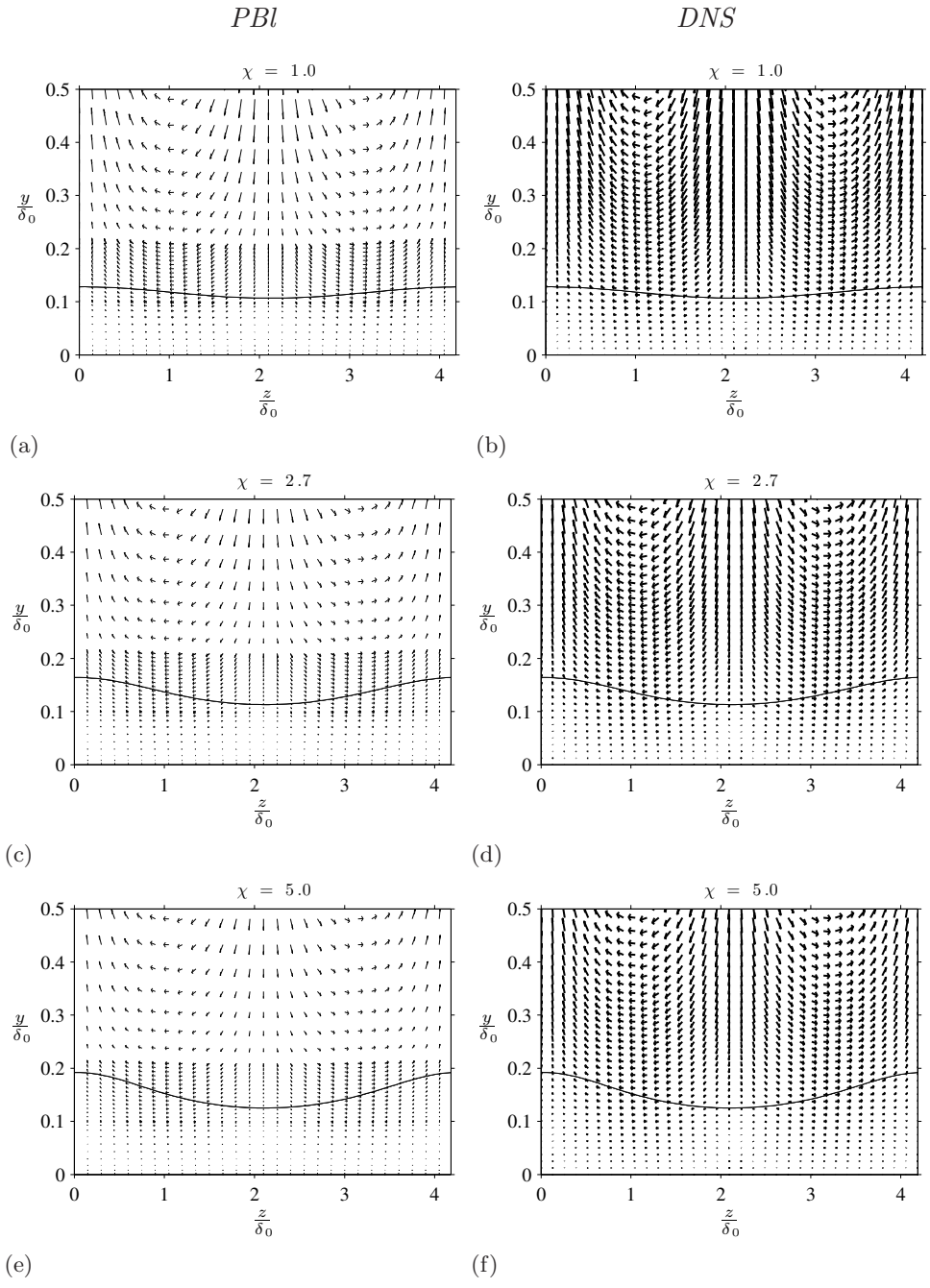


Figure 4.15: End view on zy-plane at location $\chi = \{1.0, 2.7, 5\}$, for $\omega = 0.001$ and $\epsilon = 0.1\%$ (linear). Solid line delimits the interface.

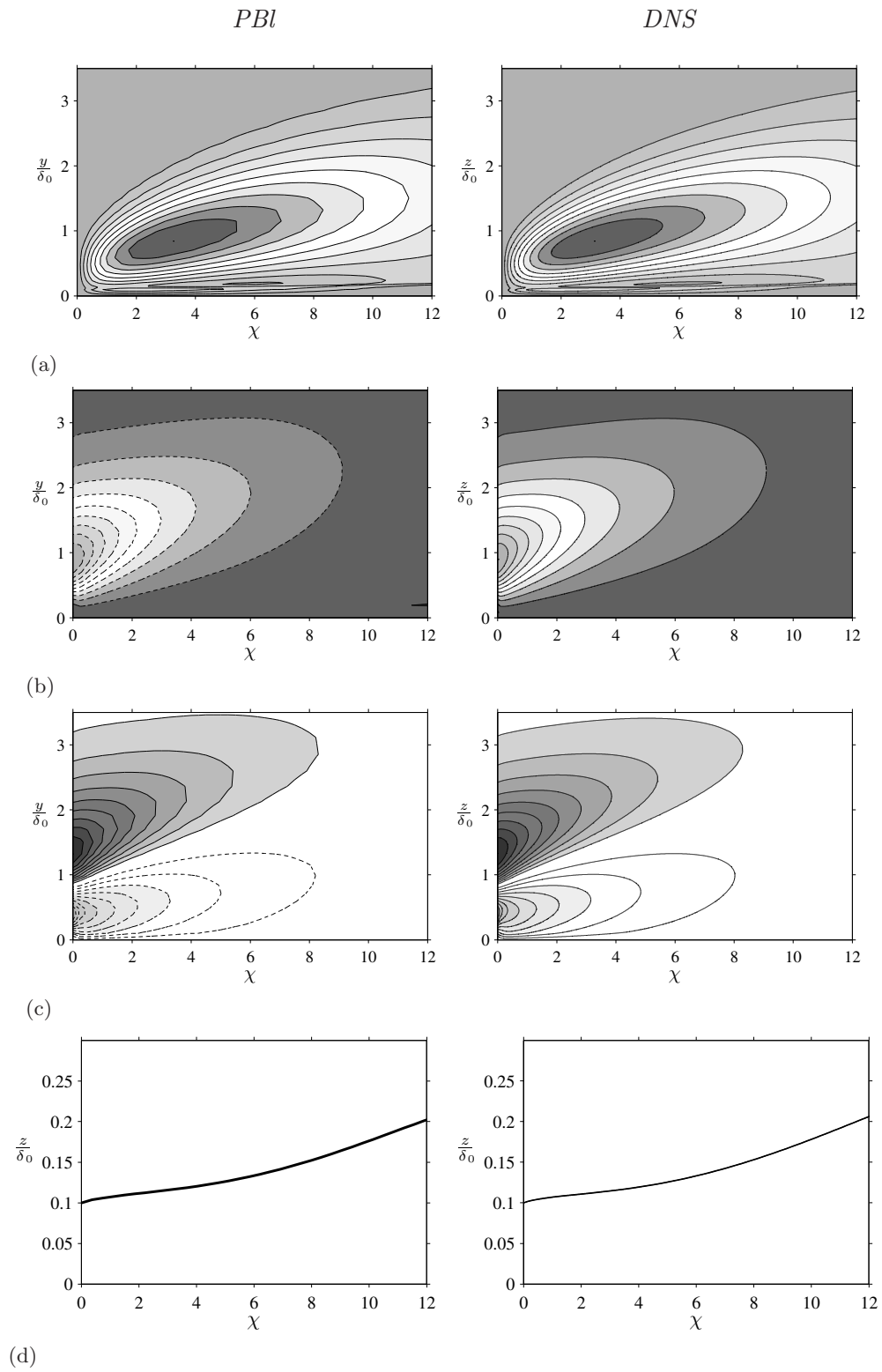


Figure 4.16: (4.16a)-(4.16c) Side view of contours of instantaneous u, v, w fluctuation in PBl (left) and linear DNS (right). (4.16d) Interface location in PBl and linear DNS, $\omega^o = 0.0010$, $\epsilon = 0.1\%$.

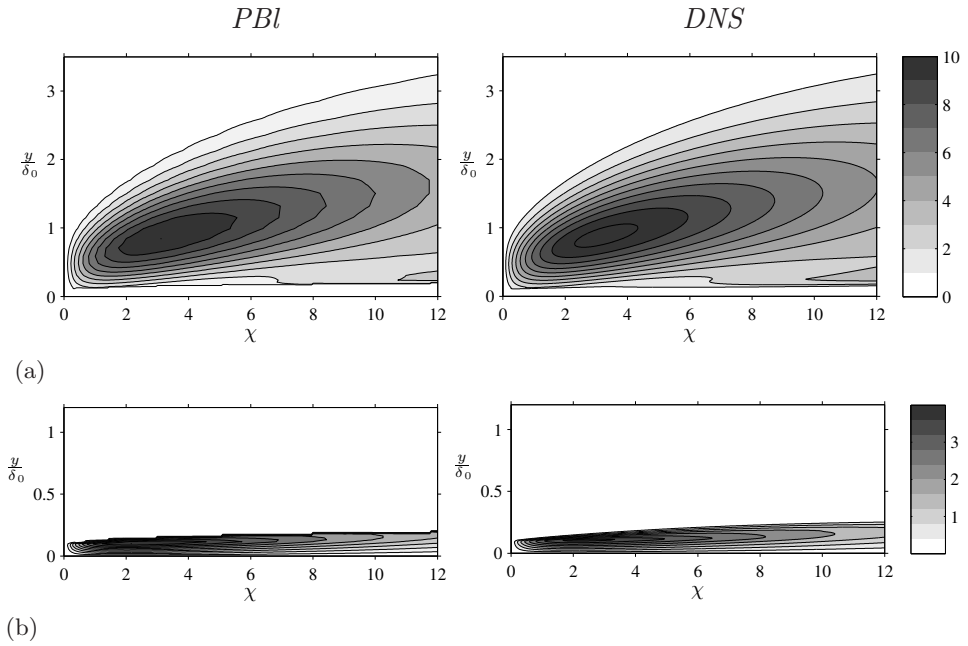


Figure 4.17: Side view of contours of conditional averaged u fluctuation in the top and bottom fluids in PBl and linear cases. (4.17a): top fluid, (4.17b): bottom fluid. $\omega^{so} = 0.0010$, $\epsilon = \{0.1\%\}$.

Averaged data Countours of conditional averages of the velocity field are depicted in figures 4.17-4.19. In particular, figures 4.18a-4.18b and 4.19a-4.19b show v_{rms}, w_{rms} components in the top and bottom fluids; the evolution of u_{rms} is depicted in figures 4.17a-4.17b. Due to the long period of oscillation of the inlet disturbance, DNS requires a very long time to reach convergence (≈ 10 longer than p^o case). Mean quantities were computed over 4 oscillation periods.

Figures 4.20-4.22 report the comparison between PBl and linear DNS of the quantities $u^j_M, y^j_{M_u}$, $v^j_M, y^j_{M_v}$ and $w^j_M, y^j_{M_w}$, as defined in eq. 4.16.

As in p^o case, the prediction of the maximum value of averaged velocities and its relative location in the top fluid is consistent between PBl and DNS. The decay of $v-$ and $w-$components in bottom and top fluids forces the growth of u fluctuations in the streamwise directions in both fluids. The growth of the boundary layer leaves the normal location of the maximum streamwise velocity $y^T_{M_u}$ unaffected; the location $y^B_{M_u}$ is driven by the spreading of the interface, reaching half of its inlet location. The retrival of the locations of maximum averaged velocities in the DNS is affected by the reduced number of sampling cycles.

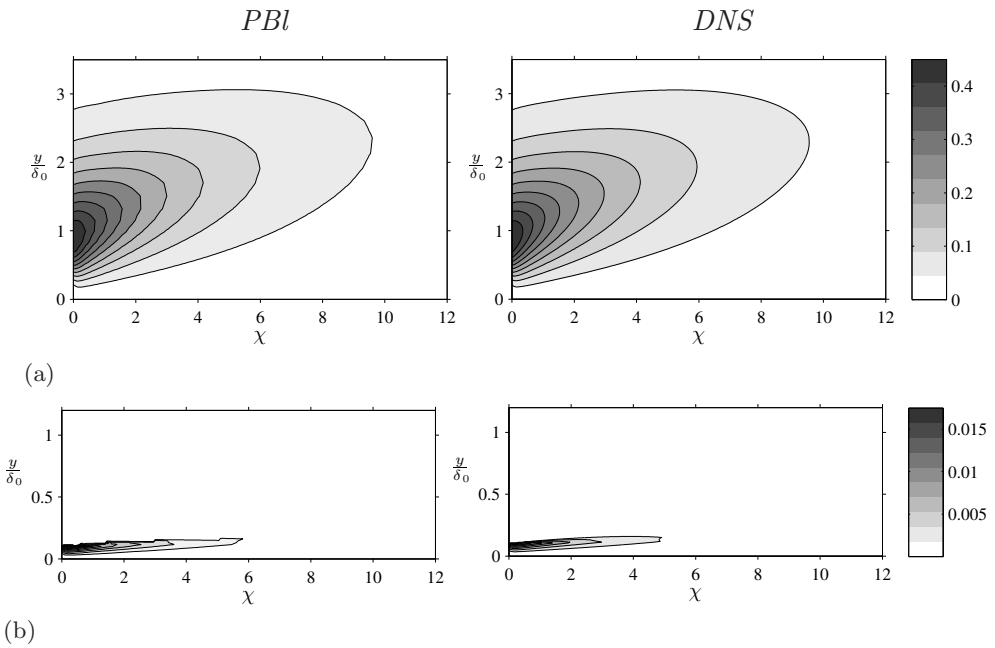


Figure 4.18: Side view of contours of conditional averaged v fluctuation in the top and bottom fluids in PBl and linear cases. (4.18a): top fluid, (4.18b): bottom fluid. $\omega^{so} = 0.0010$, $\epsilon = \{0.1\%\}$.

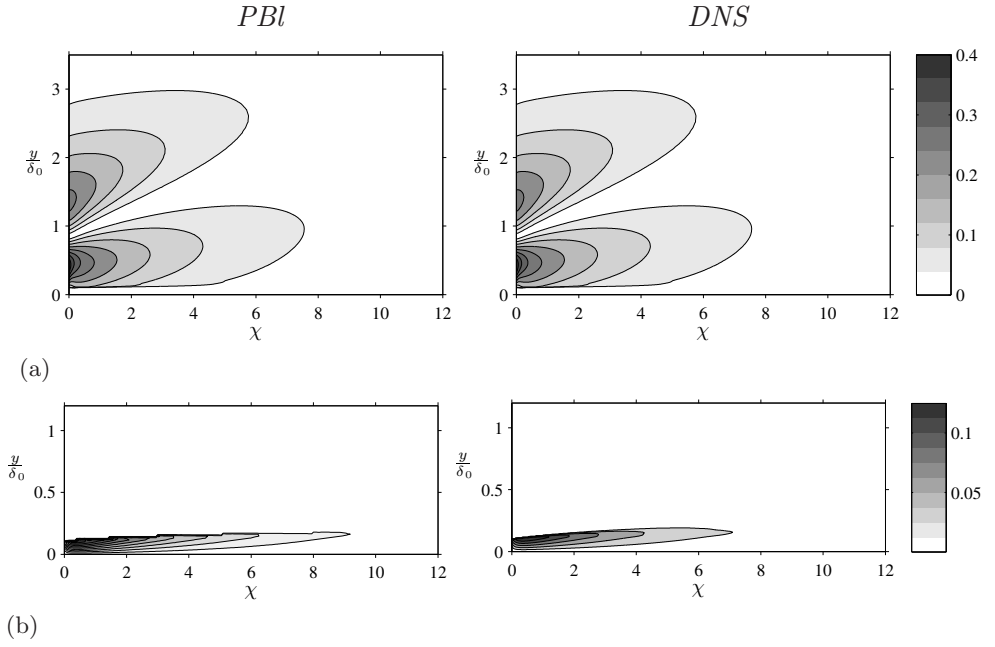


Figure 4.19: Side view of contours of conditional averaged w fluctuation in the top and bottom fluids in PBl and linear cases. (4.19a): top fluid, (4.19b): bottom fluid. $\omega^{so} = 0.0010$, $\epsilon = \{0.1\%\}$.

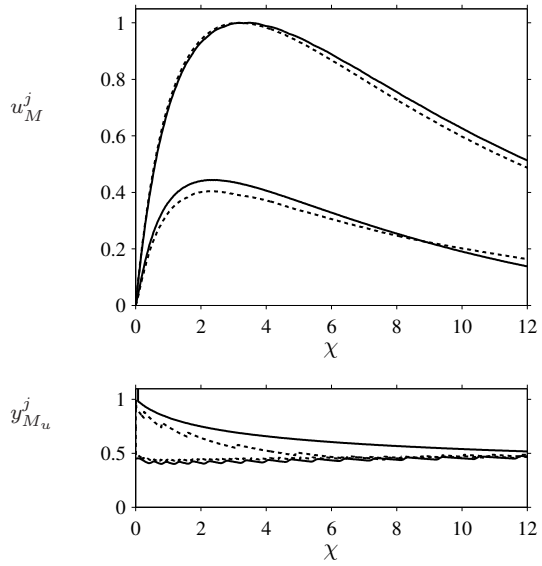


Figure 4.20: Comparison of maximum of conditional averaged u fluctuation, $\epsilon = 0.1\%$, $\omega^{so} = 0.0010$ between PBl and DNS. ——: PBl, - - -: DNS

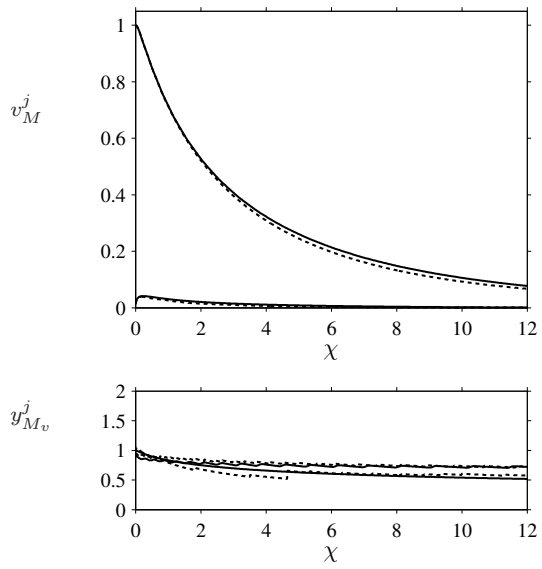


Figure 4.21: Comparison of maximum of conditional averaged v fluctuation, $\epsilon = 0.1\%$, $\omega^{so} = 0.0010$ between PBl and DNS. ——: PBl, - - -: DNS

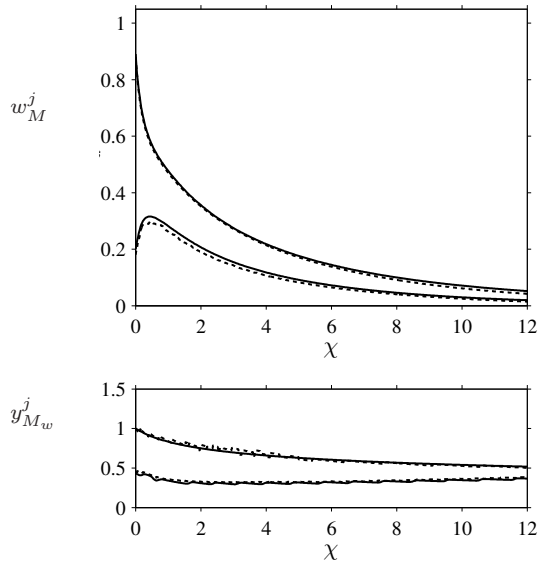


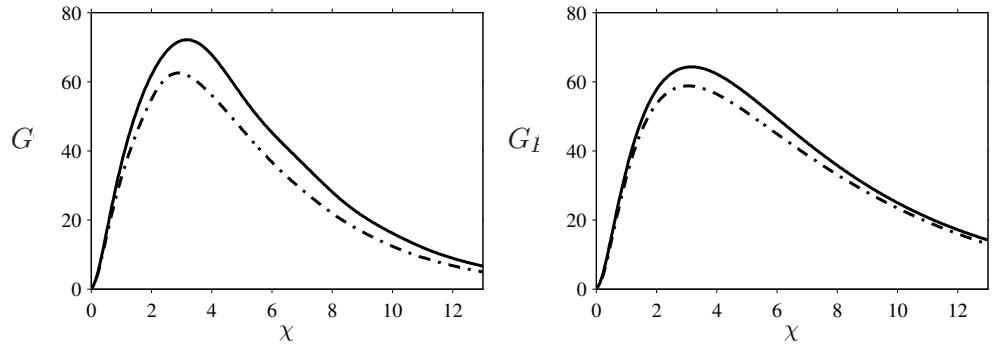
Figure 4.22: Comparison of maximum of conditional averaged w fluctuation, $\epsilon = 0.1\%$, $\omega^{so} = 0.0010$ between PBl and DNS. ——: PBl, - - -: DNS

Observations

The comparison presented up to this point showed very good agreement between PBl and linear DNS for the optimal and suboptimal parameter sets p^o and p^{so}. The DNS code is fully validated against extensive literature; the fact that PBl and DNS yield to the same physical description of the linear evolution of optimal disturbances is a firm point on the validation of the PBl approach.

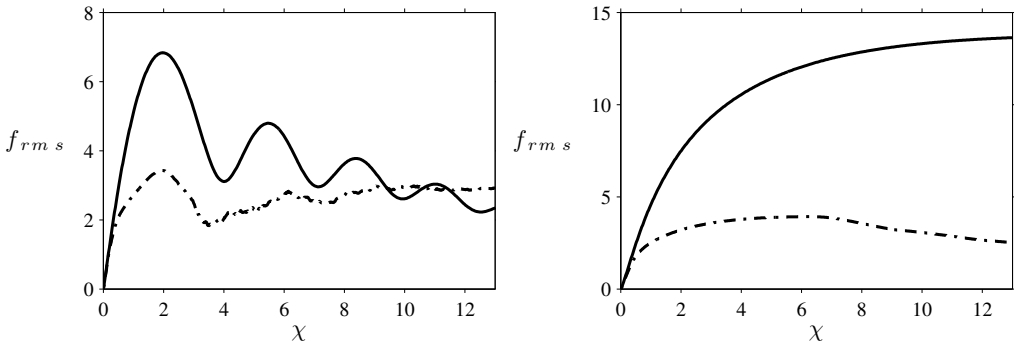
In the quasi-steady case p^{so}, the reduced number of sampling of DNS data show some degree of noise in the retrival of values and location of maximum averaged velocities.

The retrieval of the interface disturbance in DNS is achieved through solving for $h = 0.5$ in equation 4.8 rather than by direct tracking, as in PBl. The solution of $h = 0.5$ depends on the choice of the parameter e, which controls the thickness of the interfacial layer, and the inversion of the hyperbolic function; these differences lead to small discrepancies in the description of the interface deflection between DNS and PBl.



(a) p^o (b) p^{so}

Figure 4.23: Comparison of streamwise evolution of amplification of kinetic energy G_E for (4.3a) $\omega^o = 0.0125$, (4.3b) $\omega^{so} = 0.0010$, ${k_z}^o$, m^o, ——: PBl, - · - non-linear DNS ($\epsilon = 0.5\%$) regime.



(a) p^o (b) p^{so}

Figure 4.24: Comparison of streamwise evolution of normalised interface displacement for (4.24b) $\omega^o = 0.0125$, $\omega^{so} = 0.0010$, (4.24a) ${k_z}^o = 1.5$, $m^o = 0.55$, $Re = 800$, ——: PBl, - · - non-linear DNS ($\epsilon = 0.5\%$) regime.

4.4.2 Non-linear regime

The aim of this subsection is not to provide an extensive and complete study on non-linearity, but to characterise how the non-linear evolution of kinetic energy differs from linear predictions.

The disturbances determined previously for optimal, $p^o : \{\omega = \omega^o = 0.0125;\ {k_z}^o = 1.5;\ m^o = 0.55;\ d^o = 0.1\}$, and sub-optimal, $p^{so} : \{\omega = 0.0010;\ {k_z}^o = 1.5;\ m^o = 0.55;\ d^o = 0.1\}$, set of parameters are prescribed at the inlet of the computational domain and their evolution is investigated.

The initial amplitude, ϵ, of inlet disturbance is set to $\epsilon = 0.5\%$ and it is found that non-linear effects cannot be discarded.

In this section, the evolution of optimal disturbances for $\epsilon = 0.1\%, 0.5\%$ is presented.

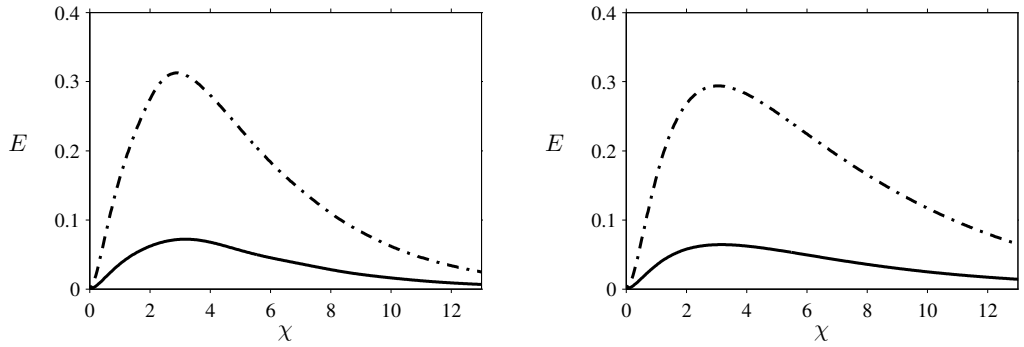


Figure 4.25: Comparison of streamwise evolution of kinetic energy E for (4.25a) $\omega^o = 0.0125$, (4.25b) $\omega^{so} = 0.0010$, ${k_z}^o$, m^o, ——: PBl, - · - non-linear DNS ($\epsilon = 0.5\%$) regime.

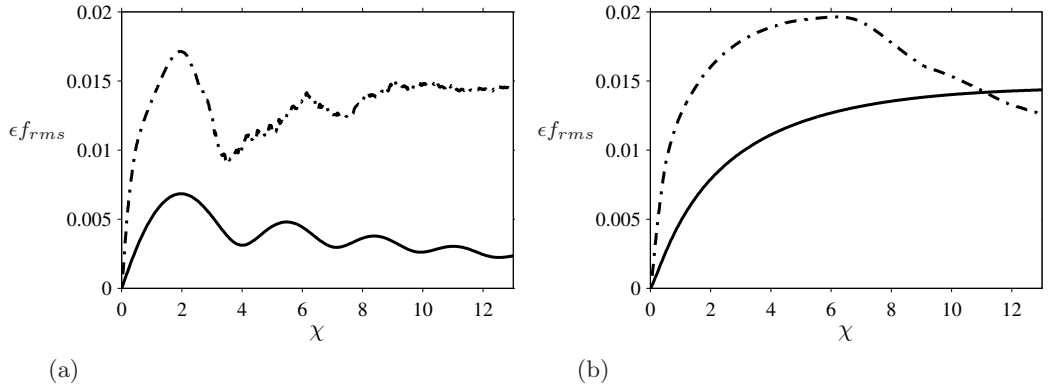


Figure 4.26: Comparison of streamwise evolution of interface displacement for (4.26a) $\omega^o = 0.0125$, (4.26b) $\omega^{so} = 0.0010$, ${k_z}^o = 1.5$, $m^o = 0.55$, $Re = 800$, ——: PBl, - · - non-linear DNS ($\epsilon = 0.5\%$) regime.

At first, an overview of energy growth and interface perturbation is given; then detailed view of streamwise and spanwise sections of the velocity flowfield are compared.

Transient energy amplification, G_E, versus streamwise distance, χ, for linear and nonlinear cases is shown in figure 4.23; the streamwise evolution of the interfacial perturbation is presented in figure 4.24. Non-linearity introduces lower energy gain than in the linear case, with reduced interface deflection. However, note that the quantities presented are normalised by their initial amplitude ϵ; hence, despite nonlinear effect yield to lower normalised energy growth than their linear counterparty, they overall reach higher values of kinetic energy. This is shown in figure 4.25, which depicts the evolution of kinetic energy, E, versus streamwise distance, χ for PBl and nonlinear DNS. Although the initial energy of the inlet perturbation is amplified less in the non-linear case, it reaches higher absolute

values. The same considerations apply to the interface perturbation: figure 4.26 presents the non-normalised interface displacement ϵf_{rms}. Non-linear DNS show more prominent interfacial distortion and significant deviation of the interface disturbance from the theoretical value predicted by linear theory is appreciable.
Figure 4.23 highlights that non-linearity acts as a limiting mechanism for algebraic growth of disturbances; this could be seen as a stabilising effect. However, the introduction of nonlinear contribution yields to higher levels of kinetic energy than linear cases (figure 4.25), which can have destabilising effects on the mean flow (Cheung & Zaki, 2010), and appreciable interface distortion (4.26), which can lead to film break-up.

The next two subsections investigate the nonlinear evolution of optimal disturbances for the parameter sets p^o and p^{so} with the purpose of highlighting the mechanism responsible for changes in energy amplification and interface deformation.

Nonlinear evolution optimal disturbance p^o

Consider now the nonlinear ($\epsilon = 0.5\%$) evolution of the optimal disturbance for the parameter set p^o. A comparison with its linear evolution is presented. Note that all results presented in the next subsection are normalised by ϵ; this choice was made to highligh the distortion of the perturbation flowfield introduced by nonlinearity.

Instantaneous field Sections of yz-plane at streamwise locations $\chi = \{1.0, 2.7, 5.0\}$ are depicted in figure 4.27. The vector plots show the normal and spanwise velocity fluctuations (v, w); the streamwise velocity fluctuation, u, is represented by contour lines. Solid and dashed lines mark positive and negative values. The interface location is also shown. As ϵ increases to 0.5%, a certain degree of distortion of the instantaneous flowfield is evident (figure 4.27), mainly towards the interface, where the combined effect of positive and negative streaks induce severe interface deflection. A close view of the interface evolution in spanwise planes at the streamwise locations $\chi = \{1.0, 2.7, 5.0\}$ is reported in figure 4.28, where it is visible how the intermittent effect of downward and upward motion of the flow forces the interface, which creates plume-like structures.

The streamwise extent of these plume-like structures is fairly limited and proportional to U/ω^o; the alternation of positive and negative streaks also limits the streamwise extent of and forces interface breakup. This is particularly evident in figure 4.29, where

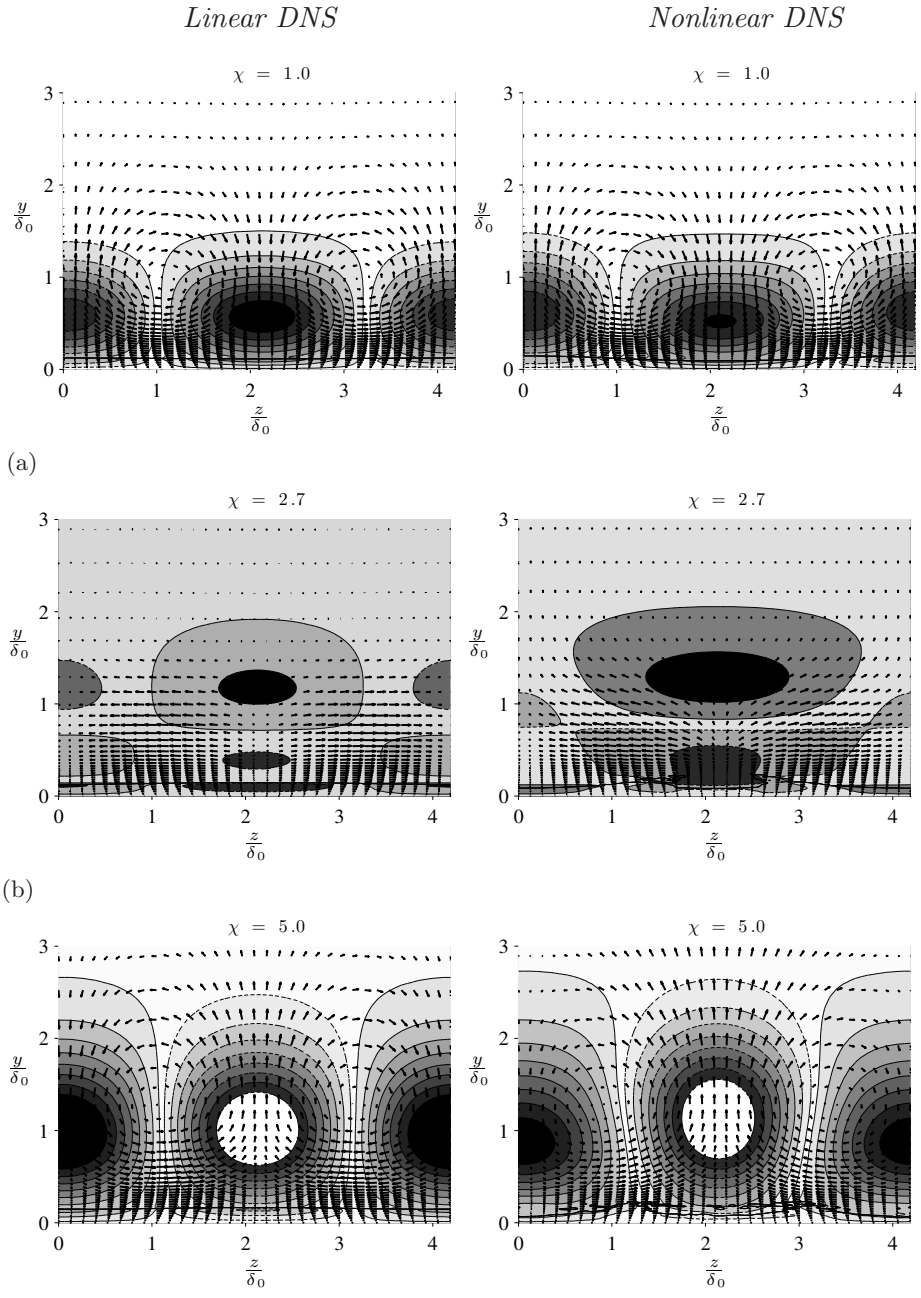


Figure 4.27: End view on zy-plane at location $\chi = \{1.0, 2.7, 5.0\}$, for $\omega^o = 0.0125$ and $\epsilon = \{0.1\%\, 0.5\%\}$ (linear an nonlinear regimes). Solid line delimits the interface; arrows show the vector field (v, w). Contours of streamwise velocity u are also represented.

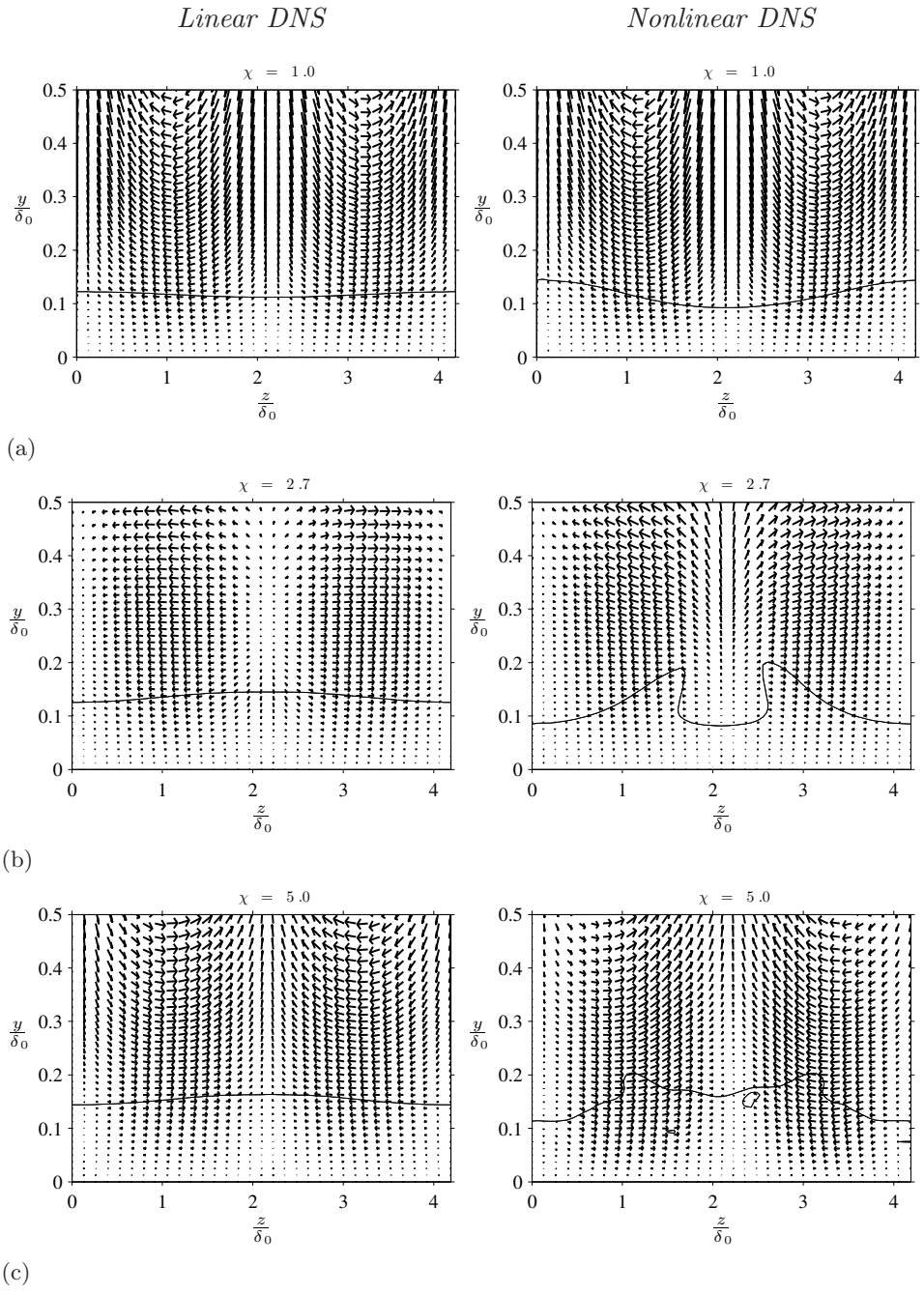


Figure 4.28: End view on zy-plane at location $\chi = \{1.0, 2.7, 5.0\}$, for $\omega^o = 0.0125$ and $\epsilon = \{0.1\%\, 0.5\%\}$ (linear and nonlinear). Solid line delimits the interface.

side views of linear and nonlinear evolution of streamwise velocity fluctuations and interface location are compared. The nonlinear interface distortion is captured in figure 4.29d, where it is compared to its linear counterpart (figure 4.29c).

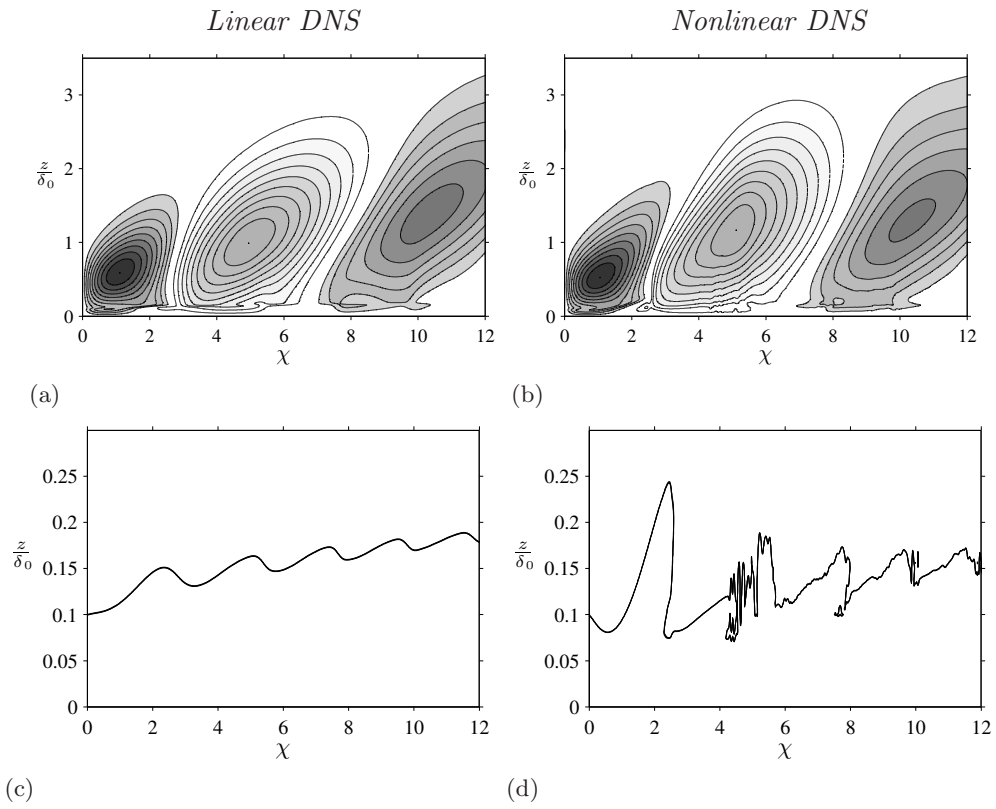


Figure 4.29: Side view of contours of instantaneous u fluctuation in linear (4.29a) and non-linear (4.29b) case. Interface location in linear (4.29c) and non-linear (4.29d) case. $\omega^o = 0.0125$, $\epsilon = \{0.1\%, 1\%\}$.

Instantaneous data show how nonlinearity distorts the streaks in the spanwise (figure 4.27b)and streamwise (figure 4.29b) direction and how the interface is affected. In particular, the plume-like structure at $\chi = 2$ is related to the alternation of positive and negative streaks in the streamwise direction. Also, figure 4.29d highlights that the riconstruction of the interface is challenged for $\chi > 4$; this suggests that increasing grid resolution in the streamwise direction might provide better resolved interface dynamics[1].

[1] A lower resolution grid in the streamwise direction was orignally run ($N_x = 513$); the results presented in this thesis were computed on a finer grid ($N_x = 1025$), which provided marginal improvements. Higher resolutions have not ben investigated in this work.

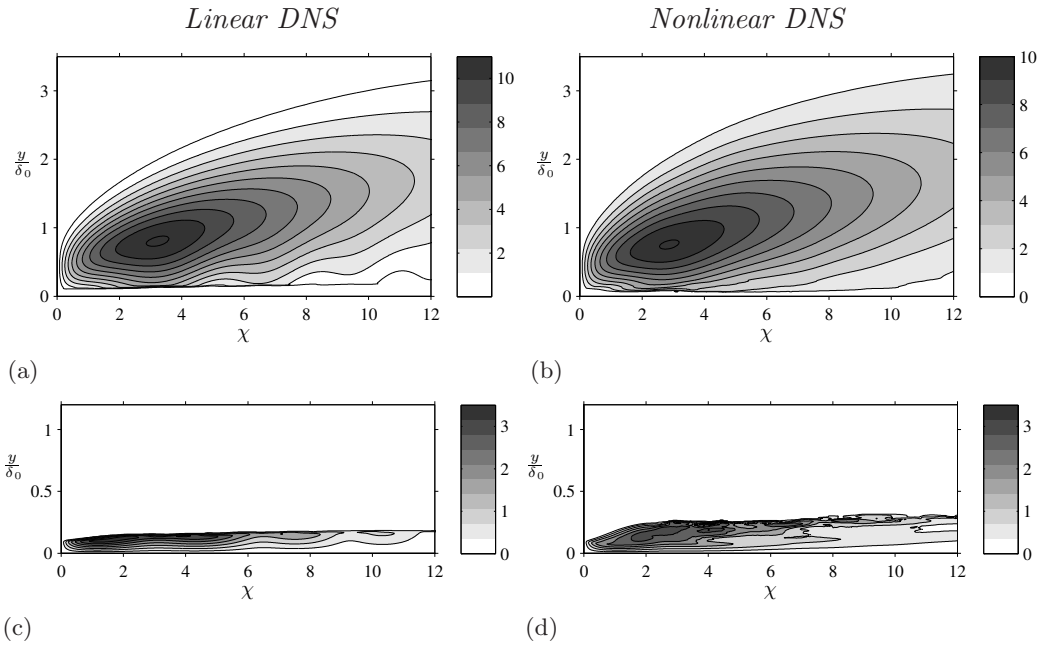


Figure 4.30: Side view of contours of conditional averaged u fluctuation in the top and bottom fluids in linear and non-linear cases. (4.30a): top fluid, linear; (4.30b): top fluid, non linear; (4.30c): bottom fluid, linear; (4.30b): bottom fluid, non linear. $\omega^o = 0.0125$, $\epsilon = \{0.1\%, 0.5\%\}$.

Averaged data Conditional averages of u_{rms}, v_{rms} and w_{rms} velocity fluctuations for top and bottom fluids are presented in figures 4.30-4.32. Larger interface deflections due to nonlinearity are evident in figures 4.30d, 4.31d, 4.32d, where, on average, the bottom fluid is thicker than in the linear cases (figures 4.30c, 4.31c, 4.32c). Nonlinear streamwise fluctuation velocities (figures 4.30b-4.30d) have comparable magnitude to linear case (figures 4.30a-4.30c) in the top and bottom fluid; the same relation applies to normal and spanwise velocities v_{rms} and w_{rms} in the top fluid (figure 4.31a-4.31b, 4.32a-4.32b), whilst in the bottom fluid, stronger velocity fluctuations are induced by the larger interface deformation (figures 4.31c-4.31d, 4.32c-4.32d).

Recalling the definition of u_M^j, the maximum value of u_{rms} at any location χ in the top and bottom fluid ($j = T, B$), normalised by its maximum value, and y_M^j the $y-$ location at which u_M^j occurs, normalised by δ (by $d_0\delta$, if $j = \mathrm{B}$) (eq. 4.16), plots of u_M^j, v_M^j, w_M^j and respective y_M^j are presented in figures 4.33-4.35.

The evolution of the maximum value of velocity fluctuations in the top fluid has low sensitivity to nonlinearity; this can be seen in figures 4.33, where the maximum value of streamwise velocities is plotted versus streamwise distance. In the bottom fluid, due to the high distortion of the interface, the maximum value of the averaged velocities and

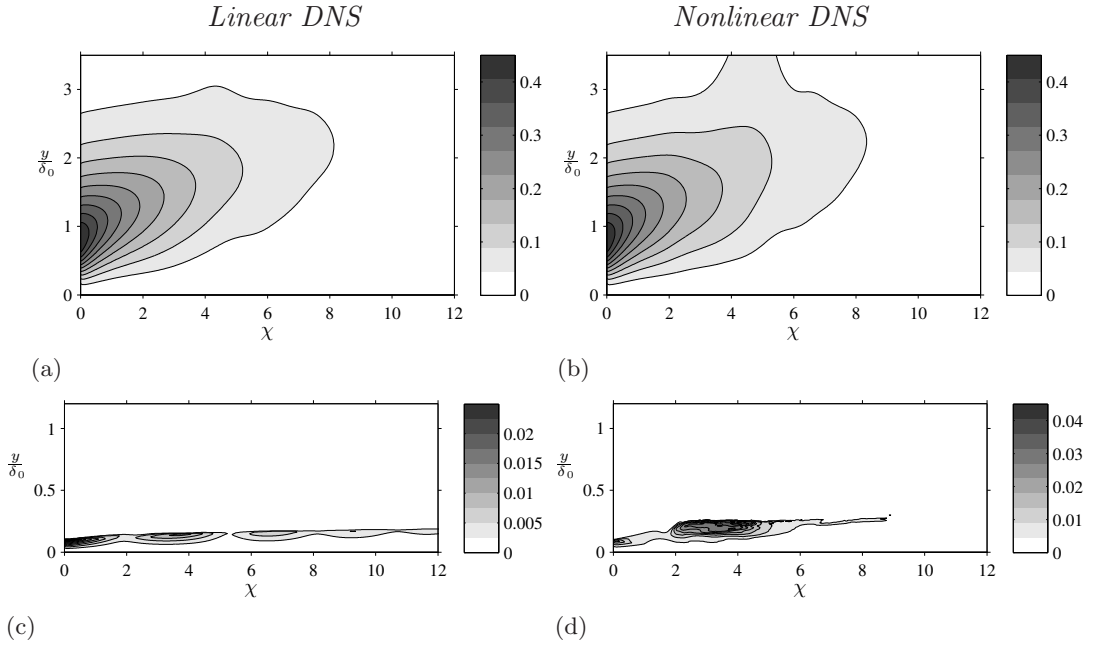


Figure 4.31: Side view of contours of conditional averaged v fluctuation in the top and bottom fluids in linear and non-linear cases. (4.31a): top fluid, linear; (4.31b): top fluid, non linear; (4.31c): bottom fluid, linear; (4.31b): bottom fluid, non linear. $\omega^o = 0.0125$, $\epsilon = \{0.1\%, 0.5\%\}$.

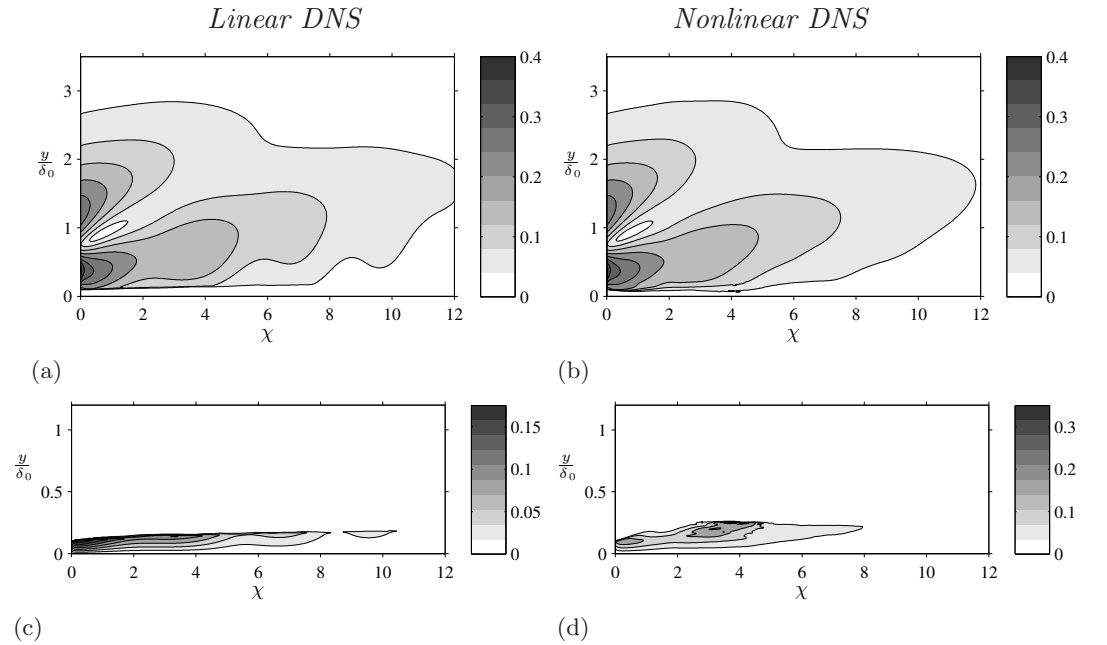


Figure 4.32: Side view of contours of conditional averaged w fluctuation in the top and bottom fluids in linear and non-linear cases. (4.32a): top fluid, linear; (4.32b): top fluid, non linear; (4.32c): bottom fluid, linear; (4.32b): bottom fluid, non linear. $\omega^o = 0.0125$, $\epsilon = \{0.1\%, 0.5\%\}$.

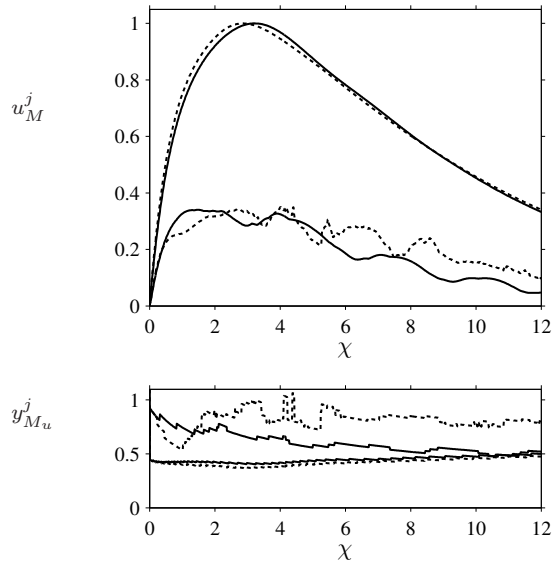
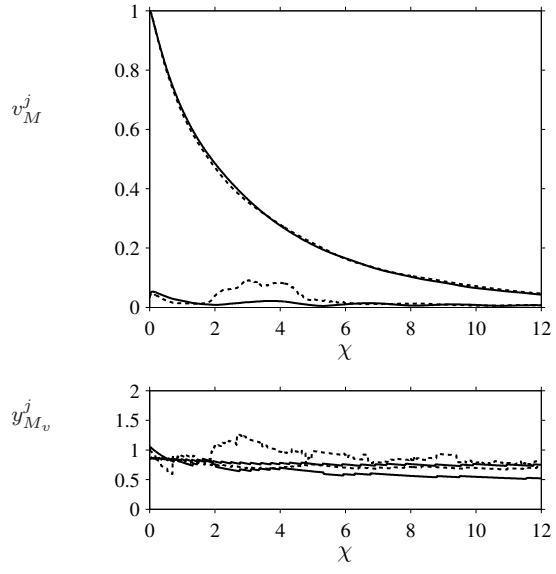


Figure 4.33: Comparison of maximum of conditional averaged u fluctuation, ϵ = 0.1%, 0.5%, $\omega^o = 0.0125$ between linear and nonlinear DNS. ——: linear DNS, – – –: nonlinear DNS



(a)

Figure 4.34: Comparison of maximum of conditional averaged v fluctuation, ϵ = 0.1%, 0.5%, $\omega^o = 0.0125$ between linear and nonlinear DNS. ——: linear DNS, – – –: nonlinear DNS

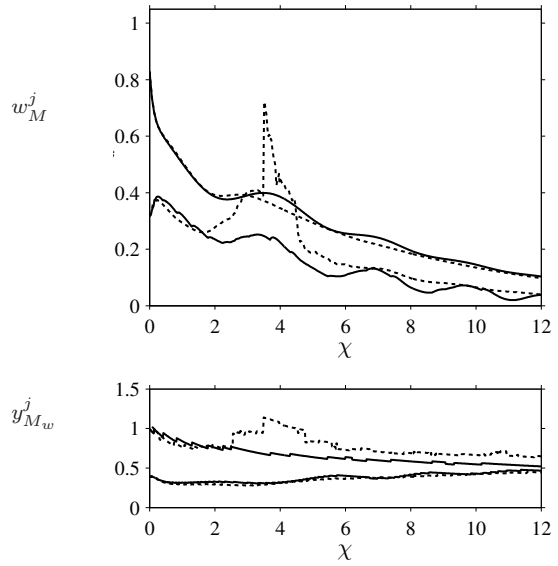


Figure 4.35: Comparison of maximum of conditional averaged w fluctuation, $\epsilon = 0.1\%, 0.5\%$, $\omega^o = 0.0125$ between linear and nonlinear DNS. ——: linear DNS, – – –: nonlinear DNS

its location are significantly affected; in particular, since the bottom fluid is on averaged thicker in the nonlinear case, the quantities $y^B_{M_u}$, $y^B_{M_v}$, $y^B_{M_w}$ are larger than in the linear case. Also, due to the fragmentation of the interface, u^j_M, v^j_M, w^j_M are non-smooth and can exhibit higher maximum values than in the linear cases (particularly evident in figure 4.35). The combined effect of bottom fluid thickening, which leads on average to increased absorption of mean shear, and higher velocities in the bottom fluid, determine lower transient growth (figure 4.23a).

In the next section, a similar analysis is carried out on the suboptimal disturbance.

Nonlinear evolution suboptimal disturbance p^{so}

Consider the nonlinear ($\epsilon = 0.5\%$) evolution of the suboptimal disturbance for the parameter set p^{so}. The comparison with its linear counterparty is presented in this section.

Instantaneous fields Sections of yz-plane at streamwise locations $\chi = \{1.0, 2.7, 5.0\}$ are depicted in figure 4.36, where a comparison to the linear evolution is presented. The vector plots show the normal and spanwise velocity fluctuations (v, w); the streamwise velocity fluctuation, u, is represented by contour lines. Solid and dashed lines mark positive and negative values. The interface location is also shown. Figure 4.36 remarks that the streaks are generated by the lift-up mechanism and that, in the case of low temporal frequency, nonlinearity does not significantly alter the shape of the streaks in the top fluid. However, bottom fluid and the interface undergo sever distortion. The distortion of the interface is shown in figure 4.37, where a close view of the interface and (v, w) velocity field underlines how the interface is stretched and strained by the counterrotating motion in the zy-plane. The streamwise evolution of the inlet suboptimal streamwise vortex forces forward and backward propagating fluctuation streaks, which shear the film, causing the formation of ligament-like structures (figure 4.37c). A streamwise view of u, v, w, f is given in figure 4.38. As v and w decay in the streamwise direction, a streamwise velocity perturbation u is forced to grow, causing strong deformation of the interface. The interface is subject to substantial nonlinear deformation (figure 4.38h) over a lengthscale proportional to U/ω^{so}. Due to the quasi-steadiness motion of the perturbation streaks, the interface doesn't break but evolves into ligament-like structures (figure 4.38h).

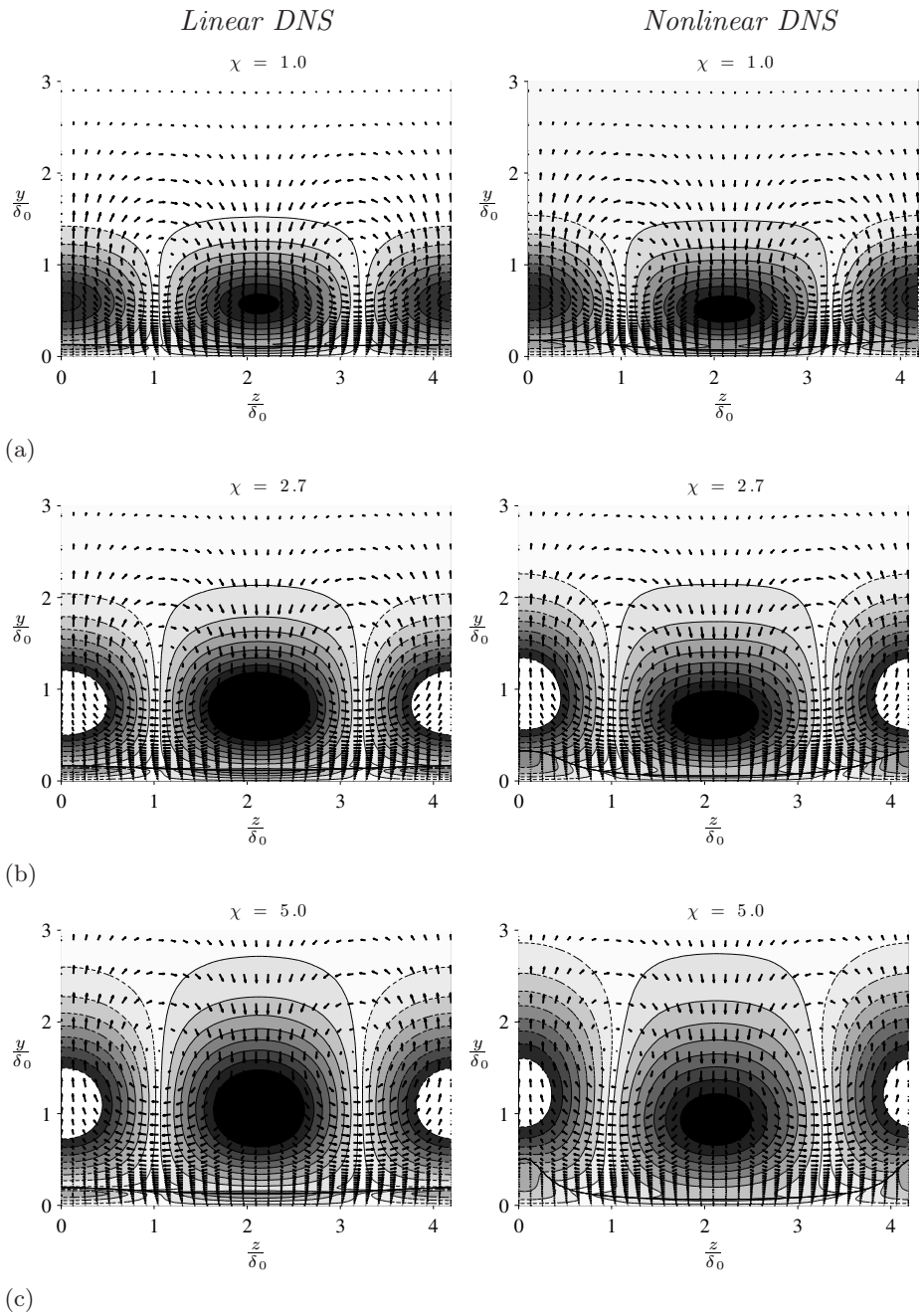


Figure 4.36: End view on zy-plane at location $\chi = \{1.0, 2.7, 5.0\}$, for $\omega^{so} = 0.0010$ and $\epsilon = 0.1\%$ (linear) , 0.5% (non-linear). Solid line delimits the interface; arrows show the vector field (v, w). Contours of streamwise velocity u are also represented.

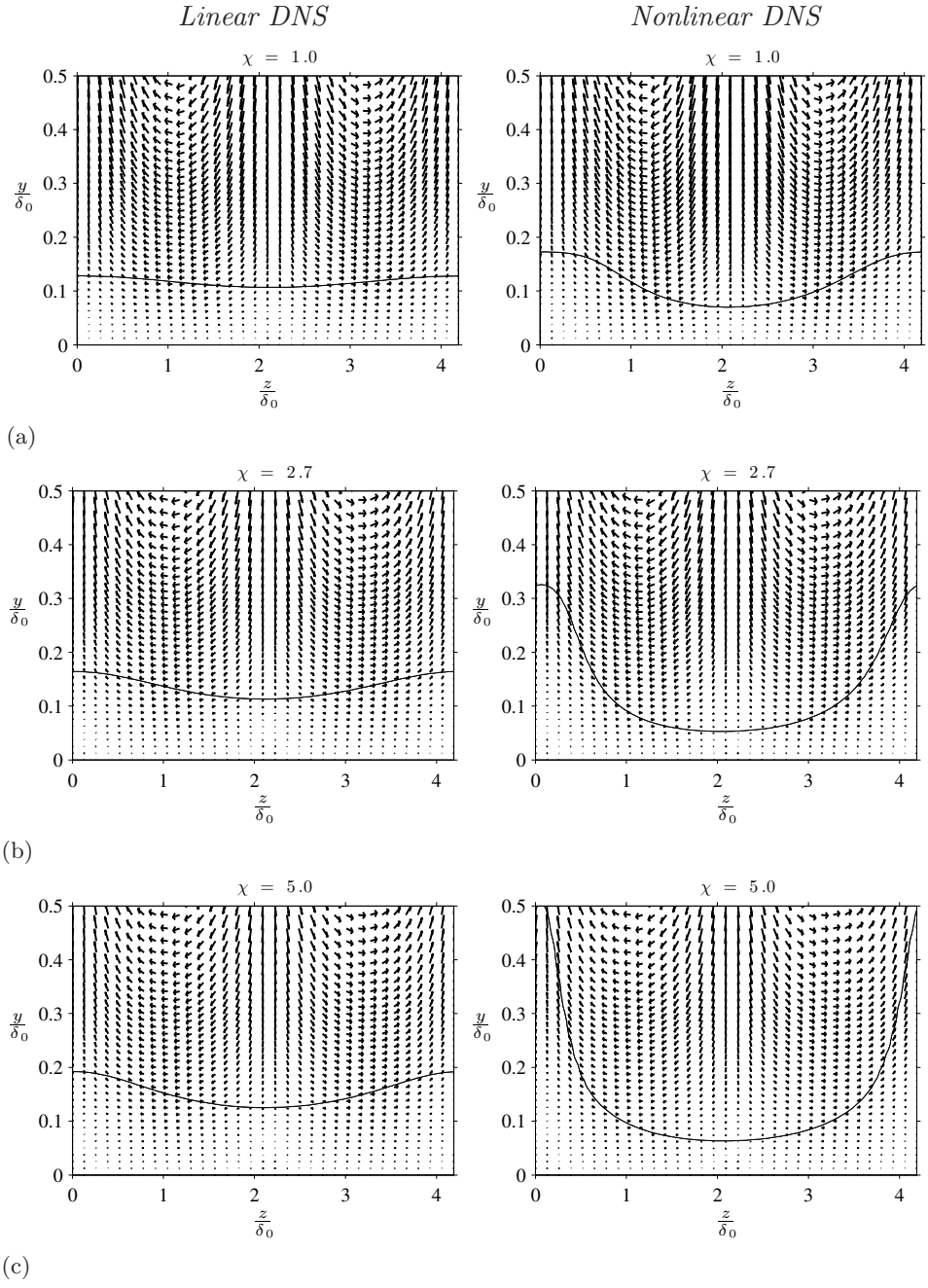


Figure 4.37: End view on zy-plane at location $\chi = \{1.0, 2.7, 5.0\}$, for $\omega^{so} = 0.0010$ and $\epsilon = 0.1\%$ (linear) , 0.5% (non-linear). Solid line delimits the interface.

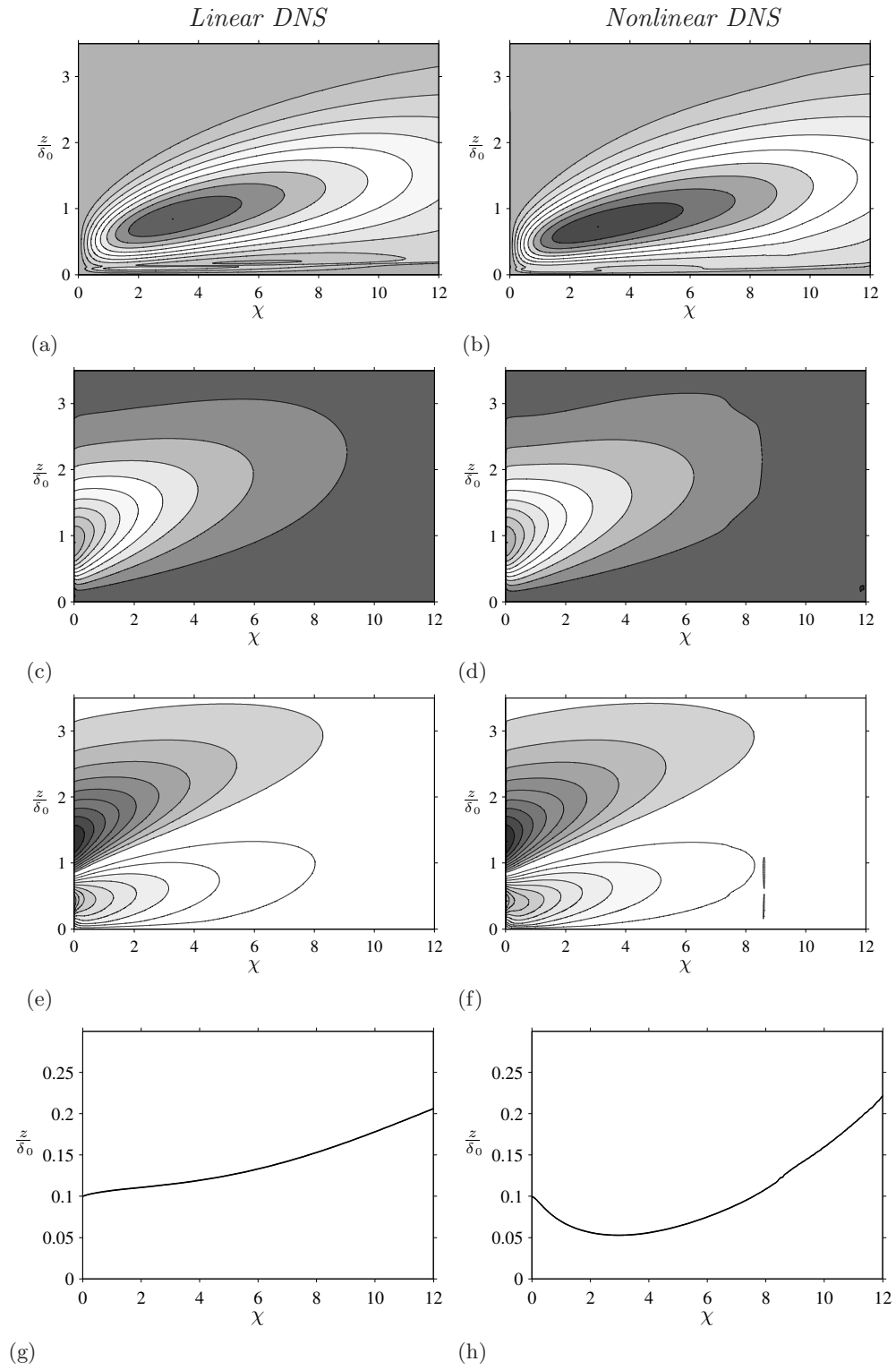


Figure 4.38: Side view of contours of instantaneous u fluctuation in linear (4.38e) and non-linear (4.38f) case. Interface location in linear (4.38g) and non-linear (4.38h) case. $\omega^{so} = 0.0010$, $\epsilon = \{0.1\%, 0.5\%\}$.

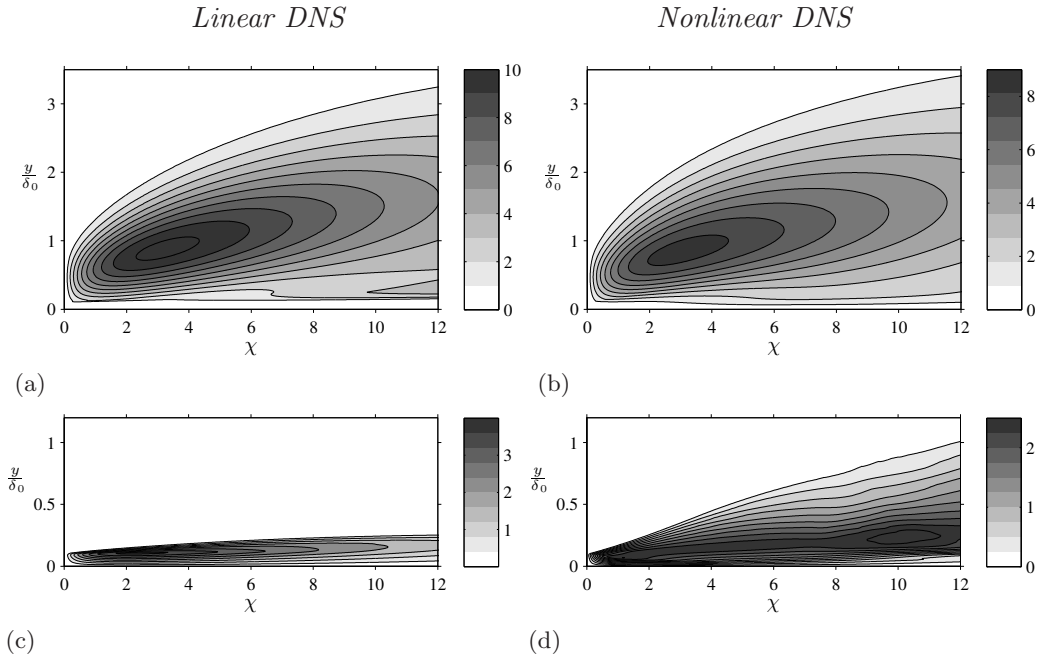


Figure 4.39: Side view of contours of conditional averaged u_{rms} fluctuation in the top and bottom fluids in linear and non-linear cases. (4.39a): top fluid, linear; (4.39b): top fluid, non linear; (4.39c): bottom fluid, linear; (4.39b): bottom fluid, non linear. $\omega^{so} = 0.0010$, $\epsilon = \{0.1\%, 0.5\%\}$.

Averaged data Conditional averaged data provide a good measure of the deformation of the bottom film. In particular, contours of conditional averaged of u_{rms}, v_{rms}, w_{rms} velocity fluctuations are depicted in figure 4.39-4.41 for linear and nonlinear cases. In the linear case, the bottom and top fluid occupy separate and distinct portions of the domain; in the nonlinear case, on average, they overalap over a region of thickness of order of the boundary layer thickenss. This means that the interface heavily oscillates driven by the alternance of quasi-steady positive and negative streaks. The nonlinear case shows a comparable response to the linear case in the streamwise direction in the top (figure 4.39b) and bottom fluids (figure 4.39d). Due to nonlinearity, the bottom film is subject to strong deformation and spanwise and streamwise velocities mainlyin the bottom fluid are also affected (figures 4.40d-4.41d).

In figures 4.42-4.44, the maximum values u_M^j, v_M^j, w_M^j and location of velocity fluctuations $y_{M_u}^j$, $y_{M_v}^j$, $y_{M_w}^j$ are given. The analysis of the values and location of maximum averaged fluctuation velocties highlights that nonlinearity has little effect on the top fluid. In particular, the streamwise evolution of maximum u_{rms}, v_{rms}, w_{rms} fluctuations and their $y-$locations are almost unaffected by nonlinearity in the top fluid; in the bottom fluid, due to the strong deflection of the interface, the value and location of u_M^B, v_M^B,

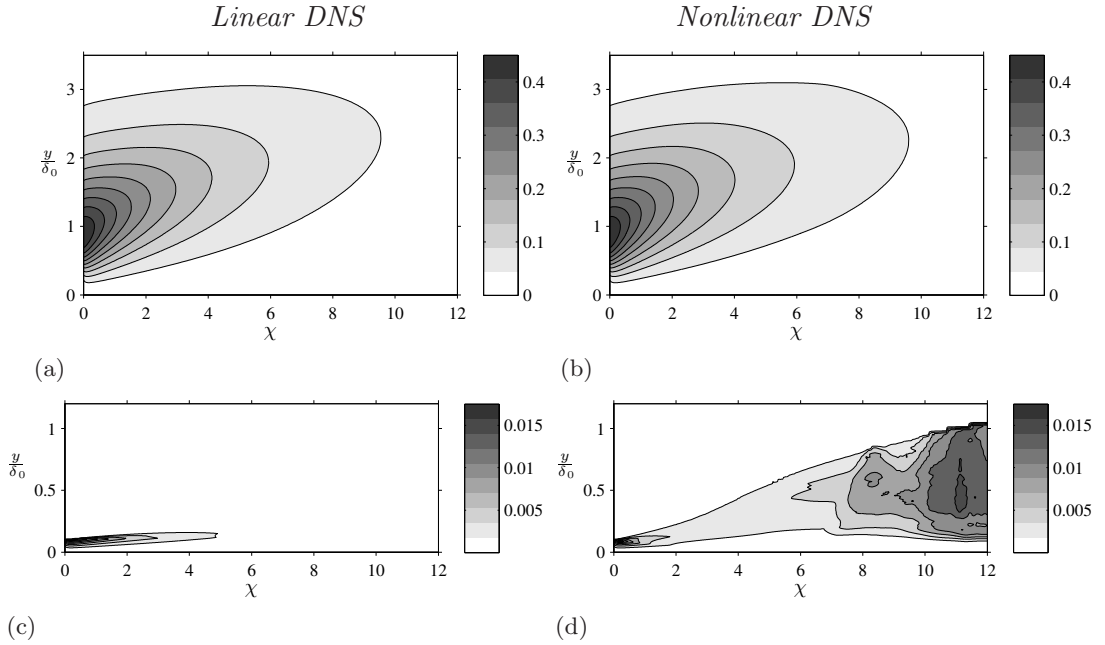


Figure 4.40: Side view of contours of conditional averaged v_{rms} fluctuation in the top and bottom fluids in linear and non-linear cases. (4.40a): top fluid, linear; (4.40b): top fluid, non linear; (4.40c): bottom fluid, linear; (4.40b): bottom fluid, non linear. $\omega^{so} = 0.0010$, $\epsilon = \{0.1\%, 0.5\%\}$.

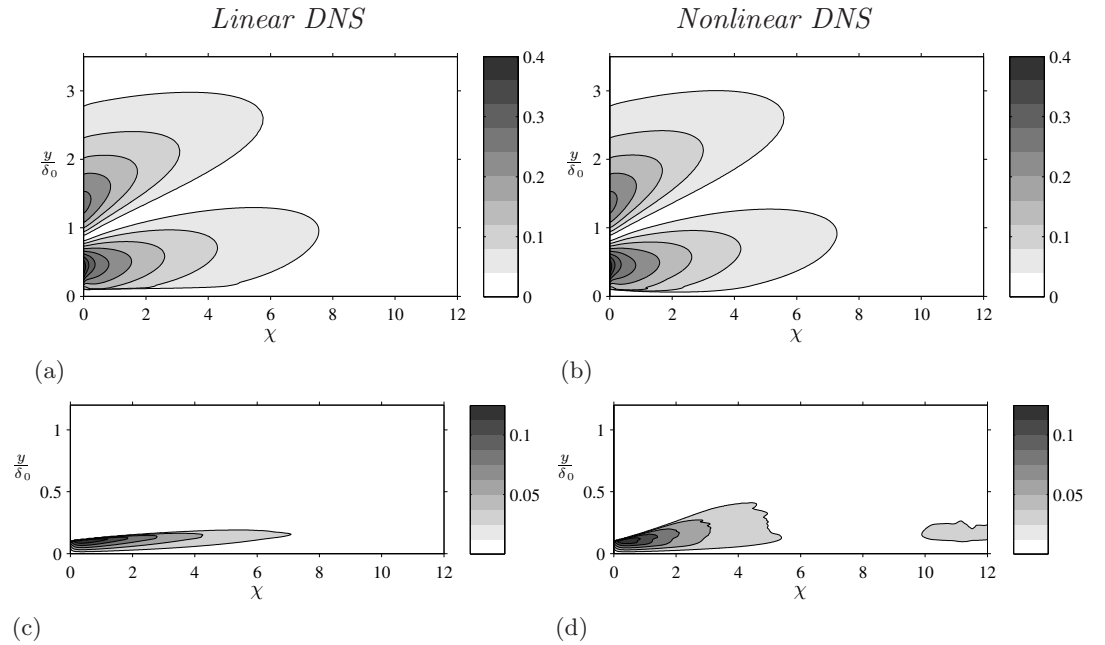


Figure 4.41: Side view of contours of conditional averaged w_{rms} fluctuation in the top and bottom fluids in linear and non-linear cases. (4.41a): top fluid, linear; (4.41b): top fluid, non linear; (4.41c): bottom fluid, linear; (4.41b): bottom fluid, non linear. $\omega^{so} = 0.0010$, $\epsilon = \{0.1\%, 0.5\%\}$.

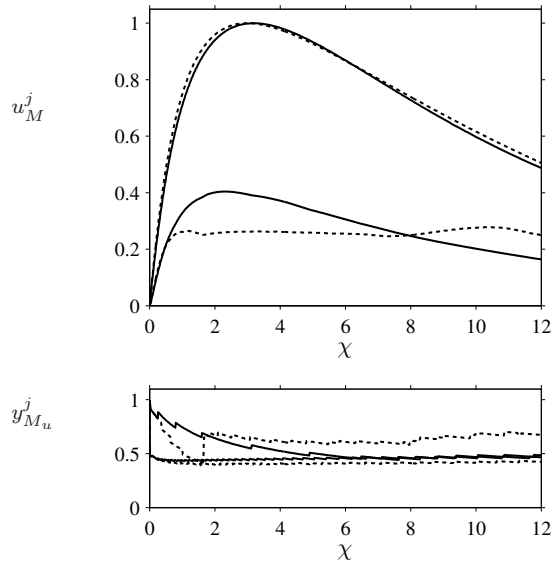


Figure 4.42: Comparison of maximum of conditional averaged u fluctuation, $\omega^{so} = 0.0010$ between linear and nonlinear DNS. ——: linear DNS, - - -: nonlinear DNS

w_M^B can vary substantially with the degree of nonlinearity involved (figures 4.42, 4.43, 4.44). Given the boundary conditions at the bottom wall, the location of the maximum velocity in the bottom fluid naturally happens close to the interface. Hence, since the interface location is distorted by nonlinearity, the quantities $y_{M_u}^B$, $y_{M_v}^B$, $y_{M_w}^B$ are larger than the in the single fluid case.

Observations

In the previous two sections, a comparison between linear and non linear DNS was presented, analysing energy growth, interface deflection, instantaneous and conditional averaged data.

In Chapter 3, it was shown that one effect of mean flow evolution was the relative thinning of the film layer with respect to the boundary layer, due to the different spreading rate of the interface. This resulted in a streamwise decay of the capacity to absorb mean shear by the bottom layer, limiting the beneficial effects of the near-wall, low-viscosity film. In the nonlinear case, this phenomenon is even more evident due to the strong deflection of the interface.

In the case of higher temporal frequency (p^o), the quick alternation of fast and slow moving streaks forces the interface into plume-like structures, which eventually break as

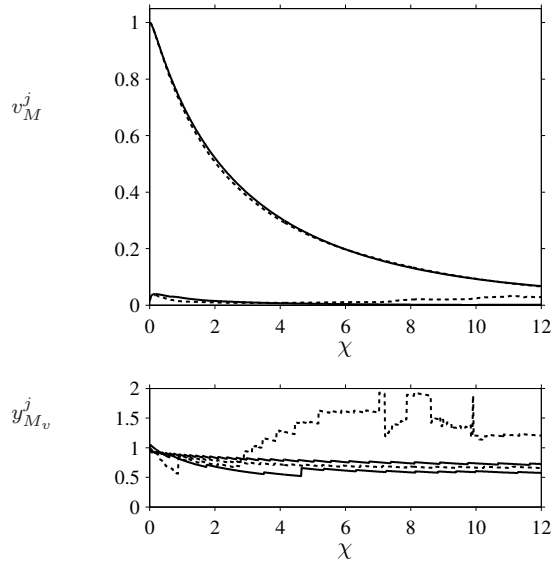


Figure 4.43: Comparison of maximum of conditional averaged v fluctuation, $\omega^{so} = 0.0010$ between linear and nonlinear DNS. ——: linear DNS, - - -: nonlinear DNS

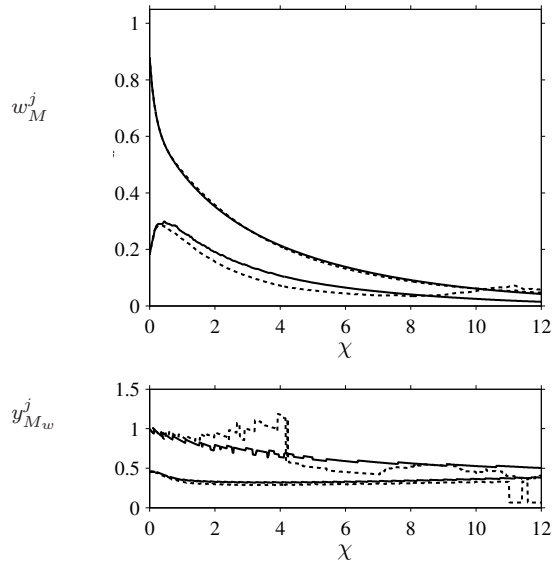


Figure 4.44: Comparison of maximum of conditional averaged w fluctuation, $\omega^{so} = 0.0010$ between linear DNS and nonlinear DNS. ——: linear DNS, - - -: nonlinear DNS

propagating downstream; in the low temporal frequency case (p^{so}), the interface does not undergo rupture but is deflected and strained into ligament-like structures that are carried downstream.

4.5 Conclusions

This chapter has presented the effects of nonlinearity after the early linear stage of the amplification process. Although linear models successfully describe the evolution of infinitesimal disturbances, later stages of amplification involve non-linear effects. Therefore, Direct Numerical Simulations were carried out to investigate the non-linear evolution of optimal disturbances in two-fluid boundary layers.
This chapter had the dual purpose of:

a) comparing and validating PBl and DNS evolution in the linear regime;

b) showing effects of nonlinearity on transient growth and interface deformation.

The linear regime in DNS simulations was determined by increasing the initial amplitude of the inlet disturbance from $\epsilon = 0.01\%$ to $\epsilon = 0.1\%$ and comparing the evolution of the normalized solution field $\mathbf{u}/\epsilon$.
The linear evolution ($\epsilon = 0.1\%$) of optimal disturbances with DNS showed very good agreement with linear, spreading predictions from PBl, both in terms of energy growth and physical features. Thanks to a discountinuous formulation, the description of the interface deflection and evolution in PBl is accurate and smooth; in the DNS, the interface perturbation is retrieved via the inversion of the sign distance equation, resulting in a non-smooth function. Both methods were found to agree on the magnitude and spatial frequency of the interface displacement.

To assess the effects of nonlinearity on the evolution of optimal disturbances, their streamwise evolution in linear ($\epsilon = 0.1\%$) and nonlinear ($\epsilon = 0.5\%$) regimes was compared. The disturbaces for optimal, $p^o : \{\omega^o = 0.0125;\ {k_z}^o = 1.5;\ m^o = 0.55;\ d^o = 0.1\}$, and sub-optimal, $p^{so} : \{\omega^{so} = 0.0010;\ {k_z}^o = 1.5;\ m^o = 0.55;\ d^o = 0.1\}$, set of parameters were used as inlet condition for the spatial DNS investigation. It was found that for initial amplitude equal to $\epsilon = 0.5\%$ non-linear effects become non-negligible and can alter the predictions of linear stability theory. In particular, for high temporal frequencies ($\omega^o = 0.0125$), the interface undergoes large deformation; the combined effect of non linearity and alternation of positive and negative streaks induces the interface into plume-like structures, which eventually break. In the low-omega case ($\omega^{so} = 0.0010$), the quasi-steady motion of streaks, although creating large interface deflection, does not break the film layer but induces the growth of ligament-like structures.

The analysis of conditional averaged data showed the impact of nonlinearity on top and bottom fluid maximum velocities and their evolution in the streamwise direction. The interface deflection was shown to be sensitive to non linearity; as a consequence, the flowfield in the bottom fluid is affected by nonlinearity more than the top fluid. Maximum velocities in the bottom velocities are driven in fact by the interface deflection, whilst the location and magnitude of maximum velocities in the top fluid is almost unaffected by nonlinearity.

Chapter 5

Conclusions

5.1 Summary and key results

Amplification of free-stream disturbances that have penetrated into the boundary layer has an important role in bypass transition. The focus of this work has been to assess the extent to which the amplification mechanism is affected by a wall-film. In order to accurately address this problem, a spatial framework has been adopted, namely:

1. Spatial transient amplification of linear disturbances in *parallel* two-fluid boundary layers.

2. Spatial transient amplification of linear disturbances in *spreading* two-fluid boundary layers.

3. Non-linear evolution of optimal spatially-evolving disturbances.

The following subsections summarise the key results and findings. The last section of this chapter includes a discussion of how the findings of the current work lay the foundation for future investigations.

5.1.1 Transient amplification under locally-parallel assumption

In Chapter 2, the non-modal stability of locally-parallel two-fluid boundary layers was examined. The Orr-Sommerfeld and Squire equations, which govern the linear stability of an infinitesimal disturbance, were solved in order to determine continuous and discrete spectra. This modal information is key to the solution of the optimization problem leading to the determination of parallel optimal disturbances. The solution to the optimal growth problem has revealed the presence of a mechanism of energy production,

which competes against the vorticity tilting mechanism. This amplification mechanism was found to be similar to the one investigate by Saha (2011) in a temporal framework and therefore it was denoted as interface deformation mechanism. The interface deformation mechanism is driven by the jump in mean vorticity across the interface, which introduces normal vorticity perturbations proportional to its displacement and occurs on longer lengthscales than the vortex tilting mechanism. This, instead, is driven by normal velocity, which tilts the mean spanwise vorticity into the wall-normal direction and occurs on a lengthscale corresponding to the viscous decay of the normal velocity component. The optimal conditions associated with these mechanisms are streamwise oriented vortices.

As the viscosity ratio is reduced, the lift-up mechanism weakens, whilst the interfacial energy generation strengthens. The competition between these two vorticity generating mechanisms leads to an optimal viscosity ratio, for which maximum transient growth is achieved, at a given film thickness. A parametric optimization was performed and the optimal viscosity ratio m^o and film thickness d^o that maximise the reduction of transient amplification were determined. The set is: $p^o : \{\omega^o = 0.0125, k_z = 1.5, m^o = 0.55, d^o = 0.1\}$, at $Re = 800$.

5.1.2 Transient amplification and nonparallelism

Chapter 3 was centred on developing a new framework for the study of optimal disturbance and transient amplification in spreading two-fluid boundary layers. The motivation for this chapter was driven by the need to relax the parallel assumption that permeated the Linear Stability Theory, without having to recourse to more complex methods. Under the boundary-layer assumption, the optimization problem leading to the determination of spatially-evolving optimal disturbances and energy growth was formulated and solved. The formulation of the optimal growth problem involved the derivation of the two-fluid spreading adjoint equations of the Navier-Stokes equations, which are new and a powerful tool for optimization and sensitivity analyses.

Due to the spreading of the interface, a mapped computation domain was used, in order to allow for an easy implementation of interfacial boundary conditions and for improved grid resolution near the interface.

The optimal set of parameters determined in the previous chapter and the additional

case with $\omega^{so} = 0.0010$ was considered. An investigation on how nonparallelism affects the amplification mechanisms and optimal disturbances was carried out. It was found that, as the flow spreads, the mean shear weakens and jumps of mean quantities diminish. The former phenomenon results in a weaker lift-up effect due to a reduction in the coupling term between normal velocity and normal vorticity; the latter drastically reduces the effectiveness of the interface deformation mechanism, which becomes unable to produce substantial energy amplification. Note also that the mean interface height spreads proportionally to $\chi^{\frac{1}{4}}$, while the edge of the boundary layers grows as $\chi^{\frac{1}{2}}$. Thus, as the streamwise distance increases, the effects of the lower viscosity film on the boundary layers decrease.

Comparisons of transient growth under parallel and spreading base flow assumptions suggest that results from linear parallel stability can be inaccurate and misleading and that the growth of the mean flow must be taken into account in transient growth computations.

5.1.3 Non-linearity

Chapter 4 had the dual purpose of providing a validation for the spreading two-fluid linear analyses presented in Chapter 3 and extending those findings to the non-linear regime. The DNS of the optimal inlet condition from linear (spatially-evolving) optimization for very low initial amplitude $\epsilon = 0.01\%, 0.1\%$ was considered and very good agreement with the linear prediction of energy growth presented in the previous chapter was shown. The inclusion of non-parallelism in the two-fluid optimal disturbance formulation was therefore an important modelling effort towards a more accurate characterization of the optimal linear amplification mechanism in two-fluid boundary layers. It was also found that, due to its discountinuous formulation, the PBl provides a smooth and continuous description of the interface deflection.

As the initial amplitude of the inlet disturbance is increased, non-linear effects are no longer negligible and cannot be discarded. For $\epsilon = 0.5\%$, the introduction of non-linearity results in larger interface deflection, which strongly affects the flowfield in the bottom fluid.

It was found that the nonlinear effects on the interface vary with its temporal frequency of oscillation. In particular, in the quasi-steady case ($\omega^{so} = 0.0010$), the introduction

of nonlinearity lead to the formation of ligament-like structures; at higher frequency, $\omega^{so} = 0.0125$, the interface is induced into plume-like structures, which eventually break. These structures drive the location and magnitude of the maximum averaged velocities in the bottom fluid; nonlinear DNS simulations of quasi-steady optimal disturbances on much longer domains would be required to investigate their potential evolution into ligaments.

5.2 Future work

The main conclusions of this thesis indicate that the transient amplification of energy is reduced significantly by the introduction of lower viscosity wall-film under parallel base flow assumptions. A similar boundary layer profile to the one investigated in this work can be determined by wall heating, which lowers the viscosity near the wall; passive control techniques, such as wall heating/cooling, can delay transition by stabilization of the boundary layer (Lauchle & Gurney, 1984). However, an accurate description of the optimal transient energy evolution in two-fluid boundary layers must account for mean flow non-parallelism. Optimal growth studies carried out on a spatially-evolving base flow showed that the stabilising effects of the wall layer quickly decrease with streamwise distance from the leading edge.

The mathematical framework on two-phase adjoint equations for spatially-evolving flows can be extended to include (weakly) nonlinearity. In particular, under the assumption that the interface is a function on the chosen domain (i.e. no change of topology takes place), one can incorporate nonlinear terms in the forward equation and solve for (weakly) nonlinear optimal disturbances. A similar result can be obtained by performing direct optimization on the (nonlinear) Navier-Stokes equations (Monokrousos, 2011); the extention of two-fluid flows, however, might be possible only under restricitve condition on the interface deflection.

The formulation of the two-phase spatially-evolving adjoint Navier-Stokes equations can be used to investigate receptivity in two-fluid boundary layers and to design optimal control algorithms that minimize the transient energy response. On the contrary, the same framework could be successfully applied to determine optimal disturbances that facilitate the atomization of the wall layer.

Appendix A

Two-fluid adjoint perturbation equations

This appendix presents the derivation on the two-fluid adjoint equations for spatially-developing flows.

The adjoint system can be derived by imposing the relation in (3.42) and choosing appropriate adjoint boundary conditions such that the internal product in (3.36) is identically satisfied on $\mathcal{H}(\Omega \cup \partial\Omega)$.

Introduce $\psi = \left[\mathbf{q}^\dagger, f^\dagger\right]^\mathsf{T}$ and $\phi = [\mathbf{q}, f]^\mathsf{T}$ vectors with $\mathbf{q}^\dagger = \left[u^\dagger, v^\dagger, w^\dagger, p^\dagger\right]^\mathsf{T}$, $\mathbf{q} = [u, v, w, p]^\mathsf{T}$ and consider the adjoint relation:

$$\left\langle \psi, \mathbf{S}\phi \right\rangle = \left\langle \mathbf{S}^\dagger \psi, \phi \right\rangle \tag{A.1}$$

that is

$$\left\langle \begin{bmatrix} \mathbf{q}^\dagger \\ f^\dagger \end{bmatrix}, \begin{bmatrix} \mathcal{L} & 0 \\ \mathcal{C} & \mathcal{I} \end{bmatrix} \begin{bmatrix} \mathbf{q} \\ f \end{bmatrix} \right\rangle = \left\langle \begin{bmatrix} \mathcal{L}^\dagger & 0 \\ \mathcal{C}^\dagger & \mathcal{I}^\dagger \end{bmatrix} \begin{bmatrix} \mathbf{q}^\dagger \\ f^\dagger \end{bmatrix}, \begin{bmatrix} \mathbf{q} \\ f \end{bmatrix} \right\rangle \tag{A.2}$$

where $\mathcal{L}$ denotes the boundary layer operator, $\mathcal{C}$ the coupling operator between $\mathbf{q}$ and f, and $\mathcal{I}$ the interfacial operator, respectively defined in equations 3.22 and 3.24.

$$\left\langle \begin{bmatrix} \mathbf{q}^\dagger \\ f^\dagger \end{bmatrix}, \begin{bmatrix} \mathcal{L} & 0 \\ \mathcal{C} & \mathcal{I} \end{bmatrix} \begin{bmatrix} \mathbf{q} \\ f \end{bmatrix} \right\rangle = \int_\Omega {\mathbf{q}^\dagger}^H \mathcal{L}\mathbf{q} \, d\Omega + \int_{\Omega_x} {f^\dagger}^H \left(\mathcal{C}\mathbf{q} + \mathcal{I}f\right) \, dx \tag{A.3}$$

$$\left\langle \begin{bmatrix} \mathcal{L}^\dagger & 0 \\ \mathcal{C}^\dagger & \mathcal{I}^\dagger \end{bmatrix} \begin{bmatrix} \mathbf{q}^\dagger \\ f^\dagger \end{bmatrix}, \begin{bmatrix} \mathbf{q} \\ f \end{bmatrix} \right\rangle = \int_\Omega \left(\mathcal{L}^\dagger \mathbf{q}^\dagger\right)^H \mathbf{q} \, d\Omega + \int_{\Omega_x} \left(\mathcal{C}^\dagger \mathbf{q}^\dagger + \mathcal{I}^\dagger f^\dagger\right)^H f \, dx \tag{A.4}$$

Note the interface displacement f is a distribution at the interface: $f := f\delta\left(y-d\right)$.
The aim is to find the operators $\mathcal{L}^\dagger,\ \mathcal{C}^\dagger,\ \mathcal{I}^\dagger$ such that the relation:

$$\int_\Omega {\mathbf{q}^\dagger}^H \mathcal{L}\mathbf{q}\ d\Omega + \int_{\Omega_x} {f^\dagger}^H \left(\mathcal{C}\mathbf{q}+\mathcal{I}f\right)\ dx = \int_\Omega \left(\mathcal{L}^\dagger\mathbf{q}^\dagger\right)^H \mathbf{q}\ d\Omega + \int_{\Omega_x} \left(\mathcal{C}^\dagger\mathbf{q}^\dagger + \mathcal{I}^\dagger f^\dagger\right)^H f\ dx \tag{A.5}$$

is satisfied $\forall\ \mathbf{q},\mathbf{q}^\dagger,f,f^\dagger \in \mathcal{H}(\Omega)$.
The derivation proceeds by explicitly computing the integral on the left hand side of (A.5) and finding interfacial and wall boundary conditions such that right hand side satisfies the equation.
Before explicitly computing the integral on the left hand side of (A.5), the adjoint derivation of a general viscous term is presented:

$$\begin{aligned}
&\int_\Omega -u_i'^* \mu \frac{\partial^2 u_i}{\partial x_j \partial x_j}\ d\Omega = \int_\Omega -u_i'^* \mu \frac{\partial}{\partial x_j}\left(\frac{\partial u_i}{\partial x_j}\right)\ d\Omega = \int_\Omega -u_i'^* \mu \frac{\partial}{\partial x_j}\left(\frac{\partial u_i}{\partial x_j}+\frac{\partial u_j}{\partial x_i}\right)\ d\Omega \\
&= \int_\Omega \frac{\partial}{\partial x_j}\left(-\mu u_i'^* \left(\frac{\partial u_i}{\partial x_j}+\frac{\partial u_j}{\partial x_i}\right)\right)\ d\Omega - \int_\Omega -\mu \frac{\partial u_i'^*}{\partial x_j}\left(\frac{\partial u_i}{\partial x_j}+\frac{\partial u_j}{\partial x_i}\right)\ d\Omega = \\
&= \int_\Gamma -\mu u_i'^* \left(\frac{\partial u_i}{\partial x_j}+\frac{\partial u_j}{\partial x_i}\right)\hat{n}_j\ d\Gamma + \int_\Omega \mu \frac{\partial u_i'^*}{\partial x_j}\frac{\partial u_i}{\partial x_j}\ d\Omega + \int_\Omega \mu \frac{\partial u_i'^*}{\partial x_j}\frac{\partial u_j}{\partial x_i}\ d\Omega = \\
&= \int_\Gamma -\mu u_i'^* \left(\frac{\partial u_i}{\partial x_j}+\frac{\partial u_j}{\partial x_i}\right)\hat{n}_j\ d\Gamma + \int_\Omega \frac{\partial}{\partial x_j}\left(\mu \frac{\partial u_i'^*}{\partial x_j}u_i\right)\ d\Omega - \int_\Omega \mu \frac{\partial^2 u_i'^*}{\partial x_j \partial x_j}u_i\ d\Omega \\
&+ \int_\Omega \frac{\partial}{\partial x_i}\left(\mu \frac{\partial u_i'^*}{\partial x_j}u_j\right)\ d\Omega - \int_\Omega \mu \frac{\partial^2 u_i'^*}{\partial x_j \partial x_i}u_j\ d\Omega = \\
&= \int_\Gamma -\mu u_i'^* \left(\frac{\partial u_i}{\partial x_j}+\frac{\partial u_j}{\partial x_i}\right)\hat{n}_j + \mu \frac{\partial u_i'^*}{\partial x_j}u_i\hat{n}_j + \mu \frac{\partial u_i'^*}{\partial x_j}u_j\hat{n}_i\ d\Gamma - \int_\Omega \mu\left(\frac{\partial^2 u_i'^*}{\partial x_j \partial x_j}u_i\right)\ d\Omega
\end{aligned} \tag{A.6}$$

Γ being the boundary set of Ω, i.e. $\Gamma = \partial\Omega$.
In the particular case of boundary layer approximation, the term $\frac{\partial}{\partial x^2}$ is dropped; hence, the corresponding adjoint term does not appear and the relation A.6 equates to zero. However, first order terms can be retained to facilitate the dermination of the adjoint stress interfacial conditions.

So, from (A.5):

$$
\begin{aligned}
&\int_\Omega {\mathbf{q}^\dagger}^H \mathcal{L}\mathbf{q}\; d\Omega = \qquad\qquad (A.7)\\
&\int_{x_0}^{x_f}\int_d^{+\infty} {\mathbf{q}_T^\dagger}^H \left[\mathbf{A}_T\frac{\partial}{\partial x}\mathbf{q}_T - \mathbf{B_0}_T\mathbf{q}_T - \mathbf{B_1}_T\frac{\partial}{\partial y}\mathbf{q}_T - \mathbf{B_2}_T\frac{\partial}{\partial y^2}\mathbf{q}_T\right]\; dy\\
&+\int_0^d {\mathbf{q}_B^\dagger}^H \left[\mathbf{A}_B\frac{\partial}{\partial x}\mathbf{q}_B - \mathbf{B_0}_B\mathbf{q}_B - \mathbf{B_1}_B\frac{\partial}{\partial y}\mathbf{q}_B - \mathbf{B_2}_B\frac{\partial}{\partial y^2}\mathbf{q}_B\right]\; dy\; dx =\\
&\int_{x_0}^{x_f}\int_d^{+\infty} \mathbf{q}_T \left[-\mathbf{A}_T^H\frac{\partial}{\partial x}{\mathbf{q}_T^\dagger}^H - {\mathbf{B_0}_T}^H{\mathbf{q}_T^\dagger}^H + \frac{\partial}{\partial y}\left(\mathbf{B_1}_T^H{\mathbf{q}_T^\dagger}^H\right) - {\mathbf{B_2}_T}^H\frac{\partial}{\partial y^2}{\mathbf{q}_T^\dagger}^H\right]\; dy\\
&+\int_0^d \mathbf{q}_B \left[-\mathbf{A}_B^H\frac{\partial}{\partial x}{\mathbf{q}_B^\dagger}^H - \mathbf{B_0}_B^H{\mathbf{q}_B^\dagger}^H + \frac{\partial}{\partial y}\left(\mathbf{B_1}_B^H{\mathbf{q}_B^\dagger}^H\right) - \mathbf{B_2}_B^H\frac{\partial}{\partial y^2}{\mathbf{q}_B^\dagger}^H\right]\; dy\; dx\\
&\underbrace{+\int_d^{+\infty} {\mathbf{q}_T^\dagger}^H\mathbf{A}_T^H\mathbf{q}_T\Big|_{x_0}^{x_f}\; dy + \int_0^d {\mathbf{q}_B^\dagger}^H\mathbf{A}_B^H\mathbf{q}_B\Big|_{x_0}^{x_f}\; dy}_{BC_x}\\
&-\int_{x_0}^{x_f} \mathbf{q}_T^H\mathbf{B_1}_T^H\mathbf{q}_T^\dagger\Big|_d^{+\infty} - \mathbf{q}_B^H\mathbf{B_1}_B^H\mathbf{q}_B^\dagger\Big|_0^d\\
&+\frac{\partial}{\partial y}\mathbf{q}_T^H\mathbf{B_2}_T^H\mathbf{q}_T^\dagger\Big|_d^{+\infty} + \frac{\partial}{\partial y}\mathbf{q}_B^H\mathbf{B_2}_B^H\mathbf{q}_B^\dagger\Big|_0^d - \mathbf{q}_T^H\mathbf{B_2}_T^H\frac{\partial}{\partial y}\mathbf{q}_T^\dagger\Big|_d^{+\infty} - \mathbf{q}_B^H\mathbf{B_2}_B^H\frac{\partial}{\partial y}\mathbf{q}_B^\dagger\Big|_0^d\\
&+\frac{\partial}{\partial x}\mathbf{q}_T^H\mathbf{B_2}_T^H\mathbf{q}_T^\dagger\Big|_d^{+\infty} + \frac{\partial}{\partial x}\mathbf{q}_B^H\mathbf{B_2}_B^H\mathbf{q}_B^\dagger\Big|_0^d - \mathbf{q}_T^H\mathbf{B_2}_T^H\frac{\partial}{\partial x}\mathbf{q}_T^\dagger\Big|_d^{+\infty} - \mathbf{q}_B^H\mathbf{B_2}_B^H\frac{\partial}{\partial x}\mathbf{q}_B^\dagger\Big|_0^d\\
&\underbrace{+\frac{\partial}{\partial z}\mathbf{q}_T^H\mathbf{B_2}_T^H\mathbf{q}_T^\dagger\Big|_d^{+\infty} + \frac{\partial}{\partial z}\mathbf{q}_B^H\mathbf{B_2}_B^H\mathbf{q}_B^\dagger\Big|_0^d - \mathbf{q}_T^H\mathbf{B_2}_T^H\frac{\partial}{\partial z}\mathbf{q}_T^\dagger\Big|_d^{+\infty} - \mathbf{q}_B^H\mathbf{B_2}_B^H\frac{\partial}{\partial z}\mathbf{q}_B^\dagger\Big|_0^d\; dx}_{BC_y}
\end{aligned}
$$

that is

$$\int_\Omega {\mathbf{q}^\dagger}^H \mathcal{L}\mathbf{q}\; d\Omega = \int_\Omega \left(\mathcal{L}^\dagger\mathbf{q}^\dagger\right)^H \mathbf{q}\; d\Omega + \int_{\Omega_y} BC_x^H\; dy + \int_{\Omega_x} BC_y^H\; dx \qquad (A.8)$$

If it is shown that:

$$\int_{\Omega_y} BC_x\; dy + \int_{\Omega_x} BC_y\; dx = \int_{\Omega_x}\left(\mathcal{C}^\dagger\mathbf{q}^\dagger + \mathcal{I}^\dagger f^\dagger\right)^H f\; dx - \int_{\Omega_x} {f^\dagger}^H\left(\mathcal{C}\mathbf{q} + \mathcal{I}f\right)\; dx \quad (A.9)$$

then it is proved that $\mathcal{L}^\dagger$, $\mathcal{C}^\dagger$, $\mathcal{I}^\dagger$ satisfy the adjoint definition in (A.1).

Consider BC_y term and denote with $[\![a]\!]$ the difference of a quantity $a(y)$ through the

interface, i.e. $[\![a]\!] = a_T(y=d) - a_B(y=d)$:

$$\int_{\Omega_x} BC_y \, dx = -\int_{x_0}^{x_f} \left[-u_B^H V u_B^\dagger - 2v_B^H V v_B^\dagger - w_B^H V w_B^\dagger - v_B^H p_B^\dagger - p_B^H v_B^\dagger\right]_0^d \tag{A.10}$$
$$+ \left[-u_T^H V u_T^\dagger - 2v_T^H V v_T^\dagger - w_T^H V w_T^\dagger - v_T^H p_T^\dagger - p_T^H v_T^\dagger\right]_d^{+\infty}$$
$$+ \left[\mu_B \frac{\partial u_B^H}{\partial y} u_B^\dagger + \mu_B \frac{\partial v_B^H}{\partial y} v_B^\dagger + \mu_B \frac{\partial w_B^H}{\partial y} w_B^\dagger\right]_0^d + \left[\mu_T \frac{\partial u_T^H}{\partial y} u_T^\dagger + \mu_T \frac{\partial v_T^H}{\partial y} v_T^\dagger + \mu_T \frac{\partial w_T^H}{\partial y} w_T^\dagger\right]_d^{+\infty}$$
$$- \left[\mu_B u_B^H \frac{\partial u_B^\dagger}{\partial y} + \mu_B v_B^H \frac{\partial v_B^\dagger}{\partial y} + \mu_B w_B^H \frac{\partial w_B^\dagger}{\partial y}\right]_0^d - \left[\mu_T u_T^H \frac{\partial u_T^\dagger}{\partial y} + \mu_T v_T^H \frac{\partial v_T^\dagger}{\partial y} + \mu_T w_T^H \frac{\partial w_T^\dagger}{\partial y}\right]_d^{+\infty}$$
$$+ \left[\mu_B \frac{\partial v_B^H}{\partial x} u_B^\dagger + \mu_B \frac{\partial v_B^H}{\partial y} v_B^\dagger + \mu_B \frac{\partial v_B^H}{\partial z} w_B^\dagger\right]_0^d + \left[\mu_T \frac{\partial v_T^H}{\partial x} u_T^\dagger + \mu_T \frac{\partial v_T^H}{\partial y} v_T^\dagger + \mu_T \frac{\partial v_T^H}{\partial y} w_T^\dagger\right]_d^{+\infty}$$
$$- \left[\mu_B u_B^H \frac{\partial v_B^\dagger}{\partial x} + \mu_B v_B^H \frac{\partial v_B^\dagger}{\partial y} + \mu_B w_B^H \frac{\partial v_B^\dagger}{\partial z}\right]_0^d - \left[\mu_T u_T^H \frac{\partial v_T^\dagger}{\partial x} + \mu_T v_T^H \frac{\partial v_T^\dagger}{\partial y} + \mu_T w_T^H \frac{\partial v_T^\dagger}{\partial z}\right]_d^{+\infty} \; dx$$
$$= -\int_{x_0}^{x_f} -p_B^H v_B^\dagger\Big|_0 - v_T^H p_T^\dagger\Big|_{+\infty} + \left[\!\!\left[u^H V u^\dagger + v^H p^\dagger + 2v^H V v^\dagger + w^H V w^\dagger + p^H v^\dagger\right]\!\!\right] - 2\, v_T^H V v_T^\dagger\Big|_{+\infty}$$
$$+ \left(\mu_B \frac{\partial u_B^H}{\partial y} u_B^\dagger + \mu_B \frac{\partial v_B^H}{\partial y} v_B^\dagger + \mu_B \frac{\partial w_B^H}{\partial y} w_B^\dagger\right)\Big|_0 + \left(\mu_T \frac{\partial u_T^H}{\partial y} u_T^\dagger + \mu_T \frac{\partial v_T^H}{\partial y} v_T^\dagger + \mu_T \frac{\partial w_T^H}{\partial y} w_T^\dagger\right)\Big|_{+\infty}$$
$$- \mu_T v_T^H \frac{\partial v_T^\dagger}{\partial y}\Big|_{+\infty} - \left[\!\!\left[\mu \frac{\partial u^H}{\partial y} u^\dagger + \mu \frac{\partial v^H}{\partial y} v^\dagger + \mu \frac{\partial w^H}{\partial y} w^\dagger\right]\!\!\right] + [\![\mu u^H \frac{\partial u^\dagger}{\partial y} + \mu v^H \frac{\partial v^\dagger}{\partial y} + \mu w^H \frac{\partial w^\dagger}{\partial y}]\!]$$
$$+ \left(\mu_B \frac{\partial v_B^H}{\partial x} u_B^\dagger + \mu_B \frac{\partial v_B^H}{\partial y} v_B^\dagger + \mu_B \frac{\partial v_B^H}{\partial z} w_B^\dagger\right)\Big|_0 + \left(\mu_T \frac{\partial v_T^H}{\partial x} u_T^\dagger + \mu_T \frac{\partial v_T^H}{\partial y} v_T^\dagger + \mu_T \frac{\partial v_T^H}{\partial z} w_T^\dagger\right)\Big|_{+\infty}$$
$$- \left(\mu_B u_B^H \frac{\partial v_B^\dagger}{\partial x} + \mu_B v_B^H \frac{\partial v_B^\dagger}{\partial y} + \mu_B w_B^H \frac{\partial v_B^\dagger}{\partial z}\right)\Big|_0 + \left(\mu_T u_T^H \frac{\partial v_T^\dagger}{\partial x} + \mu_T v_T^H \frac{\partial v_T^\dagger}{\partial y} + \mu_T w_T^H \frac{\partial v_T^\dagger}{\partial z}\right)\Big|_{+\infty}$$
$$+ \left[\!\!\left[\mu u^H \frac{\partial v^\dagger}{\partial x} + \mu v^H \frac{\partial v^\dagger}{\partial y} + \mu w^H \frac{\partial v^\dagger}{\partial z}\right]\!\!\right] - \left[\!\!\left[\mu \frac{\partial v^H}{\partial x} u^\dagger + \mu \frac{\partial v^H}{\partial y} v^\dagger + \mu \frac{\partial v^H}{\partial z} w^\dagger\right]\!\!\right] \; dx$$

Applying the forward boundary conditions at wall and free stream:

$$u(0) = 0 \; ; \quad v(0) = 0 \; ; \quad w(0) = 0 \; . \tag{A.11}$$

$$u(+\infty) = 0 \; ; \quad w(+\infty) = 0 \; ; \quad p(+\infty) = 0 \; . \tag{A.12}$$

leads to a choice[1] of wall and free-stream adjoint boundary conditions as the following:

$$u_B^\dagger(0) = 0 \; ; \qquad v_B^\dagger(0) = 0 \; ; \qquad w_B^\dagger(0) = 0 \; . \tag{A.13}$$

$$p_T^\dagger(+\infty) + 2Vv_T^\dagger(+\infty) + \mu_T \frac{\partial v^\dagger}{\partial y}(+\infty) = 0 \; ; \quad u_T^\dagger(+\infty) = 0 \; ; \quad w_T^\dagger(+\infty) = 0 \; . \tag{A.14}$$

Interfacial adjoint boundary conditions on the adjoint velocities can be fixed to:

$$\left[\!\left[u^\dagger\right]\!\right] = 0 \; ; \qquad \left[\!\left[v^\dagger\right]\!\right] = 0 \; ; \qquad \left[\!\left[w^\dagger\right]\!\right] = 0 \; . \tag{A.15}$$

leaving BC_y to be:

$$\int_{\Omega_x} BC_y \, dx = \int_{x_0}^{x_f} - \left[\!\left[v^H p^\dagger + \mu u^H \left(\frac{\partial u^\dagger}{\partial y} + \frac{\partial v^\dagger}{\partial x} \right) + \mu v^H \left(\frac{\partial v^\dagger}{\partial y} + \frac{\partial v^\dagger}{\partial y} \right) + \mu w^H \left(\frac{\partial w^\dagger}{\partial y} + \frac{\partial v^\dagger}{\partial z} \right) \right]\!\right] \tag{A.16}$$

$$- \left[\!\left[-p^H v^\dagger + \mu \left(\frac{\partial u^H}{\partial y} + \frac{\partial v^H}{\partial x} \right) u^\dagger + \mu \left(\frac{\partial v^H}{\partial y} + \frac{\partial v^H}{\partial y} \right) v^\dagger + \mu \left(\frac{\partial w^H}{\partial y} + \frac{\partial v^H}{\partial z} \right) w^\dagger \right]\!\right] \, dx$$

$$= \int_{x_0}^{x_f} BC_y^A + BC_y^F \, dx \; .$$

At this point, impose the forward velocity and stress boundary conditions (3.28)-(3.33) at the linearized interface location.

Analysis of BC_y^A term

$$BC_y^A = - \left[\!\left[v^H \mu \left(p^\dagger + 2\mu \frac{\partial v^\dagger}{\partial y} \right) \right]\!\right] - \left[\!\left[u^H \mu \left(\frac{\partial u^\dagger}{\partial y} + \frac{\partial v^\dagger}{\partial x} \right) \right]\!\right] - \left[\!\left[w^H \mu \left(\frac{\partial w^\dagger}{\partial y} + \frac{\partial v^\dagger}{\partial z} \right) \right]\!\right] \tag{A.17}$$

Note that in general, for any $A, \; B \in \Omega$

$$[\![(A,B)]\!] = A_T B_T - A_B B_B = A_T [\![B]\!] + B_B [\![A]\!] = A_B [\![B]\!] + B_T [\![A]\!] \tag{A.18}$$

[1] The choice of adjoint boundary condition is somehow arbitrary. However, some conditions on adjoint velocities result in forward/adjoint coupled boundary conditions

Therefore, with use of (A.15)

$$BC_y^A = -w_T^H \left[\!\!\left[\mu \left(\frac{\partial w^\dagger}{\partial y} + \frac{\partial v^\dagger}{\partial z} \right) \right]\!\!\right] - u_T^H \left[\!\!\left[\mu \left(\frac{\partial u^\dagger}{\partial y} + \frac{\partial v^\dagger}{\partial x} \right) \right]\!\!\right] \tag{A.19}$$
$$- \mu_B \left(\frac{\partial u^\dagger}{\partial y} + \frac{\partial v^\dagger}{\partial x} \right) [\![u^H]\!] - v_T^H \left[\!\!\left[\left(p^\dagger + 2\mu \frac{\partial v^\dagger}{\partial y} \right) \right]\!\!\right] - \left(p_B^\dagger + 2\mu_B \frac{\partial v_B^\dagger}{\partial y} \right) [\![v^H]\!] .$$

Imposing the conditions (3.28)-(3.30) leads to the following choice of adjoint stress boundary conditions:

$$\left[\!\!\left[\mu \left(\frac{\partial u^\dagger}{\partial y} + \frac{\partial v^\dagger}{\partial x} \right) \right]\!\!\right] = 0 \ ; \tag{A.20}$$
$$\left[\!\!\left[\mu \left(\frac{\partial w^\dagger}{\partial y} + \frac{\partial v^\dagger}{\partial z} \right) \right]\!\!\right] = 0 \ ; \tag{A.21}$$
$$\left[\!\!\left[\left(p^\dagger + 2\mu \frac{\partial v^\dagger}{\partial y} \right) \right]\!\!\right] = f^\dagger \ . \tag{A.22}$$

BC_y^A reduces to

$$BC_y^A = -v_T^H f^\dagger + \mu_B \left(\frac{\partial u^\dagger}{\partial y} + \frac{\partial v^\dagger}{\partial x} \right) \left[\!\!\left[\frac{\partial U}{\partial y} \right]\!\!\right] f^H + \left(p_B^\dagger + 2\mu_B \frac{\partial v_B^\dagger}{\partial y} \right) \left[\!\!\left[\frac{\partial V}{\partial y} \right]\!\!\right] f^H \tag{A.23}$$

In the next paragraphs, the residual terms are analysed to determine the adjoint bondary conditions.

Analysis of BC_y^F term

$$BC_y^F = - \left[\!\!\left[v^\dagger \left(-p^H + 2\mu \frac{\partial v^H}{\partial y} \right) \right]\!\!\right] - \left[\!\!\left[u^\dagger \mu \left(\frac{\partial u^H}{\partial y} + \frac{\partial v^H}{\partial x} \right) \right]\!\!\right] - \left[\!\!\left[w^\dagger \mu \left(\frac{\partial w^H}{\partial y} + \frac{\partial v^H}{\partial z} \right) \right]\!\!\right] \tag{A.24}$$

With the use of (A.18),

$$BC_y^F = -v^\dagger \left[\!\!\left[\left(-p^H + 2\mu \frac{\partial v^H}{\partial y} \right) \right]\!\!\right] - u^\dagger \left[\!\!\left[\mu \left(\frac{\partial u^H}{\partial y} + \frac{\partial v^H}{\partial x} \right) \right]\!\!\right] - w^\dagger \left[\!\!\left[\mu \left(\frac{\partial w^H}{\partial y} + \frac{\partial v^H}{\partial z} \right) \right]\!\!\right] \tag{A.25}$$

The application of (A.15), (A.18) and of the forward stress conditions (3.31)-(3.33) results

in:

$$BC_y^F = -v^\dagger \left(\sigma\kappa^H - \left[\!\left[2\mu \frac{\partial^2 V}{\partial y^2} \right]\!\right] f^H \right) - u^\dagger \left[\!\left[\mu \frac{\partial^2 U}{\partial y^2} \right]\!\right] f^H + w^\dagger \left[\!\left[\mu \frac{\partial^2 V}{\partial y \partial z} \right]\!\right] f^H \tag{A.26}$$

Under the assumption of small curvature of the interface, κ can be expressed as a linear function of the interfacial displacement, i.e. $\kappa = \Delta f$.

The total residual after applying forward and adjoint boundary conditions is given by:

$$\begin{aligned} BC_y^A + BC_y^F = &-v_T^H f^\dagger + \mu_B \left(\frac{\partial u^\dagger}{\partial y} + \frac{\partial v^\dagger}{\partial x} \right) \left[\!\left[\frac{\partial U}{\partial y} \right]\!\right] f^H + \left(p_B^\dagger + 2\mu_B \frac{\partial v_B^\dagger}{\partial y} \right) \left[\!\left[\frac{\partial V}{\partial y} \right]\!\right] f^H \\ &- v^\dagger \left(\sigma\kappa^H - \left[\!\left[2\mu \frac{\partial^2 V}{\partial y^2} \right]\!\right] f^H \right) - u^\dagger \left[\!\left[\mu \frac{\partial^2 U}{\partial y^2} \right]\!\right] f^H + w^\dagger \left[\!\left[\mu \frac{\partial^2 V}{\partial y \partial z} \right]\!\right] f^H \end{aligned} \tag{A.27}$$

Recall now the kinematic condition for the interfacial displacement f:

$$\left(\frac{\partial}{\partial t} + U \frac{\partial}{\partial x} \right) f = v_T \tag{A.28}$$

it follows that:

$$-v_T^H f^\dagger = -\left(\frac{\partial}{\partial t} + U \frac{\partial}{\partial x} \right)^H f^H f^\dagger \tag{A.29}$$

Introduce the following operators:

$$\begin{aligned} \mathcal{C}^\dagger \mathbf{q}^\dagger = &\mu_B \left(\frac{\partial u_B^\dagger}{\partial y} + \frac{\partial v_B^\dagger}{\partial x} \right) \left[\!\left[\frac{\partial U}{\partial y} \right]\!\right] + \left(p_B^\dagger + 2\mu_B \frac{\partial v_B^\dagger}{\partial y} \right) \left[\!\left[\frac{\partial V}{\partial y} \right]\!\right] \\ &- v^\dagger \left(\sigma\Delta^H - \left[\!\left[2\mu \frac{\partial^2 V}{\partial y^2} \right]\!\right] \right) - u^\dagger \left[\!\left[\mu \frac{\partial^2 U}{\partial y^2} \right]\!\right] + w^\dagger \left[\!\left[\mu \frac{\partial^2 V}{\partial y \partial z} \right]\!\right] \end{aligned} \tag{A.30}$$

$$\mathcal{I}^\dagger f^\dagger = -\left(\frac{\partial}{\partial t} + U \frac{\partial}{\partial x} \right)^H f^\dagger \tag{A.31}$$

Thefore,

$$BC_y^A + BC_y^F = f^H \left(\mathcal{C}^\dagger q^\dagger + \mathcal{I}^\dagger f^\dagger \right) - \left(\mathcal{C} q + \mathcal{I} f \right)^H f^\dagger \tag{A.32}$$

from which it follows that:

$$\int_{\Omega_x} BC_y \, dx = \int_{\Omega_x} f^H \left(\mathcal{C}^\dagger q^\dagger + \mathcal{I}^\dagger f^\dagger \right) \, dx - \int_{\Omega_x} \left(\mathcal{C} q + \mathcal{I} f \right)^H f^\dagger \, dx \tag{A.33}$$
$$\Rightarrow BC_x \equiv 0 \quad \forall \, \mathbf{q}, f, \mathbf{q}^\dagger, f^\dagger \in \mathcal{H}(\Omega)$$

For the adjoint relation (3.42) to hold, the residual term BC_x must vanish.

Analysis of BC_x and rescaling conditions

$$\int_{\Omega_y} BC_x \, dy = \int_d^{+\infty} {\mathbf{q}_T^\dagger}^H \mathbf{A}_T^H \mathbf{q}_T \Big|_{x_0}^{x_f} \, dy + \int_0^d {\mathbf{q}_B^\dagger}^H \mathbf{A}_B^H \mathbf{q}_B \Big|_{x_0}^{x_f} \, dy \tag{A.34}$$

For $BC_x = 0$ to be satisfied $\forall \, \mathbf{q}, f, \mathbf{q}^\dagger, f^\dagger \in \Omega$, the following conditions must be met:

$${\mathbf{q}_T^\dagger}^H \mathbf{A}_T^H \mathbf{q}_T \Big|_{x_0}^{x_f} = 0 \tag{A.35}$$
$${\mathbf{q}_B^\dagger}^H \mathbf{A}_B^H \mathbf{q}_B \Big|_{x_0}^{x_f} = 0 \tag{A.36}$$

that is

$${\mathbf{q}_T^\dagger}^H \mathbf{A}_T^H \mathbf{q}_T \Big|_{x_f} = {\mathbf{q}_T^\dagger}^H \mathbf{A}_T^H \mathbf{q}_T \Big|_{x_0} \tag{A.37}$$
$${\mathbf{q}_B^\dagger}^H \mathbf{A}_B^H \mathbf{q}_B \Big|_{x_f} = {\mathbf{q}_B^\dagger}^H \mathbf{A}_B^H \mathbf{q}_B \Big|_{x_0} \tag{A.38}$$

The relations (A.37)-(A.38) provide the projection condition between forward and adjoint systems at x_0 and x_f.

Provided that (A.37)-(A.38) hold, it is proved the existence of the adjoint system $\mathbf{S}^\dagger$:

$$\mathcal{S}^\dagger \phi^\dagger = \begin{bmatrix} \mathcal{L}^\dagger & 0 \\ \mathcal{C}^\dagger & \mathcal{I}^\dagger \end{bmatrix} \begin{bmatrix} \mathbf{q}^\dagger \\ f^\dagger \end{bmatrix} = 0 \tag{A.39}$$

with

$$\mathcal{L}^\dagger \mathbf{q}^\dagger = \left[-\mathbf{A}^H \frac{\partial}{\partial x} - \left(\mathbf{B_0} - \frac{\partial \mathbf{B_1}}{\partial y} \right)^H + \mathbf{B_1}^H \frac{\partial}{\partial y} - \mathbf{B_2} \frac{\partial^2}{\partial y^2} \right] \mathbf{q}^\dagger \tag{A.40}$$

$$\begin{aligned} \mathcal{C}^\dagger \mathbf{q}^\dagger = {} & \mu_B \left(\frac{\partial u_B^\dagger}{\partial y} + \frac{\partial v_B^\dagger}{\partial x} \right) \left[\!\!\left[\frac{\partial U}{\partial y} \right]\!\!\right] + \left(p_B^\dagger + 2\mu_B \frac{\partial v_B^\dagger}{\partial y} \right) \left[\!\!\left[\frac{\partial V}{\partial y} \right]\!\!\right] \\ & - v^\dagger \left(\sigma \Delta^H - \left[\!\!\left[2\mu \frac{\partial^2 V}{\partial y^2} \right]\!\!\right] \right) - u^\dagger \left[\!\!\left[\mu \frac{\partial^2 U}{\partial y^2} \right]\!\!\right] + w^\dagger \left[\!\!\left[\mu \frac{\partial^2 V}{\partial y \partial z} \right]\!\!\right] \end{aligned} \tag{A.41}$$

$$\mathcal{I}^\dagger f^\dagger = - \left(\frac{\partial}{\partial t} + U \frac{\partial}{\partial x} \right)^H f^\dagger \tag{A.42}$$

boundary conditions:

$$u_B^\dagger (0) = 0 \tag{A.43}$$

$$v_B^\dagger (0) = 0 \tag{A.44}$$

$$w_B^\dagger (0) = 0 \tag{A.45}$$

$$p_T^\dagger (+\infty) + 2V v_T^\dagger (+\infty) + \mu_T \frac{\partial v^\dagger}{\partial y} (+\infty) = 0 \tag{A.46}$$

$$u_T^\dagger (+\infty) = 0 \tag{A.47}$$

$$w_T^\dagger (+\infty) = 0 \tag{A.48}$$

$$\left[\!\!\left[u^\dagger \right]\!\!\right] = 0 \tag{A.49}$$

$$\left[\!\!\left[v^\dagger \right]\!\!\right] = 0 \tag{A.50}$$

$$\left[\!\!\left[w^\dagger \right]\!\!\right] = 0 \tag{A.51}$$

$$\left[\!\!\left[\mu \left(\frac{\partial u^\dagger}{\partial y} + \frac{\partial v^\dagger}{\partial x} \right) \right]\!\!\right] = 0 \tag{A.52}$$

$$\left[\!\!\left[\mu \left(\frac{\partial w^\dagger}{\partial y} + \frac{\partial v^\dagger}{\partial z} \right) \right]\!\!\right] = 0 \tag{A.53}$$

$$\left[\!\!\left[\left(p^\dagger + 2\mu \frac{\partial v^\dagger}{\partial y} \right) \right]\!\!\right] = f^\dagger \tag{A.54}$$

and rescaling conditions as in (A.37)-(A.38).

Appendix B

Validation

Some of the validation results for the two-phase parallel and spreading code are presented in this appendix.
This sections refers to the validation of the two-phase spatial codes used for the computations in this thesis:

1. *eigOS-Sq*, *eigOS-SqAdj* : parallel OS-Sq eigenvalue solver, parallel adjoint OS-Sq eigenvalue solver;

2. *tgOS-Sq*: parallel optimal growth (via SVD);

3. *tgBL*: spreading optimal growth (via Adjoint Looping).

Due to the lack of literature results on two-phase spatial Orr-Sommerfeld and Squire eigenvalue problem, the author has validated the spectral parallel code using several methods. It is important to highlight that there is a one-to-one relation between transient growth mechanism and eigenvalues. Therefore, the validation of an optimal growth curve (computed via SVD) implies that the underlying eigenvalue problem (and its adjoint) is accurate. Moreover, the transient amplification of the solution to the initial value problem of an optimal disturbance, by definition, must reach the G_{max} value at the same streamwise location χ_M. On the basis of these considerations and using the well-established PSE (Cheung & Lele, 2009) and DNS (Zaki, 2005) codes, a rigorous validation pattern was followed.
First of all, the ability to correctly represent single-fluid-limit features was constantly monitored throughtout the implementation and validation (fig. B.2).
The code *eigOS-Sq* was at first validated against the two-phase Orr-Sommerfeld solver

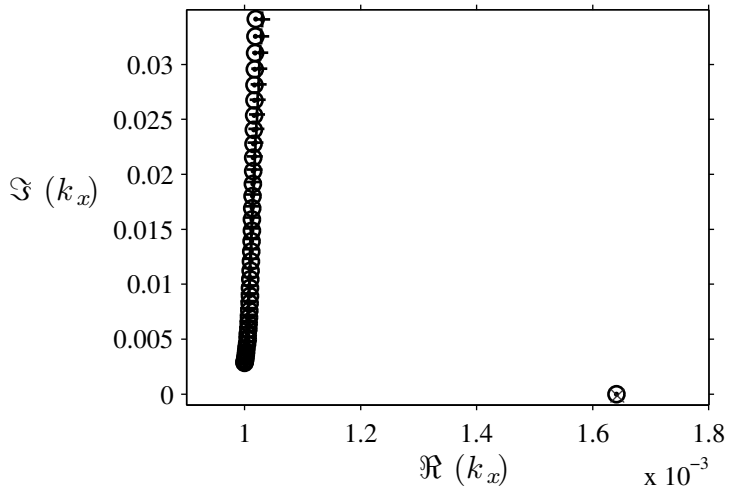


Figure B.1: Two-fluid boundary layer eigenvalue spectrum, $\omega = 0.001$, $k_z = 1.5$, $r = \frac{\rho_B}{\rho_T} = 10$, $m = 0.55$, $Re = 800$. ∘: Orr-Sommerfeld eigenvalues (OS), +: Squire eigenvalues (SQ); •: complex conjugate OS and SQ adjoint eigenvalues. ×: data from Cheung & Zaki (2010), obtained via Parabolized Stability Equation code in parallel limit.

built in the PSE code. Then adjoint code *eigOS-SqAdj* was developed and consistency between eigenvalues and adjoint eigenvalues was checked for any viscosity and density ratio and Weber number (fig. B.1).

The code *eigOS-Sq* uses the eigenvalues computed by *eigOS-Sq* and *eigOS-SqAdj* to compute optimal growth. Two different and independent implementation of the optimal growth problem (via SVD and via Adjoint Looping) were compared, yielding to identical results. However, additional and conclusive validation was provided by direct comparison with *tgBL*, run in parallel-flow limit (fig. B.3).

The spreading single and two-phase capabilities of *tgBL* were tested against results from DNS. Optimal single and two-phase disturbances were computed with *tgBL* via the adjoint looping method and provided as inlet condition to the DNS solver. The linear evolution of kinetic energy (normalised by its inlet value) of the optimal disturbance was compared with the G_{max} envelope computed with *tgBL*, via Adjoint Looping (fig. B.4), showing perfect agreement. This validates the two-phase spreading forward and adjoint solutions and the choice of the boundary layer approximation for the chosen Re number. More details of the comparison with DNS data can be found in Chapter 4.

Additional validation of the temporal problem was originally carried out. Temporal eigenvalues were validated against literature; figure B.5 show a comparison against Malik

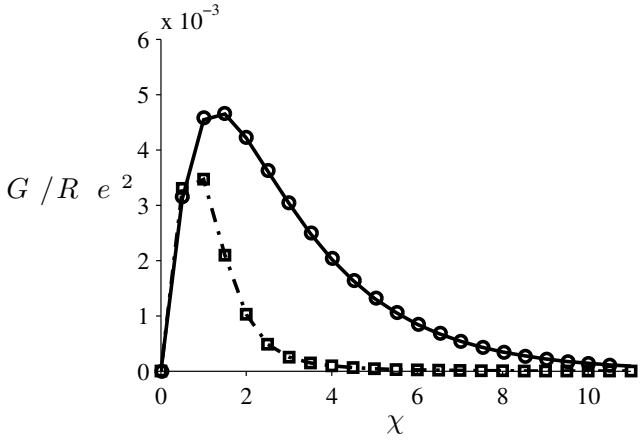


Figure B.2: Comparison of optimal growth in single fluid Blasius boundary layer. Reference, data from Tumin & Reshotko (2001): ∘, $\omega = 0$; □, $\omega = 0.005$. ——, – · – two-phase parallel and spreading spectral code in single-phase parallel limit.

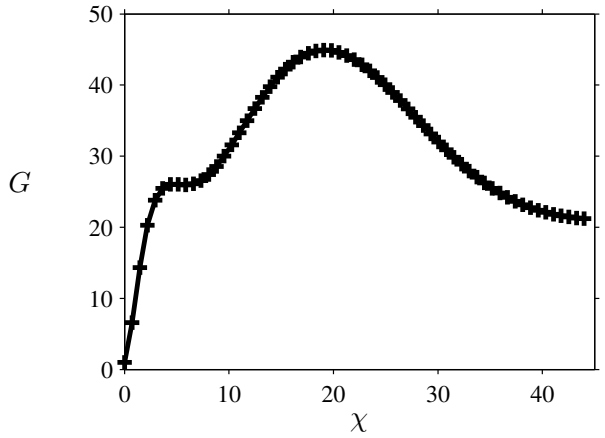


Figure B.3: Comparison of optimal growth in two-fluid boundary layer, $Re = 800$, $\omega = 0.002$, $k_z = 1.2$, $r = 0.5$, $m = 0.5$. ——: *tgOS-Sq*; +: *tgBL*, parallel-limit.

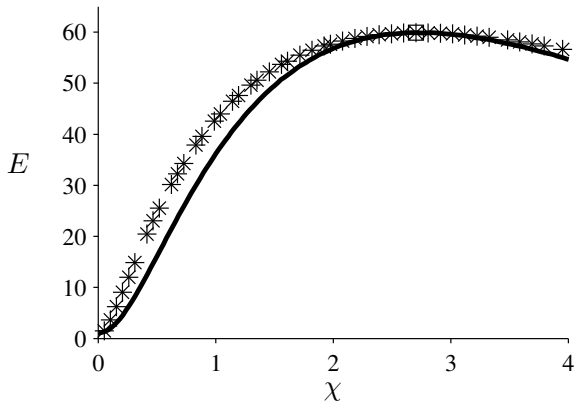
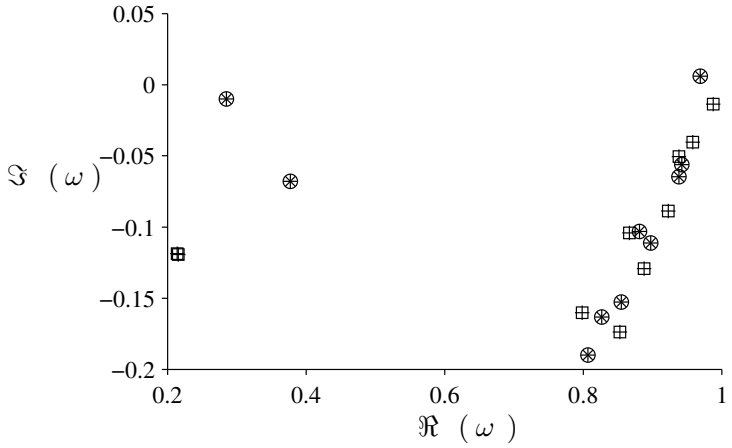


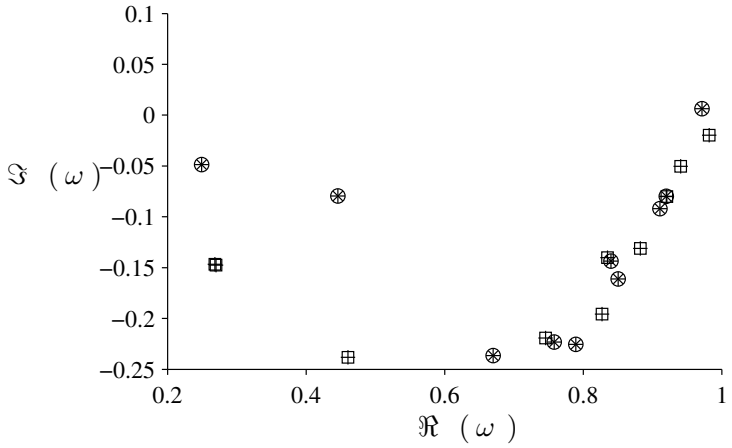
Figure B.4: Streamwise evolution of kinetic energy E for $\omega = 0.001$, $k_z = 1.5$, $m = 0.55$, $Re = 800$, $\epsilon = 0.01\%$, computed with DNS; $*$: Evelope of G_{max}, computed with *tgBL*

& Hooper (2007).

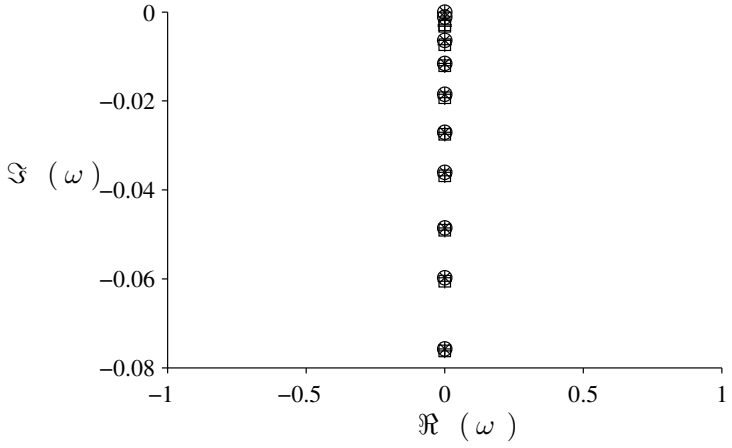
Transient growth was computed for various viscosity and density ratios and Weber numbers; figure B.6 shows a comparison of transient growth at different Weber numbers versus Yecko (2008).



(a)



(b)



(c)

Figure B.5: Three-dimensional two-fluid flow eigenvalues, $Re = 3000$, $m = 2$, $r = 0$ for *a)* $k_x = 1$, $k_z = 0$, *b)* $k_x = 0.5$, $k_z = 0.5$ *c)* $k_x = 0$, $k_z = 1$. $*$ OS mode, $+$ SQ mode Malik & Hooper (2007); $\circ$ OS mode, $\square$ SQ mode, temporal SVD code

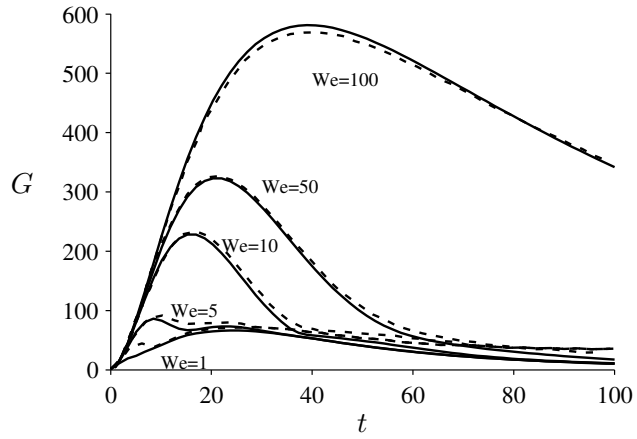


Figure B.6: Energy growth $G(t)$ for $k_x = 0$, $k_z = 1$, $r = 0.9$, $m = 20$, $Re = 900$. - - - Yecko (2008), —— temporal SVD code

Appendix C

Non-linear mapping of Chebyshev polynomials

Define $T_n(y) := \tilde{T}_n\left(\vartheta^{-1}(y)\right)$ as the mapped Chebyshev polynomial onto the domain Ω. The mapping function is ϑ and relates the Chebyshev interval $I = [-1, 1]$ to physical space Ω, such that $y = \vartheta(\zeta),\ \forall\, \zeta \in I\,, y \in \Omega$.

Two sets of Chebyshev polynomial have been used to represent, independently, the bottom and the top fluid. In particular, $T_n^T = \tilde{T}_n\left(\vartheta^{-1}(y)\right)$, $y \geq d$ and $T_n^B = \tilde{T}_n\left(\vartheta^{-1}(y)\right)$, $y \leq d$.

To achieve high accuracy in calculations, it is important to control the number of collocation points in the mapped domain. Rational maps on a semi-infinite domain have proved successful in distributing grid points so that the interface region is highly resolved (Schmid & Henningson, 2001). The mapping function ϑ has been chosen to be:

$$\textit{non-linear:} \quad y_j = \vartheta(\zeta_j) = \begin{cases} \frac{L(\zeta_j+1)y_i^T}{L-(L-2y_c^T)\zeta_j} & \text{if} \quad y \geq d \\ \frac{d(\zeta_j-1)y_i^B}{d+(d-2y_c^B)\zeta_j} & \text{if} \quad y \leq d \end{cases} \tag{C.1}$$

where the parameters y_c^T, y_c^B control the clustering location of half of the Gauss-Lobatto points (respectively, in the intervals $[d, y_c^T]$, $[y_c^B, d]$). In the case that $y_c^T = \frac{L}{2}$, $y_c^B = \frac{d}{2}$, a linear mapping is recovered:

$$\textit{linear:} \quad y_j = \vartheta(\zeta_j) = \begin{cases} \frac{\zeta_j+1}{2}L & \text{if} \quad y \geq d \\ \frac{\zeta_j-1}{2}d & \text{if} \quad y \leq d \end{cases} \tag{C.2}$$

Details of the Chebyshev differentiation polynomials in physical space are given below.

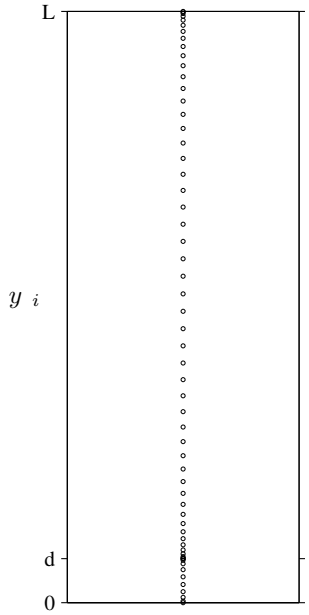


Figure C.1: Chebyshev collocation points under linear mapping.

$$T_n^{'} = \frac{\tilde{T}_n^{'}\left(\vartheta^{-1}(y)\right)}{\vartheta^{'}\left(\vartheta^{-1}(y)\right)} \tag{C.3}$$

$$T_n^{''} = -\frac{\tilde{T}_n^{'}\left(\vartheta^{-1}(y)\right)\vartheta^{''}\left(\vartheta^{-1}(y)\right)}{\vartheta^{'}\left(\vartheta^{-1}(y)\right)^3} + \frac{\tilde{T}_n^{''}\left(\vartheta^{-1}(y)\right)}{\vartheta^{'}\left(\vartheta^{-1}(y)\right)^2} \tag{C.4}$$

$$\begin{aligned} T_n^{'''} =& \frac{3\tilde{T}_n^{'}\left(\vartheta^{-1}(y)\right)\vartheta^{''}\left(\vartheta^{-1}(y)\right)^2}{\vartheta^{'}\left(\vartheta^{-1}(y)\right)^5} - \frac{3\tilde{T}_n^{''}\left(\vartheta^{-1}(y)\right)\vartheta^{''}\left(\vartheta^{-1}(y)\right)}{\vartheta^{'}\left(\vartheta^{-1}(y)\right)^4} \\ & - \frac{\tilde{T}_n^{'}\left(\vartheta^{-1}(y)\right)\vartheta^{'''}\left(\vartheta^{-1}(y)\right)}{\vartheta^{'}\left(\vartheta^{-1}(y)\right)^4} + \frac{\tilde{T}_n^{'''}\left(\vartheta^{-1}(y)\right)}{\vartheta^{'}\left(\vartheta^{-1}(y)\right)^3} \end{aligned} \tag{C.5}$$

$$\begin{aligned} T_n^{''''} =& -\frac{15\tilde{T}_n^{'}\left(\vartheta^{-1}(y)\right)\vartheta^{''}\left(\vartheta^{-1}(y)\right)^3}{\vartheta^{'}\left(\vartheta^{-1}(y)\right)^7} + \frac{15\tilde{T}_n^{''}\left(\vartheta^{-1}(y)\right)\vartheta^{''}\left(\vartheta^{-1}(y)\right)^2}{\vartheta^{'}\left(\vartheta^{-1}(y)\right)^6} \\ & + \frac{10\tilde{T}_n^{'}\left(\vartheta^{-1}(y)\right)\vartheta^{''}\left(\vartheta^{-1}(y)\right)\vartheta^{'''}\left(\vartheta^{-1}(y)\right)}{\vartheta^{'}\left(\vartheta^{-1}(y)\right)^6} - \frac{4\tilde{T}_n^{''}\left(\vartheta^{-1}(y)\right)\vartheta^{'''}\left(\vartheta^{-1}(y)\right)}{\vartheta^{'}\left(\vartheta^{-1}(y)\right)^5} \\ & - \frac{6\tilde{T}_n^{'''}\left(\vartheta^{-1}(y)\right)\vartheta^{''}\left(\vartheta^{-1}(y)\right)}{\vartheta^{'}\left(\vartheta^{-1}(y)\right)^5} - \frac{\tilde{T}_n^{'}\left(\vartheta^{-1}(y)\right)\vartheta^{''''}\left(\vartheta^{-1}(y)\right)}{\vartheta^{'}\left(\vartheta^{-1}(y)\right)^5} + \frac{\tilde{T}_n^{''''}\left(\vartheta^{-1}(y)\right)}{\vartheta^{'}\left(\vartheta^{-1}(y)\right)^4} \end{aligned} \tag{C.6}$$

These relations were derived by the Author and verified with the help of Mathematica.

Appendix D

Energy norm and expansion convergence

The convergence of the mechanical energy norm of a perturbation stated in equation (2.57) is address in this section. This norm is based on Yecko and Zaleski's formulation (Yecko & Zaleski, 2005*b*).

Consider a perturbation expanded in terms of N Orr-Sommerfeld and Squire eigenfunctions. The maximum transient growth value G_{max} can be considered as the value of a convergent series in terms of well-resolved modes that constitute the projection basis of cardinality N. The quantity ΔG, denoted as *residual* and defined as $\Delta G = \frac{\Delta G_{max}(N)}{G_{max}(N)}$, where $\Delta G_{max}(N) \equiv G_{max}(N+1) - G_{max}(N)$, is used to study how G_{max} varies as N is increased, conditioned to the inclusion of well-resolved modes.

A plot of the value of the residual versus the number of well-resolved modes N is depicted in fig. D.1.

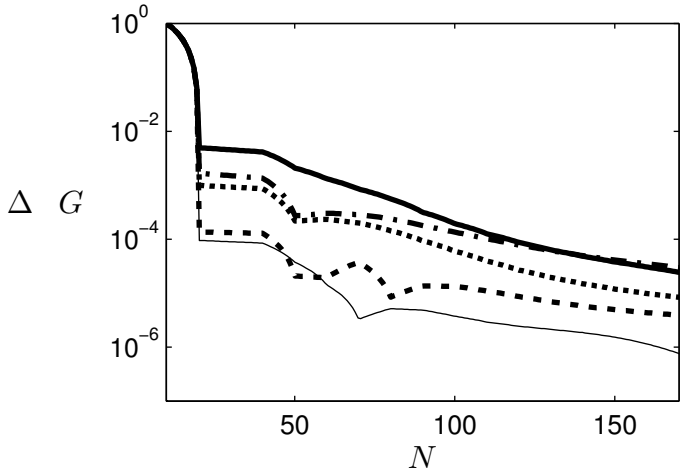


Figure D.1: Convergence residual of the energy norm for different values of viscosity ratio m, $\omega = 0.001$, $k_z = 1.5$, $Re = 800$. ——: $m = 1.0$; – ·–: $m = 0.8$; – – –: $m = 0.6$; · · · ·: $m = 0.4$; ——: $m = 0.2$.

Appendix E

Other applications

This Appendix brings together work undertaken by the Author during his PhD studies on subjects related to the application of single- and two-fluid adjoint equations. The aim of this Appendix is to collect notes that can be useful to other students but are not strictly related to the main subject of this thesis.
In particular, in the next section, attention is given to:

E.1 derivation of two phase adjoint Navier-Stokes, PSE and Orr-Sommerfeld equations;

E.1 Adjoint Navier-Stokes equations

The aim of this section is to fomulate and present the adjoint of linear Navier-Stokes equations, governing the evolution of an infinitesimal perturbation in two-phase shear flow.
Let $\Phi = [u \quad v \quad w \quad p]^T$ be the vector containing the forward perturbation variables and $\bar{\Phi} = [U \quad V \quad W \quad P]^T$ the mean variables, $\Psi = [u' \quad v' \quad w' \quad p']^T$ the vector containing the adjoint variables.

Define the operator

$$\mathcal{H} = \begin{bmatrix} \rho\left[\partial_t + \mathcal{L}\right] - \mu\Delta & \nabla \\ \nabla\cdot & 0 \end{bmatrix} \tag{E.1}$$

with

$$\mathcal{L}\mathbf{u} = \mathbf{U}_j \frac{\partial \mathbf{u}_i}{\partial x_j} + \mathbf{u}_j \frac{\partial \mathbf{U}_i}{\partial x_j} \tag{E.2}$$

where $\mathbf{u} = [u \quad v \quad w]^T$ and $\mathbf{U} = [U \quad V \quad W]^T$.

Note that the evolution of a generic perturbation in each fluid can be re-written as

$$\mathcal{H}\Phi = 0 \tag{E.3}$$

Suppose that $\mathbb{S}$ is a Hilbert space, with inner product $< \cdot, \cdot >$. Consider the continuous linear operator $\mathcal{H} : \mathbb{S} \rightarrow \mathbb{S}$. There exists a unique continuous linear operator $\mathcal{H}^\dagger : \mathbb{S} \rightarrow \mathbb{S}$ with the following property:

$$< \Psi, \mathcal{H}\Phi >=< \Psi\mathcal{H}^\dagger, \Phi > \quad \forall\Psi, \Phi \in \mathbb{S} \tag{E.4}$$

Finding the adjoint of the problem defined by the relation (E.3) is equivalent to determine the operator $\mathcal{H}^\dagger$ that fulfils the relation (E.4), provided an inner product $< \cdot, \cdot >$.

Define an inner product as the following:

$$< \mathbf{a}, \mathbf{b} > \quad = \int_0^t \int_\Omega \mathbf{a}^* \cdot \mathbf{b} \quad d\Omega d\tau \quad , \quad \forall \mathbf{a}, \mathbf{b} \in \mathbb{S} = [0, t] \times \Omega \tag{E.5}$$

The inner product $< \Psi, \mathcal{H}\Phi >$ is constructed explicitly using the index notation:

$$< \Psi, \mathcal{H}\Phi >= \int_0^t \int_\Omega \Psi_i^* \left(\mathcal{H}\Phi\right)_i d\Omega d\tau = \tag{E.6}$$

$$\int_0^t \int_\Omega \Big(\mathbf{u}_i'^* \left[\underbrace{\rho \left(\frac{\partial \mathbf{u}_i}{\partial t} + \mathbf{U}_j \frac{\partial \mathbf{u}_i}{\partial x_j} + \mathbf{u}_j \frac{\partial \mathbf{U}_i}{\partial x_j} \right)}_{\text{Convective}} + \underbrace{\frac{\partial p}{\partial x_i}}_{\text{Pressure}} - \underbrace{\mu \frac{\partial^2 \mathbf{u}_i}{\partial x_j \partial x_j}}_{\text{Viscous}} \right] + \underbrace{p'^* \frac{\partial u_i}{\partial x_i}}_{\text{Mass}} \Big) d\Omega d\tau$$

Consider each term separately:

Pressure term

$$P = \int_0^t \int_\Omega \mathbf{u}_i'^* \frac{\partial p}{\partial x_i} \, d\Omega d\tau = \int_0^t \int_\Gamma \mathbf{u}_i'^* p \hat{\mathbf{n}}_i \, d\Gamma d\tau - \int_0^t \int_\Omega \frac{\partial \mathbf{u}_i'^*}{\partial x_i} p \, d\Omega d\tau \tag{E.7}$$

where $\Gamma = \partial\Omega$ denotes the boundary surface of the domain Ω and $\hat{\mathbf{n}}$ is the normal unit versor to the surface Γ.

Mass term

$$M = \int_0^t \int_\Omega p'^* \frac{\partial \mathbf{u}_i}{\partial x_i}\, d\Omega d\tau = \int_0^t \int_\Gamma p'^* \mathbf{u}_i \hat{\mathbf{n}}_i\, d\Gamma d\tau - \int_0^t \int_\Omega \frac{\partial p'^*}{\partial x_i} \mathbf{u}_i\, d\Omega d\tau \tag{E.8}$$

Convective term

$$\begin{aligned}
C &= \int_0^t \int_\Omega \underbrace{\mathbf{u}_i'^* \rho \frac{\partial \mathbf{u}_i}{\partial t}}_{\mathrm{C_1}} + \underbrace{\mathbf{u}_i'^* \rho \mathbf{U}_j \frac{\partial \mathbf{u}_i}{\partial x_j}}_{\mathrm{C_2}} + \underbrace{\mathbf{u}_i'^* \rho \mathbf{u}_j \frac{\partial \mathbf{U}_i}{\partial x_j}}_{\mathrm{C_3}}\, d\Omega d\tau \qquad \text{(E.9)}\\
C_1 &= \int_0^t \int_\Omega \mathbf{u}_i'^* \rho \frac{\partial \mathbf{u}_i}{\partial t}\, d\Omega d\tau = \int_\Omega \rho \mathbf{u}_i'^* \mathbf{u}_i \,|_0^t\, d\Omega - \int_0^t \int_\Omega \rho \frac{\partial \mathbf{u}_i'^*}{\partial t} \mathbf{u}_i\, d\Omega d\tau\\
C_2 &= \int_0^t \int_\Omega \mathbf{u}_i'^* \rho \mathbf{U}_j \frac{\partial \mathbf{u}_i}{\partial x_j}\, d\Omega d\tau = \int_0^t \int_\Gamma \rho \mathbf{U}_j \mathbf{u}_i'^* \mathbf{u}_i \hat{\mathbf{n}}_j\, d\Gamma d\tau\\
&\qquad - \int_0^t \int_\Omega \rho \frac{\partial \mathbf{u}_i'^*}{\partial x_j} \mathbf{U}_j \mathbf{u}_i\, d\Omega d\tau\\
C_3 &= \int_0^t \int_\Omega \mathbf{u}_i'^* \rho \mathbf{u}_j \frac{\partial \mathbf{U}_i}{\partial x_j}\, d\Omega d\tau = \int_0^t \int_\Omega \rho \mathbf{u}_i'^* \frac{\partial \mathbf{U}_i}{\partial x_j} \mathbf{u}_j\, d\Omega d\tau
\end{aligned}$$

Viscous term

$$\begin{aligned}
V &= \int_0^t \int_\Omega -\mathbf{u}_i'^* \mu \frac{\partial^2 \mathbf{u}_i}{\partial x_j \partial x_j}\, d\Omega d\tau = \int_0^t \int_\Omega -\mathbf{u}_i'^* \mu \frac{\partial}{\partial x_j} \left(\frac{\partial \mathbf{u}_i}{\partial x_j} \right) d\Omega d\tau \qquad \text{(E.10)}\\
&= \int_0^t \int_\Omega -\mathbf{u}_i'^* \mu \frac{\partial}{\partial x_j} \left(\frac{\partial \mathbf{u}_i}{\partial x_j} + \frac{\partial \mathbf{u}_j}{\partial x_i} \right) d\Omega d\tau\\
&= \int_0^t \int_\Omega \frac{\partial}{\partial x_j} \left(-\mu \mathbf{u}_i'^* \left(\frac{\partial \mathbf{u}_i}{\partial x_j} + \frac{\partial \mathbf{u}_j}{\partial x_i} \right) \right) d\Omega d\tau + \int_0^t \int_\Omega -\mu \frac{\partial \mathbf{u}_i'^*}{\partial x_j} \left(\frac{\partial \mathbf{u}_i}{\partial x_j} + \frac{\partial \mathbf{u}_j}{\partial x_i} \right) d\Omega d\tau\\
&= \int_0^t \int_\Gamma -\mu \mathbf{u}_i'^* \left(\frac{\partial \mathbf{u}_i}{\partial x_j} + \frac{\partial \mathbf{u}_j}{\partial x_i} \right) \hat{\mathbf{n}}_j\, d\Gamma d\tau + \int_0^t \int_\Omega \mu \frac{\partial \mathbf{u}_i'^*}{\partial x_j} \frac{\partial \mathbf{u}_i}{\partial x_j}\, d\Omega d\tau\\
&\qquad + \int_0^t \int_\Omega \mu \frac{\partial \mathbf{u}_i'^*}{\partial x_j} \frac{\partial \mathbf{u}_j}{\partial x_i}\, d\Omega d\tau\\
&= \int_0^t \int_\Gamma -\mu \mathbf{u}_i'^* \left(\frac{\partial \mathbf{u}_i}{\partial x_j} + \frac{\partial \mathbf{u}_j}{\partial x_i} \right) \hat{\mathbf{n}}_j\, d\Gamma d\tau + \int_0^t \int_\Omega \frac{\partial}{\partial x_j} \left(\mu \frac{\partial \mathbf{u}_i'^*}{\partial x_j} \mathbf{u}_i \right) d\Omega d\tau\\
&- \int_0^t \int_\Omega \mu \frac{\partial^2 \mathbf{u}_i'^*}{\partial x_j \partial x_j} \mathbf{u}_i\, d\Omega d\tau + \int_0^t \int_\Omega \frac{\partial}{\partial x_i} \left(\mu \frac{\partial \mathbf{u}_i'^*}{\partial x_j} \mathbf{u}_j \right) d\Omega d\tau - \int_0^t \int_\Omega \mu \frac{\partial^2 \mathbf{u}_i'^*}{\partial x_j \partial x_i} \mathbf{u}_j\, d\Omega d\tau\\
&= \int_0^t \int_\Gamma -\mu \mathbf{u}_i'^* \left(\frac{\partial \mathbf{u}_i}{\partial x_j} + \frac{\partial \mathbf{u}_j}{\partial x_i} \right) \hat{\mathbf{n}}_j + \mu \frac{\partial \mathbf{u}_i'^*}{\partial x_j} \mathbf{u}_i \hat{\mathbf{n}}_j + \mu \frac{\partial \mathbf{u}_i'^*}{\partial x_j} \mathbf{u}_j \hat{\mathbf{n}}_i\, d\Gamma d\tau\\
&- \int_0^t \int_\Omega \mu \left(\frac{\partial^2 \mathbf{u}_i'^*}{\partial x_j \partial x_j} \mathbf{u}_i + \frac{\partial^2 \mathbf{u}_j'^*}{\partial x_j \partial x_i} \mathbf{u}_i \right) d\Omega d\tau
\end{aligned}$$

Combining terms Combining all terms together, the quantity

$$A =< \Psi, \mathcal{H}\Phi >= C + P + V + M$$

can be written as the following:

$$A = \int_0^t \int_\Omega \Bigg(\Bigg[\underbrace{\rho \left(\frac{\partial \mathbf{u}_i'^*}{\partial t} - \mathbf{U}_j \frac{\partial \mathbf{u}_i'^*}{\partial x_j} + \frac{\partial \mathbf{U}_j}{\partial x_i} \mathbf{u}_j'^* \right)}_{\text{Convective}} - \underbrace{\frac{\partial p'^*}{\partial x_i}}_{\text{Pressure}} - \underbrace{\mu \frac{\partial^2 \mathbf{u}'^*{}_i}{\partial x_j \partial x_j}}_{\text{Viscous}} \Bigg] \mathbf{u} - \underbrace{\frac{\partial u_i'^*}{\partial x_i} p}_{\text{Mass}} \Bigg) d\Omega d\tau + \partial A \tag{E.11}$$

$$\begin{aligned} \partial A = & \underbrace{\int_\Omega \rho \mathbf{u}_i'^* \mathbf{u}_i \mid_0^t \; d\Omega}_{\partial \mathrm{A_t}} + \\ & + \int_0^t \int_\Gamma \left(\rho \mathbf{U}_i \mathbf{u}_j'^* \mathbf{u}_j + p'^* \mathbf{u}_i + \mathbf{u}_i'^* p \right) \hat{\mathbf{n}}_i \; d\Gamma d\tau \\ & \underbrace{+ \int_0^t \int_\Gamma \left(-\mu \mathbf{u}_i'^* \left(\frac{\partial \mathbf{u}_i}{\partial x_j} + \frac{\partial \mathbf{u}_j}{\partial x_i} \right) + \mu \frac{\partial \mathbf{u}_i'^*}{\partial x_j} \mathbf{u}_i \right) \hat{\mathbf{n}}_j + \mu \frac{\partial \mathbf{u}_i'^*}{\partial x_j} \mathbf{u}_j \hat{\mathbf{n}}_i \; d\Gamma d\tau}_{\partial \mathrm{A}_\Gamma} \end{aligned} \tag{E.12}$$

Equation (E.12) satisfies the condition (E.4) when the boundary term ∂A vanishes.

It is straightforward to prove that in the single fluid case, due to the vanishing boundary conditions at infinity on the forward variables, the choice $\mathbf{u}'^*(\mathbf{x}, t) = 0$ and $\mathbf{u}'^*(\Gamma) = 0$ provides correct boundary conditions for the adjoint linearized Navier Stokes system, so that $\partial A \equiv 0$, defined as the following:

$$\mathcal{H}^\dagger \Psi = 0 \tag{E.13}$$

with

$$\begin{aligned} \mathcal{H}^\dagger &= \begin{bmatrix} \rho\left[-\partial_t + \mathcal{L}^\dagger\right] - \mu\Delta & -\nabla \\ -\nabla\cdot & 0 \end{bmatrix} \\ \mathcal{L}^\dagger \mathbf{u}' &= -\mathbf{U}^*{}_j \frac{\partial \mathbf{u}'_i}{\partial x_i} + \frac{\partial \mathbf{U}^*{}_j}{\partial x_i}\mathbf{u}'_j \end{aligned} \tag{E.14}$$

where $\mathbf{u}' = [u' \quad v' \quad w']^T$ and $\mathbf{U}^* = [U^* \quad V^* \quad W^*]^T$.

two-phase case In the two-phase case, the situation is much more complex, due to the jump conditions on the forward variables at the interface.

Define the jump operator $[\![\cdot]\!]$ as $[\![\xi]\!] = \xi_{\text{bottom}} - \xi_{\text{top}}$, where ξ represents any variable experiencing a jump across the interface.

The matching conditions on the forward variables at the interface are:

$$\begin{gathered} [\![u]\!] = 0 \qquad [\![v]\!] = 0 \qquad [\![w]\!] = 0 \\ [\![\mu\left(\tfrac{\partial u}{\partial y} + \tfrac{\partial v}{\partial x}\right)]\!] = 0 \qquad [\![-p + 2\mu\tfrac{\partial v}{\partial y}]\!] = \sigma\kappa \qquad [\![\mu\left(\tfrac{\partial w}{\partial y} + \tfrac{\partial v}{\partial z}\right)]\!] = 0 \end{gathered} \tag{E.15}$$

Consider the boundary term $\partial A = \partial A_t + \partial A_\Gamma$.

$$\partial A_t = \int_\Omega \rho \mathbf{u}'^*_i(t)\mathbf{u}_i(t) - \rho \mathbf{u}'^*_i(0)\mathbf{u}_i(0)\ d\Omega \quad \Longrightarrow \quad \boxed{\mathbf{u}'^*(\mathbf{x}, t) = \mathbf{u}_t} \tag{E.16}$$

$$\begin{aligned} \partial A_\Gamma = &\int_0^t \int_\Gamma \left(\rho \mathbf{U}_i \mathbf{u}'^*_j \mathbf{u}_j + p'^* \mathbf{u}_i + \mathbf{u}'^*_i p\right)\hat{\mathbf{n}}_i\ d\Gamma d\tau \\ &+ \int_0^t \int_\Gamma \left(-\mu \mathbf{u}'^*_i \left(\frac{\partial \mathbf{u}_i}{\partial x_j} + \frac{\partial \mathbf{u}_j}{\partial x_i}\right) + \mu \frac{\partial \mathbf{u}'^*_i}{\partial x_j}\mathbf{u}_i\right)\hat{\mathbf{n}}_j + \mu \frac{\partial \mathbf{u}'^*_i}{\partial x_j}\mathbf{u}_j \hat{\mathbf{n}}_i\ d\Gamma d\tau \end{aligned} \tag{E.17}$$

Consider a generic integral $\mathrm{I} = \int_\Gamma \mathbf{q}\cdot\hat{\mathbf{n}}\ d\Gamma$.

Assuming

- periodicity of the function q in the $\hat{z}$ direction
- vanishing boundary conditions at infinity

the only relevant normal versor $\hat{\mathbf{n}}_j$ to the surface Γ is $\hat{\mathbf{n}}_j = \hat{y}$. The I can be written as:

$$\mathrm{I} = \int_\Gamma \mathbf{q} \cdot \hat{y} \; d\Gamma = Q(+\infty) - Q_T(\bar{h}) + Q_B(\bar{h}) - Q(-\infty) = [\![Q]\!] \tag{E.18}$$

where $y = \bar{h}$ identifies the position of the interface and T, B denote "top" and "bottom" fluid quantities. The following relation holds.

$$\begin{aligned}
\partial A_\Gamma = & \int_0^t \int_\Gamma \rho \left(\mathbf{u}_i'^* \mathbf{u}_i\right) V \; d\Gamma d\tau \\
& + \int_0^t \int_\Gamma \left[v'^* p - \mu \mathbf{u}_i'^* \left(\frac{\partial \mathbf{u}_i}{\partial y} + \frac{\partial v}{\partial x_i} \right) \right] \; d\Gamma d\tau \\
& + \int_0^t \int_\Gamma \left[p'^* v + \mu \mathbf{u}_i \left(\frac{\partial \mathbf{u}_i'^*}{\partial y} + \frac{\partial v'^*}{\partial x_i} \right) \right] \; d\Gamma d\tau \\
& = [\![\rho \left(\mathbf{u}_i'^* \mathbf{u}_i\right) V]\!] + [\![v'^* p - \mu \mathbf{u}_i'^* \left(\frac{\partial \mathbf{u}_i}{\partial y} + \frac{\partial v}{\partial x_i} \right)]\!] + [\![p'^* v + \mu \mathbf{u}_i \left(\frac{\partial \mathbf{u}_i'^*}{\partial y} + \frac{\partial v'^*}{\partial x_i} \right)]\!]
\end{aligned} \tag{E.19}$$

Consider a three-dimensional perturbation and base flow. The time integration does not affect the derivation of the adjoint boundary conditions, since they must be satisfied at any time. The boundary term ∂A can be expanded as

$$\begin{aligned}
\partial A_\Gamma = & [\![\rho \left(u'^* u + v'^* v + w'^* w\right) V]\!] \\
& + [\![v'^* p - \mu u'^* \left(\frac{\partial u}{\partial y} + \frac{\partial v}{\partial x} \right) - \mu v'^* \left(\frac{\partial v}{\partial y} + \frac{\partial v}{\partial y} \right) - \mu w'^* \left(\frac{\partial w}{\partial y} + \frac{\partial v}{\partial z} \right)]\!] \\
& + [\![p'^* v + \mu u \left(\frac{\partial u'^*}{\partial y} + \frac{\partial v'^*}{\partial x} \right) + \mu v \left(\frac{\partial v'^*}{\partial y} + \frac{\partial v'^*}{\partial y} \right) + \mu w \left(\frac{\partial w'^*}{\partial y} + \frac{\partial v'^*}{\partial z} \right)]\!]
\end{aligned} \tag{E.20}$$

$$\begin{aligned}
\partial A_\Gamma = & [\![v'^* \left(p - 2\mu \frac{\partial v}{\partial y} \right)]\!] - [\![u'^* \mu \left(\frac{\partial u}{\partial y} + \frac{\partial v}{\partial x} \right)]\!] - [\![w'^* \mu \left(\frac{\partial w}{\partial y} + \frac{\partial v}{\partial z} \right)]\!] \\
& + [\![v \left(p'^* + 2\mu \frac{\partial v'^*}{\partial y} \right)]\!] + [\![\mu u \left(\frac{\partial u'^*}{\partial y} + \frac{\partial v'^*}{\partial x} \right)]\!] + [\![\mu w \left(\frac{\partial w'^*}{\partial y} + \frac{\partial v'^*}{\partial z} \right)]\!] \\
& + [\![\rho u'^* u V]\!] + [\![\rho v'^* v V]\!] + [\![\rho w'^* w V]\!] \\
& = [\![v'^* \left(p - 2\mu \frac{\partial v}{\partial y} \right)]\!] - [\![u'^* \mu \left(\frac{\partial u}{\partial y} + \frac{\partial v}{\partial x} \right)]\!] - [\![w'^* \mu \left(\frac{\partial w}{\partial y} + \frac{\partial v}{\partial z} \right)]\!] \\
& + [\![v \left(p'^* + 2\mu \frac{\partial v'^*}{\partial y} \rho v'^* V \right)]\!] + [\![u \left(\mu \left(\frac{\partial u'^*}{\partial y} + \frac{\partial v'^*}{\partial x} \right) + \rho u'^* V \right)]\!] \\
& + [\![w \left(\mu \left(\frac{\partial w'^*}{\partial y} + \frac{\partial v'^*}{\partial z} \right) + \rho w'^* V \right)]\!]
\end{aligned} \tag{E.21}$$

Recalling the forward boundary conditions (E.15) and choosing the adjoint velocities to verify the jump condition at the interface as the following:

$$\boxed{[\![u']\!] = 0} \qquad \boxed{[\![v']\!] = 0} \qquad \boxed{[\![w']\!] = 0} \tag{E.22}$$

the boundary term ∂A_Γ can be written as:

$$\begin{aligned}
\partial A_\Gamma &= v'^*[\![p - 2\mu\frac{\partial v}{\partial y}]\!] - u'^*[\![\mu\left(\frac{\partial u}{\partial y} + \frac{\partial v}{\partial x}\right)]\!] - w'^*[\![\mu\left(\frac{\partial w}{\partial y} + \frac{\partial v}{\partial z}\right)]\!] \\
&+ v[\![p'^* + 2\mu\frac{\partial v'^*}{\partial y} + \rho v'^* V]\!] + u[\![\mu\left(\frac{\partial u'^*}{\partial y} + \frac{\partial v'^*}{\partial x}\right) + \rho u'^* V]\!] \\
&+ w[\![\mu\left(\frac{\partial w'^*}{\partial y} + \frac{\partial v'^*}{\partial z}\right) + \rho w'^* V]\!] \\
&= v'^*\sigma\kappa + v[\![p'^* + 2\mu\frac{\partial v'^*}{\partial y} + \rho v'^* V]\!] + u[\![\mu\left(\frac{\partial u'^*}{\partial y} + \frac{\partial v'^*}{\partial x}\right) + \rho u'^* V]\!] \\
&+ w[\![\mu\left(\frac{\partial w'^*}{\partial y} + \frac{\partial v'^*}{\partial z}\right) + \rho w'^* V]\!]
\end{aligned} \tag{E.23}$$

Consider a spectral expansion of the forward variables: $\Phi = \hat{\Phi}e^{i\alpha x + i\beta z - i\omega t}$, the normal stress condition is:

$$[\![\tau_{yy}]\!] = -\frac{i\left(\alpha^2 + \beta^2\right)v}{We\left(\alpha U + \beta W - \omega\right)} = -\gamma_\omega v \tag{E.24}$$

where We denotes the Weber number and the $\hat{\cdot}$ notation has been discarded.

As a result:

$$\begin{aligned}
\partial A_\Gamma &= v\left([\![p'^* + 2\mu\frac{\partial v'^*}{\partial y} + \rho v'^* V]\!] - \gamma_\omega v'^*\right) \\
&+ u[\![\mu\left(\frac{\partial u'^*}{\partial y} + \frac{\partial v'^*}{\partial x}\right) + \rho u'^* V]\!] + w[\![\mu\left(\frac{\partial w'^*}{\partial y} + \frac{\partial v'^*}{\partial z}\right) + \rho w'^* V]\!]
\end{aligned} \tag{E.25}$$

In order to fulfil the requirement expressed in eq. (E.4), ∂A_Γ must vanish, so that:

$$\boxed{[\![p'^* + 2\mu\frac{\partial v'^*}{\partial y} + \rho v'^* V]\!] = \gamma_\omega v'^*} \tag{E.26}$$

$$\boxed{[\![\mu\left(\frac{\partial u'^*}{\partial y} + \frac{\partial v'^*}{\partial x}\right) + \rho u'^* V]\!] = 0} \tag{E.27}$$

$$\boxed{[\![\mu\left(\frac{\partial w'^*}{\partial y} + \frac{\partial v'^*}{\partial z}\right) + \rho w'^* V]\!] = 0} \tag{E.28}$$

Two-Phase adjoint linearized Navier-Stokes equations

Under the assumption presented in the previous paragraphs, adjoint linearized Navier-Stokes equation have been derived. The adjoint problem is formulated as the following:

$$\mathcal{H}^{\dagger}\Psi = \begin{bmatrix} \rho\left(-\dfrac{\partial u_i'}{\partial t} - U_j^*\dfrac{\partial u_i'}{\partial x_j} + \dfrac{\partial U_j^*}{\partial x_i}u_j'\right) - \dfrac{\partial p'}{\partial x_i} - \mu\dfrac{\partial^2 u_i'}{\partial x_j \partial x_j} \\ \\ -\dfrac{\partial u_i'}{\partial x_i} \end{bmatrix} = 0 \tag{E.29}$$

with the initial condition:

$$\mathbf{u}'(\mathbf{x}, t) = 0 \tag{E.30}$$

and boundary conditions:

at infinity (E.31)

$$u'(\pm\infty) = v'(\pm\infty) = w'(\pm\infty) = 0$$

at the interface (E.32)

$$[\![u']\!] = [\![v']\!] = [\![w']\!] = 0$$

$$[\![p' + 2\mu\frac{\partial v'}{\partial y} + \rho v' V^*]\!] = \gamma_\omega^* v' \tag{E.33}$$

$$[\![\mu\left(\frac{\partial u'}{\partial y} + \frac{\partial v'}{\partial x}\right) + \rho u' V^*]\!] = 0 \tag{E.34}$$

$$[\![\mu\left(\frac{\partial w'}{\partial y} + \frac{\partial v'}{\partial z}\right) + \rho w' V^*]\!] = 0 \tag{E.35}$$

□

From Adjoint Linear Navier-Stokes to Adjoint Linear Parabolised Stability Equations

It is possible to derive the Adjoint Linear Parabolized Stability Equations (A-LPSE) from Adjoint Linear Navier-Stokes (A-LNS) equations.

Assume that $x = \epsilon\xi$ and $z = \epsilon\zeta$, where $\epsilon = O(Re^{-1})$ are slowly-varying spatial variables and $\mathbf{U} = (U(x,y,z), \epsilon V(x,y,z), W(x,y,z))$ is a slowly-varying base flow.

Under the normal mode assumption, a generic adjoint variable ϕ can be written as:

$$\phi(x,y,z,t) = \sum_{m,n}^{M,N} \hat{\phi}(x,y) A_{mn}(x) B_{mn}(z,t) \tag{E.36}$$

with

$A_{mn}(x) = \epsilon_{mn} e^{-i\int_0^x \alpha_{mn}(\chi)\ d\chi}$

$B_{mn}(z,t) = e^{-i\beta_n z + i\omega_m t}$

The first and second derivatives can be written as:

$$\frac{\partial\phi}{\partial x} = \sum_{m,n}^{M,N} \frac{\partial}{\partial x}\left(\hat{\phi}(x,y)A_{mn}(x)\right) B_{mn}(z,t) = \tag{E.37}$$
$$\sum_{m,n}^{M,N} \frac{\partial\hat{\phi}(x,y)}{\partial x} A_{mn}(x)B_{mn}(z,t) + \sum_{m,n}^{M,N} \hat{\phi}(x,y)\frac{\partial A_{mn}(x)}{\partial x} B_{mn}(z,t) =$$
$$\sum_{m,n}^{M,N} \left(\frac{\partial\hat{\phi}(x,y)}{\partial x} - i\alpha_m(x)\phi(x,y)\right) A_{mn}(x)B_{mn}(z,t)$$

$$\frac{\partial\phi}{\partial y} = \sum_{m,n}^{M,N} \frac{\partial\hat{\phi}(x,y)}{\partial y} A_{mn}(x)B_{mn}(z,t) \tag{E.38}$$

$$\frac{\partial\phi}{\partial z} = \sum_{m,n}^{M,N} \frac{\partial}{\partial z}\left(\hat{\phi}(x,y)A_{mn}(x)B_{mn}(z,t)\right) = \sum_{m,n}^{M,N} -i\beta_n\hat{\phi}(x,y)A_{mn}(x)B_{mn}(z,t) \tag{E.39}$$

$$\frac{\partial\phi}{\partial t} = \sum_{m,n}^{M,N} (i\omega_m)\,\hat{\phi}(x,y)A_{mn}(x)B_{mn}(z,t) \tag{E.40}$$

$$\frac{\partial^2\phi}{\partial x^2} = \frac{\partial}{\partial x}\left(\frac{\partial\phi}{\partial x}\right) = \sum_{m,n}^{M,N}\frac{\partial}{\partial x}\left(\frac{\partial\hat{\phi}(x,y)}{\partial x} - i\alpha_m(x)\phi(x,y)\right)A_{mn}(x)B_{mn}(z,t) \tag{E.41}$$

$$= \sum_{m,n}^{M,N}\frac{\partial}{\partial x}\left(\frac{\partial\hat{\phi}(x,y)}{\partial x} - i\alpha_m(x)\hat{\phi}(x,y)\right)A_{mn}(x)B_{mn}(z,t)$$

$$+ \sum_{m,n}^{M,N}\left(\frac{\partial\hat{\phi}(x,y)}{\partial x} - i\alpha_m(x)\hat{\phi}(x,y)\right)\frac{\partial A_{mn}(x)}{\partial x}B_{mn}(z,t)$$

$$= \sum_{m,n}^{M,N}\left(\frac{\partial^2\hat{\phi}(x,y)}{\partial x^2} - i\frac{\partial\alpha_m(x)\hat{\phi}(x,y)}{\partial x}\right)A_{mn}(x)B_{mn}(z,t)$$

$$+ \left(\frac{\partial\hat{\phi}(x,y)}{\partial x} - i\alpha_m(x)\hat{\phi}(x,y)\right)(-i\alpha_m(x))\,A_{mn}(x)B_{mn}(z,t)$$

$$= \sum_{m,n}^{M,N}\left(\frac{\partial^2\hat{\phi}(x,y)}{\partial x^2} - \frac{\partial a(x)}{\partial x}\hat{\phi}(x,y) - i2\alpha_m\frac{\partial\hat{\phi}(x,y,)}{\partial x} + \alpha_m^2\hat{\phi}(x,y)\right)A_{mn}(x)B_{mn}(z,t)$$

$$\frac{\partial^2\phi}{\partial y^2} = \sum_{m,n}^{M,N}\frac{\partial^2\hat{\phi}(x,y)}{\partial y^2}A_{mn}(x)B_{mn}(z,t) \tag{E.42}$$

$$\frac{\partial^2\phi}{\partial z^2} = \sum_{m,n}^{M,N}\beta_n^2\hat{\phi}(x,y)A_{mn}(x)B_{mn}(z,t) \tag{E.43}$$

Under the slowly-varying assumption, some derivatives can be discarded. In fact:

$$\frac{\partial^2\hat{\phi}}{\partial x^2} \ll O(1) \qquad \frac{\partial^2\alpha_m}{\partial x^2} \ll O(1)$$

$$\frac{1}{Re}\frac{\partial\bar{\phi}}{\partial x} \ll O(1) \qquad \frac{\partial^2\bar{\phi}}{\partial x^2} \ll O(1)$$

It is possible to write the eq.(E.29) as the following:

$$\begin{aligned}
\rho\left(-i\omega_m u - U\frac{\partial u}{\partial x} + Ui\alpha_m u - V\frac{\partial u}{\partial y} + Wi\beta_n u + \frac{\partial U}{\partial x}u + \frac{\partial V}{\partial x}v + \frac{\partial W}{\partial x}w\right) =& \frac{\partial p}{\partial x} - i\alpha_m p \\
&+\frac{\mu}{Re}\left(-i\frac{\partial a}{\partial x}u + 2i\alpha_m\frac{\partial u}{\partial x} + \left(\alpha_m^2+\beta_n^2\right)u + \frac{\partial^2 u}{\partial y^2}\right) \\
\rho\left(-i\omega_m v - U\frac{\partial v}{\partial x} + Ui\alpha_m v - V\frac{\partial v}{\partial y} + Wi\beta_n v + \frac{\partial U}{\partial y}u + \frac{\partial V}{\partial y}v + \frac{\partial W}{\partial y}w\right) =& \frac{\partial p}{\partial y} \\
&+\frac{\mu}{Re}\left(-i\frac{\partial a}{\partial x}v + 2i\alpha_m\frac{\partial v}{\partial x} + \left(\alpha_m^2+\beta_n^2\right)v + \frac{\partial^2 v}{\partial y^2}\right) \\
\rho\left(-i\omega_m w - U\frac{\partial w}{\partial x} + Ui\alpha_m w - V\frac{\partial w}{\partial y} + Wi\beta_n w + \frac{\partial U}{\partial z}u + \frac{\partial V}{\partial z}v + \frac{\partial W}{\partial z}w\right) =& \frac{\partial p}{\partial z} - i\beta_n p \\
&+\frac{\mu}{Re}\left(-i\frac{\partial a}{\partial x}w + 2i\alpha_m\frac{\partial w}{\partial x} + \left(\alpha_m^2+\beta_n^2\right)w + \frac{\partial^2 w}{\partial y^2}\right) \\
-\frac{\partial u}{\partial x} + i\alpha_m u - \frac{\partial v}{\partial y} + i\beta_n w =& 0
\end{aligned}$$

The adjoint Parabolized Stability Equations can be written as:

$$\mathcal{L}^{\dagger}_{mn}\mathbf{\Psi}_{mn} = 0 \tag{E.44}$$

where

$$\begin{aligned}
\mathcal{L}^{\dagger}_{mn} &= -i\omega_m + i\alpha_m\mathbf{A} - \mathbf{B}\frac{\partial}{\partial y} - \mathbf{C}\frac{\partial^2}{\partial y^2} + i\beta_n\mathbf{D} + \mathbf{E} - \mathbf{M}\frac{\partial}{\partial x} + \frac{\partial \alpha_m}{\partial x}\mathbf{N} \qquad \text{(E.45)} \\
\mathbf{\Psi}_{mn} &= [u'_{mn}\ v'_{mn}\ w'_{mn}\ p'_{mn}]^T
\end{aligned}$$

and generic component of $\mathbf{\Psi}_{mn}$ is written as:

$$\psi'(x,y,z) = \sum_{m,n}^{M,N} \hat{\psi}'(x,y)A^{\dagger}_{mn}(x)B^{\dagger}_{mn}(z,t) \tag{E.46}$$

with

$$A^{\dagger}_{mn}(x) = \epsilon_{mn}e^{-i\int_0^x \alpha_{mn}(\chi)\ d\chi}$$

$$B^{\dagger}_{mn}(z,t) = e^{-i\beta_n z + i\omega_m t}$$

The matrices $\mathbf{G}, \mathbf{A}, \mathbf{B}, \mathbf{C}, \mathbf{D}, \mathbf{E}, \mathbf{N}, \mathbf{M}$ are now given.

$$\mathbf{A}=\begin{bmatrix}\rho U & 0 & 0 & 1\\ 0 & \rho U & 0 & 0\\ 0 & 0 & \rho U & 0\\ 1 & 0 & 0 & 0\end{bmatrix}\qquad \mathbf{B}=\begin{bmatrix}\rho V & 0 & 0 & 0\\ 0 & \rho V & 0 & 1\\ 0 & 0 & \rho V & 0\\ 0 & 1 & 0 & 0\end{bmatrix}\qquad \mathbf{D}=\begin{bmatrix}\rho W & 0 & 0 & 0\\ 0 & \rho W & 0 & 0\\ 0 & 0 & \rho W & 1\\ 0 & 0 & 1 & 0\end{bmatrix}$$

$$\mathbf{C}=\frac{\mu}{Re}\begin{bmatrix}1 & 0 & 0 & 0\\ 0 & 1 & 0 & 0\\ 0 & 0 & 1 & 0\\ 0 & 0 & 0 & 0\end{bmatrix}\qquad \mathbf{G}=\begin{bmatrix}\rho & 0 & 0 & 0\\ 0 & \rho & 0 & 0\\ 0 & 0 & \rho & 0\\ 0 & 0 & 0 & 0\end{bmatrix}\qquad \mathbf{N}=\frac{i\mu}{Re}\begin{bmatrix}1 & 0 & 0 & 0\\ 0 & 1 & 0 & 0\\ 0 & 0 & 1 & 0\\ 0 & 0 & 0 & 0\end{bmatrix}$$

$$\mathbf{E}=\begin{bmatrix}\rho\frac{\partial U}{\partial x}-\frac{\mu}{Re}\left(\alpha_m^2+\beta_n^2\right) & \rho\frac{\partial V}{\partial x} & \rho\frac{\partial W}{\partial x} & 0\\ \rho\frac{\partial U}{\partial y} & \rho\frac{\partial V}{\partial y}-\frac{\mu}{Re}\left(\alpha_m^2+\beta_n^2\right) & \rho\frac{\partial W}{\partial y} & 0\\ \rho\frac{\partial U}{\partial z} & \rho\frac{\partial V}{\partial z} & \rho\frac{\partial W}{\partial z}-\frac{\mu}{Re}\left(\alpha_m^2+\beta_n^2\right) & 0\\ 0 & 0 & 0 & 0\end{bmatrix}$$

$$\mathbf{M}=\begin{bmatrix}\rho U+2i\alpha_m\frac{\mu}{Re} & 0 & 0 & 1\\ 0 & \rho U+2i\alpha_m\frac{\mu}{Re} & 0 & 0\\ 0 & 0 & \rho U+2i\alpha_m\frac{\mu}{Re} & 0\\ 1 & 0 & 0 & 0\end{bmatrix}$$

The adjoint interfacial jump conditions can be derived applying the parabolization technique to eq.(E.35):

at infinity (E.47)

$$u'(\pm\infty)=v'(\pm\infty)=w'(\pm\infty)=0$$

at the interface (E.48)

$$[\![u']\!]=[\![v']\!]=[\![w']\!]=0$$

$$[\![p'+2\mu\frac{\partial v'}{\partial y}+\rho v'V^*]\!]=\gamma_\omega^* v' \tag{E.49}$$

$$[\![\mu\left(\frac{\partial u'}{\partial y}+(\frac{\partial}{\partial x}-i\alpha_m)v'\right)+\rho u'V^*]\!]=0 \tag{E.50}$$

$$[\![\mu\left(\frac{\partial w'}{\partial y}-i\beta_n v'\right)+\rho w'V^*]\!]=0 \tag{E.51}$$

□

From Adjoint Linea Navier-Stokes to Adjoint Orr-Sommerfeld and Squire

It is possible to derive the Adjoint Orr-Sommerfeld and Squire Equations (A-OSSq) from A-LNS.

Assume a parallel base flow $\mathbf{U} = (U(y), 0, 0)$. Under the normal mode assumption, a generic adjoint variable ϕ can be written as:

$$\phi(x, y, z, t) = \hat{\phi}(y) e^{-i\alpha x - i\beta z + i\omega t} \tag{E.52}$$

Write the first and second derivatives as:

$$\frac{\partial \phi}{\partial x} = -i\alpha\phi \tag{E.53}$$
$$\frac{\partial \phi}{\partial z} = -i\beta\phi \tag{E.54}$$
$$\frac{\partial \phi}{\partial t} = i\omega\phi \tag{E.55}$$
$$\Delta\phi = \left(\frac{\partial^2}{\partial x^2} + \frac{\partial^2}{\partial y^2} + \frac{\partial^2}{\partial z^2}\right)\phi = \left(D^2 - k^2\right)\phi \tag{E.56}$$
$$\tag{E.57}$$

where $D := \frac{\partial}{\partial y}$ and $k^2 = \alpha^2 + \beta^2$.

Discarding the $\hat{\cdot}$ notation, we can then write the eq.(E.29) as the following:

$$\rho\left(-i\omega u + i\alpha U u\right) = -i\alpha p + \mu\left(D^2 - k^2\right)u \tag{E.58}$$
$$\rho\left(-i\omega v + i\alpha U v + \frac{\partial U}{\partial y}u\right) = Dp + \mu\left(D^2 - k^2\right)v \tag{E.59}$$
$$\rho\left(-i\omega w + i\alpha U w\right) = -i\beta p + \mu\left(D^2 - k^2\right)w \tag{E.60}$$
$$i\alpha u - Dv + i\beta w = 0 \tag{E.61}$$

Adjoint Squire Equation Define:

$$\eta = \frac{\partial u}{\partial z} - \frac{\partial w}{\partial x} = -i\beta u + i\alpha w \tag{E.62}$$

The Adjoint Squire equation is:

$$\left[-i\omega\rho + i\alpha U - \mu\left(D^2 - k^2\right)\right]\eta = 0 \tag{E.63}$$

Let $\mathcal{H}$ be an operator such that $\mathcal{H} = \rho\mathcal{M} - \mu\Delta$ and $\mathcal{H}^{-1}$ exists, where $\mathcal{M} = (-i\omega + i\alpha U)$; then the adjoint adjoint Squire equation satisfies:

$$\mathcal{H}\eta = 0 \tag{E.64}$$

Adjoint Orr-Sommerfeld Equation Re-write eq.(E.58)-(E.61) using the operator $\mathcal{H}$.

$$\mathcal{H}u = -i\alpha u \tag{E.65}$$

$$\mathcal{H}v + \frac{\partial U}{\partial y}u = Dp \tag{E.66}$$

$$\mathcal{H}w = -i\beta w \tag{E.67}$$

$$\mathcal{H}v = i\alpha u + i\beta w \tag{E.68}$$

From eq.(E.65), (E.67) and with the use of eq.(E.68), we have that:

$$\mathcal{H}(i\alpha u + i\beta w) = \mathcal{H}(Dv) = k^2 p \tag{E.69}$$

Pressure is then proportional to the operator $\mathcal{H}$ acting on a linear combination of Dv and η, since eq.(E.64) holds. In fact,

$$p = \frac{1}{k^2}\mathcal{H}(Dv + c\eta) \tag{E.70}$$

where c is a constant to be determined.

From eq.(E.65) and (E.67):

$$u = \mathcal{H}^{-1}(-i\alpha p) = -i\alpha\mathcal{H}^{-1}(p) = \frac{-i\alpha}{k^2}(Dv + c_1\eta) \tag{E.71}$$

$$w = \mathcal{H}^{-1}(-i\beta p) = -i\beta\mathcal{H}^{-1}(p) = \frac{-i\beta}{k^2}(Dv + c_2\eta) \tag{E.72}$$

Using eq.(E.68):

$$\begin{aligned} Dv &= \frac{\alpha^2}{k^2}(Dv + c_1\eta) + \frac{\beta^2}{k^2}(Dv + c_2\eta) \\ &= Dv + \frac{1}{k^2}\left(\alpha^2 c_1 + \beta^2 c_2\right)\eta \Longleftrightarrow \alpha^2 c_1 + \beta^2 c_2 = 0 \end{aligned} \tag{E.73}$$

An additional condition can be derived from the kinetic energy, known to be $E = \frac{1}{k^2}\left(|Dv|^2 + k^2|v| + |\eta|^2\right)$.

$$E = |u|^2 + |v|^2 + |w|^2 = \frac{1}{k^2}\left(|Dv|^2| + k^2|v|^2 + \frac{\alpha^2 c_1^2 + \beta^2 c_2^2}{k^2}|\eta|^2\right) \tag{E.74}$$
$$\implies \frac{\alpha^2 c_1 + \beta^2 c_2}{k^2} = 1$$

Constants c_1 and c_2 can be easily determined:

$$\left\{ \begin{array}{rcl} \alpha^2 c_1^2 + \beta^2 c_2^2 & = & \alpha^2 + \beta^2 \\ \alpha^2 c_1 + \beta^2 c_2 & = & 0 \end{array} \right. \implies \begin{array}{rcl} c_1 & = & \beta/\alpha \\ c_2 & = & -\alpha/\beta \end{array}$$

Consider eq.(E.66)

$$\mathcal{H}v + \frac{\partial U}{\partial y}\left(-i\frac{\alpha}{k^2}(Dv + \tfrac{\beta}{\alpha}\eta)\right) = D\left(\frac{1}{k^2}\mathcal{H}(Dv + \tfrac{\beta}{\alpha}\eta)\right) = D\left(\frac{1}{k^2}\mathcal{H}(Dv)\right) \tag{E.75}$$
$$k^2\mathcal{H}v - i\alpha\frac{\partial U}{\partial y}Dv - i\beta\frac{\partial U}{\partial y}\eta = D(\mathcal{H}(Dv)) \tag{E.76}$$
$$k^2\left(-i\omega\rho v + i\alpha\rho U v - \mu(D^2 - k^2)v\right) - i\alpha\rho\frac{\partial U}{\partial y}Dv - i\beta\frac{\partial U}{\partial y}\eta = \tag{E.77}$$
$$- i\omega\rho D^2 v + i\alpha\rho\frac{\partial U}{\partial y}Dv + i\alpha\rho U D^2 v + \mu(D^2 - k^2)^2 v$$
$$\left[i\rho(\omega - i\alpha U)(D^2 - k^2) - \mu(D^2 - k^2)^2\right]v - i2\alpha\rho\frac{\partial U}{\partial y}Dv - i\beta\frac{\partial U}{\partial y} = 0 \tag{E.78}$$

The adjoint Orr-Sommerfeld equation is then:

$$\left[i\rho(\omega - i\alpha U)(D^2 - k^2) - \mu(D^2 - k^2)^2\right]v - i2\alpha\rho\frac{\partial U}{\partial y}Dv - i\beta\frac{\partial U}{\partial y} = 0 \tag{E.79}$$

Adjoint Orr-Sommerfeld and Squire equations Under the assumption of parallel flow and normal modes, A-LNS take the form:

$$\left[\begin{array}{cc} \mathcal{L}_{OS}^{\dagger} & -i\beta\frac{\partial U}{\partial y} \\ 0 & \mathcal{L}_{Sq}^{\dagger} \end{array}\right]\left[\begin{array}{c} v \\ \eta \end{array}\right] = 0 \tag{E.80}$$

with

$$\mathcal{L}_{OS}^{\dagger} = \left[i\rho(\omega - i\alpha U)(D^2 - k^2) - \mu(D^2 - k^2)^2\right] - i2\alpha\rho\frac{\partial U}{\partial y}D \tag{E.81}$$
$$\mathcal{L}_{Sq}^{\dagger} = \left[-i\omega\rho + i\alpha U - \mu\left(D^2 - k^2\right)\right]$$

and interfacial boundary conditions as the following:

$$\begin{aligned}
&[\![\alpha Dv + \beta\eta]\!] = 0 \\
&[\![v]\!] = 0 \\
&[\![\beta Dv - \alpha\eta]\!] = 0 \\
&[\![\left(-i\omega\rho + i\alpha\rho U - \mu(D^2 - k^2 - 2)\right) Dv]\!] = \frac{-ik^4}{We(\alpha U - \omega)}v \\
&[\![\mu(\alpha D^2 v + \beta D\eta)]\!] = 0 \\
&[\![\mu(\beta D^2 v - \alpha D\eta)]\!] = 0
\end{aligned} \tag{E.82}$$

□

Bibliography

Andersson, P., Berggren, M. & Henningson, D. S. 1997 Optimal disturbances in boundary layers. *Progress in System Control* .

Andersson, P., Berggren, M. & Henningson, D. S. 1999 Optimal disturbances and bypass transition in boundary layers. *Physics of Fluids* **11**, 134–150.

Andersson, P., Brandt, L., Bottaro, A. & Henningson, D. S. 2001 On the breakdown of boundary layer streaks. *Journal of Fluid Mechanics* **428**, 29–60.

Ashpis, D. E. & Reshotko, E. 1990 The vibrating ribbon problem revisited. *Journal of Fluid Mechanics* **213**, 513 – 547.

Benjamin, T. B. 1959 Shearing flow over a wavy boundary. *Journal of Fluid Mechanics* **6**, 161 – 170.

Benney, D. J. & Gustavsson, L. H. 1981 A new mechanism for linear and nonlinear hydrodynamic instability. *Studies in Applied Mathematics* **64** (3), 185–209.

Beres, J. H., Alexander, M. J. & Holton, J. R. 2002 Effects of tropospheric wind shear on the spectrum of convectively generated gravity waves. *Journal of Atmospherical Science* **59**, 1805–1824.

Berggren, M. 1995 Optimal control of time evolution systems: Controllability investigations and numerical algorithms. PhD thesis.

Berggren, M., Glowinski, R. & Lions, J. L. 1996 A computational approach to controllability issues for flow-related models. i. pointwise control of the viscous burgers equation. *International Journal of Computational Fluid Dynamics* **237** (7).

Berlin, S. & Henningson, D. S. 1999 A nonlinear mechanism for receptivity of free-stream disturbances. *Physics of Fluids* **11**, 3749–3760.

Bohr, N. 1909 Determination of surface-tension of water by the method of jet vibration. *Philosophical Transaction of the Royal Society* **174**, 935 – 982.

Boomkamp, P. A. M., Boersma, B. J., Miesen, R. H. M. & Beijnon, G. V. 1997 A Chebyshev collocation method for solving two-phase flow stability problems. *Journal of Computational Physics* **132** (2), 191 – 200.

Brackbill, J., Kothe, D. & Zemach, C. 1992 A continuum method for modeling surface tension. *Journal of Computational Physics* **100**, 335–354.

Brandt, L. & Henningson, D. S. 2002 Transition of streamwise streaks in zero-pressure gradient boundary layers. *Journal of Fluid Mechanics* **472**, 229–262.

Brandt, L., Schlatter, P. & Henningson, D. 2004 Transition in boundary layers subject to free-stream turbulence. *Journal of Fluid Mechanics* **517**, 167–198.

Butler, K. M. & Farrell, B. F. 1992 Three-dimensional optimal perturbations in viscous shear flow. *Physics of Fluids* **4**, 1637–1650.

Cheung, L. C. 2007 Aeroacoustic noise prediction and the dynamics of shear layers and jets using the nonlinear parabolized stability equations. PhD thesis, Stanford University.

Cheung, L. C. & Lele, S. K. 2009 Linear and non-linear processes in two-dimensional mixing layer dynamics and sound radiation. *Journal of Fluid Mechanics* **625**, 321–351.

Cheung, L. C. & Zaki, T. A. 2010 Linear and nonlinear instability waves in spatially developing two-phase mixing layers. *Physics of Fluids* **22**, 052103.

Corbett, P. & Bottaro, A. 2000 Optimal perturbations for boundary layers subject to streamwise pressure gradient. *Physics of Fluids* **12**, 120–131.

Danabasoglu, G. & Biringen, S. 1990 A Chebyshev matrix method for the spatial modes of the Orr-Sommerfeld equation. *International Journal of Numerical Methods in Fluids* **11**, 1033 – 1037.

Desjardins, O., Moureau, V. & Pitsch, H. 2008 An accurate conservative level set/ghost fluid method for simulating turbulent atomization. *Journal of Computational Physics* **227**, 8395–8416.

Drazin, P. G. & Rein, W. H. 1981 *Hydrodynamic stability*. Cambridge, UK: Cambridge University Press.

Ellingsen, T. & Palm, E. 1975 Stability of linear flow. *Physics of Fluids* **18** (4), 487–488.

Fedkiw, R., Aslam, T., Merriman, B. & Osher, S. 1999 A non-oscillatory eulerian approach to interfaces in multimaterial flows (the ghost fluid method). *Journal of Computational Physics* **152**, 457–492.

Gaster, M. 1975 A theoretical model of a wave packet in the boundary layer on a flat plate. *Proceedings of the Royal Society of London. Series A, Mathematical and Physical Sciences* **347** (1649), 271–289.

Grosch, C. E. & Salwen, H. 1978 The continuous spectrum of the Orr-Sommerfeld equation. Part 1. The spectrum and the eigenfunctions. *Journal of Fluid Mechanics* **87**.

Guillame, P. 1999 Nonlinear eigenproblems. *SIAM Journal of Matrix Analysis and Applications* **20** (3), 575–595.

Gustavsson, L. H. 1981 Resonant growth of three-dimensional disturbances in plane Poiseuille flow. *Journal of Fluid Mechanics* **112**, 253–264.

Gustavsson, L. H. & Hultgren, L. S. 1980 A resonance mechanism in plane Couette flow. *Journal of Fluid Mechanics* **98**, 149–159.

Haj-Hariri, H. 1988 Transformations reducing the order of the parameter in differential eigenvalue problems. *Journal of Computational Physics* **77**, 472–484.

Gad-el Hak, M. 2000 *Flow control: passive, active, and reactive flow management*. Cambridge Univ. Press, London.

Heisenberg, W. 1951 On stability and turbulence of fluid flows. *Technical Memoranda of the National Advisory Committee for Aeronautics* **1291**.

Henningson, D. S. & Reddy, S. C. 1994 On the role of linear mechanism in transition to turbulence. *Physics of Fluids* **6**, 1949.

Herbert, T. 1997 Parabolized stability equations. *Ann. Rev. of Fluid Mech.* **29**, 245–283.

Higham, N. J., Li, R. & Tisseur, F. 2007 Backward error of polynomial eigenproblems solved by linearization. *SIAM Journal of Matrix Analysis and Applications* **29**, 1218–1241.

Hinch, E. J. 1984 A note on the mechanism of the instability at the interface between two shearing fluids. *Journal of Fluid Mechanics* **144**, 463–465.

Hodson, H. P. & Howell, R. J. 2005 Bladerow interactions, transition, and high-lift aerofoils in low-pressure turbines. *Annual Review of Fluid Mechanics.* **37**, 71–98.

Hooper, A. P. & Boyd, W. G. C. 1983 Shear flow instability at the interface between viscous fluids. *Journal of Fluid Mechanics* **128**, 507–528.

Hooper, A. P. & Boyd, W. G. C. 1987 Shear flow instability due to a wall and a viscosity discontinuity at the interface. *Journal of Fluid Mechanics* **179**, 201–205.

Hultgren, L. S. & Gustavsson, L. H. 1981 Algebraic growth of disturbances in a laminar boundary layer. *Physics of Fluids* **924**, 1000.

Jacobs, R. G. & Durbin, P. A. 1998 Shear sheltering and the continuous spectrum of the orr-sommerfeld equation. *Physics of Fluids* **10**.

Jacobs, R. G. & Durbin, P. A. 2001 Simulations of bypass transition. *Journal of Fluid Mechanics* **428**, 185–212.

Kendall, J. M. 1991 Studies on laminar boundary layer receptivity to free-stream turbulence near a leading edge. *ASME Fluids Engineering Division* **114**, 43.

Kim, J. & Bewley, T. R. 2007 A linear systems approach to flow control. *Annual Review of Fluid Mechanics.* **39**, 383417.

Kim, J. & Moin, P. 1991 Application of a fractional-step method to incompressible navier-stokes equations. *Journal of Computational Physics* **92**, 369–379.

Klebanoff, P. 1971 Effect of freestream turbulence on the laminar boundary layer. *Bullettin of American Physics Society* **10** (11), 1323.

Landau, L. D. 1944 On the problem of turbulence. *Comptes Rendus de l'Acadmie des Sciences de l'URSS* **44**, 311–314.

Landau, L. D. & Lifshitz, E. M. 1959 *Course of Theoretical Physics - Fluid Mechanics*, , vol. 6.

Landhal, M. T. 1980 A note on algebraic instability in inviscid parallel shear flows. *Journal of Fluid Mechanics* **98**, 243.

Lasseigne, D. G., Joslin, R. D., Jackson, T. L. & Criminale, W. O. 1999 The transient period for boundary layer disturbances. *Journal of Fluid Mechanics* **381**, 89.

Lauchle, G. & Gurney, G. 1984 Laminar boundary-layer transition on a heated underwater body. *Journal of Fluid Mechanics* **144**, 79–101.

Luchini, P. 1996 Reynolds number independent instability of the blasius boundary layer over a flat surface. *Journal of Fluid Mechanics* **327**, 101.

Luchini, P. 2000 Reynolds number independent instability of the blasius boundary layer over a flat surface, part 2: Optimal disturbances. *Journal of Fluid Mechanics* **404**, 289.

Malik, S. V. & Hooper, A. P. 2005 Linear stability and energy growth of viscosity stratified flows. *Physics of Fluids* **17**, 024101.

Malik, S. V. & Hooper, A. P. 2007 Three-dimensional disturbances in channel flows. *Physics of Fluids* **19**.

Mason, J. C. & Phillis, T. N. 2005 Chebyshev polynomials and spectral methods. *Numerical Algorithms* **38**.

Matsubara, M. & Alfredsson, P. H. 2001 Disturbance growth in boundary layers subjected to free-stream turbulence. *Journal of Fluid Mechanics* **430**, 149–168.

Miesen, R. & Boersma, B. J. 1995 Hydrodynamic stability of a sheared liquid film. *Journal of Fluid Mechanics* **301**, 175–202.

Miles, J. W. 1960 The hydrodynamic stability of a thin film of liquid in uniform shearing motion. *Journal of Fluid Mechanics* **8**, 593.

Miles, J. W. 1962*a* A note on the inviscid Orr-Sommerfeld equation. *Journal of Fluid Mechanics* **13**, 427.

Miles, J. W. 1962*b* On the generation of surface waves by shear flows. part 4. *Journal of Fluid Mechanics* **13**, 433.

Monokrousos, A. 2011 Optimizationa and control of shear flows. PhD thesis, KTH.

Nelson, J. J., Alving, A. E. & Joseph, D. D. 1995 Boundary layer flow of air over water on a flat plate. *Journal of Fluid Mechanics* **284**, 159–169.

Noether, F. 1921 Das turbulenzproblem. *Z. Angew. Math. Mech.* **1**, 125 – 138 and 218–219.

van Noorden, T. L., Boomkamp, P. A. M., Knaap, M. C. & Verheggen, T. M. M. 1998 Transient growth in parallel two-phase flow: Analogies and differences with single-phase flow. *Physics of Fluids* **10**.

Olsson, E. & Kreiss, G. 2005 A conservative level set method for two phase flow. *Journal of Computational Physics* **210**, 225–246.

Olsson, E. & Kreiss, G. 2007 A conservative level set method for two phase flow ii. *Journal of Computational Physics* **225**, 785–807.

Orszag, S. A. 1971 Accurate solution of the Orr-Sommerfeld stability equation. *Journal of Fluid Mechanics* **50** (4), 689–703.

Ozgen, S., Carbonaro, M. & Sarma, G. S. R. 2002 Experimental study of wave characteristics on a thin layer of de/anti-icing fluid. *Physics of Fluids* **14** (10), 3391–3402.

Ozgen, S., Degrez, G. & Sarma, G. S. R. 1998 Two-fluid boundary layer instability. *Physics of Fluids* **10**, 2746 – 2757.

Panton, R. L. 1996 *Incompressible flow*. John Wiley & Sons, Inc.

Phillips, O. M. 1957 On the generation of waves by turbulent wind. *Journal of Fluid Mechanics* **2**, 417.

Pringle, C. C. T. & Kerswell, R. R. 2010 Using nonlinear transient growth to construct the minimal seed for shear flow turbulence. *Physics Review Letters* **10**, 154505–1/4.

Reed, H. L., Saric, W. S. & Arnal, D. 1996 Linear stability theory applied to boundary layers. *Annual Review of Fluid Mechanics.* **28**, 389–428.

Renardy, Y. 1987 The thin layer effect and interfacial stability in a two-layer couette flow with similar liquids. *Physics of Fluids* **30**, 1627–1637.

Reynolds, O. 1883 An experimental investigation of the circumstances which determine whether the motion of water shall be direct or sinuous, and of the law of resistance in parallel channels. *Philosophical Transaction of the Royal Society* **174**, 935 – 982.

Rosenfeld, M., Kwak, D. & Vinokur, M. 1991 A fractional step solution method for the unsteady incompressible navier–stokes equations in generalised coordinate systems. *Journal of Computational Physics* **94**, 102–137.

Ruhe, A. 1973 Algorithms for the nonlinear eigenvalue problem. *SIAM Journal of Numerical Analysis* **10** (4), 674–689.

S. C. Reddy, P. J. S. & Henningson, D. H. 1993 Pseudospectra of the orr-sommerfeld operator. *SSIAM Journal of Applied Mathematics* **53**, 15–47.

Saha, S. 2011 On vortical disturbances in single and two-fluid boundary layers. PhD thesis, Imperial College London.

Salwen, H. & Grosch, C. E. 1981 The continuous spectrum of the Orr-Sommerfeld equation. Part 2. Eigenfunction expansions. *Journal of Fluid Mechanics* **104**, 445–465.

Saric, W. S., Reed, H. L. & Kerschen, E. J. 2002 Boundary layer receptivity to free-stream disturbances. *Annual Review of Fluid Mechanics.* **34**, 291–319.

Schlichting, H. 1933 Berechnung der Anfachung kleiner Störungen bei der Plattenströmung. *ZAMM* **13**, 171–174.

Schlichting, H. 1987 *Boundary-layer theory*. Springer.

Schmid, P. J. 2007 Nonmodal stability theory. *Ann. Rev. of Fluid Mech.* **39**, 129–162.

Schmid, P. J. & Henningson, D. S. 2001 *Stability and transition in Shear Flows*. New York, USA: Springer.

Schmid, P. J., Lundbladh, A. & Henningson, D. S. 1994 Spatial evolution of disturbances in plane poiseuille flow. *Transition, Turbulence and Combustion* **1**, 287.

Schubauer, G. & Skramstad, H. 1941 Laminar boundary-layer oscillations and stability of laminar flow. *N.A.C.A Rep* **W8**.

South, M. J. & Hooper, A. P. 1999 Linear growth in two-fluid plane poiseuille flow. *Journal of Fluid Mechanics* **381**, 121–139.

Tempelmann, D., Hanifi, A. & Henningson, D. S. 2010 Spatial optimal growth in three-dimensional boundary layers. *Journal of Fluid Mechanics* **646**, 5–37.

Tisseur, F. & Meerbegen, K. 2001 The quadratic eigenvalue problem. *SIAM Review* **43** (2), 235–286.

Tollmien, W. 1929 Über die Entstehung der Turbulenz. *Nachr. Ges. Wiss. Göttingen* **1**, 21–44.

Trefethen, L. N., Trefethen, A. E., Reddy, S. C. & Driscoll, T. A. 1993 Hydrodynamics stability without eigenvalues. *Science* **261**, 578.

Tumin, A. & Reshotko, E. 2001 Spatial theory of optimal disturbances in boundary layers. *Physics of Fluids* **13**, 2097–2104.

Westin, K. J. A., Boiko, A. V., Klingmann, B. G. B., Kozlov, V. V. & Alfredsson, P. H. 1994 Studies on laminar boundary layer receptivity to free-stream turbulence near a leading edge. *Journal of Fluid Mechanics* **281**, 193–218.

Yecko, P. 2003 Disturbance growth in primary atomization: three-dimensionality, transient amplification and non-parallel flow effects. *ILASS Americas* .

Yecko, P. 2008 Disturbance growth in two-fluid channel flow: The role of capillarity. *International Journal of Multiphase flow* **34**, 272–282.

Yecko, P. & Zaleski, S. 2005*a* Transient growth in two-phase mixing layers. *Journal of Fluid Mechanics* **528**, 43–52.

Yecko, P. & Zaleski, S. 2005*b* Transient growth in two-phase mixing layers. *Journal of Fluid Mechanics* **528**, 43–58.

Yih, C. 1990 Wave formation on a liquid layer for de-icing airplane wings. *Journal of Fluid Mechanics* **212**, 41–53.

Yih, C. S. 1967 Instability due to viscosity stratification. *Journal of Fluid Mechanics* **27**, 337–352.

Zaki, T. A. 2005 Continuous mode interaction and the bypass route to transition. PhD thesis, Stanford University.

Zaki, T. A. & Durbin, P. A. 2005 Mode interaction and the bypass route to transition. *Journal of Fluid Mechanics* **531**, 85–111.

Zaki, T. A. & Durbin, P. A. 2006 Continuous mode transition and the effects of pressure gradient. *Journal of Fluid Mechanics* **563**, 357–388.

Zaki, T. A. & Saha, S. 2009 On shear sheltering and the structure of vortical modes in single- and two-fluid boundary layers. *Journal of Fluid Mechanics* **626**, 111–147.

Zhang, X. F., Vera, M., Hodson, H. & Harvey, N. 2006 Separation and transition control on an aft-loaded ultra-high-lift LP turbine blade at low Reynolds numbers: Low-speed investigation. *Journal of Turbomachinery* **128** (3), 517–527.

Zhigulev, V. N., Sidorenko, N. V. & Tumin, A. 1980 Generation of instability waves in a boundary layer by external turbulence. *Journal of Applied Mechanics and Technical Physics* **21**, 774.

Zuccher, S., Bottaro, A. & Luchini, P. 2005 Algebraic growth in a blasius bounday layer: Nonlinear optimal disturbances. *European Journal of Mechanics B/Fluids* pp. 1 – 17.